UC San Diego
UC San Diego Electronic Theses and Dissertations

Title
Molecular targeting with peptide based probes for the imaging and treatment of cancer

Permalink
https://escholarship.org/uc/item/6br1p66m

Author
Crisp, Jessica Leigh

Publication Date
2012

Peer reviewed|Thesis/dissertation

UNIVERSITY OF CALIFORNIA SAN DIEGO

Molecular Targeting with Peptide Based Probes for the Imaging and Treatment of Cancer

A dissertation submitted in partial satisfaction of the requirements for the degree Doctor of Philosophy

in

Chemistry

by

Jessica Leigh Crisp

Committee in charge:

  Professor Roger Y. Tsien, Chair
  Professor Partho Ghosh
  Professor Pat Jennings
  Professor Robert Mattrey
  Professor Jerry Yang

2012

The Dissertation of Jessica Leigh Crisp is approved, and it is acceptable in quality and form for publication on microfilm and electronically:

_____

_____

_____

_____

_____
Chair

University of California, San Diego

2012

iii

DEDICATION

In dedication to Dr. William Earl Crisp Jr.,

a man who had a true love for science

TABLE OF CONTENTS

LIST OF FIGURES

LIST OF TABLES

ACKNOWLEDGEMENTS

I would like to acknowledge the following people for without whom this research would not have been possible:

Dr. Roger Y. Tsien	Dr. Mike Whitney
Paul Steinbach	Dr. Elamprakash Savariar
Dr. Todd Aguilera	Dr. Stephen Adams
Dr. Lesley Ellies	Dr. Quyen Nguyen
Dr. Tao Jiang	Dr. Emilia Olson
Qing Xiong	Dr. Larry Gross
Perla Arcaira	Heather Glasgow
Dr. Beth Friedman	Joan Kanter
Rachel Levin	Timothy Salazar

I would also like to acknowledge my parents, Bill and Dale Crisp, for their continuous love and support, and for always telling me that my dreams could come true. I would also like to thank my husband, Cameron McKenzie, for listening to my gripe about the numerous failures, opening a bottle of wine to celebrate the few successes.

Chapter 3, in part, is currently being prepared for submission for publication of the material. Crisp, J.L.; Savariar E.N.; Tsien R.Y. The dissertation author was the primary author of this material

Chapter 4, in part, is currently being prepared for submission for publication of the material. Crisp, J.L.; Savariar E.N.; Glasgow, H.; Whitney, M.; Tsien R.Y. The dissertation author was the primary author of this material.

Chapter 6, in full, is a reprint of the work as it appears in Journal of Biological Chemistry, published May 2010. The dissertation author was the secondary author of this material and contributed to experimental design, execution of experiments, interpretation of data, generation of figures and editing of manuscript. Whitney, M., Crisp, J.L., Olson, E.S., Aguilera, T.A., Gross, L.A., Ellies, L.G., and Tsien, R.Y. Parallel *in Vitro* and *in Vivo* Selection Using Phage Display Identifies Protease-dependent Tumor-targeting Peptides. Journal of Biological Chemistry **285**(29): 22532-22541 (2010).

Chapter 8, in full, is a reprint of the work as it appears in Nature Biotechnology, published February 2011. The dissertation author was the secondary author of this material and contributed to experimental design, execution of experiments, interpretation of data, and editing of manuscript. Whitney, M., Crisp, J.L., Nguyen L.T., Friedman, B., Gross, L.A., Steinbach, P., Tsien, R.Y., and Nguyen, Q.T. Fluorescent peptides highlight peripheral nerves during surgery in mice. Nature Biotechnology **4:**352-356 (2011).

VITA

2005   Bachelor of Science in Engineering, Arizona State University

2008   Master of Science, University of California, San Diego

2012   Doctor of Philosophy, University of California, San Diego

PUBLICATIONS

Olson ES, Whitney MA, Friedman B, Aguilera TA, **Crisp JL**, Baik FM, Jiang T, Baird SM, Tsimikas S, Tsien RY, Ngyen QT. *In vivo fluorescence imaging of atherosclerotic plaques with activatable cell-penetrating peptides targeting thrombin activity.* Integrative Biology. 2012 doi: 10.1039/c2ib00161f. Epub 2012 Apr.

Shen J, Whitney MA, **Crisp JL**, Jiang T, Steinbach P, Levins R, Tsien RY, Nguyen QT. *Visualizing transgenic murine papillary thyroid cancer with novel nerve peptide and protease dependent tumor targeting peptide.* The Laryngoscope. 2011; 121:S293. doi: 10.1002/lary.22249. Epub 2011 Aug 15.

Wu AP, Whitney MA, **Crisp JL**, Friedman B, Tsien RY, Nguyen QT. *Improved facial nerve identification with novel fluorescently labeled probe*. Laryngoscope. 2011 Apr;121(4):805-10. doi: 10.1002/lary.21411. Epub 2011 Feb 16.

Whitney MA, **Crisp JL**, Nguyen LT, Friedman B, Gross LA, Steinbach P, Tsien RY, Nguyen QT. *Fluorescent peptides highlight peripheral nerves during surgery in mice.* Nature Biotechnology. 2011 Apr;29(4):352-6. Epub 2011 Feb 6.

Shu X, Lev Ram, V, Olson ES, Aguilera TA, Jiang T, Whitney MA, **Crisp JL**, Steinbauch P, Deerinck T, Ellisman MH, Ellies LG, Nguyen QT , Tsien RY. *Spiers Memorial Lecture: Breeding and building molecular spies.* Faraday Discussions. 2011 Jan; 149, 9-9. doi: 10.1039/C0FD90021D. Epub 2010 Dec 13.

Ting R, Aguilera TA, **Crisp JL**, Hall DJ, Eckelman WC, Vera DR, Tsien RY. *Fast 18F labeling of a near-infrared fluorophore enables positron emission tomography and optical imaging of sentinel lymph nodes.* Bioconjugate Chemistry. 2010 Oct 20;21(10):1811-9.

Whitney MA, **Crisp JL,** Olson ES, Aguilera TA, Gross LA, Ellies LG, Tsien RY. *Parallel in vivo and in vitro selection using phage display identifies protease-dependent tumor-targeting peptides.* Journal of Biological Chemistry. 2010 Jul 16;285(29):22532-41. Epub 2010 May 11.

ABSTRACTS AND POSTER PRESENTATIONS

Savariar EN, **Crisp JL,** Felsen C, Whitney MA, Friedman B, Olson ES, Levin R, Nashi N, Aguilera TA, Jiang T, Nguyen QT, Steinbach P, Ellies LG, Tsien RY. *In vivo imaging of extracellular proteases using FRET and protease targeted fluorescent peptides.* Presented at Gordon Research Seminars on Plasminogen and Extracellular Proteases, Ventura, California (2012).

Savariar EN, Felsen C, **Crisp JL**, Nashi N, Nguyen QT, Steinbach P, Ellies LG, Tsien RY. *Amplified detection of MMP activities in tumors of live mice using FRET-based Activatable Cell Penetrating Peptides.* Presented at Gordon Research Conferences on Plasminogen and Extracellular Proteases, Ventura, California (2012).

Crisp JL, Whitney MA, Aguilera TA, Ellies LG, Olson ES, Steinbauch P, Gross L, Tsien RY. *Phage display identifies protease dependent tumor targeting peptide.* Presented at World Molecular Imaging Congress, San Diego, California (2011).

Savariar EN, Hall DJ, **Crisp JL**, Steinbach P, Ellies LG, Tsien RY. *Fluorescence resonance energy transfer accelerates and amplifies tumor:background contrast from activatable cell penetrating peptides.* Presented at World Molecular Imaging Congress, San Diego, California (2011).

Ting R, Aguilera TA, **Crisp JL**, Hall DJ, Eckelman WC, Vera DR, Tsien RY. *Elution of PET-NIRF probes in exchange for aqueous 18F-.* Presented at World Molecular Imaging Congress, San Diego, California (2011).

Whitney MA, Olson ES, Friedman B, **Crisp JL**, Nguyen QT, Aguilera TA, Tsimikas S, Jiang T, Chen B, Davalos D, Baeten K, Shih AY, Lyden P, Kleinfeld D, Akassoglou K, Tsien RY. *In vivo detection of coagulation enzymes using protease targeted fluorescent peptides.* Presented at World Molecular Imaging Congress, San Diego, California (2011).

Savariar EN, Felsen C, Hall DJ, **Crisp JL**, Shen J, Nguyen QT, Steinbach P, Ellies LG, Tsien RY. *In vivo imaging of MMP activities using FRET probes.* Presented at Gordon Research Conferences on Matrix Metalloproteinases, Smithfield, Rhode Island (2011).

Crisp JL, Whitney MA, Aguilera TA, Ellies LG, Olson ES, Steinbauch P, Gross LA, Tsien RY. *In-vivo phage selection identifies protease dependent tumor homing peptide.* Presented at UCSD Pharmacology department retreat, San Diego, California (2011).

Savariar EN, Hall D, **Crisp JL**, Steinbach P, Ellies, LG, Tsien, RY. *Imaging MMP activities in tumors of living mice in real time.* Presented at UCSD Pharmacology department retreat, San Diego, California (2011).

Shen J, Whitney MZ, **Crisp JL**, Tsien RY, Nguyen QT. *Thyroidectomy under molecular fluorescence imaging with novel nerve peptide in rodent model of papillary thyroid cancer.* Presented at Triological Society Annual Meeting, Chicago, Illinois (2011).

Crisp JL, Aguilera TA, Savariar EN, Ellies LG, Jiang T, Whitney MA, Tsien RY. *Activatable Cell Penetrating Peptides for targeting clinical therapeutics and imaging agents.* Presented at Howard Hughes Medical Institute investigators meeting, Ashburn, Virginia (2010).

Gross LA, Jiang T, Olson ES, Aguilera TA, Whitney MA, **Crisp JL**, Tsien RY. *Extraction of Activatable Cell Penetrating Peptides from mouse organs and analysis with Orbitrap mass spectrometer.* Presented at the American Society for Mass Spectrometry, Philadelphia, Pennsylvania (2009).

Aguilera TA, **Crisp JL,** Jiang T, Wong EH, Savariar EN, Ellies LG, Tsien RY. *Activatable Cell Penetrating Peptides for use in clinical contrast agent and therapeutic development. Imaging single molecule to whole animal.* Presented at Howard Hughes Medical Institute, Ashburn, Virginia (2009).

Aguilera TA, Olson ES, Jiang T, Barder TE, **Crisp JL**, Nguyen QT, Scadeng M, Ellies LG, Tsien RY. *Translation of Activatable Cell Penetrating Peptides for use in clinical contrast agent and therapeutic development.* Presented at World Molecular Imaging Congress, Nice, France (2008).

ORAL PRESENTATIONS

December 2009	Pharmacology Department Research Discussions, *"Activatable Cell Penetrating Peptides for Therapeutic Delivery."*
April 2011	Experimental Biology Conference, *"Identification of Novel Peptides for Tumor Targeting and In-vivo Imaging."*
July 2011	National Institutes of Health: NICHD Chronic Pain Meeting, *"Development of Novel Peptides for In-vivo Imaging of Nerves."*
January 2012	Pharmacology Department Research Discussions, *"Modifications of Activatable Cell Penetrating Peptides to Enhance Tumor Targeting and Increase Contrast."*

FIELDS OF STUDY

2006-2012 Molecular Imaging under Dr. Roger Tsien

2008-2012 Targeted Therapeutic Development under Dr. Roger Tsien

ABSTRACT OF THE DISSERTATION

Molecular Targeting with Peptide Based Probes for the Imaging and Treatment of Cancer

by

Jessica Leigh Crisp

Doctor of Philosophy in Chemistry

University of California, San Diego, 2012

Professor Roger Y. Tsien, Chair

This dissertation aims to validate that molecular targeting with activatable cell penetrating peptides (ACPPs) and nerve-homing peptides (NHPs) improve imaging and therapeutic delivery techniques in order to combat the progression of cancer. ACPPs successfully identify and mediated therapeutic delivery to cancer cells and NHPs distinguish nerves from surrounding tissue, with the goal of reducing surgically related morbidity during tumor resection. ACPPs are protease sensitive peptides that once cleaved by their target enzyme become a powerful tool for probe retention and cellular uptake. When administered systemically, ACPPs provide significant contrast for both primary tumors and metastatic lesions. The first portion of this thesis focuses on ACPPs that are activated by matrix metalloproteinases (MMPs) because upregulation of these enzymes is well documented in tumorgenesis. However, substrate specificity, turnover and pharmacokinetic properties of the peptide can be improved. Multiple peptide constructs were tested with these goals in mind and the modification that yielded the best

result was the addition of cyclic-RGD, a common ligand for integrins overexpressed in neovasculature. The combination of integrin and MMP targeting significantly enhanced tumor contrast and peptide uptake and provided the first results where ACPP mediated delivery improved the efficacy of a chemotherapeutic drug. ACPP targeting was also tested with Doxil, the FDA approved liposomal formulation of doxorubicin, and *in vivo* testing with this construct has laid the groundwork for translation of ACPP targeting to other nanoparticle therapeutics. Moving beyond MMPs, a novel phage display selection scheme identified an ACPP substrate sequence, RLQLKL, that was a target for tumor associated elastases. Further characterization of this probe revealed that is also a marker for macrophages that are involved in metastatic progression. Finally, NHPs provide significant nerve contrast when imaged in a surgical setting and can be combined with ACPPs to navigate tumor resection during fluorescent-guided surgery. The combination of these molecularly targeted peptides can facilitate the identification of cancer *in vivo*, increase the efficacy of chemotherapeutics and will lead to improvements in early detection and tumor resection, which are the ultimate cures for cancer.

CHAPTER 1: Introduction

1.1. Importance of molecular targeting for imagining and therapeutic development

It is estimated that in 2012, over 577,000 Americans are expected to die of cancer, more than 1,500 people a day. Cancer is the second leading cause of death in the US, exceeded only by heart disease. Despite this staggering statistic, there is hope. The 5-year relative survival rate for all cancers diagnosed between 2001 and 2007 is 67%, up from 49% in 1975-1977 and the 5-year survival for cancers such as breast, melanoma, prostate and thyroid have rates that exceed 90% (Society 2012). These numbers reflect progress in both diagnosing certain cancers at an earlier stage and advances in treatment. The number of combinational therapies available for patients is increasing and there is substantial focus on the development of targeted therapeutics. This field of research aims to raise a drug's therapeutic index (lethal dose/effective dose) by improving efficacy and reducing toxic side effects, as well as design new drugs that exploit cancer associated markers. In parallel, molecular targeting has the potential to increase sensitivity and specificity of contrast agents, which can aid in early detection of cancer, identification of metastatic lesions, and improved surgical outcomes

1.2. Modes of targeting, their clinical applications and ongoing developments

Currently, targeted agents exist for only a small percentage of the molecular markers associated with cancer (Weissleder and Pittet 2008). It is not trivial to design molecules that provide sufficient tumor specificity and high contrast. The optimal probe

should have insignificant background uptake but generate a high local concentration at its target site. Ideally, the probe would have limited non-specific tissue retention, minimal internalization by macrophages and bypass renal and hepatic elimination. There are numerous strategies that attempt to accomplish these goals, and some of them will be disused below.

1.2.1. Passive Targeting

The two basic categories for targeting are passive and active. Passive targeting relies of the microscopic anatomy of the tumor and its microenvironment to drive accumulation and contrast of therapeutic and imaging agents. Molecules that utilize passive targeting tend to localize to the extracellular space of the tumor are the basis of most clinically approved contrast agents used in diagnostic radiology. Some of these compounds include iodinated agents for CT (Speck 2008) and Gadolinium DTPA, also known as Magnevist, for MRI (Burtea, Laurent et al. 2008). One phenomenon that is utilized extensively for passive targeting is the enhanced permeability and retention (EPR) effect, which is the combination of leaky tumor vasculature and dysfunctional lymphatic drainage resulting in non-specific extravasation and deposition (Matsumura and Maeda 1986; Maeda, Wu et al. 2000; Greish 2007). There are a number of imaging agent formulations in preclinical and clinical development that conjugate or encapsulate contrast molecules in polymers or inside nanoparticles to take advantage of EPR.

This type of nanoparticle platform is also being used to successfully target chemotherapeutic molecules. Traditional cancer therapies consist of cytotoxic small molecules that target various aspect of cell replication. Unfortunately, these molecules tend to have unfavorable pharmacokinetics, poor biodistribution and off target toxicities.

To try and solve these problems, nanoparticle drug formulations are being developed that include vesicles, like liposomes and micelles (Matsumura, Hamaguchi et al. 2004; Orditura, Quaglia et al. 2004), and polymers (Haag and Kratz 2006). These preparations have longer circulation times, can evade the reticuloendothelial system, and take full advantage of EPR. Also, the biological fate of these particles can be manipulated by changing their size and surface characteristics, which is a topic of extensive research (Couvreur and Vauthier 2006; Cho, Wang et al. 2008; Schadlich, Caysa et al. 2011). Two significant advances that have fueled nanoparticle drug delivery are the FDA approval of Doxil, a liposomal formulation of doxorubicin (Muggia 2001; Safra, Groshen et al. 2001), and Abraxane, an albumin suspension of paclitaxel (Gradishar 2006).

1.2.2. Active targeting

Active targeting requires specific molecular interactions and can be divided into two general categories: affinity and stimuli-sensitive. Affinity based targeting relies on precise molecular recognition of a biological target whereas stimuli-sensitive targeting requires some form of modification due to a particular environmental cue.

1.2.2.1. Affinity based mechanisms

The most successful affinity based mechanism for cancer therapy to date is the development of monoclonal antibodies to surface antigens and receptors on tumor cells. Rituximab was the first mAb to be FDA approved for the treatment of cancer (Maloney, Grillo-Lopez et al. 1997) and since then numerous antibodies have made it to the clinic. Variations include antibody conjugated therapeutics such as Mylotarg and Brentuximab

vedotic (Senter 2009). Antibodies are also used extensively for imaging with multiple modalities in preclinical development.

Peptide mediated affinity also provides a versatile platform to target a variety of cancer associated processes. The cyclic RGD peptide is a ligand for various integrins that are overexpressed on endothelial cells in tumor neovasculature (Hallahan, Geng et al. 2003) and has successfully targeted both imaging and therapeutic agents (Bibby, Talmadge et al. 2005). Phage display has also been used to find novel tumor-homing peptide sequences that can enhance the efficacy of paxlitaxel-loaded albumin (Karmali, Kotamraju et al. 2009). This is one example of how easily peptide targeting can be incorporated into previously established therapeutics.

Receptor mediated targeting is another affinity based strategy that can lead to the internalization of the ligand along with the associated cargo. There are numerous receptors implicated in cancer progression and metastesis and two common targets are folate and transferrin. Folate conjugation has been proposed for drug delivery, targeted phototherapy and generating optical contrast with luminescent quantum dots (Low and Kularatne 2009; Pan and Feng 2009). Furthermore, folate has been shown to increase drug efficacy in a number of mouse cancer models (Gabizon, Shmeeda et al. 2004; Pan and Lee 2005; Shmeeda, Mak et al. 2006).

1.2.2.2. Stimuli-sensitive mechanisms

Stimuli-sensitive mechanisms are often referred to as activatable or "smart". These molecules are typically inactive or inhibited when first administered but become functional upon modification by a specific environmental stimuli. The stimuli can be naturally occurring, such as a change in pH or presence of a specific antigen or enzyme,

or can be controlled externally, as is the case with light and ultrasound (Arias 2011). Signal amplification is one feature of activatable probes that makes them more attractive than affinity-based mechanisms. One enzyme can turn over multiple copies of a probe, unlike ligands and antibodies that typically bind to their targets in a 1:1 stoichiometry.

With most stimuli sensitive targeting mechanisms, the focus is more on selective release of a drug molecule or stimulation of an imaging agent and not the enrichment of a molecule within the tumor tissue. pH sensitive release is a popular strategy used in the literature. It takes advantage of the slightly acidic tumor microenvironment (pH~6.6), and can also be used for release of a cargo molecule in the acidic organelles within the endocytic pathway (Stubbs, McSheehy et al. 2000). Other release mechanisms allow the agent to reach the tumor before selective application of an external stimuli. Some of these include thermo-sensitive drug delivery with hydrogels or polymers (Guo, Cui et al. 2011), accumulation of drug-loaded nanoparticles with magnets (Ciofani, Riggio et al. 2009) and release of drugs from liposomal carriers using light and ultrasound (Bisby, Mead et al. 2000; Gao, Fain et al. 2004; Rapoport, Christensen et al. 2004; Larina, Evers et al. 2005).

The last form of stimuli-sensitive targeting that will be discussed is enzymatic activation. A large portion of this dissertation involves generating optical tumor contrast using peptides that are sensitive to proteases known to be associated with cancer progression. This technology utilizes activation to promote accumulation in the tumor, which allows it to be a platform for both contrast agent development and therapeutic delivery.

1.3. Development of protease activatable probes

Two major considerations when developing protease activatable probes are the stability and specificity of the peptide substrate and the *in vivo* localization of the target enzyme. The substrate sequence is the most important variable to optimize for efficient protease targeting. It must remain stable in the blood and plasma during circulation, be fairly specific for its target protease and have efficient enzymatic turnover. This is a lot to ask of peptide sequences that are typically only two to eight amino acids long. Furthermore, there are numerous substrate sequences in the literature that claim to be specific for a given enzyme, but are not always tested for cleavage with other classes of proteases. It is important to do the proper control experiments to ensure that a given substrate is sufficiently specific and is still cleavable when incorporated into the final probe.

The location of protease expression is also important to consider during the molecular design process. First, is the target protease maintained inside the cell or secreted to the extracellular environment? If enzymatic cleavage is what activates tumor uptake or if cellular uptake is not required (which can be the case for molecule imaging), then targeting of extracellular proteases is necessary. These extracellular proteases should be highly upregulated in diseased tissue and have minimal expression in off target sites. If targeting moieties, like aptamers, ligands and antibodies, are already in place to deliver the cargo to the site of the cancer, enzymatic activation is typically reserved for the intracellular release of a drug from the targeting molecule. Therefore, it is advantageous to target intracellular proteases, especially those associated with the endosomal and lysosomal compartments.

Currently there are only a few protease activatable drugs in the clinic or in various stages of clinical trials. Most of these drugs target Cathepsin B, a lysosomal protease, to release chemotherapeutics from targeting molecules (Seymour, Ferry et al. 2002; Chipman, Oldham et al. 2006; Seymour, Ferry et al. 2009; Alley, Okeley et al. 2010). There is one drug in phase II of clinical development that targets prostate specific antigen (PSA) for the selective release doxorubicin in cases of prostate cancer (DiPaola, Rinehart et al. 2002).

1.4. Activatable cell penetrating peptides

1.4.1. History of cell penetrating peptides

Cell penetrating peptides (CPPs) or protein transduction domains (PTDs) are short polycationic peptides that are known to efficiently bind to the outer surface of cells and be internalized. Early studies claimed that these peptides could translocate across the plasma membrane and gain access to the cytoplasm and nucleus of the cell (Schwarze, Ho et al. 1999; Schwarze, Hruska et al. 2000; Yang and May 2008). It was later discovered that the observed subcellular distribution of the peptide was a result of fixation artifacts and that under physiological conditions, the mechanism of uptake and peptide distribution were significantly different (Vives 2003). When CPPs are applied at low micromolar concentrations and imaged on live cells, most of the peptide is confined to endocytic vesicles. However, there are cases when CPPs and PTDs have been applied directly to their targets *in vivo* and successfully delivered cargo to its intracellular destination (Mai, Mi et al. 2001; Richard, Melikov et al. 2003; Snyder, Meade et al. 2003). The inherent "stickiness" of these highly charged peptides was cause concern

when determining the feasibility of systemic administration, especially because the PTD

from the HIV-TAT protein was rapidly cleared from plasma circulation when tested in

mice (Lee and Pardridge 2001). In order to successfully translate CPPs to *in vivo*

targeting molecules, the positive charges on the peptide need to be blocked during

circulation and selectively unmasked at the site of interest. This led to the development of

activatable cell penetrating peptides (ACPPs).

1.4.2. Introduction to ACPPs

It was hypothesized that cellular uptake of CPPs could be diminished by

appending them with a short polyanionic sequence. The electrostatic interactions between

the positive and negative charges should promote the formation of a hairpin structure and

forestall membrane adhesion. This peptide construct is referred to as an activatable cell

penetrating peptide (ACPP) because the linker region that joins the two charged domains

is designed for cleavage by extracellular proteases characteristic of the tumor

microenvironment. Cleavage of the linker jettisons the polyanionic domain, freeing the

polycationic domain to carry the contrast or therapeutic agent into the adjacent tumor and

stromal cells (Figure 1.1). Thus, the cargo preferentially accumulates in areas of tumor

invasion, where there are elevated level of protease activity.
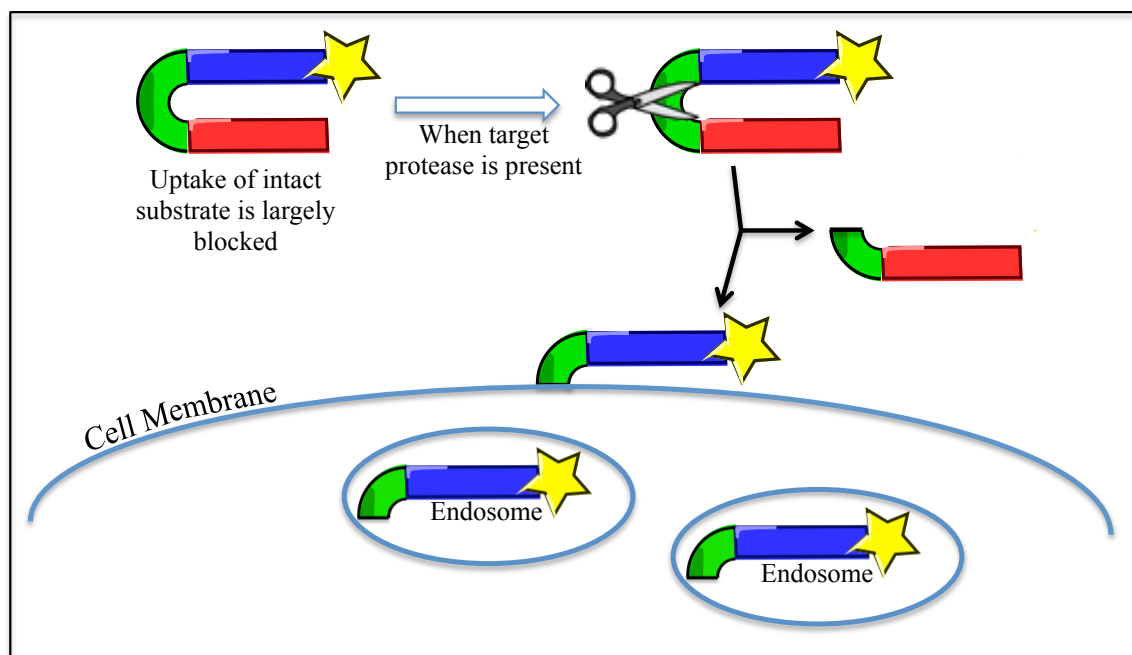
Figure 1.1 Activation of ACPPs by tumor associated proteases. ACPPs contain three distinct domains, a polycationic CPP domain (blue), a polyanionic inhibitory domain (red) and a protease cleavable linker (green). Upon cleavage of the linker by its target protease, the inhibitor domain is free to dissociate, allowing the CPP to bind to neighboring cells and be taken up by endocytosis. The star in this cartoon represents any cargo molecule covalently attached to the CPP domain, in most cases this cargo is the far-red fluorescent dye, Cy5.

1.4.3. Previous validations

The ACPP targeting mechanism has been previously validated both *in vitro* and *in vivo*. NMR data confirmed the peptide's hairpin structure and cleavage of the linker substrate resulted in up to 123 fold increase in uptake when tested in tissue culture. (Jiang, Olson et al. 2004). Pharmacokinetic, biodistribution and toxicity studies established that the activatable form of the peptide was superior when administered systemically (Aguilera, Olson et al. 2009). ACPPs were also validated in a variety of tumor models and uptake was found to be reliant on the expression of MMP-2 and MMP-9 with the use of genetic knockout mice (Olson, Aguilera et al. 2009). ACPPs were conjugated to dendrimeric nanoparticles and found to help identify margins during tumor resection and increase tumor free survival when used during fluorescence guided surgery

(Nguyen, Olson et al. 2010). These nanoparticles were then loaded with gadolinium and ACPP targeting improved the detection of cancerous lesion with the use of MRI (Olson, Jiang et al. 2010).

1.4.4. ACPP modifications presented in this dissertation

While the previous body of work is impressive, there is still a lot to be done with ACPP development to incresae tumor uptake, enhance contrast and improve peptide pharmacokinetics and biodistribution. Some of the modifications that will be addressed in the following chapters are: i) alterations in the substrate sequence to improve enzyme selectivity, cleavage kinetic and to target different proteases, ii) various mechanisms of cargo release to manipulate Cy5 biodistribution and work toward future therapeutic applications, and iii) amendments to the peptide structure that permit the attachment of large molecular weight carriers, inclusion of other targeting moieties and conjugation of the peptide to clinically relevant nanoparticles. These modifications are depicted in Figure 1.2.

MODIFY CARGO LINKAGE:
- Enzymatic release (Chapter 2, Chapter 5)
- Disulfide bond mediated release (Chapter 3)

MODIFY LINKER:
- Improve enzyme kinetics (Chapter 2)
- Modify sequence specificity (Chapter 2, Chapter 6)
- Target enzymes other than MMP- and MMP-9 (Chapter 2, Chapter 6, Chapter 7)

MODIFY N-TERMINUS:
- Attachment to large molecular weight carriers (Chapter 2, Chapter 5, Chapter 6)
- Multiple targeting ligands (Chapter 4)
- Additional imaging moieties
- Conjugation of therapeutic molecules (Chapter 4)

Figure 1.2 Potential modifications to the ACPPs structure.

1.5. Summary of Chapters

The chapters of this dissertation can be divided into three areas of study. The first part focuses on the further evolution and development of MMP targeted ACPPs for optical imaging and therapeutic delivery (Chapters 2-5). The second portion moves beyond MMP targeting, and introduces a new substrate sequence that was discovered using a novel phage display technique (Chapters 6-7). The final chapters in this dissertation introduce the idea of fluorescence-guided surgery and the discovery of a peptide sequences that bind preferentially to nerves. The goal of this probe is to help prevent nerve damage that can occur during surgery (Chapters 8-9).

Part 1: Further evolution and development of MMP targeted ACPPs for optical imaging and therapeutic delivery.

Chapter 2 is an overview of the numerous peptide modifications that were tested in an effort to increase tumor uptake, enhance tumor contrast and decrease peptide uptake in off target organs.

Chapter 3 discusses disulfide bond reduction as a means to release cargo molecules from CPPs once the peptides have been endocytosed by cancer cells. This is one of the hurdles that must be overcome to establish ACPPs as therapeutic delivery agents.

Chapter 4 demonstrates that ACPP targeting can be enhanced by the addition of a pretargeting ligand, specifically cyclic(RGD). These two strategies combine to significantly improve tumor uptake and therapeutic efficacy of the potent chemotherapy drug, monomethyl auristatin E.

Chapter 5 summarizes the first attempts at conjugating ACPPs to clinically relevant nanoparticles, doxorubicin loaded liposomes.

Part 2: Utilizing phage display to generate ACPPs that target proteases other than MMP-2 and MMP-9.

Chapter 6 is an insert of the Journal of Biological Chemistry manuscript that describes the discovery of the RLQLKL substrate sequence, attempts to determine its target enzyme and *in vivo* tests for optical contrast of both primary tumors and metastases.

Chapter 7 demonstrates that the substrate RLQLK(Ac)L is specific to a subset of

activated macrophages in metastatic lungs and postulates how this probe could be

developed as a tool for studying tumor associated macrophages.

Part 3: Introduction to fluorescence-guided surgery and how surgical outcomes could be

improved by reducing morbidity associated with nerve damage.

Chapter 8 details the discovery of a peptide sequences that binds preferentially to

nerves and its ability to guild surgeons.

Chapter 9 chronicles the attempt to find the target protein for the nerve homing

peptide and all of the various modifications that were made to try and improve

nerve contrast. It also introduced the results of two subsequenct phage selections

and the *in vivo* performance of the peptide sequences that resulted from them.

CHAPTER 2: Modifications to Activatable Cell Penetrating Peptides to Enhance Tumor Selectivity and Reduce Background Uptake

2.1. Abstract

Targeting tumors and metastases with activatable cell penetrating peptides (ACPPs) has been validated with optical imaging, but there is still a need to improve tumor selectivity and contrast as well as peptide biodistribution. To accomplish these goals a multitude of peptide variations have been tested *in vivo*, some generating more success than others. Selecting enzymes other than matrix metallo-proteinases 2 and 9 (MMP-2 and MMP-9) increased tumor uptake in some models, but that result was not universal. Generating dimeric and cyclic peptides did not improve the absolute level of probe in the tumor, but were successful at reducing background uptake in nearby tissues and cartilage, resulting in better contrast. Attempting to release the Cy5 from the CPP in the liver and kidneys did dramatically reduce the fluorophores concentration in those organs, but also diminished the dye's retention in the tumor. The *in situ* conjugation of ACPPs to serum albumen resulted in superior tumor uptake, biodistribution and pharmacokinetics, but the enzyme dependence was lost. The most significant lead from all of the modifications was the attachment of pre-targeting ligands, more specifically cyclic RGD. This cyclic peptide is a common ligand for integrin $\alpha_v\beta_3$ and its combination with MMP cleavable ACPPs significantly enhanced uptake into MDA-231 breast cancer tumors.

2.2. Introduction

Activatable cell penetrating peptides provide an excellent platform for molecular targeting because they can be modified in a plethora of ways. The amino acid sequence of the linker region can be changed to improve enzyme specificity and cleavage kinetics or to target an entirely different protease. The peptide is also conducive to having release mechanisms for the cargo molecules built in, dimeric and circular peptides can be generated and additional targeting moieties can be added. Furthermore, attaching ACPPs to large molecular weight carrier molecules can modulate the pharmacokinetic properties of the peptide. The goals of all these variations are to improve the tumor:background contrast ratio, increase to absolute uptake of the peptide in tumors and reduce the amount of probe deposited in undesired tissues. Because this chapter covers a wide range of peptide modifications, each of them will be introduced in more detail within their respective results subheading.

2.3. Methods

2.3.1. Peptide synthesis

2.3.1.1. Free peptides

Peptides were synthesized on an automatic peptide synthesizer (PTI Prelude) using standard protocols for fluorenylmethoxy-carbonyl (Fmoc) solid-phase synthesis. Peptides were cleaved from the resin using standard trifluoroacetic acid (TFA) protocols and precipitated with a 1:1 mixture of diethyl ether and hexane on ice. Peptides were labeled with either Cy5 monomaleimide or Cy5 NHS ester (GE Healthcare) and purified

using reverse phase high performance liquid chromatography, HPLC. The standard sequence for free peptides is Ac-e_9-*x*-cleavage sequence-r_9-c(Cy5) or Suc-e_8-O-cleavage sequence-r_9-c(Cy5), where the D-amino acids are denoted by lower case letters, the *x* denotes 6-aminohexanoyl, the O represents 5-amino-3-oxapentanoy, and the N terminus is capped using either acetic anhydride (Ac) or succinic anhydride (Suc). The succinyl cap is similar to a deamidated glutamate. The cleavage sequences are always L-amino acids and the peptides are commonly named using the single letter code of that amino acid sequence. Uncleavable control peptides were synthesized by replacing the cleavage sequence with a -HN(CH2CH2O)6CH2CH2CO- (peg_6) linker, which has a similar length as a strand of 6 amino acids.

2.3.1.2. Dimer ACPP

ACPPs with the sequence of Suc-e_8-OPLGC(Me)AG-r_9-c were reacted with a bis functional Cy5 maleimide (GE Healthcare) to generate a molecule that had two ACPPs conjugated to a single Cy5 dye.

2.3.1.3. Cyclic ACPP

The sequence of the cyclic ACPP is c-e_9-OPLGC(Me)AG-r_9-k-OPLGC(Me)AG-c-NH2. Forming a disulfide bond between the N terminal and C terminal cysteine residues generated the circular peptide and Cy5 N-hydroxysuccinimide (NHS) ester was reacted to the peptide through the internal lysine.

2.3.1.4. Maleimide ACPP

Free peptides were synthesized as described above but the N terminus of the peptide was not capped. The N terminal amine was reacted with β-maleimidoproprionic

acid-PFP ester (Molecular BioSciences) then purified on HPLC. Purified peptide was stored as a lyophilized power to prevent the reactive maleimide group from hydrolyzing while in storage.

2.3.1.5. Folate and cyclic-RGD pretargeted ACPPs

Folate was dissolved in dry dimethylformamide (DMF) and reacted with N,N'-dicyclohexyl –carbodiimde (DCC) with the addition of N-methylmorpholine (NMM). Folate anhydride was then reacted with NH_2-peg_4-e_9-OPLGC(Me)AG-r_9-c(Cy5)-NH_2 (2460) or NH_2-peg_4-e_9-Oplgc(Me)ag-r_9-c(Cy5)-NH_2 (2503).

For cyclic RGD peptides: NH_2-peg_4-e_9-OPLGC(Me)AG-r_9-c(Cy5)-NH_2 was reacted with β-maleimidoproprionic acid-PFP ester (Molecular BioSciences) in DMF with NMM. This was then reacted with cyclic(RGDfC) to generate 2570. For the RAD control peptide 2455, cycic(RGDfC) was replaced with cyclic (RADfC). To generate 2416: NH_2-peg_4-e_9-PEG6-r_9-c(Cy5)-NH_2 reacted with β-maleimidoproprionic acid-PFP ester followed by conjugation of cycic(RGDfC). All peptides were purified by HPLC with identity confirmation using mass spectroscopy.

2.3.2. Enzyme cleavage assay

Enzymes where purchased from Calbiochem as either purified recombinant active enzymes or purified active catalytic domains. Cy5 labeled peptides were diluted to a concentration in 5.55 μM in cleavage buffer (150 mM NaCl, 20 mM Tris, 2 mM $CaCl_2$ and trace amounts of $ZnCl_2$ at pH 7.4). Peptide dilutions were then aliquoted into round bottom 96 well plates and placed on ice. Enzymes were spiked into the peptide solutions so the final enzyme concentration was 50 nM and the final peptide concentration was 5

μM. The 96 well plates were removed from the ice and placed in a 37°C incubator. After

1 hour, the cleavage reaction was stopped by adding and equal volume of 2X Novex

Tricine SDS Sample Buffer (Life Technologies) and heating the samples to 90°C for 60

seconds.

2.3.3. Gel electrophoresis and percent cleavage quantification

Samples were run on Novex 10-20% Tricine gels (Life Technologies) at 100mV

for 100 minutes. To visualize peptide cleavage, gels were imaged in a Maestro Imager

(CRI) using an excitation filter of 620/22nm and a 645nm long pass emission filter.

Images were processed in ImageJ and integrated fluorescent intensities for the intact

peptide and cleavage bands were measured to determine the % peptide cleavage.

2.3.4. *In vivo* animal imaging

2.3.4.1.   Free peptide imaging in various cancer models

Transgenic mouse mammary tumor virus promoter-Polyoma Middle T (MMTV-

PyMT) spontaneous breast tumor mice were provided by Lesley Ellies. 8119 PyMT cells

were also provided by Lesley Ellies and injected into syngeneic Black-6 Albino mice.

MDA-MB-435 (human melanoma), Bx-PC3 (human prostate), PC3-Ex (human prostate),

Du-145 (human prostate) and HT1080 (human fibrosarcoma) cells were acquired from

ATCC and injected into immune incompetent, athymic nu/nu, mice. All cells were

cultured in eagle's minimum essential media (EMEM from ATCC) with 10% fetal

bovine serum (FBS) in a 5% CO_2 incubator maintained at 37°C with 90% humidity. For

all non-spontaneous tumor models, between $5x10^5$ to $1x10^6$ cells were injected

subcutaneously or in the mammary fat pads and allowed to grow for 5-10 days or until

the tumors reached approximately 5 mm in diameter. 10 nanomoles of Cy5 labeled

peptides were injected intravenously (IV) via the tail vein and allowed to circulate for 6

hours prior to imaging and animal sacrifice. For imaging, mice were anesthetized with an

intraperitoneal (IP) injection of 50 μL of 1:1 Ketamine:Midazolam and imaged on the

Maestro using 620/22 nm excitation and 645 nm long pass emission with the tunable

filter set at 670 nm. Mice where sacrificed with an overdose of isofluorane and images

were taken before and after removal of skin.

2.3.4.2. Maleimide peptide imaging

Peptides were stored as lyophilized solids and resuspended in nanopure water to a

final concentration of 30μM. Peptides were injected IV at a dose of 3 nanaomoles/mouse

and animal imaging and sacrifice occurred 48 hours post peptide injection.

2.3.4.3. Folate peptide imaging

For the SK-OV-3 tumor model, mice were placed on a folate deficient diet

(Harlan) for three weeks prior to tumor cell injection and remained on that diet for the

duration of the experiments. SK-OV-3 cells (ATCC) were cultured in folate deficient

RPMI media (Clontech) for two week prior to cell harvesting and tumor cell injections.

Peptides were injected at a standard 10 nanomole dose and imaged 6 hours later.

Standardized uptake value (SUV) calculations

Target organs such as tumor, liver, kidney and muscle were harvested from the

animals, weighed and placed in 15ml plastic vials. SUV buffer (150 mM NaCl, 10 mM

Tris, 2g/100ml SDS, 0.25 mg/ml Proteinease K and 0.1 mg/ml DNase pH 8.0) was added

to the tissue at a ratio of 9μL buffer to 1mg tissue. Tissues were then homogenized with a

probe sonicator (Fisher Scientific) using an amplitude range of 5-15% for a maximum of 20 seconds. Tissue solutions were placed in a 37°C incubator with constant agitation and allowed to incubate overnight. 200μL of each tissue solution was transferred to a well on a black, plastic bottom, 96-well plate (Costar) for fluorescent analysis. Fluorescent measurements were performed on a plate reader (Tecan Safire) using 630nm excitation with a 12nm slit and a 680nm emission with a 12nm slit. Fluorescent counts were converted to Cy5 concentrations using tissue specific calibration curves.

To generate the calibration curves, tissues were collected from mice that had never been injected with peptide and homogenized in SUV buffer containing known amounts of Cy5. Tissues were processed and analyzed in the same manner as described above. For each tissue, a calibration curve was generated by plotting fluorescence as a function of Cy5 concentration then performing a linear regression analysis to obtain an equation that related fluorescence to peptide concentration.

To calculate the SUV value, the peptide concentration in molarity in the homogenate was converted to molality in the original tissue, then normalized by the injected dose and animal weight. The equation for an SUV is: (moles of peptide in tissue/weight of tissue)/(moles of peptide injected/weight of animal).

2.3.5. Cryosection imaging

Tissues were harvested from the animals, placed in OCT and flash frozen in liquid nitrogen and stored in a -80C freezer. Frozen tissues were processed using a cryostat (Leica) and 10μm sections were mounted by melting onto Superfrost Plus slides (VWR). Sections were kept dry and imaged on Lumar fluorescence stereomicroscope (Zeiss) with a Cy5 filter set.

2.4. Results

2.4.1. Enzyme specificity for various MMP targeted ACPPs

For ACPPs to accurately monitor disease related enzyme activity *in vivo*, it is important to know that the substrate sequence is selective for the target enzyme. The sequence PLGLAG is relatively selective for MMP-2 and MMP-9 (Aguilera, Olson et al. 2009), and a slightly altered sequence of PLGC(Me)AG was found to have faster cleavage kinetics for those target MMPs (Olson, Aguilera et al. 2009). These two peptides were tested against a panel of MMPs (Figure 2.1 A) and by changing the leucine to a methyl cysteine, cleavage of the peptide by MMP-7 and MT2-MMP was diminished with a slight increase in cleavage by MT3-MMP.

MT1-MMP is a membrane type MMP that is anchored to the extra cellular surface of the plasma membrane. It was first known to activate pro-MMP-2, but is now implicated in the degradation of extracellular matrix proteins and activation of various cell surface molecules that promote angiogenesis and metastasis (Sato, Takino et al. 2005). This enzyme has the potential to be a superior target for ACPPs because it is tethered to the cancer cell, whereas MMP-2 and MMP-9 are secreted and have the ability to diffuse away. ACPPs were synthesized with various substrates for MT1-MMP. Dr. Patrick Daugherty suggested the following substrates: PQGLL, PQGMRL, PQGC(Me)AG (Jabaiah and Daugherty 2011), Dr. Peter Wang recommended RPAHLRDSG (Ouyang, Huang et al. 2010), and finally RSCitG(homoF)YLY was found in the literature (Atkinson, Falconer et al. 2010). When incorporated into ACPPs, all of these substrates were cleaved by MMPs other than MT1-MMP, and PQGLL showed

minimal cleavage by its target enzyme (Figure 2.1 A). RPAHLRDSG was cleaved the

fastest by MMP-2 and MMP-13, and was a substrate by every proteases tested except

MT2-MMP. RSCitG(homoF)YLY had the most selectivity for MT1-MMP, being cleaved

by only two other enzymes, MMP-2 and MT3-MMP. Each of the cleavage gels was

quantified using ImageJ so that the extent of peptide cleavage could easily be compared

among the peptides (Figure 2.1 B).
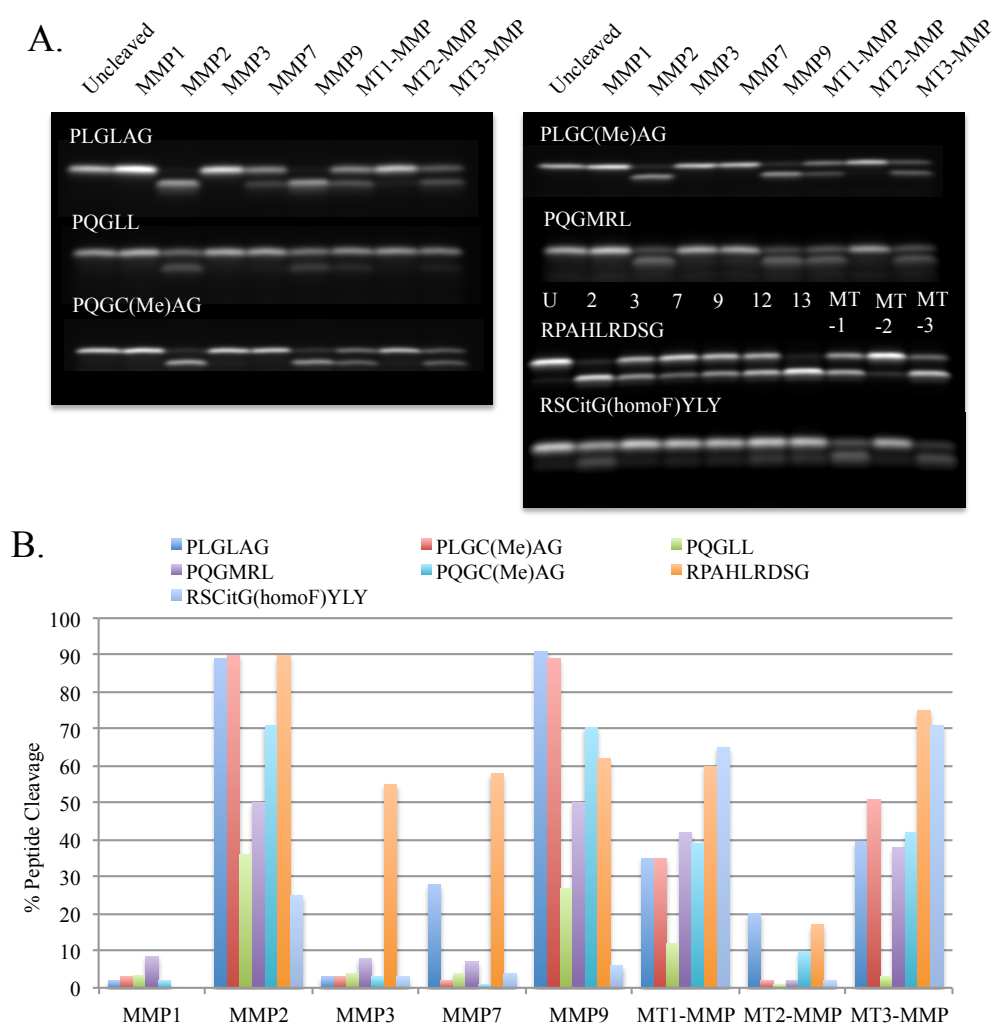
Figure 2.1 Enzyme specificity of ACPPs with various MMP substrates. A) Cy5 labeled ACPPs were synthesized with substrates for various MMPs substituted into the linker portion; substrate sequences are given as their one-letter amino acid codes with Cit short for Citruline and homoF short for homo phenylalanine. 5 μM peptide solutions were incubated with 50 nM of purified enzymes at 37°C for 1 hour and cleavage of the peptides was monitored by gel electrophoresis. B) Cleavage was quantitated in ImageJ by drawing regions around the peptide bands and measuring the integrated fluorescent intensity.

Some of these peptides were then tested in a variety of cancer models to determine which sequence provided the best tumor:background contrast ratio (Table 1.1). The PLGLAG ACPP, which demonstrated the most selectivity for MMP-2 and MMP-9, had the best contrast in the PyMT 8119 syngeneic breast cancer model, but that values also had a lot of variability. This substrate has been published in HT1080 xenografts, but that model provided the worst contrast. However the RPAHLRDSG substrate had an average tumor to background contrast of 6.0±2.0 in the HT1080 model and contrast ratios up to 9.6 in MDA-MB-435 xenograft tumors. Overall the RPAHLRDSG peptide, which was cleaved by every MMP tested except MT2-MMP, performed better than the PLGLAG. This could suggest that when trying to target imaging agents to tumors, having some substrate promiscuity could be beneficial, as long as it does not lead to higher uptake in undesired tissues.

Table 2.1 Tumor : background contrast ratios for MMP cleavable ACPPs in a variety of cancer models

Tumor Model: Cleavage Sequence ↓	Polyoma (transgenic breast)	PyMT 8119 (syngeneic breast)	MDA-MB-435 (melanoma)	HT1080 (fibrosarcoma)
PLGLAG	2.7 ± 0.7	6.7 ± 3.6	4.1 ± 1.1	1.7 ± 0.5
RPAHLRDSG	2.6 ± 2.1	2.5 ± 2.1	7.6 ± 2.0	6.0 ± 2.0

2.4.2. *In vivo* tumor targeting with ACPPs expanding beyond MMPs

MMPs play a major role in ECM degradation and tumor development, but they are not the only enzymes involved in cancer progression. The ACPPs mentioned above

were rationally designed to target a given enzyme based on previous knowledge of sequence preferences. An alternate approach would be to use a library and screen for cleavage sequences that are activated in a tumor, using no prior bias for amino acid sequence or target enzyme. This screen was preformed using phage display and produced the sequence RLQLKL, a substrate for plasmin and a variety of elastases (Whitney, Crisp et al. 2010). This selection strategy and subsequent peptide characterization will be the focus of Chapter 4 of this dissertation.

Mast cells accumulate in the stroma surrounding certain types of tumors, including mammary adenocarcinomas, and can secrete molecules and enzymes that promote tumor growth (Conti, Castellani et al. 2007). Interestingly, these inflammatory mediators can exert both pro- or anti- tumor affects depending on their concentration, location and presence of cofactors (Dyduch, Kaczmarczyk et al. 2012). An ACPP was designed as a substrate for mast cell chymase to determine if it was a valuable enzyme target. The sequence of GVAYSGA was published to have the preferred combination of amino acid residues for human mast cell chymase and was inserted into the ACPP platform (Andersson, Enoksson et al. 2009).

Both RLQLKL and GVAYSGA were tested against a broad panel of enzymes to examine their selectivity (Figure 2.2 A). RLQLKL was cleaved most efficiently by plasmin but was also a substrate for MMP-7, elastase and chymase. GVAYSGA was successfully inserted into an ACPP, and after a short incubation with enzymes it was completely cleaved by chymase with minimal cleavage by elastase.

These ACPPs were tested *in vivo* and compared to the standard MMP substrate, PLGC(Me)AG, in MDA-MB-231 human breast orthotropic tumors (Figure 2.2 B). As a

control for enzyme activity, an uncleavable peptide was generated with a peg$_6$ (mpeg) in place of an L-amino acid sequence. Peg$_6$ was chosen because its length is similar to that of six amino acids and it is impervious to proteolysis, unlike D-amino acids where glysine residues can still be cleaved. The MMP targeted PLGC(Me)AG ACPP had superior tumor uptake compared both RLQLKL and GVAYSGA, but it also had more background signal in the muscle and cartilage (Figure 2.1 C). Therefore, the tumor to muscle contrast was actually the best for RLQLKL. All enzyme targeted peptides showed significantly higher tumor uptake compared to the uncleavable mpeg peptide. Uptake is calculated as a standardized uptake value (SUV), which is the molality in the tissue normalized by the molality of the injected dose.

Retention of the peptide in off target organs such as the liver and kidneys had some sequence dependence (Figure 2.2 D). Liver SUV was highest for RLQLKL and lowest for the uncleavable peptide while in the kidneys, GVAYSGA was significantly higher than any other peptide. RLQLKL had the lowest kidney uptake, with an SUV below that of the uncleavable peptide. Both renal and biliary excretion clears these small peptides from circulation, as Cy5 fluorescence is detectable in both the urine and gal bladder as early as 30 minutes post injection. Confocal analysis of kidneys *ex vivo* demonstrated that the probe was sequestered in luminal puncta, suggesting that ACPPs were filtered and endocytosed in the renal tubules (Aguilera, Olson et al. 2009). It is still unclear as to what causes the differential uptake in these organs. It could be an enzyme depended mechanism or a result of the hydrophobicity and charge differences that arise from altering the amino acids in the linker region.
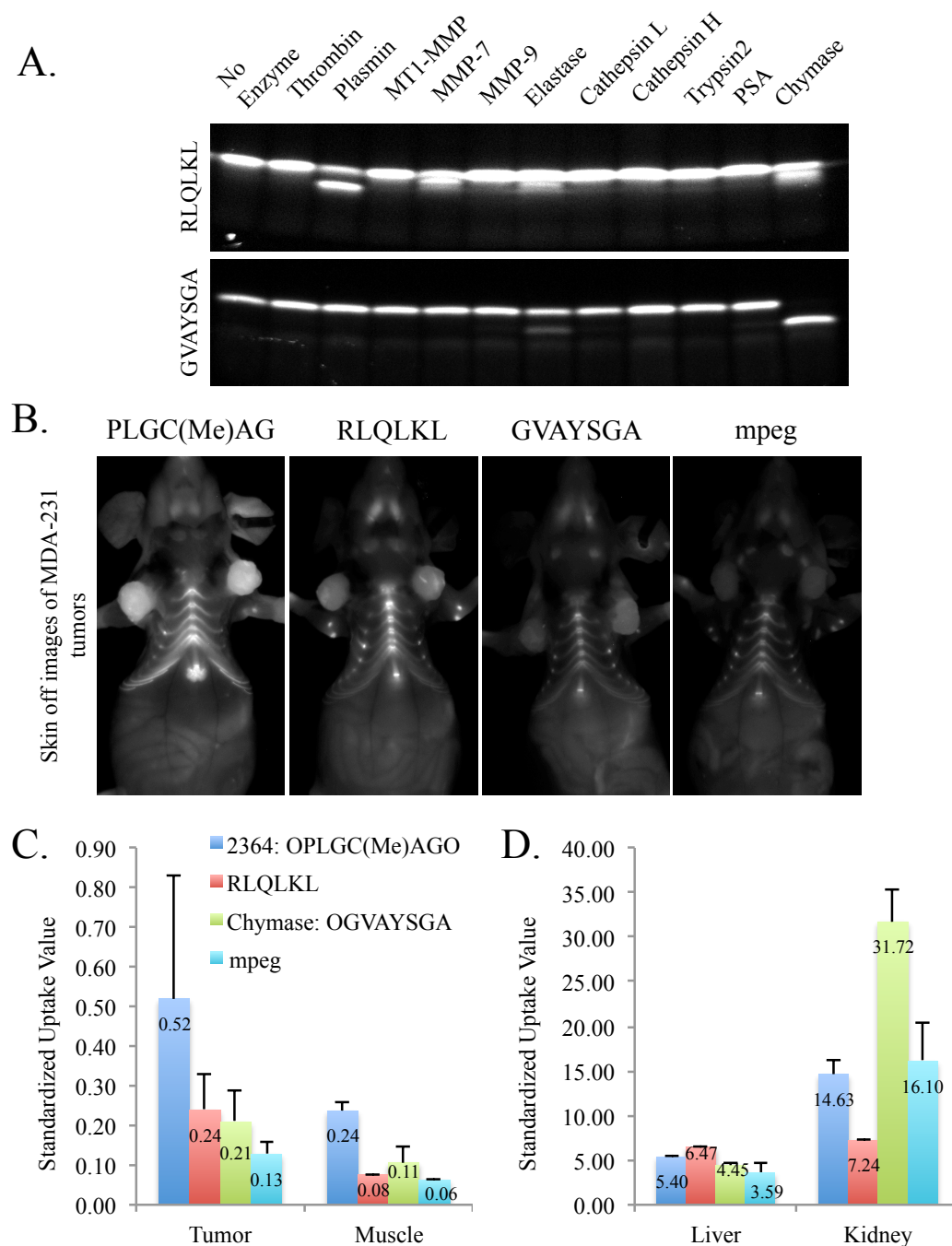
Figure 2.2 Enzyme specificity and *in vivo* tumor targeting of ACPPs that expands beyond MMPs. A) Gel electrophoresis of cleavage reactions for RLQLKL and GVAYSGA peptides; 5uM peptide was incubated with 50nM of given enzyme for 1 hour at 37°C. The top band is uncleaved peptide and smaller molecular weight band represents cleaved peptide. B) Cy5 labeled peptides were injected into MDA-MB-231 tumor bearing mice and compared with the standard MMP cleavable PLGC(Me)AG ACPP. Six hours post injection mice were sacrificed and the skin was removed to reveal tumor fluorescence in the context of the surrounding tissue. C-D) SUV values were calculated for tumor, muscle (C) liver and kidney (D) tissues from mice that had been injected with the various ACPPs.

2.4.3. Selective release of Cy5 cargo in the liver

Peptide uptake in the liver is an order of magnitude greater than that of the tumor (Figure 2.2 C and D). Therefore, it would be advantageous to selectively release the cargo molecule from the sticky r_9 peptide such that it can be cleared from the liver. To accomplish this, an additional L-amino acid cleavage sequence designed for Hepsin was inserted between the r_9 peptide and the Cy5. Hepsin is a type-II membrane protein that is predominantly expressed in normal human liver and hydrolyses the amino acid sequence of KQLR (Hooper, Campagnolo et al. 2003; Herter, Piper et al. 2005). An ACPP with a cathepsin B cleavage site, GLFG, was also generated as a comparison for KQLR selectivity. Cathepsin B is a serine protease found in lysosomes and is common target for the release of chemotherapeutic drugs from carrier molecules once they have been endocytosed by cells. The sequence of these peptides is Ac-e_9-x-PLGLAG-r_9-KQLR/GFLG-c(Cy5).

Peptides were injected into mice harboring HT1080 tumors and allowed to circulate for 6 hours prior to sacrifice and skin removal. The additional KQLR cleavage site did not affect tumor, background or cartilage fluorescence yet the GFLG peptide had significantly lower overall signal (Figure 2.3 A). Organs were removed and frozen for cryosectioning to examine the fluorescence distribution on a histological level. It is clear from imaging Cy5 in liver sections (Figure 2.3 B) that the original ACPP is confined to what appear to be single cells, probably Kuffer cells, whereas both KQLR and GFLF have diffuse Cy5 fluorescence through out the tissue. This diffuse staining makes it appear that these peptides have higher uptake in the liver, when in fact there is less Cy5 based on uptake values (Figure 2.3 E). Fluorescent images of kidney sections do not

show a significant difference in peptide localization, but do corroborate a decrease in the amount of Cy5 present for the KQLR and GFLG peptides (Figure 2.3 C).

SUV values were calculated for various tissues at both 6 hours (Figure 2.3 D) and 24 hours (Figure 2.3 E) after peptide injection. While both KQLR and GFLG were successful at decreasing Cy5 retention in the liver, kidneys and muscle, they also diminished the amount of cargo that was retained in the tumor. Tumor uptake dropped by 44% with KQLR at 6 hours and by 24 hours Cy5 fluorescence was undetectable over tissue autofluorescence. With GFLG, tumor SUVs could not be calculated at either time point. Interestingly, with the PLGLAG ACPP the SUV for the liver was constant over the span of 6 to 24 hours and there was only a 15% washout of the peptide from the kidneys. This does reiterate a need for the selective release of cargo molecules from the CPP, especially if the peptide is targeting chemotherapeutic agents that could cause toxicity in these organs.
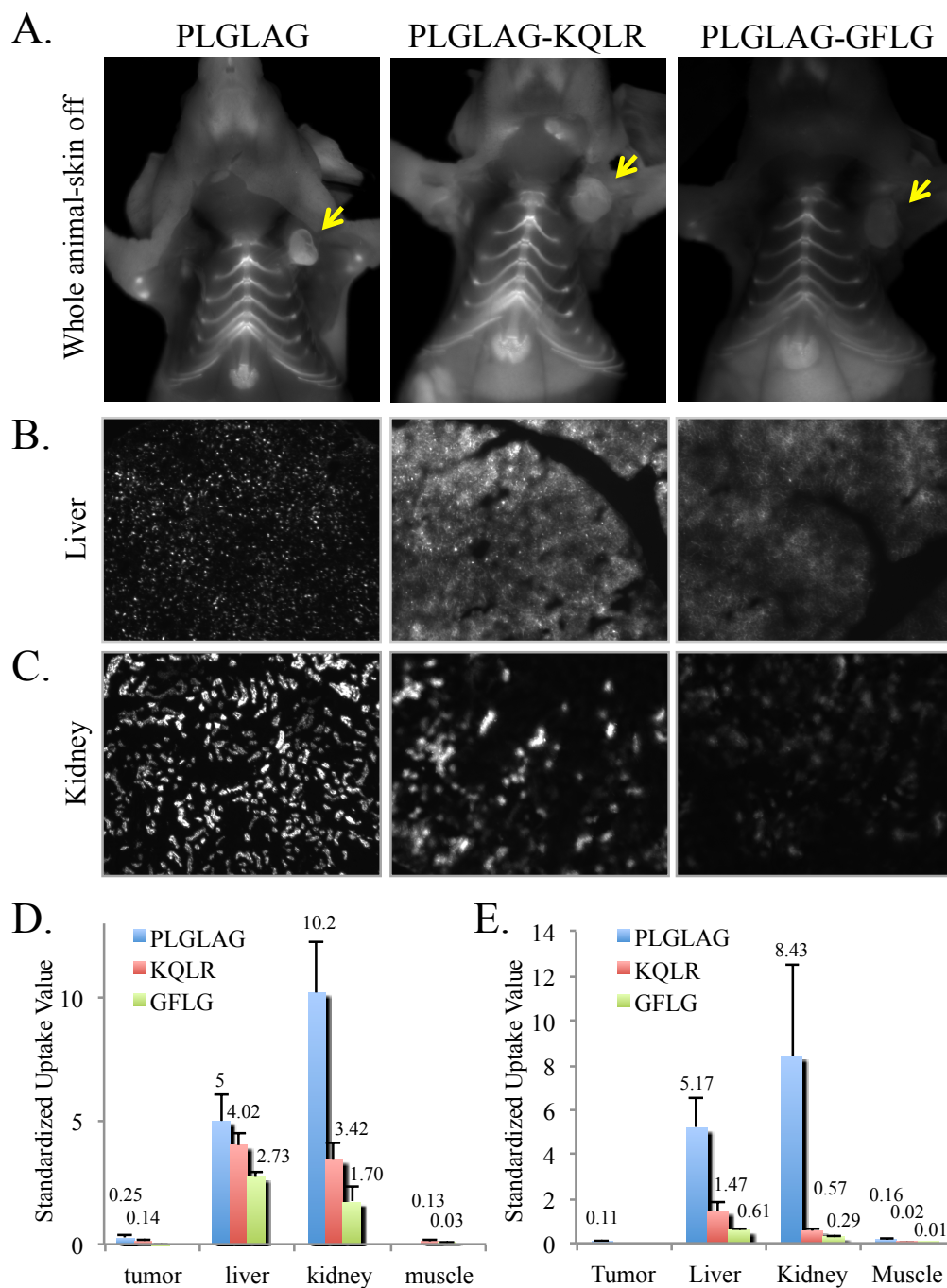
Figure 2.3 Addition of an enzyme labile sequence between the r9 and Cy5 results in clearance of the fluorescent molecule from tissues. A) Skin off images of HT1080 tumor bearing mice 6 hours after injection of 10 nanomoles of Ac-r_9-x-PLGLAG-e_9-c(Cy5), Ac-r_9-x-PLGLAG-e_9-KQLR-c(Cy5) and Ac-r_9-x-PLGLAG-r_9-GFLG-c(Cy5) peptides, yellow arrow indicate the tumor. B-C) Cy5 images of 10 μm sections of liver (B) and kidney (C) harvested and flash frozen 6 hours post peptide injection. D-E) SUV values for various tissues at either 6 hours (D) or 24 hours (E) after peptide injection. SUV values are not present for tissues where the Cy5 fluorescence could not be detected over tissue autofluorescence.

2.4.4. Construct modification to increase tumor targeting

In an attempt to improve tumor targeting and reduce off target uptake, variations were made to the standard ACPP structure (Figure 2.4 A). It was hypothesized that increasing the number of glutamates from 9 to 11 could lessen the cartilage and joint staining that distracts from the tumor contrast. It is presumed that this labeling is due to an electrostatic interaction between the positively charged polyarginine portion of the ACPP and the negative charges of the proteoglycans present in cartilage. Having a net negative charge on the ACPP could prevent this interaction. Peptides 1958 (e_9) and 2623 (e_{11}) were injected into mice with HT1080 tumors (Figure 2.4 B). The e_{11} peptide had less fluorescent signal in the cartilage, but it was not significant enough to compensate for the corresponding reduction in tumor uptake (Figure 2.4 C). The additional negative charges also reduced uptake in the muscle and liver, with an increase in the amount of probe found in the kidneys (Figure 2.4 D).

The next structural change investigated was the formation of a dimeric ACPP by conjugating two peptides via a bis reactive Cy5 dye. The rational was that multiple cleavage sites could help increase the probability of peptide activation at the site of the tumor during the short time that the probe is in circulation, and that doubling the size may decrease the diffusion into the cartilage. When injected into HT1080 tumor bearing mice, the dimeric peptide (2465) did not increase tumor uptake, but was successful at reducing peptide accumulation in the muscle and cartilage (Figure 2.4 E and F). It also had moderate elevations in liver and kidney SUVs (Figure 2.4 G).

Finally, a cyclic ACPP was generated by the addition of another PLGC(Me)AG cleavage site following the r_9 and the formation of a disulfide bridge between two

cysteine residues placed at opposite ends of the peptide. This peptide performed slightly better in the HT1080 tumor model, with a 15% increase in tumor uptake and a decrease in both muscle and cartilage staining (Figure 2.4 H and I). There was however an elevation in liver uptake and a drastic increase in the amount of peptide found in the kidneys (Figure 2.4 J). While there was a subtle improvement in tumor:muscle ratio, it was not sufficient to warrant the added time and cost associated with synthesis and formation of the cyclic ACPP.
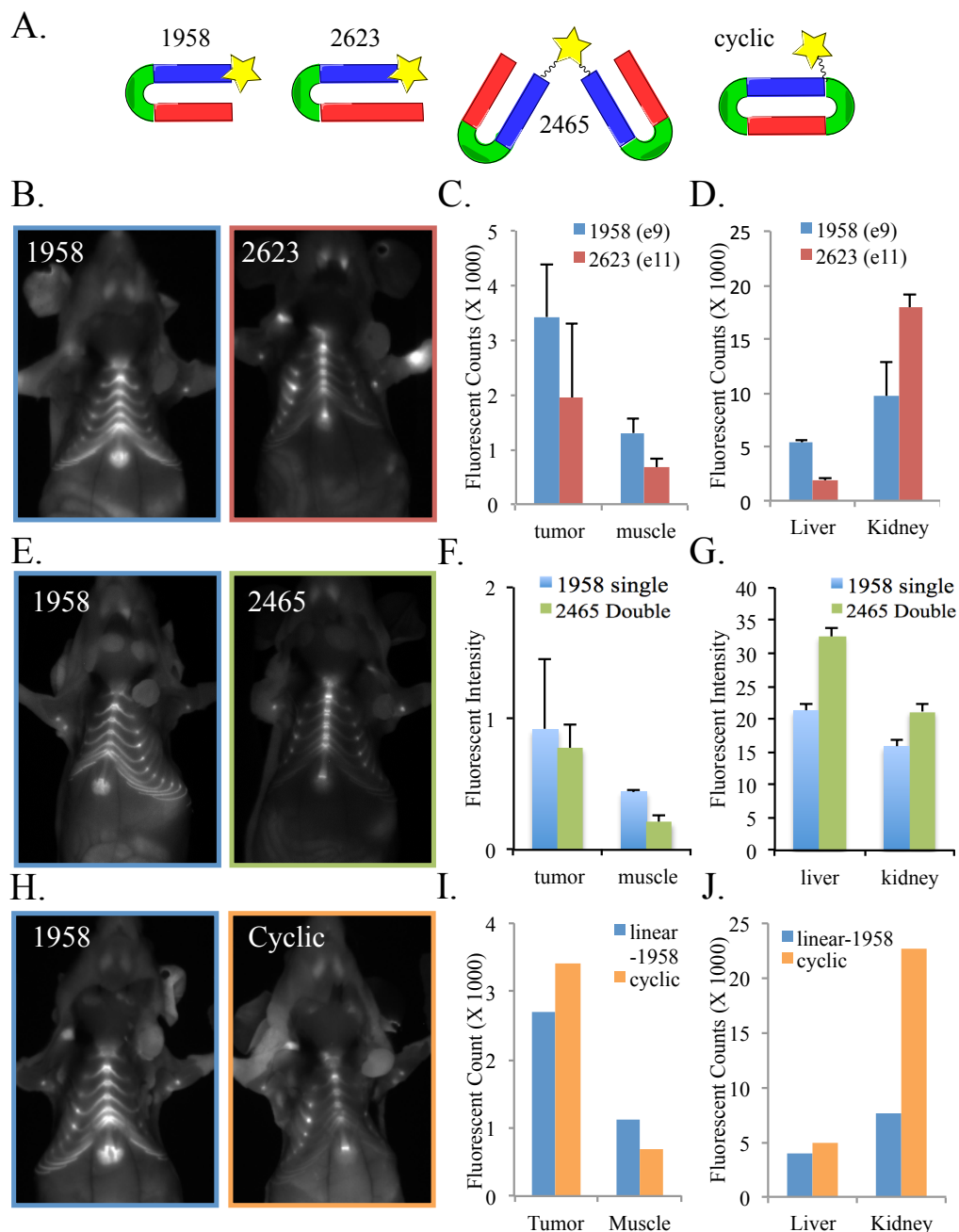
Figure 2.4 Structural modifications to ACPPs to increase tumor homing and reduce off target uptake. A) Cartoons of the various ACPPs, first the standard ACPP (1958), then the net negative charge e11 peptide (2623), the dimeric ACPP (2465) and finally the cyclic peptide. B-D) Comparison of 1958 and 2623, skin off images of HT1080 tumor bearing mice (B) fluorescent intensities of tissue homogenates for tumor and muscle (C) and the fluorescent intensities of liver and kidney tissue homogenates (D). E-G) Comparison of 1958 and the dimeric 2465, skin off images of mice with HT1080 tumors 6 hours post peptide injection (E) fluorescent intensities of tumor and muscle tissue homogenates (F) and liver and kidney tissue homogenates (G). H-J) Comparison of the standard 1958 ACPP with a cyclic ACPP, skin off images of HT1080 tumor bearing mice (H) fluorescent intensities of tumor and muscle homongenates (I) and fluorescent intensities for liver and kidney homogenates (J).

2.4.5. Attachment of ACPPs to serum albumin *in situ*

Currently, the best way to improve the pharmacokinetic properties of ACPPs is to attach them to large molecular weight carriers. Previous reports have shown that attaching ACPPs to dendrimeric nanoparticles, albumin and dextrans can improve tumor uptake, increase blood circulation time and reduce kidney accumulation due to renal filtration (Olson, Aguilera et al. 2009; Olson, Jiang et al. 2010). Unfortunately the synthesis and purification of these particles can be time consuming, there are complications with solubility, and the quality control analysis is not always obvious or informative. To remedy these issues, an ACPP was generated with a maleimide moiety on the N terminus that can covalently react *in situ* with the free thiol on C34 of serum albumin (Kratz, Muller-Driver et al. 2000; Kratz, Warnecke et al. 2002). This allowed for synthesis of a small peptide that can be well characterized prior to administration, then the attachment of a large molecular weight carrier while in the blood stream. Work by Dr. Todd Aguilera showed promising preliminary results with this strategy using fluorescent imaging (Aguilera 2009), but when this methodology was translated to other imaging modalities the difference in tumor uptake between MMP targeted and unclevable control ACPPs was lost.

A new panel of fluorescently labeled peptides was synthesized and tested in HT1080 xenograft tumors in an attempt to build upon previous results. In addition to the first configuration where enzymatic cleavage released the r_9-c(cy5) for subsequent endocytosis by cancer cells, a second peptide arrangement generated an active CPP that carried both the Cy5 and albumin into the cell (Figure 2.5 A). The sequences for these peptides are provided in Figure 2.5 B, the MMP cleavage sequence was PLGC(Me)AG

and two negative control sequences were tested, both a D-amino acid (2447 and 2473) and a peg$_4$ (2448). Maleimide ACPPs were injected into HT1080 tumor bearing mice at a dose of 3 nanomoles. Mice were then imaged and sacrificed 48 hours post injection because this time point yielded the best tumor:background contrast with minimal loss of fluorescent signal in the tumor.

Images of the anesthetized mice revealed that all tumors had nice contrast through the skin, independent of the cleavability of the ACPP (Figure 2.5 C). The reason for this contrast, even in absence of active targeting, is a phenomenon referred to as enhanced permeability and retention (EPR) (Matsumura and Maeda 1986; Maeda, Wu et al. 2000). EPR is a combination of leaky tumor vasculature and insufficient lymphatic drainage, allowing for accumulation and retention of proteins and large molecules. It was theorized that ACPPs would be able build upon this passive accumulation and increase the amount of imaging agent that remained in the tumor after a sufficient wash out period.

The skin was removed to expose the tumor, thoracic cavity and abdomen (Figure 2.5 D). Conjugation of the ACPP to albumin successfully diminished cartilage staining and significantly reduced the amount of peptide deposited in joints. The second peptide configuration had some elevation in tumor fluorescence that appeared to be enzyme depended (Figure 2.5 D), which was confirmed by homogenizing the tumor tissue and calculating SUVs (Figure 2.5 E). The amount of peptide found in the liver was fairly comparable to free peptides, but there was a reduction in kidney SUV (Figure 2.5 F). Unfortunately the 1.3 fold increase in tumor uptake with 2470 (MMP cleavable) versus 2473 (uncleavable) is not sufficient to warrant further testing of this MMP targeting strategy in primary tumors.

A) Schematic representation of ACPP configurations for before and after protease cleavage.

B)

	Peptide Sequence
2361	Mal-peg4-e$_9$-OPLGC(Me)AG-r$_9$-c(cy5)
2447	Mal-peg4-e$_9$-OplGc(me)aG-r$_9$-c(cy5)
2448	Mal-peg4-e$_9$-peg4-r$_9$-c(cy5)
2470	Suc-e$_8$-OPLGC(Me)AG-r$_9$-c(cy5)-peg4-mal
2473	Suc-e$_8$-OplGc(me)aG-r$_9$-c(cy5)-peg4-mal
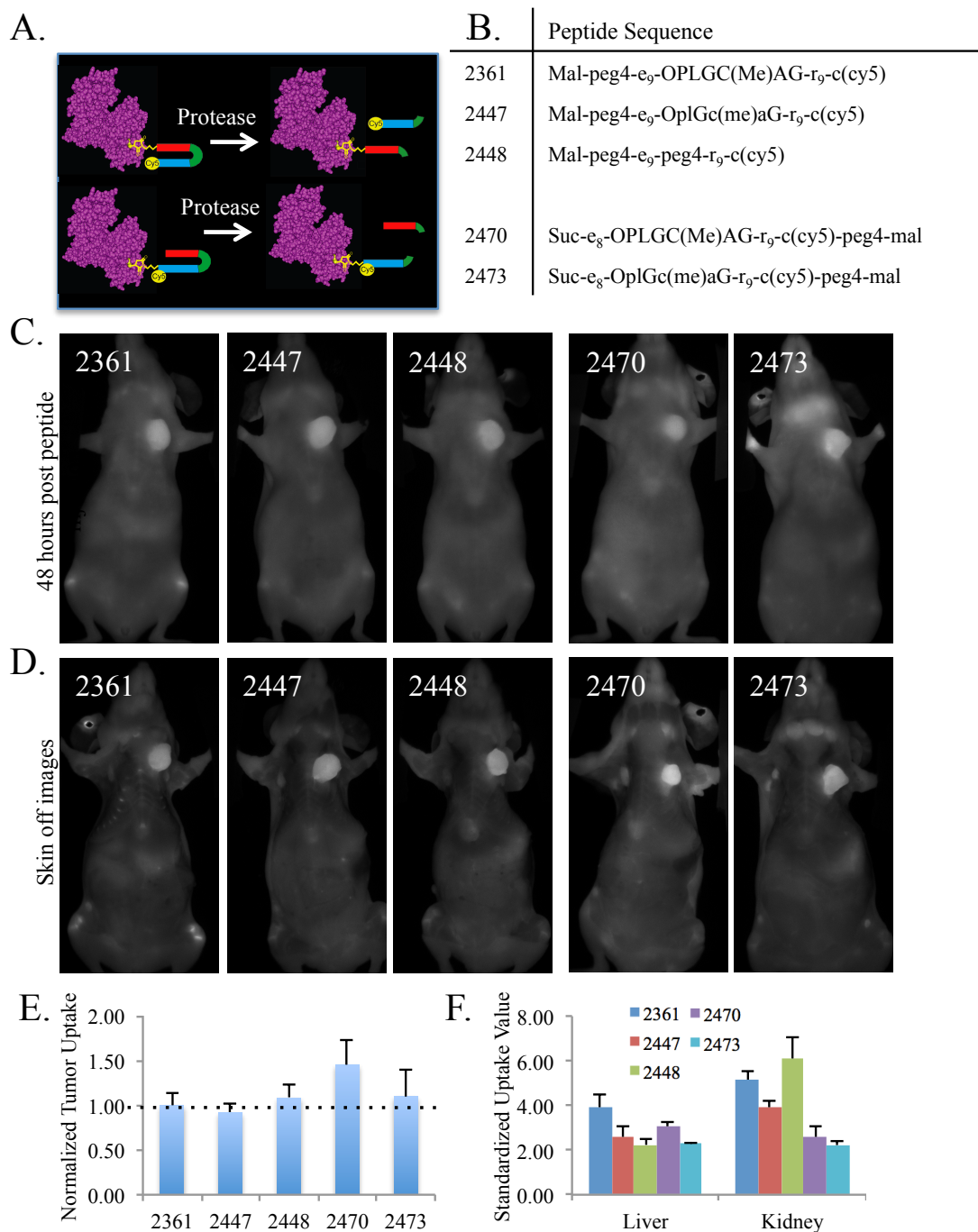
Figure 2.5 *In vivo* testing of maleimide peptides yields no significant difference between MMP cleavable and control ACPPs. A) Schematic representation of ACPP configurations for before and after protease cleavage. B) A table with all the peptide numbers and corresponding peptide sequences. C) Skin on images of mice with HT1080 tumors 48 hours after a 3 nanomole injection of Cy5 labeled maleimide peptides. D) Corresponding images of mice once the skin has been removed to expose the tumor and surrounding tissue. E) Tumor SUV values for the various maleimide peptides normalized to peptide 2361. F) Liver and kidney uptake values for each of the peptides in the panel.

2.4.6. Addition of pre targeting ligands

The final mechanism to increase tumor selectivity that will be discussed in this chapter is the addition of another targeting moiety. This ligand could function to add affinity for cancer cells, or to pre-target the ACPP in the direct vicinity of enzymatic activity and improve activation. Two molecules were tested for their ability to increase tumor uptake, folate and cyclic RGD.

Folic acid is used in the biosynthesis of nucleotide bases and required for cell survival and proliferation. It has a high affinity for the cell surface folate receptor, FRα, (K_D ~100pM). This protein exhibits very limited distribution and accessibility to blood circulation, but becomes highly unregulated in certain epithelial cancers as well as activated macrophages (Turk, Breur et al. 2002; Hilgenbrink and Low 2005). Folate has been successful at targeting both imaging and therapeutic agents, some of which are in various stages of clinical development (Low and Kularatne 2009). Therefore, it was a prime candidate for attachment to the N-terminus of an ACPP. Folate targeted ACPPs were synthesized with the general structure of folate-peg$_4$-e$_9$-OPLGC(Me)AG-r$_9$-c(Cy5) (2460) with control peptides consisting of folate-peg$_4$-e$_9$-Oplgc(Me)ag-r$_9$-c(Cy5) (2503) and Suc-e$_8$-OPLGC(Me)AG-r$_9$-c(Cy5) (1958).

Folate targeted ACPPs were first tested in mice harboring HT1080 tumors at the standard 10 nanomole dose and 6 hour terminal timpoint (Figure 2.5 A). In this model there was a 33% increase in tumor uptake with 2460 versus 2503 (Figure 2.5 B) and an increase in tumor fluorescence was observed on whole animal images. Folate targeting with an uncleavable ACPP (2503) had uptake similar to that of 1958, but better optical contrast. These results were promising for the concept of dual/pre-targeting, but overall

the tumor uptake values were relatively low. Since HT1080s are not known to

overexpress the folate receptor, this was not the optimal tumor model for testing this

targeting mechanism.
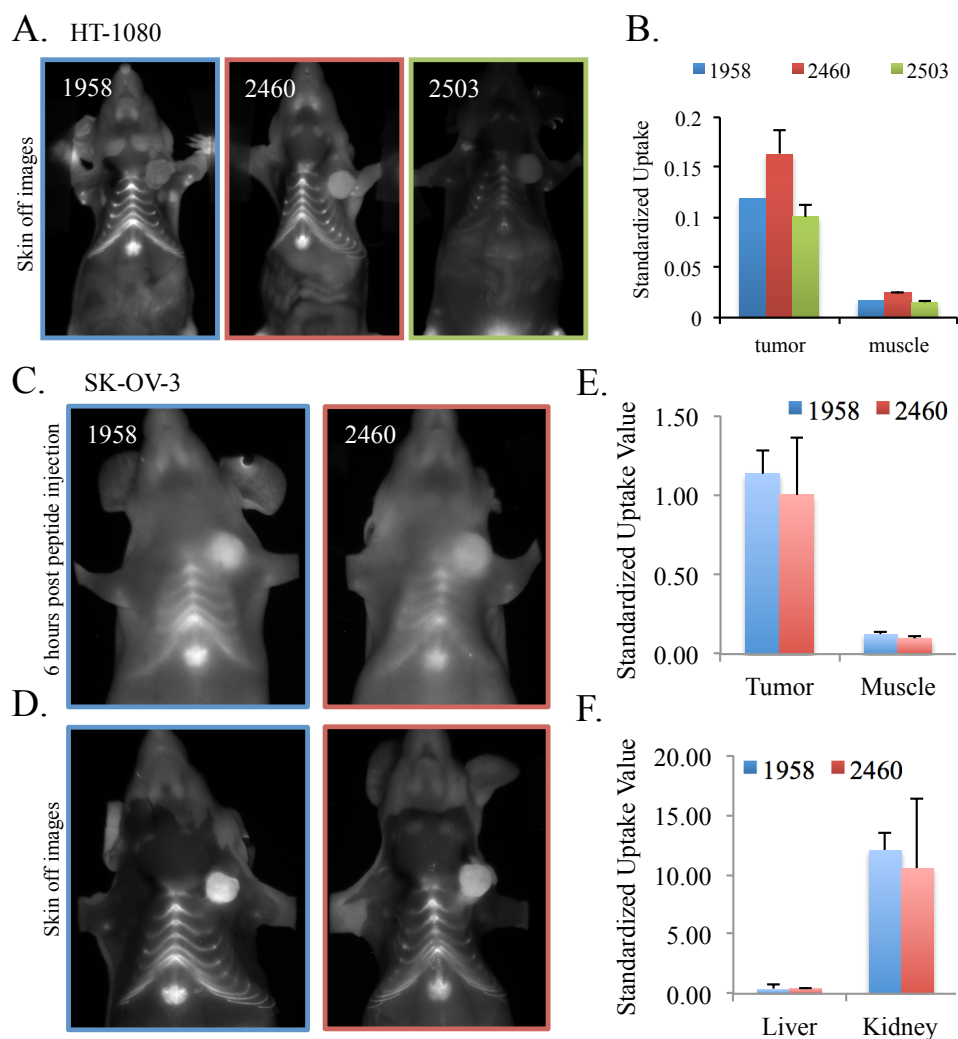
Figure 2.6 Addition of folate to ACPP moderately increased tumor uptake in HT1080 xenografts but had no additive effect in the SK-OV-3 ovarian cancer model. A) Mice harboring HT1080 tumors were injected with 10 nanomoles of either the standard ACPP, 1958: Suc-e_8-OPLGC(Me)AG-r_9-c(Cy5), folate pre targeted ACPP, 2460: folate-peg$_4$-e_9-OPLGC(Me)AG-r_9-c(Cy5), or folate pre-targeted control ACPP, 2503: folate-peg$_4$-e_9-Oplgc(Me)ag-r_9-c(Cy5). Six hours after injection mice were sacrifice and the skin was removed to visualize the tumor and surrounding tissue. B) SUV values were determined for the tumor and muscle. C) Mice were fed on a low folate diet for three weeks prior to injection of SK-OV-3 cells that had also been cultured in low folate media. Tumors were allowed to grow to approximately 5 mm prior to injection with 10 nanomoles of either 1958 or 2460. Tumor contrast was present in anesthetized mice six hours post peptide injection. D) Post mortem, skin was removed to reveal tumors and surrounding tissue. E-F) Tissues were harvested from the mice and homogenized to calculate the SUV value for the tumor and muscle (E) as well as the liver and kidney (F).

Ovarian cancers and several other epithelial-based malignancies overexpress FRα (Kalli, Oberg et al. 2008), therefore SK-OV-3 xenograft tumors were chosen as the model for the next round of folate-ACPP testing. SK-OV-3 cells were cultured in low folate media, which is closer to the physiolocal concentration found in human plasma and has been shown to induce even higher FRα expression level (Miotti, Facheris et al. 1995). Mice were also fed low folate chow for the duration of the experiment in order to bring the levels of folaic acid in their blood stream down to levels similar to humans.

Peptides 1958 and 2460 were injected into mice with SK-OV-3 tumors, and while the addition of folate had no impact on tumor uptake, tumor targeting in this model was impressive. SK-OV-3 xenografts were distinguishable through the skin (Figure 2.5 C) and had superior contrast once the skin was removed (Figure 2.5 D). There was no significant difference in tumor SUVs for 1958 and 2460 but the values were over 1.1, which is the highest tumor SUV for a free peptide to date. This cohort of mice had low liver uptake (Figure 2.5 F) and kidney SUVs similar to what has been observed in the past.

Cyclic RGD was the next pre-targeting ligand that was tested. This circular peptide is a mimetic for the exposed binding region of extracellular proteins like vitronectin and fibronectin and is a ligand for integrin receptors such as $\alpha_v\beta_3$ (Pierschbacher and Ruoslahti 1984). Integrin $\alpha_v\beta_3$ is nominally expressed in quiescent endothelial cells but becomes highly upregulated upon endothelial cell activation, which occurs during angiogenesis and tumor growth (Brooks, Clark et al. 1994; Hood and Cheresh 2002; Ruoslahti 2002). Synergy between MMP-2 and integrin targeting has a plausible molecular basis because $\alpha_v\beta_3$ is known to bind to the hemopexin domain of

MMP-2 (Brooks, Stromblad et al. 1996). Binding of cyclic RGD to $\alpha_v\beta_3$ should not interfere with MMP-2 localization since inhibitors that disrupt the $\alpha_v\beta_3$-MMP-2 interaction had no impact on the ability of the integrin to bind its target matrix proteins (Silletti, Kessler et al. 2001).

A panel of cyclic RGD peptides was synthesized where either both targeting mechanisms were active ((cRGDfC)-peg$_4$-e$_9$-OPLGC(Me)AG-r$_9$-c(cy5)), integrin targeting was controlled for by replacing cRGDfK with cRADfK, or finally the MMP-2 targeting was diminished by substituting L-amino for a polyethylene glycol (PEG6) in the substrate region. These peptides were injecting into mice with MDA-MB-231 orthotropic breast tumors and only with dual targeting were the tumors distinguishable through the skin with fluorescence (Figure 2.7 A). Once the skin was removed it was clear that the dual targeted peptide had significantly greater tumor fluorescence than either of the targeting mechanisms individually (Figure 2.7 B).
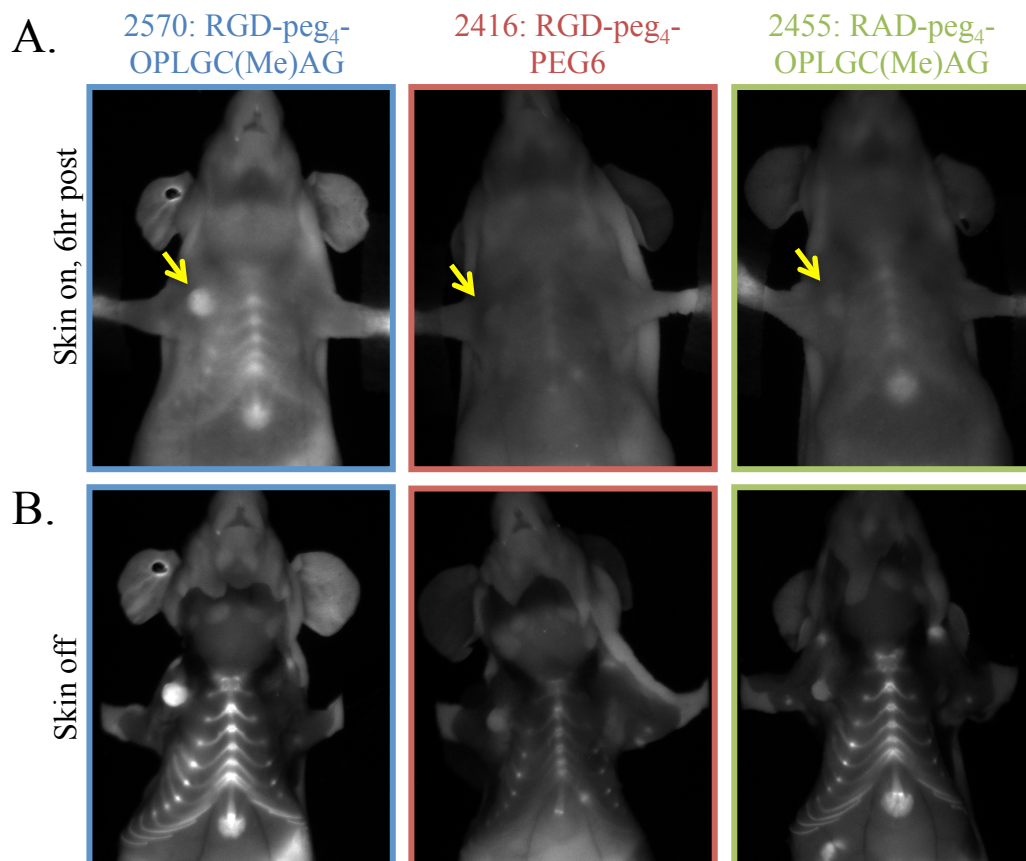
Figure 2.7 Addition of cyclic RGD ligand to MMP cleavable ACPPs greatly enhance uptake in MDA-MB-231 breast cancer tumors A) Mice harboring MDA-MB-231 tumors of approximately 2-3mm in diameter were injected with 10 nanomoles of either 2570 (dual positive), 2416 (integrin positive, MMP negative) or 2455 (integrin negative, MMP positive) Cy5 labeled ACPPs. Six hours after peptide injection, mice were anesthetized and imaged; tumors are indicated with yellow arrows. B) Mice were anesthetized and skin was removed to expose the tumor and surrounding tissue.

Next, the linkage between the cyclic RGD and ACPP was modified to see if it would impact tumor targeting. Frist, the length of the peg linker was increased from a peg$_4$ to a peg$_{12}$ and next the location of the linkage was changed from the N-terminus to a cysteine residue that was added proximal to the enzyme cleavage site (Figure 2.8 A). The additional size of the peg linker increased tumor uptake as well as lowered peptide localization in the cartilage, muscle, liver and kidney (Figure 2.8 B, C and D). Additionally, moving the attachment site further improved tumor uptake with similar

distribution to other organs. This also leaves the N-terminus of the peptide free for the addition of another fluorescent dye (and the development of FRET sensors for enzymatic activity) or the attachment of chemotherapeutic molecules, which will be one of the topics in chapter 4.
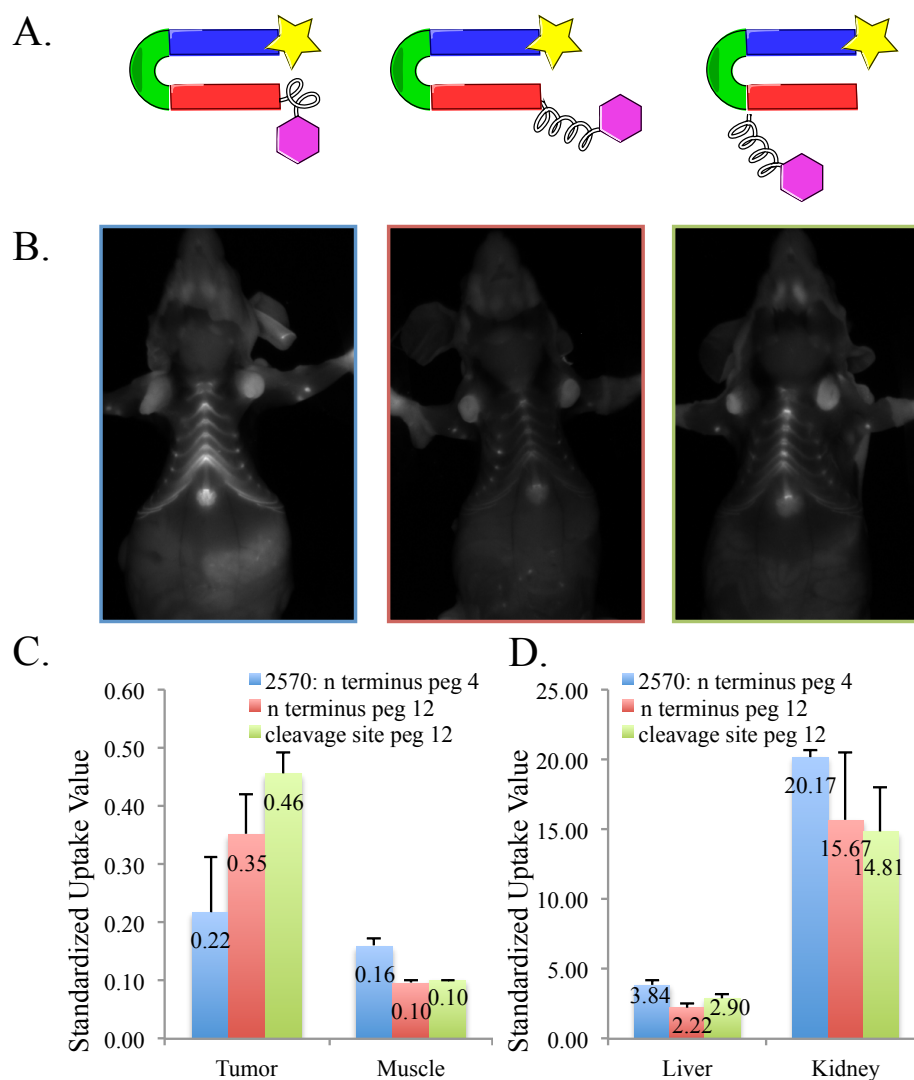
Figure 2.8 A longer peg linker and moving the attachment site of cyclic RGD ligand to the ACPP improves *in vivo* peptide distribution. A) Cartoon representations of the three cyclic RGD pretargeted ACPPs. The original construct attached the cyclic RGD on the N terminus of the peptide with a peg$_4$ linker. This peg$_4$ was then replaced by a peg$_{12}$ and the site of the attachment was moved from the N terminus to a cysteine residue that was inserted near the substrate portion of the peptide. B) Peptides were injected into mice with MDA-MB 231 breast cancer tumors and six hours after administration the animals were sacrificed and the skin was removed. Fluorescent images demonstrate that the longer peg linker increases tumor fluorescence and reduces the amount of peptide in the cartilage and the tissue surrounding the tumor. C-D) SUV values were determine for tumor and muscle (C) as well as liver and kidney (D) tissues.

2.5. Discussion

The versatility of ACPPs make them an attractive platform for molecular targeting. Almost all aspect of the peptide can be modified in attempts to increase tumor selectivity, contrast and biodistribution. One of the most profound changes that can be made is altering the amino acid sequence in the linker region. This is the portion of the peptide that gives it an "identity" and allows it to be a tool for monitoring specific protease activity *in vivo*. In order for this tool to be effective, the substrate sequence needs to be very specific for the target enzyme and unfortunately this is not an easy task. A number of the enzyme specific sequences that have been inserted into the ACPP format are either no longer cleavable by their target enzyme or get cleaved by multiple proteases. On the other hand, making ACPPs very specific may decrease the potential for peptide activation is diseases such as cancer, where protease activity can become highly unregulated. When the goal is just to increase the absolute amount of uptake in a tumor, it may be advantageous to have a substrate that is a bit promiscuous, as long as it doesn't result in a large increase in off target cleavage as well. When comparing the ACPPS presented in section 2.4.1, it appeared that fairly specific substrates had lower tumor uptake, although there were exceptions to this observation.

Once the ACPP has been deposited in a given tissues, selective release of the cargo molecule becomes a useful tool to manipulate biodistribution, and is an important barrier for eventual therapeutic applications. The data with KQLR and GFLG was promising in that it provided *in vivo* data to validate the mechanism. The substrate KQLR, designed for enzymes expressed in a distinct location (Hepsin in the liver) had higher tumor retention at earlier timepoints but was also not as successful as GFLG, a

target for a more generally expressed enzyme (cathepsin B in cell lysosomes), at clearing Cy5 from the liver and kidneys. For imaging purposes, when it is essential to maintain tumor contrast but valuable to clear the probe from off target tissues, targeting an enzyme with a limited expression profile is advantageous. KQLR was eventually cleaved in tumors as well, so it may not be useful for constructs or modalities that have long circulation times or require a wash-out period.

Significant effort was put into making structural variations on the ACPP. Changes such as the addition of negative charges and making dimeric and circular peptides did not have an impact on tumor uptake. However, they considerably reduced peptide labeling of cartilage and tissue surrounding the tumor. While there were different hypotheses to rationalize these modifications, it could be that increasing the molecular weight of the ACPP accomplished this reduction in background. It may not be necessary to go to the lengths of generating circular or dimeric peptides; it could be as easy as adding peg units to the N terminus. This would provide a similar increase in molecular weight, help with solubility, reduce hydrophobicity and it's a simple conjugation.

There is a delicate balance when it comes to the addition of molecular weight because of the EPR effect (Matsumura and Maeda 1986; Maeda, Wu et al. 2000). When molecules as large as serum albumin are added to the peptide, uptake in tumors becomes dominated by EPR and the enzymatic cleavage mechanism is overshadowed. There were some experiments where a two-fold difference in tumor uptake was noted between cleavable and uncleavable maleimide ACPPS, especially when peptides were tested in small (~3-5mm diameter) tumors. Previous results by Dr. Todd Aguilera demonstrated significant differences in optical contrast that was enzyme dependent, and it is still

unknown as to why the results were not reproducible. When ACPPs were attached to G5

PAMAM dendrimers, again a 2-fold difference in enzyme dependent uptake was

observed (Olson, Jiang et al. 2010). It may be that these high molecular weight probes

are better suited for models where ERP is not so prevalent. Successful experiments with

maleimide peptides will be reported in various lung metastasis models in Chapters 6 and

7 of this dissertation.

Finally, the addition of pre-targeting ligands to ACPPs generated some of the

most exciting data in this chapter. The addition of folate yielded a moderate enhancement

in tumor uptake in a model that was not designed to give folate an advantage (HT1080),

yet in a model where steps were taken to ensure the upregulation of the folate receptor,

no difference was observed (SK-OV-3). The ovarian cancer model did however have

some of the most impressive tumor contrast and SUVs of all the models tested with free

peptides. The cyclic RGD pre targeting drastically improved tumor contrast and uptake

and further investigation and discussion of this dual targeting strategy is the topic of

Chapter 4 in this dissertation.

2.6. Acknowledgements

The dissertation author would like to thank:

Dr. Todd Aguilera and Dr. Emilia Olson for mentoring me during my rotation in

the Tsien Lab, training with animals and the proper protocols for imaging. Dr. Tao Jiang,

Dr. Stephen Adams, Dr. Elamprakash Savariar, Dr. Mike Whitney and Qing Xiong for

synthesis of many of the peptides tested in this chapter. Dr. Tao Jiang, Dr. Stephen

CHAPTER 3: Disulfide Bond Reduction is a Viable Mechanism to Release Cargo Molecules from ACPPs confined in endocytic vesicles

3.1. Abstract

Disulfide bond reduction is a common strategy used for drug release in the design of molecular targeted therapeutics. Recent controversy about the reducing power of the endocytic pathway has lead to the investigation of bond reduction as it pertains to cell penetrating peptides (CPP). A fluorescent probe, Alexa 488-CPP-S-S-Alexa 568 (CPP-FRET), was generated to monitor disulfide reduction in live cells by observing changes in fluorophore emission. This peptide confirmed that disulfide bond reduction occurs upon CPP endocystosis by a variety of cancer cells and takes place over the course of six to eight hours. If the molecule being released from the CPP does not have the necessary characteristic to pass freely through membranes, it will remain sequestered in these vesicles and at times be differentially sorted from the CPP. The kinetics of this reduction are moderately dependent on the thiol pK_a of the linker and do not change with varying the peptide concentration over the range of 0.5-2μM. The mechanism does not required acidic conditions or involve cell surface sulfhydryls, but it can be inhibited with cell permeable sulfhydryl blockers like N-ethylmaleimde. A version of this probe was made for *in vivo* applications by designing an ACPP using the same principles of disulfide bond reduction and FRET, but with longer wavelength dyes. This peptide was found to be unstable in plasma, as the disulfide bond underwent a thiol exchange reaction with serum albumin.

3.2. Introduction

A long-term goal for ACPPs is to expand their use beyond imaging into therapeutic delivery. This adds another level of difficulty because not only do the ACPPs have to reach the cancerous microenvironment and penetrate into the tumor cells, they must also provide access to the appropriate cellular compartment for therapeutic activity. For many chemotherapeutics, this means the cytosol or the nucleus. For years CPPs or protein transduction domains (PTDs) were proposed as efficient carriers for the delivery of bioactive molecules or therapeutics to those intracellular targets. Initially, it was thought that these short peptides, once bound to the exterior membrane of a cell, had the ability transduce directly across that cellular barrier (Derossi, Chassaing et al. 1998; Schwarze, Ho et al. 1999; Schwarze, Hruska et al. 2000). Unfortunately, this distribution to the cytosol and nucleus were often an artifact introduced by fixation of the cells (Vives 2003; Vives, Richard et al. 2003; Vives 2005).

The real mechanism of CPP and PTD uptake and the efficiency of membrane translocation has been discussed and debated for many years. Currently, it is generally accepted that peptide binding is a result of electrostatic interactions between the basic cationic residues of the CPP/PTD and the negative charged proteoglycans on the surface of cells (Tyagi, Rusnati et al. 2001; Console, Marty et al. 2003; Kameyama, Horie et al. 2007). After binding, CPPs are subsequently internalized through various forms of endocytosis (Nakase, Niwa et al. 2004; Wadia, Stan et al. 2004). However, there are tissue culture conditions, such as high peptide concentrations (~10 μM) and serum depletion, for which rapid uptake in live cells is independent of endocytosis (Kosuge, Takeuchi et al. 2008). Previous observations from our lab have found both mechanisms

to be valid, with a 1-10 micromolar threshold where peptide uptake becomes rapid and endosome independent. In most cases, when peptide concentrations are lower and cells are given the proper nutrients, it is understood that a majority of the peptide is confined to endosomal puncta. Only when very sensitive genetic reporters are used has there been conclusive evidence that a small fraction of the peptide can escape the endosome (Dr. Sujata Emani unpublished results; Melikov and Chernomordik 2005; Adams 2006).

For therapeutic delivery, more than a small portion of the peptide linked chemotherapeutic needs to be released from endocytic vesicles. Two obvious routes for escape are disruption of endosomal membranes and selective release of the drug from the CPP. To accomplish the former there are many strategies proposed in the literature, some of which include: peptides such as HA2 and GALA, that in acidic environments undergo conformation changes and can then form pores in the membrane (Plank, Oberhauser et al. 1994; Li, Nicol et al. 2004; Wadia, Stan et al. 2004), toxic proteins like listeriolysin-O (Saito, Amidon et al. 2003), and the "proton sponge" hypothesis where cationic polymers cause osmotic swelling in the endosomes and subsequent membrane permeability (Jones, Cheung et al. 2003; Sonawane, Szoka et al. 2003; Yang and May 2008). One major concern is that these agents have to be treated in trans with the ACPP-drug conjugate and some of them may have their own inherent toxicities. Furthermore, the chemotherapeutic is not released in its natural form and is still attached to the CPP, which could significantly alter its potency.

For selective release of the drug from the peptide, again there are a plethora of strategies to select from. Some of these include: enzymatic release via cleavage of a peptide linker by lysosomal associated proteases like Cathepsin B (Dubowchik and

Firestone 1998), chemical conjugations that are sensitive to the acidic pH of the late

endosomes and lysosomes (Duncan, Kopeckova-Rejmanova et al. 1987; Haag and Kratz

2006; Luong, Issarapanichkit et al. 2010) and the use of disulfide bonds that can be

broken in the reducing intracellular environment.

This report chose to focus on disulfide bond reduction because of the controversy

in the literature with regards to the reducing power of endocytic vesicles (Feener, Shen et

al. 1990; Austin, Wen et al. 2005; Yang, Chen et al. 2006; Cole and Donaldson 2012).

Some reports claim that endosomes actually have an oxidizing potential while others

postulate that the glolgi apparatus is likely responsible for reduction of disulfide bonds in

endocytosed molecules. Furthermore, when disulfide bond reduction is being justified as

a mechanism for intracellular release, the cytosolic concentration of glutathione is often

referenced. Yet many of those reports never validate that their probes actually make it out

of endocytic compartments (Navath, Kurtoglu et al. 2008; Cheung, Kim Chiaw et al.

2009). The paper by Cheung et.al is particularly interesting because it utilizes a system

very similar to the one presented in this report, a CPP based reporter with a disulfide

bond linking two fluorophores. They claim their probe provides a readout for peptide

delivery into the cytosol when treated at low peptide concentrations, yet there is no

microscopic evidence to validate the peptide's location within the cell.

This chapter will detail the development and characterization of a CPP based

probe that monitors disulfide bond reduction using fluorescence resonance energy

transfer (FRET). Confocal imaging on live cells will be used to monitor changes in

peptide fluorescence and these images will help decipher where bond reduction occurs

inside the cell. Beyond subcellular location, experiments are also performed to gain

insight on the mechanism. Finally, initial attempts at translating this technology into measuring reducing *in vivo* are reported.

3.3. Methods

3.3.1. Peptide synthesis

A NH_2-c-r_9-$CONH_2$ peptide was made using standard solid phase Fmoc peptide synthesis, where lower case letters refers to D-amino acids, and the final $CONH_2$ indicates C-terminal amide. The peptide was cleaved from the resin using trifluoroacetic acid (TFA) containing 2% thioanisole, 2% water and 4% triisopropylsilane (TIPS) for 4 h under N_2. The reaction mixture was then filtered under N_2 to remove the resin. This filtrate was concentrated by evaporation and the product was precipitated by adding ice-cold 50% hexanes in methyl *tert*-butyl ether. The peptide was collected by centrifugation and careful decantation of solvents. The product was dried under vacuum and dissolved in dimethyl sulfoxide (DMSO) then purified using preparative high performance liquid chromatography (HPLC)

NH_2-c-r_9-$CONH_2$ was reacted with 2,2'-dithiobis(5-nitro-pyridine) (Sigma) in dimethylformamide (DMF) that had been purged with N_2 with the addition of 2 μL *N*-methylmorpholine (NMM) to generate NH_2-c(Npy)-r_9-$CONH_2$. The solvents were evaporated under vacuum and the reaction product was dissolved in DMSO prior to purification with HPLC. The N terminus of the thiol-protected peptide was then labeled with various green fluorescent dyes (BODIPY FL, Rhodamine Green and Alexa 488) that were purchased as NHS-esters (Invitrogen). Dyes were dissolved in DMSO and the

labeling reaction was performed in DMF that had been purged with N_2 with the addition of 2 μL NMM. Again, the solvents were evaporated under vacuum and the reaction product was dissolved in DMSO prior to purification with HPLC.

To generate the second portion of the peptide, cystamine dihydrochloride (Fluka) was reacted with various red fluorescent dyes (Tetramethyl Rhodamine, Alexa 555, ROX and Alexa 568) that were purchased as NHS-esters (Invitrogen). Cystamine dihydrochloride and the dye-NHS were first dissolved in DMSO and then diluted in DMF that had been purged with N_2. 5μL of NMM was added and the reaction was performed at room temperature and allowed to proceed overnight in the dark. Solvents were evaporated under vacuum and the reaction product was then dissolved in 30% acetonitrile (ACN)/water solution that was buffered to pH 8 using TRIS. DTT was added to a final concentration of 10mM to reduce the disulfide bond and the product was purified with HPLC. The (red dye)-$CONHCH_2CH_2SH$ was reacted with the (green dye)-c(Npy)-r_9-$CONH_2$ in DMF with 2μL NMM, note that the 5-nitro pyridine activated the cysteine residue on the peptide for attack by the free thiol associated with the red dye. The product of this disulfide bond formation is the disulfide CPP-FRET peptide. The maleimide control version of this probe was generated by reacting Alexa 488-c-r_9-$CONH_2$ with Alexa 568-maleimide (Invitrogen) under conditions similar to those previously described. The final peptide products were purified by HPLC and the identity was confirmed with mass spectroscopy.

To generate the SYBR-101 disulfide CPP, a cr_9 peptide was synthesized with an acetyl capped N- terminus, Ac-NH-c-r_9-$CONH_2$. SYBR-101 NHS (Invitrogen) was reacted with cystamine hydrochloride as previously described, and the SYBR-101-

$CONHCH_2CH_2SH$ formed a disulfide bond the with cr_9 peptide. To generate the thioether control, a Ac-NH-Cys(-$CH_2CH_2CH_2NH_2$)-r_9-$CONH_2$ peptide was synthesized by replacing the Fmoc D-cysteine with Fmoc-Cys(3-(Boc-amino)-propyl)-OH (Anaspec); during TFA cleavage from the resin the Boc protecting group was removed to generate a free amine on the modified cysteine residue. This free amine was then conjugated with SYBR-101 NHS as previously described.

To generate the nicotinic acid construct: 6,6'-dithiodinicotinic acid (Sigma) was dissolved in ice cold anhydrous DMF. While on ice, two molar equvivalents of N-hydroxybenzotriazole (HoBT) (GenScript) and N, N'-dicyclohexyl-carbodiamide (DCC) (Sigma) were added. The reaction proceeded on ice for 10 minutes then was warmed to room temperature and allowed to continue for another 20 minutes. Then 5 molar equivalents of ethylenediamine (Sigma) was added and the reaction went overnight at room temperature. Solvents were removed under vacuum and the produce was purified by HPLC. The free amine (via the ethylenediamine) was subsequently reacted with Alexa 568 NHS as previously described. This product was reduced with DTT, purified by HPLC and reacted with Alexa 488 CONH-c(Npy)-r_9-$CONH_2$ to generate the Nicotinic CPP-FRET peptide.

To generate the ACPP-FRET: NH_2-e_9-C(SS-tBu)-OPLGC(Me)AG-r_9-c-$CONH_2$ was made using standard solid phase Fmoc peptide synthesis, where lower case letters refers to D-aminoacids, O represents for 5-amino-3-oxopentanoyl, a short hydrophilic spacer, C(Me) denotes for S-methylcysteine and the final $CONH_2$ indicates C-terminal amide. The peptide was cleaved from the resin using TFA containing 2% thioanisole, 2% water and 4% TIPS for 4 h under N_2 and then the reaction mixture was filtered under N_2

to remove the resin. This filtrate was concentrated by evaporation and precipitated by adding ice cold 50% hexanes in methyl *tert*-butyl ether. The peptide was collected by centrifugation and careful decantation of solvents. The product was vacuum dried, then dissolved in DMSO and purified using HPLC with a gradient of 5-55% acetonitrile in water and 0.05% TFA over 25 min at 15mL per min flow rate. The purified product was dried using lyophilization and the product identity was confirmed by electrospray mass spectroscopy.

This purified compound was dissolved in anhydrous DMSO, then Cy5 maleimide (GE life sciences) and NMM were added. After 3 hours, the completion of the reaction was verified by LCMS. To this reaction mixture, $25\mu L$ of triethyl phosphine (TEP) was added and kept at room temperature for another 6 hours. The product was precipitated by adding 50 % hexanes in methyl *tert*-butyl ether (N_2 purged). The precipitated compound was collected by centrifugation, dissolved in DMSO and purified using HPLC with 5-55% acetonitrile gradient in water and 0.05% TFA over 25 minuets. This yielded NH_2-e_9-C(SH)-oPLGC(Me)AG-r_9-c(Cy5)-$CONH_2$, and the identity was confirmed using electrospray mass spectroscopy. This peptide was then reacted with Cy-7-CONH-PEG_2-CONH-PEG_{12}-SS-Py to generate the reduction sensitive FRET-ACPP. To synthesize the control non-reducible ACPP, the last step in the scheme was changed to Cy-7-CONH-PEG_2-CONH-PEG_{12}-Maleimide.

3.3.2. Spectral imaging of different CPP-FRET constructs

Peptides were diluted to low micromolar concentration with EMEM cell culture media without phenol red (Cellgrow) with 20mM HEPES (Gibco) buffer at pH 7.4. 100 μL of peptide solution was transferred into a well on a black 96-well, plastic bottom

plate. A plate reader (Tecan) was used to measure the emission spectrum of the peptide

using the following setting: excitation of 488nm with 6nm slit and monitoring emission

from 510nm-710nm (or values up to 750nm) with a 2nm step and an excitation of 532nm,

545nm or 565nm with a 6nm slit and monitoring emission from 565nm-710nm (or values

up to 750nm) with a 2nm step. Emission spectra were obtained before and after disulfide

reduction with 10mM dithiothreitol (DTT). 10mM stock solutions of DTT were made

fresh from powdered DTT, and 1μL was spiked into the peptide solution to ensure that

addition of the reducing agent would not significantly alter the peptide concentration.

3.3.3. Cellular imaging

HT1080 and HELA cells were obtained from ATCC and cultured in EMEM with

10% FBS. For imaging, 12×10^3 cells (in 100μL) were plated into each well of a sterile,

96-well plate with a glass coverslip for the bottom (Nunc). Cells were allowed to settle

overnight and monolayers were approximately 75% confluent prior to treatment. Media

was aspirated off and peptides at a concentration of 1μM (in serum free media) were

treated on the cells for 20 minutes at 37°C. The cells were then washed 3X for 2 minutes

each with imagining buffer (EMEM no phenol red, 10% FBS, 20mM HEPES, 1X

glutamax and 1% penicillin/streptomycin) and placed on the microscope stage in a

chamber that maintained the temperature at 37°C. Just prior to imaging, cell media was

spiked with calcein blue AM ester (Invitrogen) to a final concentration of 1μg/ml.

Imaging was performed on a Zeiss 5-Live line scanning confocal microscope with

an excitation laser of 488nm and an emission filter of 500-525nm to visualize at Alexa

488 fluorescence, 532nm excitation with an emission filter of 560-675nm to monitor

Alexa 568 fluorescence, and an excitation of 405nm with 415-480nm emission to image

calcein blue. The histogram function on the Zen software (Zeiss) was used to quantitate

Alexa 488 fluorescence. With the calcein blue channel, regions were drawn around

individual cells and the average fluorescent intensity was recorded for the Alexa 488

channel. Measurements from a minimum of 10 cells from 3 different fields of view were

combined to a average value at each time point. The first images taken for each

experiment (approx. 30 min post initiation of treatment) were used to normalize the

fluorescent intensities for every subsequent time point.

Jurkat lymphoma cells were maintained in suspension in RMPI with 10% FBS.

Cells were collected from the culture flask and centrifuged at 900RPM for 2 minutes for

form a pellet. The media was aspirated off and the pellet was then resuspended in serum

free RPMI containing a given concentration of peptide. The cells were incubated with

peptide for 20 minutes at 37°C. After that time, the cells were again pelleted and washed

3X with imaging buffer to remove any extracellular peptide. Cell solutions were

transferred to a black 96-well glass bottom plate for fluorescent analysis on a plate

reader. The cell concentration ranged from $3x10^6$-$5x10^6$ cells per well depending on the

experiment and each treatment was performed in triplicate. Emission spectra were

collected using an excitation of 485nm with 12nm slit and recording fluorescence from

515nm-680nm using a bottom read. Cells were maintained at 37°C and the plate reader

was set to take measurements every 30 minutes for up to 9 hours. Again, fluorescent

intensities were normalized to the first data point, which was collected approximately 30

minutes post the initiation of treatment, 10 minuets after the peptide was removed.

For inhibition assays, cells were first treated with the CPP-FRET peptide as

described above and after removal, the various inhibitors were added. Bafilomysin A1

(Calbiochem) was diluted to a concentration 20nM in imaging buffer containing 10% FBS. Both 5,5'-dithiobis-(2-nitrobenzoic acid) (DTNB) (Sigma) and N-ethylmaleimide (NEM) (Sigman) were first dissolved in DMSO at 100X stock solutions, then diluted to 100μM and 10μM respectively in serum free imaging buffer. For these experiments the cells remained in serum free media because DTNB and NEM are thiol reactive and could bind to serum proteins. All inhibitors remained in the media during the timecourse of the experiment.

For colocalization experiments with transferrin, r_9-Cy5 peptide at 1μM was co-treated on HT1080 cells with Alexa488-transferrin (Invitrogen) at 50μg/ml for 1 hour at 37°C in serum free media. The peptide and transferrin were washed off and cells were treated with 10μg/ml Hoechst prior to imaging. For colocalization with acidic organelles, 1μM r_9-Cy5 peptide was co-treated on HT1080 cells with 5μM Lysosensor Blue (Invitrogen) for 2 hours at 37°C. The peptide and Lysosensor were then washed off and cells were imaged with confocal microscopy.

3.3.4. Plasma stability assays

Plasma was generated by collecting blood from a mouse, via cardiac puncture post mortem, and transferring that blood to a heparinized tube for immediate centrifugation. The Plasma was aspirated from the tube and placed on ice. FRET-ACPPs were spiked into fresh plasma to a final concentration of 5μM while on ice. The initial timepoint was taken immediately after the peptide was added and then the samples were transferred to a 37°C incubator. Samples were processed and gels were run as previously described in the methods portion of Chapter 2.

3.3.5. In vivo studies with FRET-ACPP

All animal studies were done in compliance with the principles and procedures outlined by the Institutional Animal Care and Use Committee at the University of California San Diego. Female athymic nu/nu mice, 5-6 weeks of age, were purchased from Harland Labs (Placentia, California). To generate tumors, 1×10^6 MDA-MB-231 cells were injected into the mammary fat pads of female mice in a vehicle of 4mg/ml matrigel with an injection volume of 40-50μL. The cell suspension in matrigel remained on ice until immediately before the cells were aspirated into a syringe for injection. Two tumors were implanted subcutaneously, one on each side of the mouse, in the upper mammary fat pads. Tumors were allowed to grow for approximately 2 weeks, or until they reached a diameter of 3-5 mm.

Disulfide FRET-ACPPs were injected intravenously into mice at a dose of 10 nanomoles. Immediately after injection mice were placed in the Maestro small animal imager (CRI) and spectral imaging was initiated. To generate emission spectra, an excitation filter of 620/20nm was used along with a tunable dichroic emission filter. Fluorescent readings were taken at 10nm intervals over the range of 650-840nm.

3.4. Results

3.4.1. In vitro characterization of CPP FRET peptide and determining the best donor-acceptor fluorophore pair

Fluorescence resonance energy transfer (FRET) is a useful tool to visualize changes in orientation or conjugation of a molecule. FRET efficiency depends on both

the distance and the orientation between donor and acceptor fluorophores; small changes

is distance, possibly due to the breaking of a chemical bond, can result in large shifts is

spectral readout (Giepmans, Adams et al. 2006). To monitor disulfide bond reduction in

live cells, a CPP-FRET construct was made. This peptide consists of all D-amino acids

with the sequence NH_2-c-r_9-$CONH_2$-; the FRET donor is conjugated via the free amine on

the N terminus while the FRET acceptor is attached through the thiol on the cysteine

(Figure 3.1 A). When the disulfide bond is intact, excitation of the peptide using the

donor wavelength results in fluorescent emission at the acceptor wavelength. Once the

disulfide bond is reduced, acceptor fluorescence will cease and the resulting spectra will

be that of the donor (Figure 3.1 A and B).
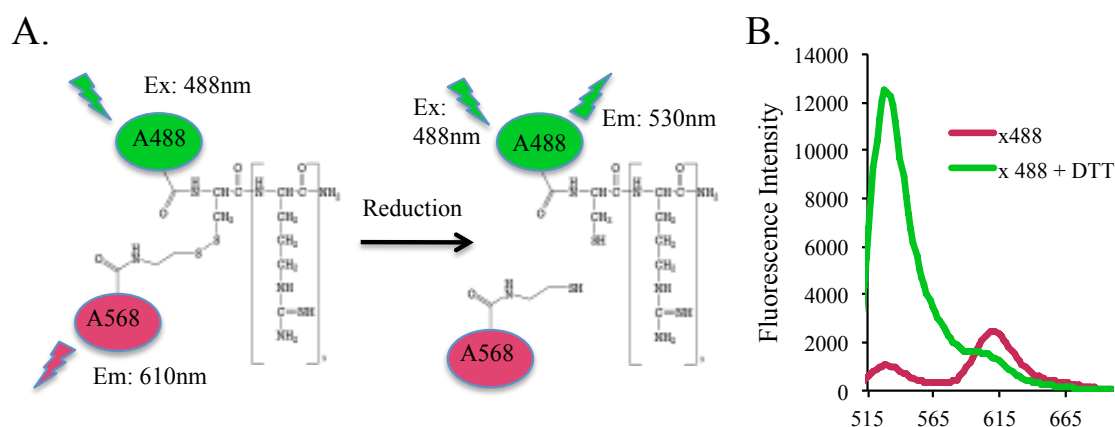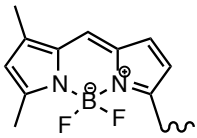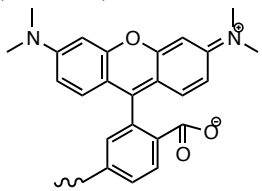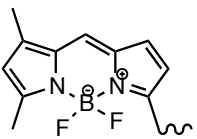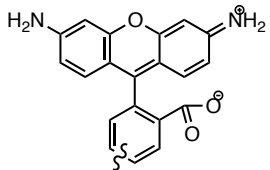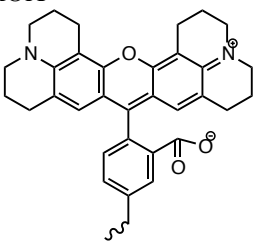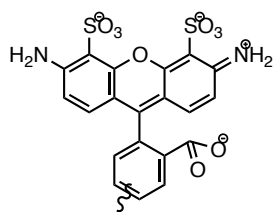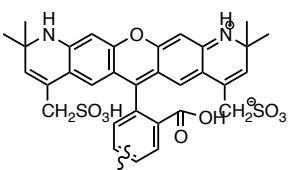
Figure 3.1 Structure and spectra of CPP-FRET disulfide peptide. A) Schematic representation of CPP-FRET before and after disulfide bond reduction. B) Emission spectra of CPP-FRET peptide in phenol red free cell culture media before and after reduction with 10mM DTT; excitation is 488nm and emission was monitored from 515-700nm with a 2 nm interval.

Choosing fluorophores that generate a FRET pair is not as simple as finding two

dyes where the emission and excitation spectra overlap. Numerous dye combinations

where attempted during the development of the CPP-FRET probe and they are detailed in

Table 3.1. With the first three fluorophore combinations, there was quenching of the

donor fluorescence but minimal to no emission at the acceptor wavelength. Fluorescent

dyes tend to be hydrophobic and when they are placed in close proximity to one another

they will stack in order to minimize contact with water. This results in static quenching.

Alexa 488 and Alexa 568 were finally selected because both of these dyes have multiple

sulphonate groups, which should decrease hydrophobic and make them less prone to

stacking. This pair successfully generated a FRET spectrum that diminished upon

disulfide bond reduction (Figure 3.1 B). HPLC-MS of peptide samples before and after

treatment with DTT also confirmed the bond breakage (Figure 3.2)

Table 3.1 Fluorophore parings for CPP-FRET peptides. All fluorophores were purchased from Invitrogen as NHS esters. Spectra were measured before and after reduction with 10mM DTT.

Donor		Acceptor		
Name/Structure	Ex/Em	Name/Structure	Ex/Em	Emission spectra upon reduction with DTT
BODIPY FL	504/513	Tetramethyl rhodamine (TAMRA)	555/580	
BODIPY FL	504/513	ALEXA 555 Structure Not Available	555/565	
Rhodamine Green	505/527	ROX	575/602	
ALEXA 488	495/519	ALEXA 568	578/603	
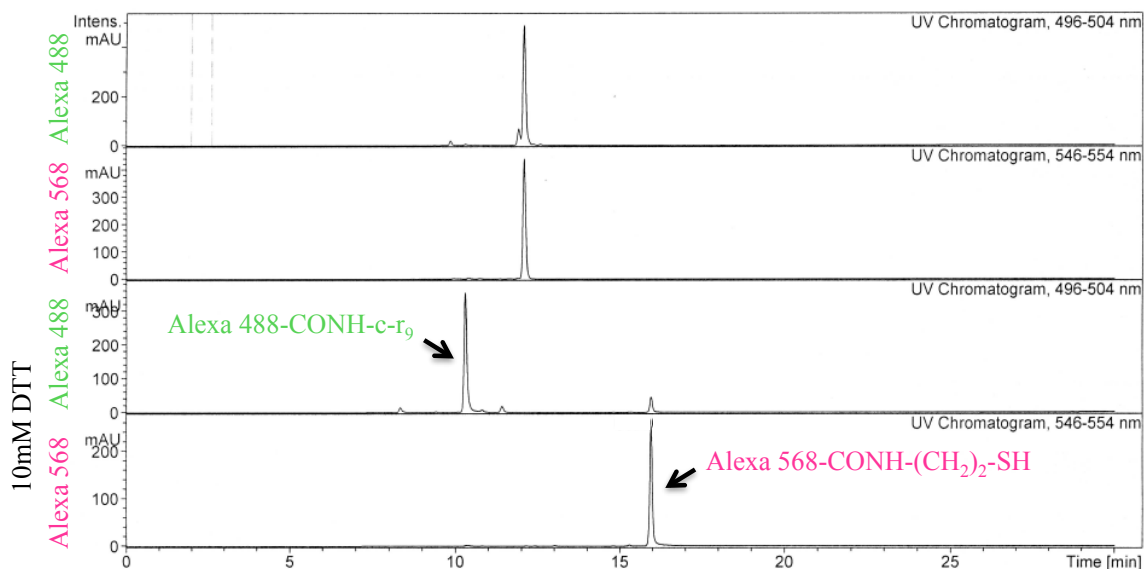
Figure 3.2 HPLC absorbance traces for CPP-FRET peptide before and after disulfide bond reduction. CPP-FRET peptide was run on a C18 reverse phase column with HPLC. Absorbance was monitored at 496-504nm (first and third panel) and 546-554nm (second and fourth panel). Absorbance traces for Alexa 488 and Alexa 568 overlap when the peptide is intact, and upon reduction it is clear that the two fluorophores have different retention times on the column.

3.4.2. Disulfide bond reduction occurs in intracellular vesicles over the course of six hours

To begin to ascertain the rate and location of disulfide bond reduction during endosomal trafficking, HT1080 and HELA cells were incubated with the CPP-FRET conjugate and monitored with confocal microscopy (Figure 3.3 A). Cells were treated for 20 minutes with the peptide at 37°C and the washed thoroughly for 10 minutes to remove any excess probe prior to imaging. Initially, Alexa 488 fluorescence is almost undetectable, but after a few hours the donor signal begins to appear in puncta within in the cell. This increase in donor fluorescence was quantitated to look at reduction rates (Figure 3.2 B). For Jurkat cells, a T cell lymphoma line that is cultured as a suspension, fluorescent reading were done on a plate reader. Reduction rates are slower for the first hour but begin to gain momentum and increase steadily until approximately 6 hours, and

at this point the signal begins to level off. The fold increase in Alexa 488 fluorescence at 8 hours is comparable to cells treated with DTT, suggesting that by this timepoint reduction is complete (data not shown). The maleimide version of the peptide, that does not posses any reducible bonds, showed no change in Alexa 488 fluorescence, confirming that the increase in donor signal was due to breakage of the disulfide bond and not peptide degradation.
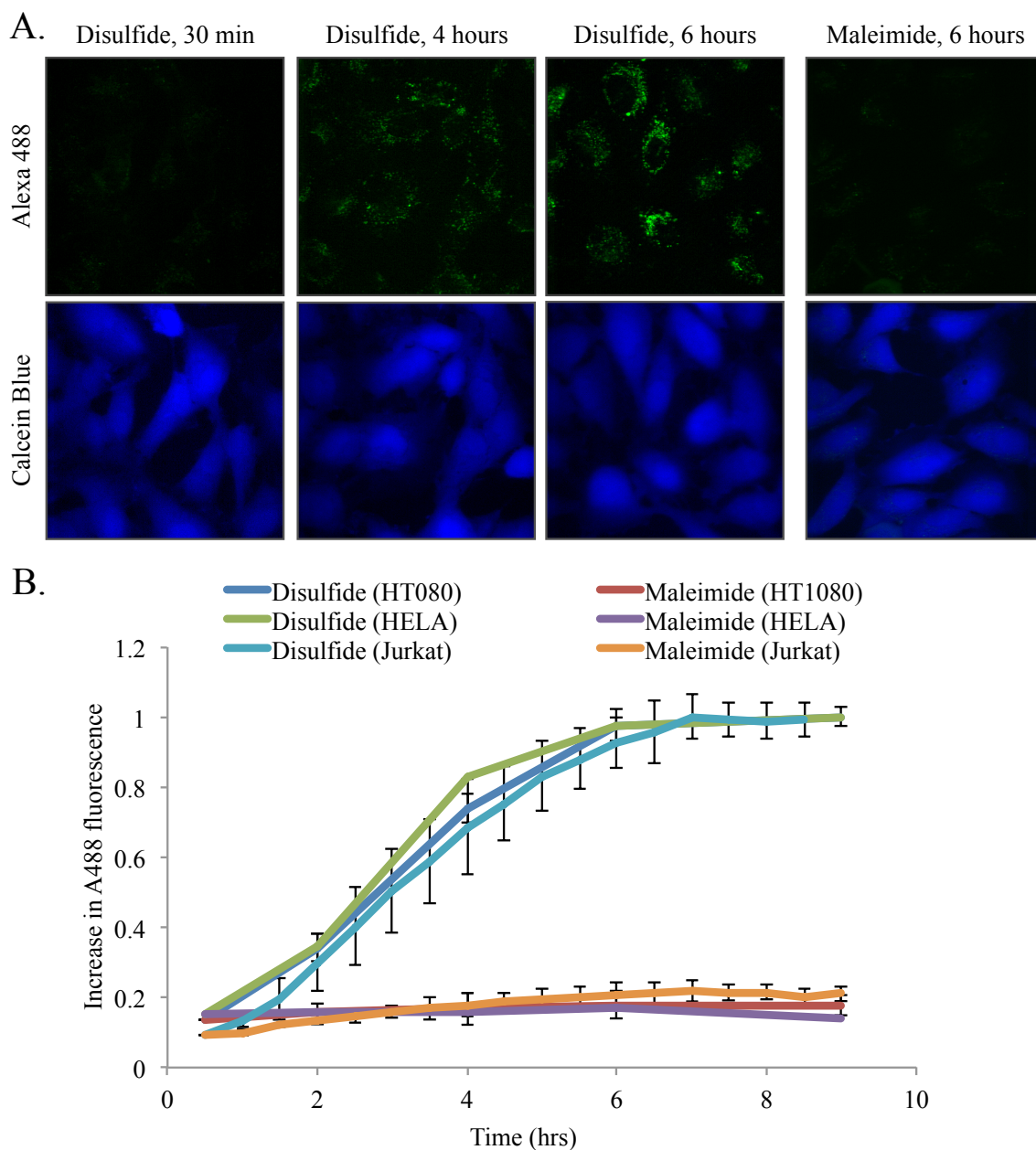
Figure 3.3 Kinetics of disulfide bond reduction after endocytosis in a variety of cancer cell lines. A) Sample images of HELA cells that have been treated with either the CPP-FRET disulfide or the CPP-FRET maleimide peptide at various timepoints. Cells were treated for 20min with peptide, then thoroughly washed for 10 minutes prior to imagining. Calcaein blue was co-stained as a cell viability marker. B) timecourse of disulfide bond reduction in HT1080, HELA and Jurkat cells. Increase in Alexa 488 fluorescence was normalized to compare data across the difference cell lines and imaging strategies. Note that the FRET channel could not be acquired accurately with filter sets installed on the confocal. The tail of the Alexa 488 fluorescence fell within the bandpass of the filter used to monitor Alexa 568, and the significant increase in Alexa 488 fluorescence upon reduction resulted in an increase in the fluorescence in the FRET channel.

3.4.3. Cargo molecules remain sequestered in vesicles unless they are membrane permeable

The goal of investigating release mechanisms from CPPs is to eventually use this knowledge to guide the design of ACPP based therapeutics. Therefore, it is important to know what the fate of the cargo molecule is after it has been released from the peptide. HT1080 cells were incubated with CPP-FRET and imaged for both Alexa 488 and Alexa 568 fluorescence before (Figure 3.4 A) and after (Figure 3.4 B) reduction occurred. The punctate appearance of the Alexa 568 fluorescence at 8 hours makes it clear that disulfide bond reduction occurs in subcellular vesicles and that "cargo" molecule, once released from the CPP, can remain sequestered within them. Interestingly, it also looks as though the Alexa 488-CPP and the Alexa 568 can be differentially sorted after reduction. Some of the punctate in Figure 3.4 B are predominantly red while others are predominantly green.

The sulphonates on Alexa 568 render the molecule somewhat unsuited for transport across a membrane, so it was unknown if Alexa 568 just could not escape the vesicles or if during bond reduction a thiol exchange bound the dye to another molecule within the vesicle and anchored it there. To answer this question, a CPP was synthesized with SYBR-101 conjugated through a disulfide bond. SYBR-101 is a nucleic acid dye that can pass easily through membranes and binds to both RNA and DNA. With this probe, the readout is not a change in fluorescence, but a redistribution of the dye from punctate staining to labeling either the endoplasmic reticulum (RNA) or the nucleus (DNA). When HT1080 cells were treated with the CPP-SYBR-101, the dye is initially present in endocytic vesicles but over time becomes more diffuse, presumable binding to

the mRNA on the endoplasmic reticulum (Figure 3.4 C). This staining pattern is similar

to that of cells that have been treated with DTT and does not occur in cells that have been

treated with the thioether control version of the CPP-SYBR-101 peptide (Figure 3.4 D).

From this data it can be concluded that as long as the cargo, or drug, molecule has the

ability to cross membranes, once released from the peptide, it is free to reach its

intracellular target.

Blue: Calcein Blue AM   Green: SYBR 101, Blue: Hoerscht
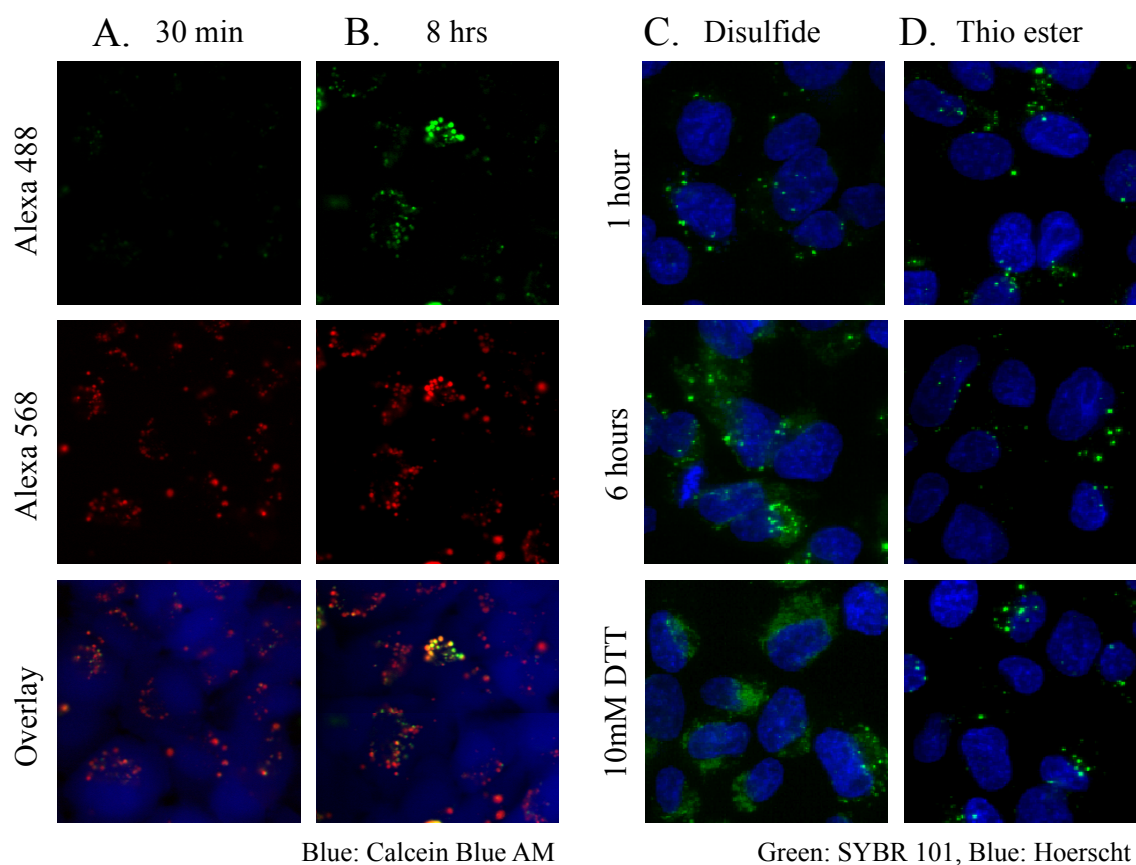
Figure 3.4 Subcellular localization of cargo molecules once they have been released from the CPP via disulfide bond reduction. A) CPP-FRET at 1μM was treated on HT1080 cells for 20 min at 37°C, peptide was removed and cells were imaged with confocal microscopy for direct excitation of Alexa 488 (ex. 488nm, em. 500-525nm) or Alexa 568 (ex. 532nm em. 560-675nm); calcein blue settings are ex. 405nm em. 415-480nm. B) Cells were imaged 8 hours after peptide treatment using direct excitation of each fluorophore and then overlaying that with Calcein Blue. D) CPP-SYBR-101 disulfide construct was incubated on HT1080 cells at 1μM for 20 min at 37°C and washed off prior to co-staining with Hoescht. SYBR-101 was visualized using ex. 488nm, em. 500-525nm at 30 min and 6 hours post treatment. Cells were also treated with 10mM DTT to ensure bond reduction. Hoescht was imaged using ex. 405nm, em. 415-480nm. D) CPP-SYBR-101 thioether control was imaged in the same manner as described in (C).

During the course of imaging, a strange phenomenon was discovered. When cells that had been treated with CPP-FRET were exposed to white light from the microscope (the same light that is used for focusing) for a prolonged period of time, the CPP-Alexa 488 redistributed to the cytoplasm and nucleus of the cell while the Alexa 568 remained inside vesicles (Figure 3.5). Because the Alexa 568 has not been released into the cytoplasm, it does not appear that the light exposure compromised the membranes. Furthermore, because the two portions of the peptide end up in two different locations in the cell, it is presumed that the prolonged exposure to light leads to disulfide bond reduction. It is not known if this mechanism is at all related to the reduction observed under normal imaging conditions, or what information can be gained from this experiment. But it was an interesting observation and one that should be pursued further.
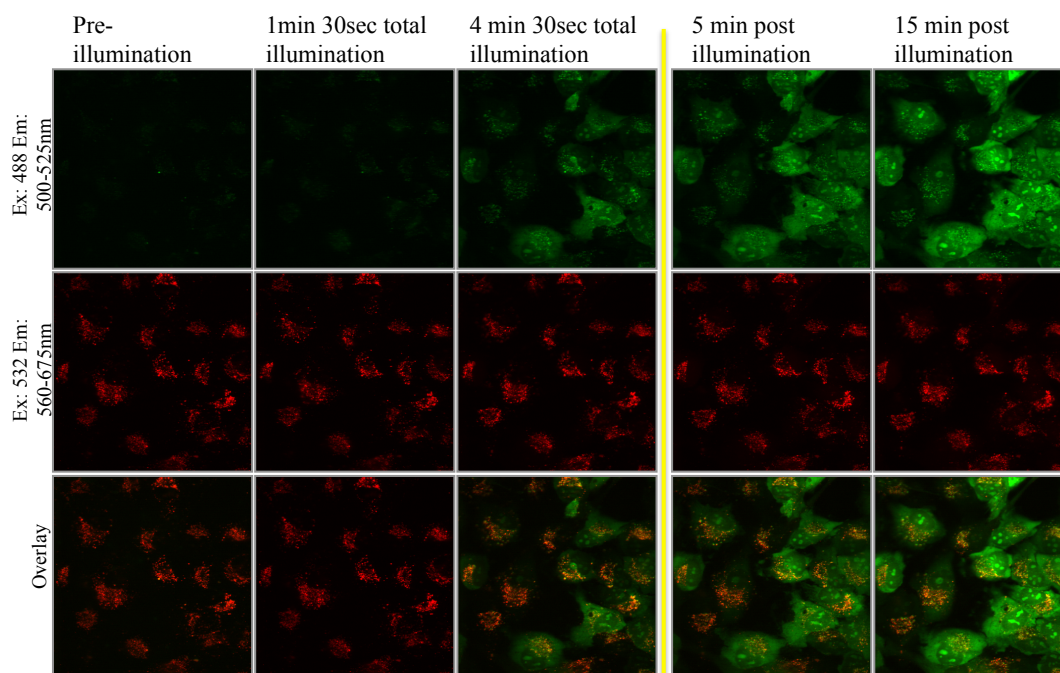
Figure 3.5 Cellular distribution of CPP-FRET upon prolonged illumination with white light. Cells were treated with CPP-FRET peptide at 1μM for 20 minutes at 37°C, washed and then exposed to white light for a given amount of time. Alexa 488 and Alexa 568 fluorescence were monitored with the given wavelengths. A total of 4.5 minutes of illumination was given to a field of view, and cells were then monitored for up to 15 minutes after the illumination had ceased (all images to the right of the yellow line)

3.4.4. Investigation into mechanism of reduction

In biological systems, breaking of a disulfide bond is typically the consequence of a thiol-disulfide exchange, and the rate of that exchange is affected by the pK_a values of all the thiols involved in the reaction (Jensen, Hansen et al. 2009). Lowering the pK_a of the leaving group thiol associated with Alexa 568 will result in a less stable disulfide bond and should generate an increase in reduction rate. A CPP-FRET construct was synthesized where the thiol for the Alexa 568 portion of the bond is connected to an aromatic ring with electron withdrawing groups. This stabilizes of the negative charge of the thiolate ion, thereby lowering the pK_a to approximately 5, whereas the pK_a of cystamine is ~8.5 (Figure 3.6 A). Because the primary reagent for generating this low pK_a linker is 6,6'-dithiodinicotinic acid, this FRET peptide is referred to as Nicotinic. There was an increase in reduction kinetics for the Nicotinic FRET probe when tested on HT1080 and Jurkat cells, but it still required 2-3 hours for full reduction to occur (Figure 3.6 B). This only decreased the reduction time by 50-60%, which is a fairly modest improvement considering the large change in thiol pK_a (>3units).

This lead to the question: what if the limiting factor is not the reducibility of the disulfide, but the rate at which the endosome can generate reducing power in its lumen? If that were the case, then reduction kinetics would reflect mainly the rate of reagent (CPP-FRET) addition rather than the molecular features of the reactant. A simple test would be to vary the amount of probe. If generation of the reductant inside the endosome is rate-limiting, then if twice as much probe enters each endosome, it should take twice as long to reduce fully. If instead the endosome generates plenty of excess reductant and the limitation is the rate of reaction with the probe, then the length of time to reach any

degree of partial reduction will be independent of the amount of probe. Reduction

kinetics were monitored over a 4 fold change in peptide concentration, 0.5μM-2.0μM

(Figure 3.6 C). The range of this experiment was somewhat limited because very low

peptide concentrations become difficult to detect on the microscope and high peptide

concentrations lead to endosome independent mechanisms of peptide uptake. In the range

of 0.5-2.0 μM CPP-FRET, there was no change in the rate of probe reduction, meaning

that the source of reductant is not the rate-limiting step.

The thiol-disulfide exchange reaction requires the presence of a thiolate anion (S^-

), but this deprotonation is thermodynamically unfavorable ($pK_a = 8.3$) in acidic

environments such as late endosomes and lysosomes. Therefore, endosome acidification

was inhibited using Bafilomycin A1, an inhibitor of vacuolar-type H^+-ATPase

(Yoshimori, Yamamoto et al. 1991). At 6 hours after treatment, there was no difference in

the fold increase in Alexa 488 fluorescence (Figure 3.6 D), and from this data it can be

concluded that the mechanism for disulfide bond reduction does not require acidic

conditions. It would be interesting to go back and look at intermediate points during the

experiment to determine if generating more favorable conditions for thiolate formation

(higher pH) causes an increase in the rate of reduction.

Finally, two sulfhydryl (SH) blockers were compared to assess the requirement of

SHs for CPP-FRET reduction. Addition of *N*-ethylmaleimide (NEM), an irreversible and

membrane-permeable SH reagent, eliminated CPP-FRET reduction (Figure 3.6 D),

suggesting that free SHs are essential for cleavage of the disulfide bond. 5,5′-dithiobis-(2-

nitrobenzoic acid) (DTNB), a membrane impermeable SH blocker, had no impact on

Alexa 488 fluorescence, demonstrating that reduction of CPP-FRET requires free thiols that are mostly inaccessible at the cell surface.
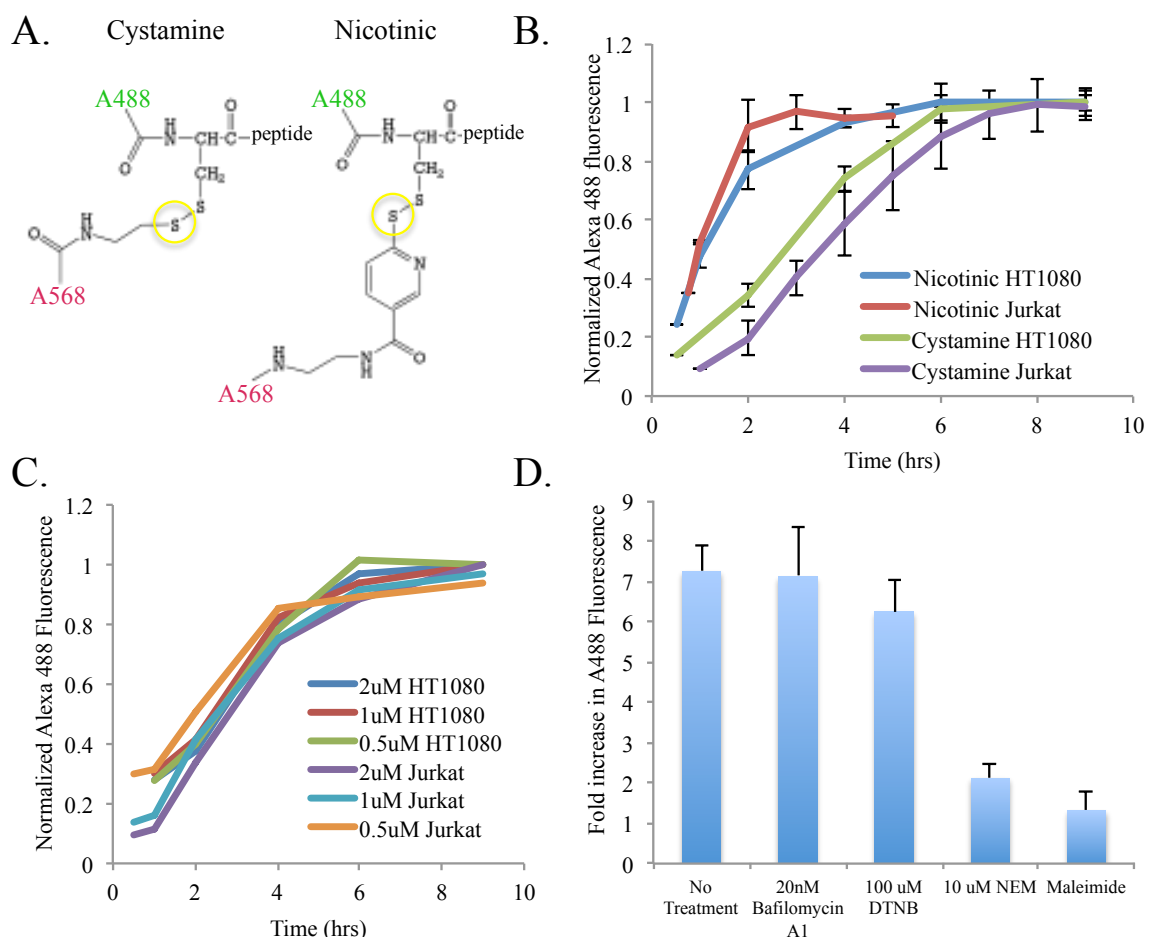
Figure 3.6 Characterization of CPP-FRET disulfide bond reduction. A) Schematic representation of CPP-FRET and the Nicotinic version of the peptide. B). Kinetic of reduction for the original CCP-FRET with a cystamine linker and the Nicotinic linker. C) Disulfide reduction kinetic for cystamine CPP-FRET at different peptide concentrations in both HT1080 and Jurkat Cells. D) HT1080 cells were incubated with 1μM CPP FRET (cystamine, or maleimide as noted) for 20 minutes at 37°C, washed and then incubated in culture media that contained 20nM Bafilomycin A1, or serum free media with 100 μM DTNB or 10 μM NEM. Fold increase in fluorescence was calculated for the 6 hour timepoint by normalizing to the 30 minute timepoint.

3.4.5. Characterization of CPP uptake

Since reduction occurs in subcellular vesicles after the peptide has been endocytosed, efforts to describe these endosomes may help provide a context for where

the CPPs are trafficked after uptake. First, colocalization experiments were performed with transferrin to compare CPP uptake with receptor-mediated endocytosis. The transferrin receptor is a marker for endocytosis via clatherin coated pits, and once these endosomes become acidic and the iron dissociates, the receptor is recycled back to the cell surface (Qian, Li et al. 2002). HT1080s were incubated for 1 hour with r_9-Cy5 in the presence of Alexa488-transferrin (Figure 3.7 A). Confocal microscopy revealed some co-registration with Cy5 and Alexa 488, as indicated by the yellow arrows, but there were also many instances when the endosome was purely red or purely green, marked by arrows in those respective colors. This reiterates that CPPs can be taken up through multiple forms of endocytosis, caltherin coated pits being one of them. Next, CPP uptake was observed in cells that had also been treated with lysosensor blue, a dye that fluoresces when protonated and has a pK_a of 5.1. From Figure 3.7 B, it is clear that the peptide does end up in acidic compartments. Further examination reveals that the larger punctate are acidic while the smaller vesicles containing Cy5 do not have lysosensor fluorescence.

A.

B.
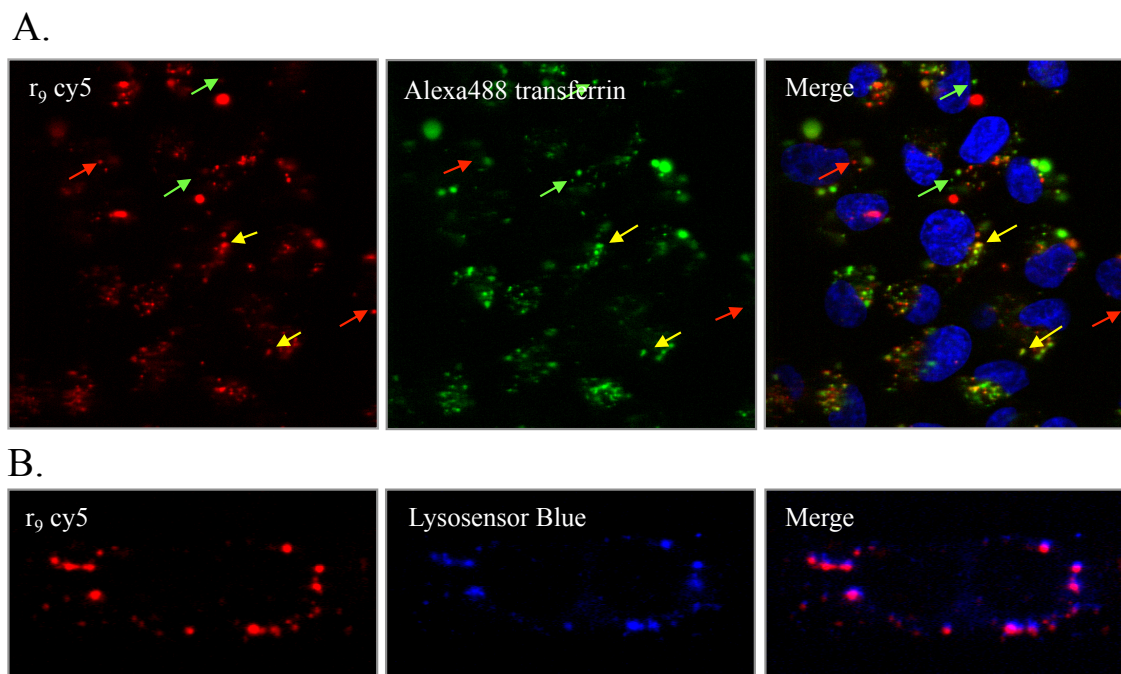
Figure 3.7 Colocalization experiments with Cy5 labeled CPP and markers for receptor mediated endocytosis and acidic vesicles. A) r_9-Cy5 peptide at 1μM was co treated on HT1080 cells with Alexa488-transferrin at 50μg/ml for 1 hour in serum free media. The peptide and transferrin were washed off and the cells were imaged with confocal microscopy. B) 1μM r_9-Cy5 peptide was co treated on HT1080 cells with 5μM Lysosensor Blue for 2 hours at 37°C in serum free media. The peptide and Lysosensor were then washed removed prior to imaging.

3.4.6. Attempts to monitor reduction *in vivo*

The goal of characterizing disulfide bond reduction was to determine if it was a viable means to release chemotherapeutic cargos from ACPPs *in vivo*. The next logical step was to make a FRET-ACPP peptide using the same principles of disulfide bond reduction and FRET but with longer wavelength dyes. A schematic representation of this peptide is presented in Figure 3.8 A. This ACPP and its non-reducible, maleimide counterpart were diluted in fresh mouse plasma and spiked with DTT, and a significant spectral shift was detected upon peptide reduction (Figure 3.8 B). Spectral unmixing was performed using the Maestro to better distinguish between the two forms of the peptide,

and spectra for the oxidized (red) and reduced (green) ACPP are presented in Figure 3.8
C.

Next, a plasma stability assay was done to ensure that the disulfide bond would
remain oxidized while the peptide was in circulation. ACPP-FRET peptides were
incubated in fresh mouse plasma and samples were taken at various timepoints. Gel
electrophoresis of these samples revealed that the peptide immediately reacts with large
molecular weight proteins, presumably serum albumin (Figure 3.8 D). The reactive
cysteine residue on albumin (discussed in Chapter 2) appears to perform a thiol exchange
with disulfide bond in the peptide, conjugating the Cy5 labeled ACPP to the protein
while releasing peg-Cy-7. This peg-Cy-7 species cannot be visualized because it is not
retained in the gel. After 30 minutes, a Cy-7 band begins to appear at a similar molecular
weight as the ACPP-albumin complex. These bands are distinct from one another,
indicating that the peg-Cy-7 is either reacting with another serum protein of similar
molecular weight and abundance, or that it is binding to a differentially modified form of
albumin. Conjugation of myritic acids, long fatty acid chains, to serum albumin leads to
conformational changes in the protein that expose the thiol of cysteine-34, thus making it
more reactive (Kratz 2008). The maleimide control peptide was stable in plasma over the
two hour incubation period, confirming that the degradation seen with the disulfide probe
was in fact due to bond reduction and not peptide proteolysis.

Even with the lack of plasma stability, the ACPP-FRET was still tested *in vivo*
with mice harboring MDA-MB-231 orthotopic tumors. After peptide administration, the
mice were subject to spectral imaging. The kinetics of bond reduction in the animal were
similar to that seen in plasma, with a significant decrease in FRET just 10 minutes after

probe injection, and almost complete loss of FRET by 30 minutes. Unfortunately, this

peptide construct is not suitable for monitoring reduction kinetics *in vivo*, and other

designs will have to be tested if this remains an avenue of research.

Red: Cy-5, Green: Cy-7, Yellow: Overlay
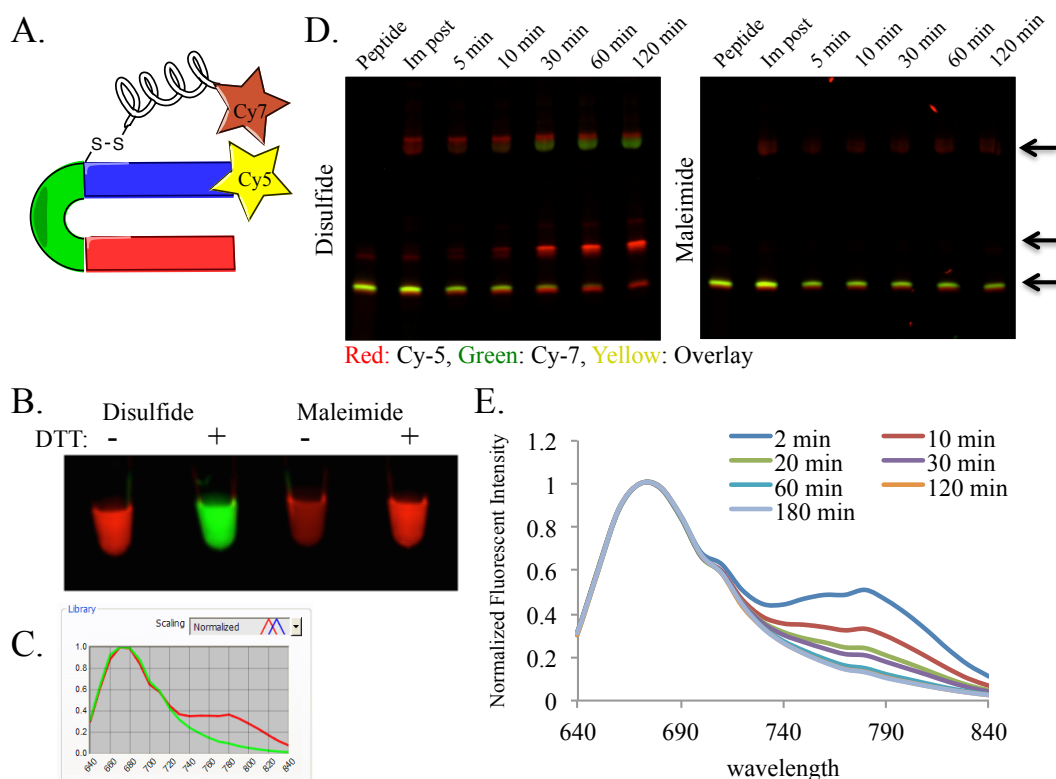
Figure 3.8 *In vivo* stability of ACPP-FRET disulfide and maleimide constructs. A) Cartoon of the ACPP-FRET peptide with Cy5 and Cy-7. B) Spectral unmixing of FRET-ACPPs diluted in fresh mouse plasma with and without the addition of 10mM DTT. C) Sample spectra for the oxidized (red) and reduced (green) forms of the FRET-ACPP, these are the spectra used to perform the unmixing on the Maestro. D) Gel Electrophoresis of FRET-ACPPs incubated in fresh mouse plasma at 37°C for various time periods. The red is Cy5 emission, the green is Cy-7 and overlap of those signals appears yellow in color. The arrows to the right of the gels indicate various forms of the peptide, the top arrow is where the peptide has bound to serum albumin and the bottom arrow is where the peptide runs when in tact. D) *In vivo* reduction of the peptide was monitored after IV injection of 10 nanomoles of ACPP-FRET. The emission spectrum of the peptide in the mouse was recorded (excitation 620/20nm and emission recorded from 650-800nm in 10nm steps). A region of interest was drawn over the tumor and the corresponding emission spectra at various timepoints after peptide injection are displayed.

3.5. Discussion

It is commonly accepted that a large difference in redox potential exists across the plasma membrane of most mammalian cells. The cytosol has an excess of reduced glutathione (GSH), nicotinamide adenine dicucleotides (NADH and NADPH), peroxiredoxins and thoiredoxins that maintain the reducing power despite the oxidizing conditions in the extracellular space (Meister and Anderson 1983; Darby, Freedman et al. 1994; Holmgren and Aslund 1995; Holmgren and Bjornstedt 1995). Isolated from the cytoplasm, the lumen of some subcellular compartments is not reducing, one example is the endoplasmic reticulum. This oxidizing organelle is responsible for disulfide bond formation in secretory proteins and the exoplasmic regions of membrane bound proteins (Hwang, Sinskey et al. 1992).

From the perspective of drug delivery, access to the cytoplasm is only for small hydrophobic molecules with relatively high membrane partition coefficients and permeability constants. This allows them to passively diffuse across the lipid bilayer. Most macromolecules do not have access to the cytoplasmic space because of low diffusivity and membrane permeability; therefore endocytosis is their main route to gain admission into the cell (Saito, Swanson et al. 2003). Functional evidence exists for disulfide bond-reduction in endosomal compartments, such as the activation of diphtheria toxin. This process requires the acid-triggered exposure of an interchain disulfide bond that must be reduced prior to endosomal escape and cell killing (Blewitt, Chung et al. 1985; Ryser, Mandel et al. 1991; Falnes and Olsnes 1995). Cholera toxin and *Pseudomonas* exotoxin also appear to required disulfide bond reduction for cytotoxicity (Falnes and Sandvig 2000). The mechanistic details pertaining to such processes, such as

kinetics and sites of disulfide reduction, remain largely controversial. Yet, understanding

the mechanism of disulfide bond reduction once a drug delivery system interacts with the

subcellular environment could help direct the molecular design as well as interpretation

of the experimental results.

One early study compared disulfide reduction upon uptake in primary mouse

macrophages using $[^{125}I]$-tyrosine-S-S-$[^{131}I]$ α_2-macroglobulin and $[^{125}I]$-tyrosine-S-S-

$[^{131}I]$ transferrin. From this study it was suggested that the primary site of bond reduction

is the lysosome because the α_2-macroglobulin conjugate was reduced once it reached that

compartment, yet the transferring conjugate that recycled between the cell surface and

early endosomes was not (Collins, Unanue et al. 1991). Another study using antibody-

maytansinoid conjugates, found that the antibody was efficiently metabolized in

lysosomes irrespective of the mechanism of drug conjugation. The difference in toxicity

between the thioether and disulfide linkages was not in the ability to release the drug

from the carrier, but in the biological activity of the degradation products. The disulfide

metabolite was reduced and methylated to generate a lypophilic and potent drug whereas

the thioether conjugate remained charged and unable to diffuse across membranes

(Erickson, Park et al. 2006). Furthermore, experiments with Her-2 antibody-TAMRA

conjugates demonstrated minimal disulfide reduction upon endocytosis and it was not

until the probe was diverted to lysosomes that fluorescent dequenching was observed.

They postulated that most of this signal was due to antibody degradation and not disulfide

bond reduction. To corroborate this, a redox sensing fluorescent protein (ro-GFP) was

used to calculate the redox potential of various intracellular organelles. It was concluded

that the environment within the endocytotic pathway in human prostate cancer PC3 cells

was oxidizing rather than reducing (Austin, Wen et al. 2005). However, within the context of those experiments, the protein was oxidized to saturation so a quantitative result could not be reported (Lohman and Remington 2008).

There have also been accounts where disulfide bond reduction is implicated during receptor-mediated endocytosis. A FRET based sensor was used to monitor bond reduction after folate-mediated endocytosis. This group found that reduction transpired with a half-time of 6 hours and that it began in endosomes and occurred independently of endocytic vesicle trafficking along microtubules. Additionally, bond reduction did not significantly depend on redox machinery located on the cell surface or within the lysosome and Golgi apparatus (Yang, Chen et al. 2006). Another group tried to monitor CPP-mediated delivery of peptide cargo using a disulfide-FRET mechanism similar to the one described in this report. They claim that treatment of the peptide on cells produced an increase donor fluorescence within 10 minutes and assumed that it was due to rapid CPP transfer into the reducing environment of the cytosol (Cheung, Kim Chiaw et al. 2009). Yet there was no live cell imaging to confirm the peptide localization. Also, this mechanism contradicts results that the CPPs are predominantly found within subcellular vesicles hours after administration, both *in vitro* and *in vivo* (Aguilera, Olson et al. 2009).

In this report, a CPP-FRET peptide confirmed that disulfide bond reduction occurs upon endocystosis by a variety of cancer cells and that those endocytic vesicles are the sites of reduction. Confocal microscopy of live cells clearly demonstrated that the peptide was confined to discrete compartments within the cell without diffuse cytoplasmic fluorescence or significant outer membrane labeling. After reduction, both

Alexa 488-CPP and Alexa 568-cargo remained confined in puncta with some evidence that the two molecules can be differentially sorted.

The kinetics of disulfide bond reduction should be dependent on both the pH of the surrounding media and the thiol pK_a of the bond participants. With the standard cystamine linkage, reduction took place over the course of six to eight hours. This linker was then compared to a probe where the thiol on the Alexa 568 molecule was also a substituent on a phenol ring with multiple electron withdrawing groups. Because the negative charge on the sulfur atom is stabilized, the pK_a of the thiol is lowered to approximately 5.5, which reduces the stability of the disulfide bond. When reduction rates of these two peptides were measured, there was only a modest change in reaction rate due to pK_a, because a 3-fold reduction in pK_a only cut the reduction rate to half. This begged the question: what if the rate-limiting factor is not the reducibility of the disulfide, but the ability of the endosome to generate reducing power in its lumen? If that were the case, reduction kinetics would depend mainly the rate of reagent (CPP-FRET) addition. A simple experiment to test this theory was to vary the amount of probe. Reduction kinetics were monitored over a 4-fold change in peptide concentration, 0.5μM-2.0μM, and no significant differences in rates were observed.

Bafilomycin A1 was used to inhibit endosome and lysosome acidification. These cells were compared to their untreated counterparts at 6 hours and there was no difference in the extent of A488 dequenching. This shows that bond reduction does not require an acidic pH and decreases the possibility that the Gamma-interferon inducible lysosomal thiol reductase (GILT) is responsible, since this enzyme has optimal activity in the pH range of 4-5.5 (Arunachalam, Phan et al. 2000). Because the functional activity of the

thioredoxin family is best at neutral pH (Noiva and Lennarz 1992; Jensen 1995), it would be interesting to look at the rates of disulfide bond reduction at earlier timepoints after treatment.

Finally the requirement of sulfhydryls (SH) for reduction was investigated. When cells were treated with N-ethylmaleimide (NEM), a cell permiant sulfhydryl inhibitor, no Alexa 488 dequenching was observed in cells that also took up calcein blue. To investigate the location of the sulfhydryls involved, cells were treated with DTNB, an inhibitor that cannot penetrate through membranes and is more specific for cell surface SHs. With the use of this compound at 10X the concentration of NEM, no significant decrease in the extent of disulfide bond reduction was observed. This implies that surface proteins, such as protein disulfide isomerase, are not responsible for bond reduction.

Disulfide bonds are generally considered to be stable in plasma during circulation that however was not the case for the FRET-ACPP. There appeared to be an almost instantaneous thiol exchange reaction between the ACPP and albumin. This is not surprising since the cystein-34 residue on the protein has been used for thiol reactive conjugations *in vivo* (Kratz, Warnecke et al. 2002). The affinity of ACPPs for plasma proteins, the most abundant being albumin, could be a result of the high charge density on the peptide or the hydrophobicity of the far-red dyes. Future attempts with disulfide FRET-ACPPs will need to prevent this interaction, one strategy would be the addition of peg chains or polymers that reduce hydrophobicity. Another possibility is the introduction of sterically hindered disulfide linkages that have been shown to be more stable in circulation (Kellogg, Garrett et al. 2011).

3.6. Acknowledgments

The dissertation author would like to thank:

Paul Steinbach and Dr. Todd Aguilera for training with confocal microscopy. Dr. Elamprakash Savariar for synthesis of the ACPP disulfide constructs. Perla Arcaira for maintenance of cell lines, cancer model generation and animal husbandry.

Chapter 3, in part, is currently being prepared for submission for publication of the material. Crisp, J.L.; Savariar E.N.; Tsien R.Y. The dissertation author was the primary author of this material.

CHAPTER 4: Synergistic Targeting of Integrin $\alpha_v\beta_3$ and Matrix Metalloproteinase-2 Improves Optical Imaging of Tumors and Enhances Efficacy of Chemotherapeutics

4.1. Abstract

Activatable cell penetrating peptides (ACPPs) provide a multimodality strategy for molecular targeting by exploiting the extracellular protease activities associated with disease. While they have successfully imaged tumors with fluorescence and MRI, their specificity and sensitivity to matrix metalloproteinase (MMP) activity could still be improved. Nature often optimizes substrates by attaching an extra domain that binds to an exosite on the enzyme, thus pre-concentrating the substrate near the active site. This report demonstrates that a similar strategy can improve ACPP targeting as well. Integrin $\alpha_v\beta_3$ is known to bind to the hemopexin domain of MMP-2 and is upregulated in many tumors and their vasculature. Cyclic(RGDfK), a popular ligand for $\alpha_v\beta_3$, was chosen as the pre-targeting moiety and attached to a Cy5-labeled MMP-2 cleavable ACPP. When the two targeting strategies were combined, there was a significant increase in peptide uptake by U87MG glioblastoma cells in culture. When tested *in vivo*, the dual targeted ACPP enhanced tumor contrast, overall uptake and improved the peptide's ability to penetrate into the core of MDA-MB-231 orthotopic breast tumors. Synergistic targeting of $\alpha_v\beta_3$ and MMP-2 was also able to significantly increase the therapeutic efficacy of monomethylauristatin E (MMAE), a potent chemotherapeutic that inhibits microtubule polymerization.

4.2. Introduction

Activatable cell penetrating peptides provide a multimodality strategy for molecular imaging of extracellular protease activity. ACPPs consist of a polycationic cell penetrating peptide (CPP) attached to a polyanionic sequence via a protease cleavable linker. The polyanion prevents the adhesion and uptake of the CPP and its cargo until the target enzyme cleaves the substrate sequence, allowing the inhibitory domain to dissociate (Jiang, Olson et al. 2004). The released CPP then binds to cells in its immediate proximity and is typically endocytosed. For tumor imaging, the main protease targets have been MMP-2 and -9, which are pivotal in matrix degradation, inflammation, and tumor cell migration, and whose activity is upregulated in most invasive cancers (Chambers and Matrisian 1997; Talvensaari-Mattila, Paakko et al. 2003; Overall and Kleifeld 2006). Although MMP-cleavable ACPPs have successfully imaged tumors with fluorescence and MRI, their specificity and sensitivity to MMP activity could still be improved (Olson, Aguilera et al. 2009; Nguyen, Olson et al. 2010; Olson, Jiang et al. 2010).

Nature often optimizes substrates by attaching an extra domain that binds to an exosite on the enzyme, thus pre-concentrating the substrate near the active site. This report shows that a similar strategy can improve ACPP targeting as well. Integrin $\alpha_v\beta_3$ is known to bind to the hemopexin domain of MMP-2 (Brooks, Stromblad et al. 1996) and is upregulated in many tumors and their vasculature (Brooks, Clark et al. 1994; Hood and Cheresh 2002; Ruoslahti 2002). Cyclic(RGDfK), a popular ligand for $\alpha_v\beta_3$, was chosen as the pre-targeting moiety, and was attached to the inhibitory portion of the ACPP so that protease attack would separate the $(D\text{-arg})_9$-Cy5 CPP from $c(RGDfK)\text{-}(D\text{-glu})_9$.

Dissociation of the latter from $\alpha_v\beta_3$ would allow the integrin-MMP complex to bind fresh substrate for continued catalytic amplification (Figure 4.1 A). Binding of cyclic RGD to $\alpha_v\beta_3$ should not interfere with MMP-2 localization, since these interactions occur at two distinct sites on the integrin. Inhibitors that disrupted the $\alpha_v\beta_3$-MMP-2 interaction had no impact on the ability of the integrin to bind its target matrix proteins (Silletti, Kessler et al. 2001)

One report in the literature has successfully combined $\alpha_v\beta_3$ and MMP-2 targeting to image U87MG glioblastmoma subcutaneous tumors (Zhu, Xie et al. 2011). While their peptide was able to obtain optical contrast ratios of 3.5 for tumor to background tissue using enzyme dependent dequenching of Cy5.5, this method for imaging provided no mechanism for retention of the probe in the tumor. This limits the tumor contrast that can be obtained and hinders the technology's translation from imaging to therapeutic delivery. ACPPs provide a superior alternative to this approach because the polyarginine offers an efficient means of cellular penetration and retention.

Monomethylauristatin E (MMAE) was selected as the chemotherapeutic cargo for initial tests with the dual targeted peptide. MMAE is a synthetic analogue of dolistatin-10, a very potent inhibitor of microtubule polymerization that was originally isolated from the Indian Ocean sea hare *Dolabella auricularia* (Pettit 1997; Mohammad, Limvarapuss et al. 1999). Problems with toxicity limit MMAE's effectiveness as a drug alone, but it has found clinical success when conjugated to antibodies against CD30 (Brentuximab) and the glycoprotein GPNMB (Glembatumumab) (Francisco, Cerveny et al. 2003; Fanale, Forero-Torres et al. 2012; Keir and Vahdat 2012).

This report will demonstrate that when integrin and MMP-2 targeting strategies are combined, there is a significant increase of peptide uptake with cancer cells in culture. When tested *in vivo*, the dual targeted ACPP improved tumor contrast, increased overall uptake and enhanced the peptide's ability to penetrate into the core of MDA-MB-231 orthotopic breast tumors. Furthermore, peptide conjugates with MMAE lead to regression and cures of established primary tumors.

4.3. Methods

4.3.1. Peptide synthesis

Pre-targeted ACPPs were synthesized with the following scheme, first NH_2-e_9-C(SS-tBu)-OPLGC(Me)AG-r_9-c-$CONH_2$ or NH_2-e_9-C(SS-tBu)-PEG_6-r_9-c-$CONH_2$ were made using regular solid phase Fmoc peptide synthesis. Lower case letters refer to D-amino acids, O-denotes 5-amino-3-oxopentanoyl, a short hydrophilic spacer, C(Me) represents S-methylcysteine and the final $CONH_2$ indicates a C-terminal amide. The peptide was cleaved from the resin using Trifluoroacetic acid (TFA) containing 2% thioanisole, 2% water and 4% triisopropylsilane (TIPS) for 4 hours under N_2 and the reaction mixture was filtered under N_2 to remove the resin. This filtrate was concentrated by evaporation and the peptide was precipitated by adding ice cold 50% hexanes in methyl *tert*-butyl ether and collected by centrifugation and careful decantation of solvents. The product was vacuum dried, then dissolved in dimethyl sulfoxide (DMSO) and purified using preparative high performance liquid chromatography (HPLC) with a gradient of 5-55% acetonitrile in water and 0.05% TFA over 25 min at 15mL per min

flow rate. The purified product was dried with lyophilization and the identity was confirmed by electrospray mass spectroscopy (EMS).

Purified peptides were dissolved in anhydrous DMSO and reacted with Cy5 maleimide (GE life sciences) with the additon 1μL of *N*-methylmorpholine (NMM). The reaction vessel was purged with N_2 and after 3 hours the completion of the reaction was verified by LCMS. To this mixture, 25μL of triethyl phosphine (TEP) was added and reaction was kept at room temperature for another 6 hours. The reduced produced was precipitated with N_2 purged 50 % hexanes in methyl tert-butyl. The precipitate was collected by centrifugation, dried under vacuum, then dissolved in DMSO prior to HPLC purification (5-55% acetonitrile gradient in water and 0.05% TFA over 25 min). The product at this step was NH_2-e_9-C(SH)-OPLGC(Me)AG-r_9-c(Cy5)-$CONH_2$ or the PEG6 counterpart. The identity of the peptide was confirmed using EMS.

Next, SPDP-peg_{12}-peg_2-peg_2-cyclo[RGDfK] or SPDP-peg_{12}-peg_2-peg_2-cyclo[RADfK] dissolved in DMSO (anhydrous), was added to the previously synthesized peptide, purged with N_2 and 0.5μL of NMM was added. This reaction was kept at room temperature for 12 hour. After completion of the reaction, the product was purified by HPLC and dried using lyophilization. The identity and purity of the compound was verified by LCMS.

To generate SPDP-peg_{12}-peg_2-peg_2-cyclo[R(A/D)DfK], SPDP-peg_{12}-NHS ester (Quanta Biodesign) was dissolved in DMSO and transferred to a vial containing Cyclo[Arg-Ala-Asp-D-Phe-Lys(peg_2-peg_2)] where peg = 8-amino-3,6 dioxaoctanoic acid (Peptide International). 1μL of NMM was added and the and reaction proceeded for 6

hours. The extent of the reaction was verified by LCMS and the product was purified using preparative HPLC and dried using lyophilization.

MMAE probes were synthesized as follows: The conjugatable form of MMAE was synthesized by reacting 3 equivalents of Fmoc-Val-Cit-PAB-NO$_2$ (Concortis, PAB=para-aminobenzyl) with 1 equivalent of MMAE (Concortis) in the presence of pyridine (30%) in DMF for two days at room temperature. NH$_2$-Val-Cit-PABC-MMAE was purified by HPLC and then reacted with a bifunctional cross linker, pentafluorophenyl-malemide (PFP-MAL), in the presence of NMM. Mal-(CH$_2$)$_2$-Val-Cit-PABC-MMAE was then reacted with previously synthesized NH$_2$-e$_9$-OPLGC(Me)AGO-C-r$_9$-c(Cy5) to generate NH$_2$-e$_9$-OPLGC(Me)AGO-C[Mal-(CH$_2$)$_2$-Val-Cit-PABC-MMAE]-r$_9$-c(Cy5). The N terminus of this peptide was reacted with MAL-peg$_{12}$-NHS and after completion of the reaction, MAL-peg$_{12}$-CONH-e$_9$-OPLGC(Me)AGO-C[Mal-(CH$_2$)$_2$-Val-Cit-PABC-MMAE]-r$_9$-c(Cy5) was isolated and reacted with 2 molar equivalents of cyclic(RGDfC) (Peptide International) in DMSO to get final cRGD-MMP-MMAE compound. The final product was purified using HPLC and the identity was verified using EMS. To generate the control peptides, cyclic(RGDfC) was replaced by cyclic(RADfC) and the OPLGC(Me)AGO sequence in the ACPP was substituted with a PEG6.

4.3.2. Enzyme cleavage assay

Peptides were diluted to 5μM in a TRIS buffer (20mM TRIS, 150mM NaCl, 2mM CaCl$_2$, pH 7.5) and placed on ice. The catalytic domain of MMP-2 (Calbiochem) was added to the dilute peptide at a final concentration of 50nM and an aliquot was removed for the t=0 time point. The peptide solutions containing MMP-2 were

transferred to a 37°C incubator. At various time points for up to 4hours, 10μL aliquots were removed from the reaction wells, immediately mixed in a 1:1 ratio with 2X tricine sample buffer (Life Technologies) and heated at 95°C for 60 seconds. Samples were then subjected to electrophoresis on 10-20% tricine gradient gels (Life Technologies) for 90 minutes at 110mV. Gels where removed from their casings and imaged on a Maestro Imager using an excitation filter of 620/22nm and an emission filter of 670/20nm. To quantitate the amount of cleaved peptide, gel images were processed using ImageJ. The integrated intensity was measured for the uncleaved and cleaved peptide bands in each lane of the gel, ensuring that the box used to define the measured area remained constant through out the analysis. An area in a lane with no peptide was measured and used for background subtraction. To determine the amount of cleaved peptide, the following equation was used: percent cleavage = 100*(cleaved peptide/(cleaved peptide+uncleaved peptide)). A plot was then generated that graphed percent of cleaved peptide as a function of time, values were presented as the average ± standard deviation of one experiment done in triplicate

4.3.3. Integrin binding assay

High protein binding 96-well plates were coated with vitronectin at a concentration of 10 μg/mL in PBS and the protein was allowed to bind at 4 degrees overnight. The plates were rinsed three times with Tris buffered saline (TBS) containing 0.02% Tween, blocked with 2% BSA in phosphate buffered saline (PBS) for at least one hour at room temperature, and rinsed again. MDA-MB-435 cells ($2x10^7$) were rinsed with PBS and detached from the culture plate by incubating with versein (Gibco) at room temperature for 15-20 minutes. Cells were resuspended in serum-free imaging buffer,

pelleted and washed, then resuspended in fresh buffer to a concentration of $1x10^6$ cells/mL. Calcein green AM ester (Invitrogrn) at 1 μg/mL in DMSO was added to cells at a dilution of 1:500. Peptides were added to cells such that the final concentration ranged from 0-10 μM and incubated at room temperature for 20 minutes. Peptide-cell mixtures were added to the vitronectin coated plates and incubated at room temperature for 20 minutes to allow cell attachement. Unbound cells were removed by gently washing the plate with serum-free imaging buffer 3 times. Calcein green fluorescence was measured on a plate reader (Tecan) with 490nm excitation and 520nm emission.

4.3.4. Cellular uptake and confocal imaging

U87MG cells (ATCC) were cultured in DMEM (CellGrow) with 10%FBS, GlutaMAX (Gibco) and 1% Penicillin/Streptomycin at 37°C with 5% CO_2. For imaging, cells were plated on sterile, glass bottom 96-wells plates at a density of 25,000 cells/well and were allowed to settle on the plates overnight. Peptides were diluted to a concentration of 1uM in serum free imagining buffer (DMEM with no phenol-red, 20mM HEPES (Gibco), 1X GlutaMAX, pH 7.4) and warmed to 37°C. Culture media was aspirated and the cells were treated with peptide for 30min at 37°C. Cells were washed 3X with imaging buffer containing 10% FBS. After washing was complete, they were placed in 100μL of imagining buffer containing 10% FBS and 20 μg/ml Calcein Blue AM ester (Invitrogen), a cell viability marker. Cells were imaged on a Zeiss 5 Live line scanning confocal microscope using a 40X water objective. Cy5 was visualized with a 635nm excitation laser and a 650nm lp emission filter and calcein blue was imaged with a 405nm excitation laser and 415-450nm emission filter.

4.3.5. Tumor generation and *in vivo* fluorescence imaging

All animal studies were done in compliance with the principles and procedures outlined by the Institutional Animal Care and Use Committee at the University of California San Diego. Female athymic nu/nu mice, 5-6 weeks of age, were purchased from Harland Labs (Placentia, California). To generate tumors, 1×10^6 MDA-MB-231 cells were injected into the mammary fat pads of female mice in a vehicle of 4mg/ml matrigel with an injection volume of 40-50μL. The cell suspension in matrigel remained on ice until immediately before the cells were aspirated into a syringe for injection. Two tumors were implanted subcutaneously, one on each side of the mouse, in the upper mammary fat pads. Tumors were allowed to grow for approximately 2 weeks, or until they reach a diameter of 3-5mm.

For optical imaging, mice were anesthetized with an intraperitoneal (IP) injection of 50μL of a 1:1 mixture of Ketamine and Midazolam (KM). Cy5 labeled peptides were then injected intravenously (IV) via the tail vein at a dose of 10 nanomoles (100μL of 100μM) and the mice were monitored as they awoke from anesthesia. After 6 hours, mice were again anesthetized with an IP injection of KM and imaged using the Maestro Small Animal Imager with an excitation filter of 620/22nm and a 645nm long pass emission filter with the dichroic emission filtered tuned to 670nm.

4.3.6. Standardized uptake value calculation

Target organs such as tumor, liver, kidney and muscle were harvested from the animals, weighed and placed in 15ml plastic vials. SUV buffer (150mM NaCl, 10mM Tris, 2g/100ml SDS, 0.25mg/ml Protinease K and 0.1mg/ml DNase, pH 8.0) was added

at a ratio of 9μL buffer to 1mg tissue. Tissues were then homogenized with point sonication (Fisher Scientific) using an amplitude range of 5-15% for a maximum of 20 seconds. Tissue solutions were placed in a 37°C incubator with constant agitation and allowed to incubate over night. 200μL of each tissue solution was transferred to a well on a black, plastic bottom, 96-well plate (Costar) for fluorescent analysis. Fluorescent measurements were preformed on a plate reader (Tecan) using 630nm excitation with a 12nm slit and a 680nm emission with a 12nm slit. Fluorescent counts were converted to Cy5 concentrations using tissue specific calibration curves.

To generate the calibration curves, tissues were collected from mice that had never been injected with peptide, and homogenized in SUV buffer containing known amounts of Cy5. These samples were processed and analyzed in the same manner as described above. For each tissue, a calibration curve was generated by plotting fluorescent counts as a function of Cy5 concentration, then performing a linear regression analysis in Excel to obtain an equation that related fluorescence to peptide concentration. For each concentration, three independent tissues were processed and the calibration was done twice, yielding a total of six data points to generate the average value.

To calculate the SUV value, the peptide concentration in molarity was converted to molality and normalized by the injected dose and animal weight. The equation for an SUV is: (moles of peptide in tissue/weight of tissue)/(moles of peptide injected/weight of animal).

4.3.7. Frozen section imaging

Sample tumors from each of the peptide treatment groups were submerged in OCT (Tissue-Tek), snap frozen in liquid nitrogen and stored at -80°C until processing.

Frozen sections were generated on a cryostat (Leica) at a width of 10 microns. Tissue

sections were then melted directly onto a coverslip and immediately chilled to -20°C. The

coverslip was placed in a custom engineered device that allowed for imaging of the tissue

section while it remained frozen. This ensured that there was no alteration to the peptide

fluorescence or distribution due to fixation or mounting of the coverslip onto a

microscope slide. Briefly, an apparatus was designed to fit the motorized microscope

stage that orients the coverslip such that the tissue was facing up and the glass side was

toward the objective. The section remained frozen with the use of dry ice and a chamber

above the coverslip containing chilled ethanol. To prevent condensation from forming on

the coverslip, a stream of nitrogen gas was forced along the bottom of the device in the

space between the coverslip and the objective. Images were generated on a Zeiss 5-Live

line scanning confocal microscope using a 20X air objective, 635nm excitation laser and

a 650 nm long pass emission filter.

4.3.8. Therapeutic studies

To generate tumors, athymic nu/nu mice were injected in the right and left

mammary fat pads with 7.5×10^5 MDA-MA-231 breast cancer cells in matrigel at a

concentration of 4mg/ml. The volume of tumor cell injections ranged from 30-40μL.

Tumor volumes were monitored at regular intervals with caliper measurements of the

length and width of the tumor. Tumor volume was calculated with the following

equation, volume = ½ (length)(width)^2. Tumors were allowed to grow to a volume

between 50-80 mm^3 prior to therapeutic intervention. MMAE was administered in a 3%

DMSO saline solution and peptides were stored as lyophilized powders and suspended in

nanopure water just prior to injection. For the survival plot presented in section 3.4.3,

mice were sacrificed once a tumor reached a diameter ≥ 10 mm. For statistical analysis with tumor growth curves, a paired student's t-test was used and for the Kaplan-Meier, a log-rank survival analysis was performed in Sigma Plot.

4.4. Results

4.4.1. *In vitro* characterization of cyclic RGD pre-targeted ACPPs

Dual targeted ACPPs were synthesized such that the cyclic RGD motif was conjugated to the inhibitory domain of the ACPP and the cargo molecule, a near far-red fluorescent dye (Cy5), was attached to the CPP portion (Figure 4.1 A). To validate the contributions of integrin binding and MMP activitvation, multiple control peptides were made. For *in vitro* analysis, each of the peptide modalities was tested individually using cyclic(RGDfC)-Cy5 and the traditional MMP-ACPP-Cy5. For *in vivo* studies, all the peptides need to have similar molecular weights and pharmacokinetic properties. To control for integrin binding the cyclic RGD (cRGD) motif was replaced with a cyclic RAD (cRAD) peptide that diminishes integrin affinity. To render the peptide uncleavable, the PLGC(Me)AG amino acid sequence was substituted with polyethylene glycol (PEG_6) linker. All of the peptides used in this study are presented in Table 4.1.

Table 4.1 Summary of pre-targeted peptide constructs for optical imaging

Peptide No.	Cartoon structure	Peptide name	Peptide sequence
1		cRGD	cyclic(RGDfC)-mal-Cy5
2		MMP-ACPP	Ac-e$_9$-O-PLGC$_{Me}$AG-r$_9$-c(Cy5)
3		cRGD-MMP	Ac-e$_9$-c[peg$_{12}$-cylic(RGDfK)]-O-PLGC$_{Me}$AG-r$_9$-c(Cy5)
4		cRAD-MMP	Ac-e$_9$-c[peg$_{12}$-cylic(RADfK)]-O-PLGC$_{Me}$AG-r$_9$-c(Cy5)
5	⭐ = Cy-5 ⬡ = RGD	cRGD-PEG$_6$	Ac-e$_9$-c[peg$_{12}$-cylic(RGDfK)]-peg$_6$-r$_9$-c(Cy5)
6	= ACPP	cRAD-PEG$_6$	Ac-e$_9$-c[peg$_{12}$-cylic(RADfK)]-peg$_6$-r$_9$-c(Cy5)

Molecular modifications to substrates and ligands can significantly reduce either the ability of a target enzyme to process the substrate or the affinity of the ligand for its receptor. To ensure that addition of the cyclic RGD to the ACPP did not diminish the substrate's cleavability, the kinetics of peptide processing by MMP-2 was examined. Various peptides, including MMP-ACPP, cRGD-MMP, cRAD MMP and cRGD-PEG$_6$, were incubated with the catalytic domain of MMP-2 at 37°C and aliquots were taken at multiple time points for up to 4 hours. Peptide cleavage was monitored by gel electrophoresis (Figure 4.1 B). Fluorescent intensity measurements were used to quantitate the gel data and generate a plot of peptide cleavage over time (Figure 4.1 C). The addition of cyclic RGD proximal to the ACPP substrate resulted in a slight reduction in cleavage rates at early time points compared to the MMP-ACPP. Substituting the cyclic RGD with cyclic RAD had no impact on kinetics and the uncleavable peptide was resistant to MMP-2 degradation at all time points.

The affinity of cyclic RGD for $\alpha_v\beta_3$ was compared between the cRGD and cRGD-MMP peptide configurations using a cell-based, competitive binding assay. MDA-MB-435 cells, which have elevated expression of $\alpha_v\beta_3$, were incubated with a range of peptide

concentrations and subsequently placed on vitronectin, a protein ligand for $\alpha_v\beta_3$, coated plates to compare their binding capacity. The premise behind the assay is: when the peptide binds to the $\alpha_v\beta_3$ receptor on the cell surface, the cells will no longer have the ability to adhere to the vitronectin on the plates, therefore cell binding is a readout for cyclic RGD affinity. The MDA-MB-435s were labeled with calcein green (a fluorescent dye) so that fluorescence could be used as the read out. With this assay, the cRGD-MMP pretargeted ACPP had the same affinity for $\alpha_v\beta_3$ as cRGD alone (Figure 4.1 D). Furthermore, the MMP cleavable ACPP without the cRGD motif had minimal effects on cell binding to vitronectin, even at high peptide concentration.
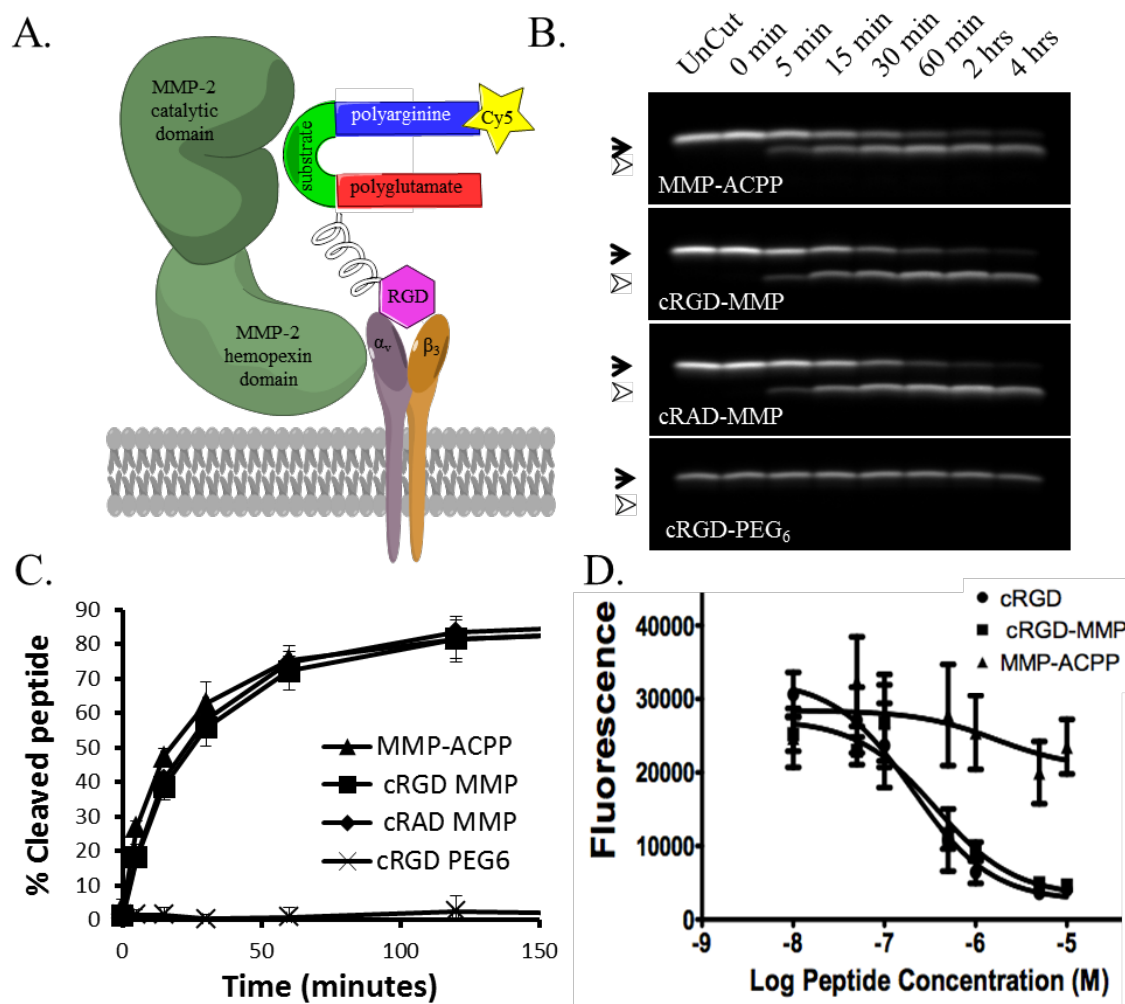
Figure 4.1 Combining cyclic RGD and MMP cleavable ACPPs did not diminish cleavability by MMP-2 or affinity of cRGD for $\alpha_v\beta_3$. A) Schematic respresentation of cRGD-MMP peptide binding to $\alpha_v\beta_3$ integrin to factilitate clevage by MMP-2. B) Gel elctrophoresis of peptide cleavage reactions with recombinant MMP-2 (5μM Cy5 labeleld petide with 50nM purified enzyme) C). Quantification of cleavage gels using the integrated intensities of the peptide bands to compare cleavage kinetics. D). Comparison of peptide binding to integrin $\alpha_v\beta_3$ on the surface of MDA-MB-435 cells. Cells were incubataed with 0-10 μM peptide for 20 minutes at room temperature and then exposed to calcein green to generate green fluorescent cells. Cells were then placed on vitronectin coated 96-well plates and the abitilty to bind vitronectin was monitored by measuring cellular fluorescence. At all peptide concentrations, cRGD had similar binding to the $\alpha_v\beta_3$ as the cRGD-MMP peptide.

To determine if there was synergy between integrin and MMP targeting, the dual

peptide was tested on U87MG glioblastoma cells. U87MGs were treated for 30 minutes

at 37°C, washed to remove all peptide from the media and imaged with confocal

microscopy to visualize peptide uptake. Cells were co-stained with calcein blue AM

ester, a cell viability marker. First, the individual building blocks of cRGD and MMP-ACPP were compared to cRGD-MMP (Figure 4.2, left column). MMP-ACPP had more cell uptake than cRGD, but when the two components where combined there was a significant increase in intracellular fluorescence. Next, control peptides **4-6** were imaged to validate the contribution of each targeting mechanism (Figure 4.2, right column). As each of the targeting moieties was systematically disabled, the fluorescent signal decreased until both means of targeting were deactivated and peptide fluorescence was almost undetectable.
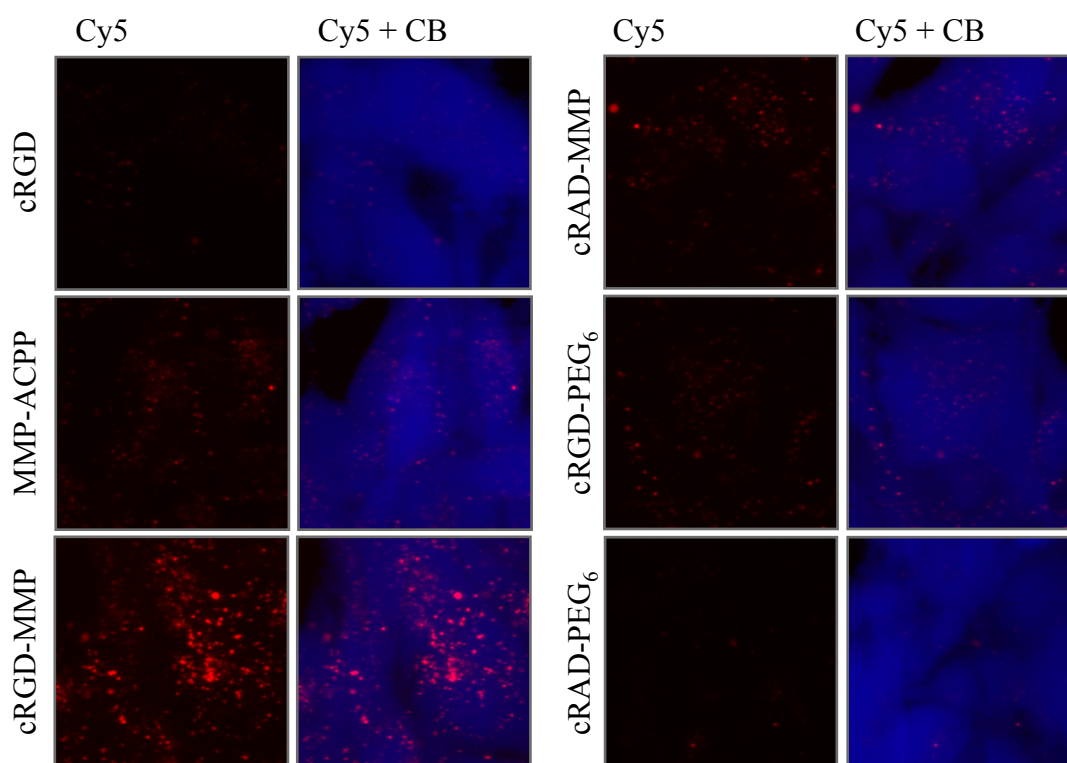
Figure 4.2 Synergistic targeting with cRGD and MMP-ACPP improved uptake in U87MG glioblastoma cells. Cells were incubated to 1μM Cy5 labeled peptide in serum free media for 25 minutes at 37°C. The peptide was washed off and cells were subsequently imaged live with confocal microscopy. Calcein blue AM ester (CB) was used as a cell viability marker. For each peptide treatment, the right image is just Cy5 and the left is an overlay of Cy5 with calcein blue.

4.4.2. *In vivo* tumor targeting and biodistribution analysis for

cRGD pretargeted ACPPs

Dual targeting was tested *in vivo* with orthotopic MDA-MB-231 mammary

tumors, imaged 6 hours after intravenous administration of Cy5 labeled peptides. Tumor

contrast was obtained with all of the probes except for the cRAD-PEG$_6$ control, and the

dual targeted probe had significantly higher tumor fluorescence, allowing for easy

identification of the tumor when the skin of the mouse was in tact (Figure 4.3 A). Post

mortem, the skin was resected to expose the tumor and surrounding tissue (Figure 4.3 B).

Tumor to background contrast was calculated using integrated intensity measurements on

ImageJ. The fluorescent intensity of the tumor was divided by average intensity of at

least 5 different regions in the surrounding area. The tumor to background ratio of cRGD-

MMP was significantly higher (p< 0.005) than any of the other peptides (cRGD-MMP:

7.8±1.6, cRAD-MMP: 3.9±0.8, cRGD-PEG6: 4.9±0.8 and cRAD-PEG6: 3.9±1.7). The

tumor uptake was also significantly higher for the pretargeted peptide with $p<1\times10^{-5}$

when compared to all the various controls (Figure 4.5 D).

Next, tumors were sectioned to examine peptide distribution on a histological

level. Previously, it has been reported that MMP cleavable free peptides home to the

stromal regions of the tumor, without much peptide penetrating into tumor cells (Olson,

Aguilera et al. 2009). With the addition of the cRGD motif, elevated Cy5 fluorescence

was seen around the perimeter of the tumor, but there was also a significant amount of

peptide found throughout the tumor cross section. With cRAD-MMP, the boundary of the

tumor had the highest peptide signal but some Cy5 was present in the tumor cells. Once

the ACPP linker was converted to PEG$_6$, tumor fluorescence dropped substantially with almost no fluorescence detectable in tumors that had been dosed with the double negative peptide.
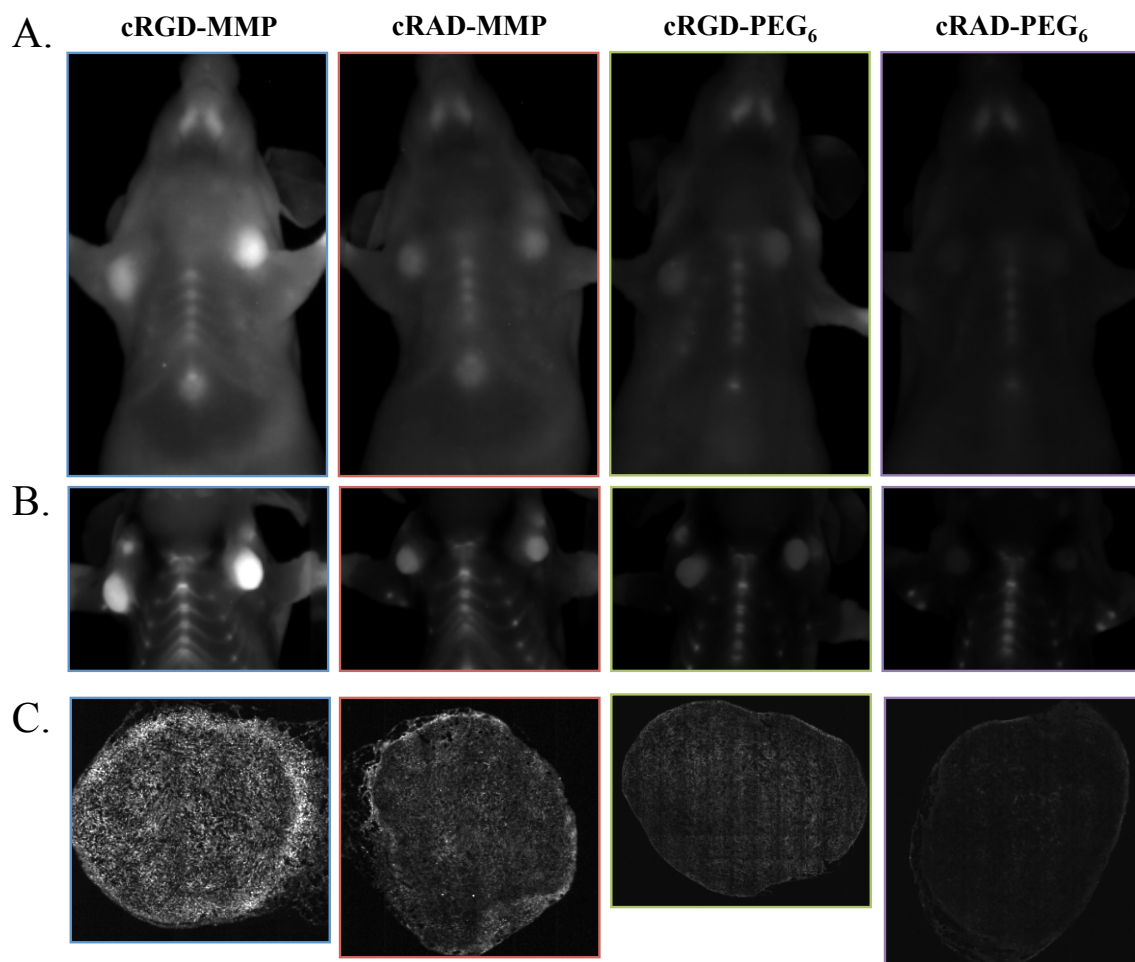
Figure 4.3 Dual targeting with cRGD and MMP-ACPP yields significantly greater tumor contrast and uptake. A) Mice harboring MDA-MB-231 breast orthotopic tumor were injected with Cy5 labeled peptides 6 hours prior to fluorescent imaging. B) Mice were sacrificed and the skin was resected to expose the tumor and surrounding tissue. C) Tumors were frozen, sectioned at 10μm thickness and cross-sections were imaged for Cy5 fluorescence with confocal microscopy.

The cRAD-MMP peptide was designed to control for the integrin component of the dual targeted system. To confirm that cRAD had in fact diminished all peptide affinity for $\alpha_v\beta_3$, the cRGD-MMP peptide was co-injected with 50 molar equivalents of unlabeled cyclic(RGDfK). Co-injecting with cold cRGD reduced tumor contrast and

uptake to values similar to cRAD-MMP (Figure 4.4). Analogous controls were tried with

IP injections of the MMP inhibitor Prinomastat, but this had no impact on tumor uptake

(data not shown).
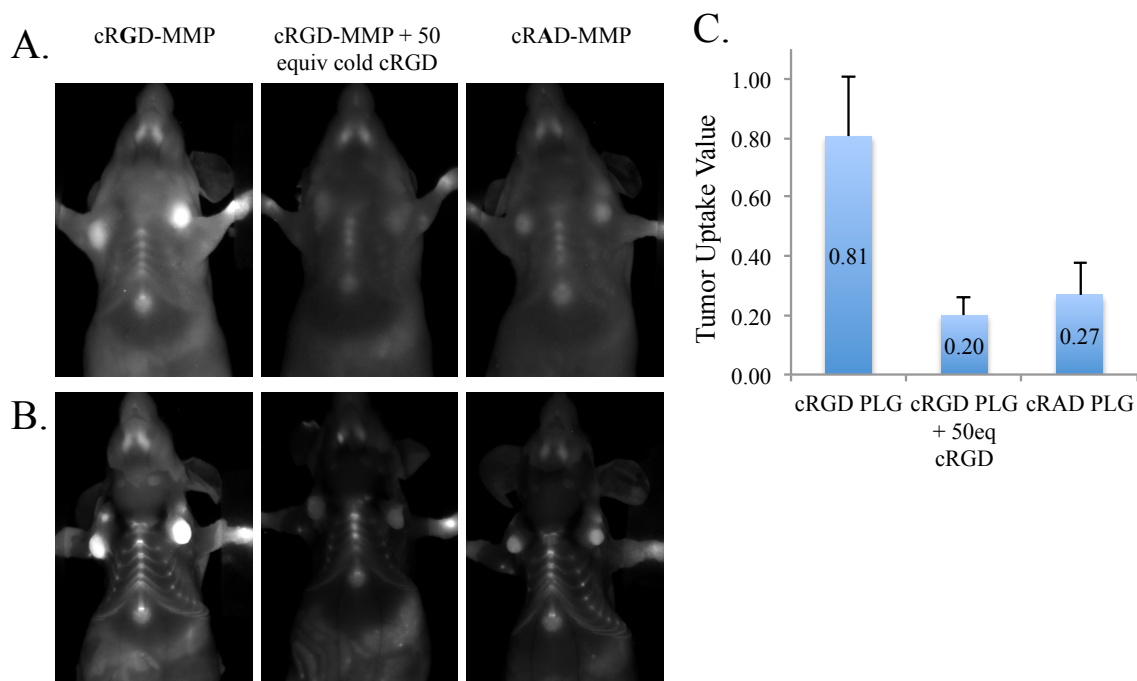
Figure 4.4 Co-injection of cRGD-MMP with excess unlabeled cyclic RGD reduced tumor uptake to levels of the cRAD-MMP control. A) Mice with MDA-231 tumors were injected with 10 nanomoles of either cRGD-MMP, cRAD-MMP or cRGD-MMP with 50 molar equivalents (500 nanomoles) of unlabeled cyclic(RGDfK) peptides. Six hours after injection, mice were imaged to evaluate tumor targeting. B) Skin was resected to expose the tumor and surrounding tissue. C) Standardized uptake values of the tumor for the various peptides tested (n ≥ 3 for each group tested).

Obtaining accurate biodistribution data is important for the development of any

molecular targeting strategy. With fluorescently labeled probes, this data is typically

obtained by harvesting specified organs from the animal at a given time point, placing

them on a black slab and imaging with planar fluorescence. Fluorescent intensities are

then calculated using a variety of software programs and those values are used to present

the relative distribution of the probe. One of the major problems with this method is that

fluorescence is not equal in all tissues. Issues such as light scattering, autofluorescence

and varying levels of absorption can generate significant artifacts. Dark tissues, such as the liver, kidney and spleen, will give relatively low "uptake" values compared to lighter tissues like tumor and muscle. This problem is exemplified in the data presented in Figure 3.5. Tissues (tumor, muscle, liver and kidney) from mice injected with Cy5 labeled peptides **3-6** were harvested six hours post injection and fluorescent images were obtained (Figure 4.5 A). From these images it appears that tumors from the cRGD-MMP mice had the highest peptide uptake over any other tissue across the board. This observation is quantitated in plot of fluorescent intensities presented in Figure 4.5 C. While this data is exciting, it unfortunately is inaccurate.

When tissues are homogenized and calibration curves are used to convert fluorescence into molality of fluorophore, probe biodistribution can change dramatically. In the protocol used to determine standardized uptake values (SUVs), buffer is added and the tissue is sonicated and enzymatically digested so it generates a homogeneous liquid. The fluorescence of this homogenate is measured and compared to a calibration standard to determine the Cy5 concentration. Sample calibration curves are presented in Figure 4.5 B. The slopes of the equations are significantly different depending on the tissue; for tumor and muscle the slopes are over 120 whereas liver and kidney have slopes of 26. Also, the y-intercept for these equations, essentially tissue autofluorescence, ranges from 81-720. When comparing the fluorescent intensity values in Figure 4.5 C with the SUV values in Figure 4.5 D, the cRGD-MMP tumor is no longer the tissue with the highest uptake; the liver and kidneys have 10 to 20 times more fluorophore than the tumor. Furthermore, this type of phenomenon only gets worse with dyes that have blue shifted

wavelengths; fluorescein (emission max ~520nm) is almost completely quenched in red

organs (data not shown, experimental observation).

A. Images of excised organs
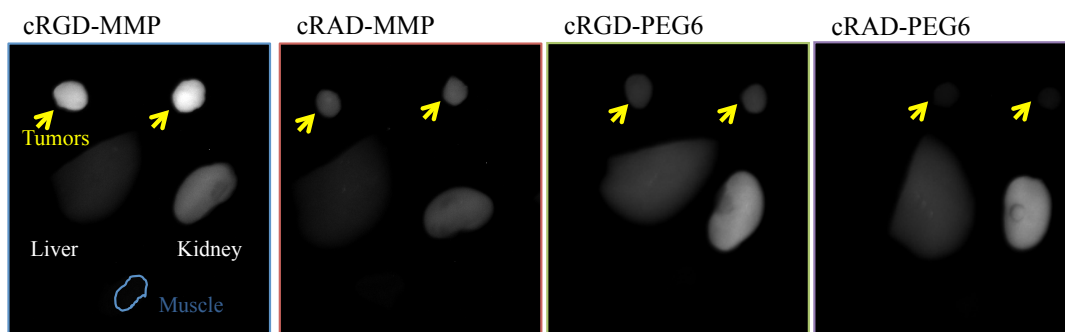
B. SUV calibration curves
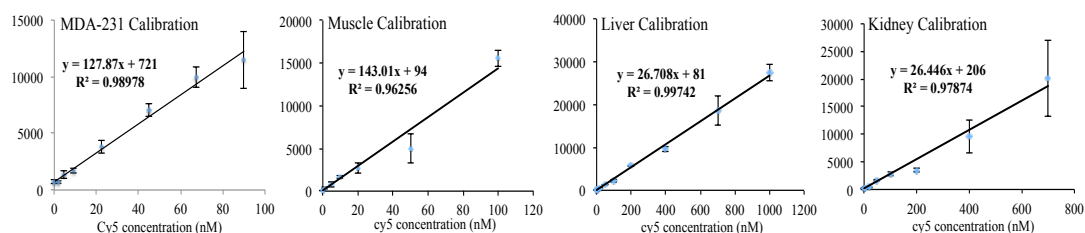
C. Fluorescent Intensities of organs   D.   Standardized uptake values for organs
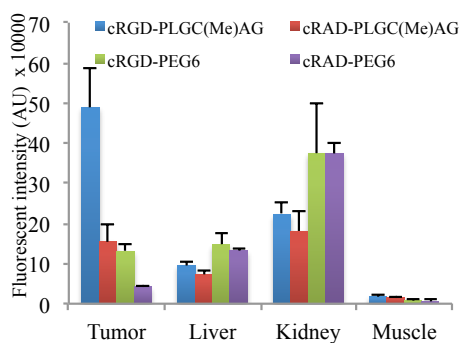
$\sharp$ p=1.63x10^{-6}, $\mathcal{H}$ p=2.68x10^{-5}, § p=1.17x10^{-8}
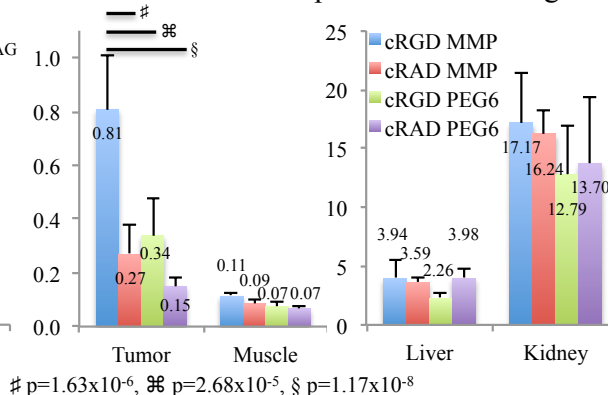
Figure 4.5 Biodistribution analysis for pretargeted ACPPs. A) Organs (tumor, muscle, liver and kidney) were harvested from mice injected with 10 nanomoles of Cy5 labeled pre-targeted ACPPs 6 hours post injection. Organs were placed on a black plate and imaged with 620/22 nm excitation and 670/20 nm emission. B) Sample calibration curves for converting tissue homogenate fluorescence into molarity of Cy5. Briefly, tissue from mice that had never been injected with fluorophore were homogenized in SUV buffer with know concentrations of Cy5. The fluorescence of the tissue homogenates was measured and plotted against Cy5 concentration. Linear regression analysis was performed in Excel to generate equations that fitted the data and those equations and their respective R^2 values are presented on the plots. C) ImageJ was used to measure the fluorescent intensities of the excised organs (as presented in A). D) SUV values for tumor and muscle (left graph) and liver and kidney (right graph). Values are presented on the graph are an average of n≥5 mice, with 2 tumors per mouse, and error bars represent standard deviation.

4.4.3. Dual targeted ACPPs improve therapeutic efficacy of monomethyl auristatin E

The ability of the dual targeted peptide to successfully delivery a chemotherapeutic cargo was investigated. MMAE was conjugated to either the cRGD-MMP or cRAD-PEG$_6$ peptide via a Cathepsin B cleavable linker. This substrate is comprised of Valine-Citrulin-$p$aminobenzyl; upon cleavage of the peptide after the citruline, there is a spontaneous fragmentation of the p-aminobenzylcarbamate intermediate that leads to the release of free, unmodified MMAE. This linker has been shown to be stable in mouse plasma for up to two days and efficiently hydrolyzed when incubated with human cathepsin B (Dubowchik and Firestone 1998).

The toxicity of MMAE limits the dose of the drug that can be administered. Studies with Dolistatin-10 found the maximum tolerated dose (MTD) to be 0.45mg/kg and the MTD for MMAE in SCID mice has been reported as 0.5-1.0mg/kg (Mirsalis, Schindler-Horvat et al. 1999; Francisco, Cerveny et al. 2003). A recent study targeting MMAE as a legumain activatable pro-drug was using free drug in the range of 0.1-0.5mg/kg (Bajjuri, Liu et al. 2011). Therefore, it was decided to begin therapy treatments at 0.2mg/kg MMAE, which equates to 6.5 nanomoles of the peptide-drug conjugate.

Mice harboring MDA-MB-231 orthotropic breast tumors were injected with the therapeutic dose of cRGD-MMP, cRGD-MMP-MMAE or cRAD-PEG6-MMAE. Because the MMAE versions of the pretargeted peptides are also labeled with Cy5, the ACPPs can be imaged to ensure that conjugation of the drug did not diminish tumor targeting. With the 6.5 nanomole dose, tumor contrast through the skin was lower than previously seen with the imaging dose of 10 nanomoles, but cRGD-MMP-MMAE and

cRGD-MMP had equivalent tumor uptake and both were superior to cRAD-PEG6-

MMAE (Figure 3.6). Also, the addition of the drug reduced the cartilage labeling in the

rib cage (Figure 3.6 bottom row).
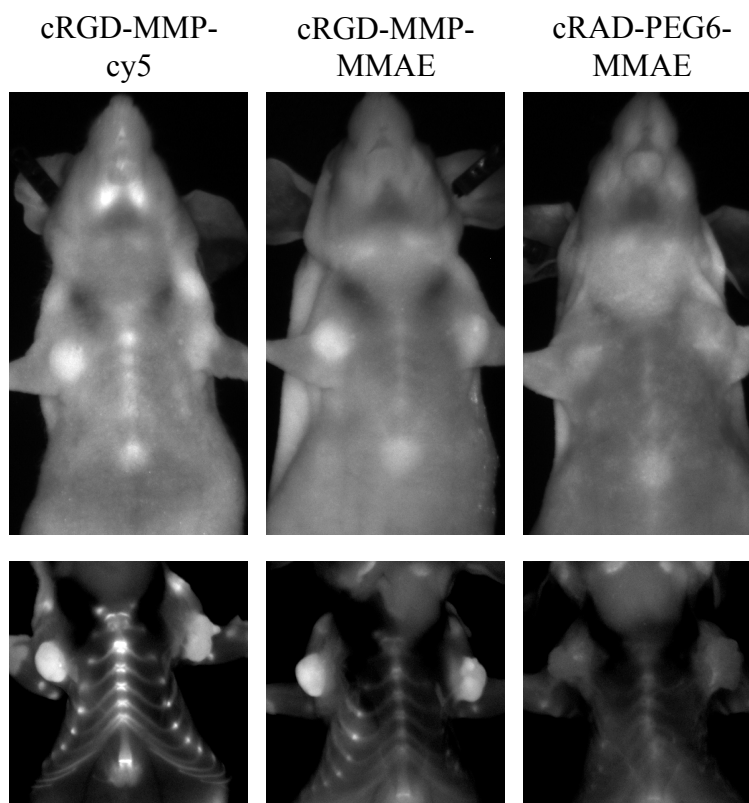
Figure 4.6 cRGD-MMP-MMAE maintains contrast similar to that of cRGD-MMP and is superior to cRAD-PEG$_6$-MMAE. Mice harboring MDA-MB-231 tumors were injected with 6.5 nanomoles of Cy5 labeled peptide. Six hours post injection mice were imaged for Cy5 fluorescence (top panel). Post mortem the skin was resected to reveal the tumor and surrounding tissue (bottom panel).

Next, mice were injected with MMAE peptide conjugates and tumor volumes

were monitored to determine if the dual targeted ACPP could increase the drug's

efficacy. MDA-MA-231 orthotopic tumors were implanted into the left and right

mammary fats pads of female mice and therapeutic intervention was initiated once the

tumors reached the approximate volume of 50mm^3. Seven mice per treatment group were

randomly assigned to receive either no treatment, MMAE free drug, cRAD-PEG6-

MMAE or cRGD-MMP-MMAE at a dose of 0.2 mg/kg auristatin. The drug was administered every three days for a total of 4 doses. cRGD-MMP targeting of MMAE significantly (p=0.0031) reduced the average tumor volume over treatment with the drug alone (Figure 4.7 A). When the targeting mechanisms were controlled for using a cRAD-PEG$_6$ peptide, it generated a prodrug form of MMAE that hindered the drug's effect. Once tumors grew to a diameter of 10mm, the animal was sacrificed and it was no longer possible to monitor therapy using tumor growth curves. To continue to observer the animals, the data is presented as a Kaplan-Meier survival plot that begins after the last therapy injection (Figure 4.7 B). Conjugating MMAE to cRGD-MMP significantly prolonged the animals' survival, with three out of the seven mice either having their tumors completely regress or stop growing. With both MMAE and cRAD-PEG$_6$-MMAE treatments, all mice were sacrificed by19 days post therapy.

The initial experiment was able slow tumor growth but only lead to complete disease regression in one of the animals in the cRGD-MMP-MMAE treatment group, therefore a higher dose of 0.32 mg/kg (10 nanomole peptide-drug equivalent) was tested. With the increased dose, tumor growth curves for both cRGD-MMP-MMAE and MMAE had a reduction in average volume (Figure 4.7 C) and the treatment resulted in multiple tumor cures (Figure 4.7 D). cRGD-MMP-ACPP targeting was able to cure 4 of the 8 tumors in the study whereas MMAE cured only 1 of 8, with another tumor having a mass of 5.5mg. Because of the large variation in tumor mass, the difference between cRGD-MMP-MMAE and MMAE did not have statistical significance, with p=0.077. During therapy treatments animals were monitored and no weight loss or overt toxicity was observed (Figure 4.7 E).

A)

B)

C)

D)

	cRGD-MMP-MMAE	MMAE
Tumor 1	0	5.5
Tumor 2	0	41.5
Tumor 3	36.7	124.8
Tumor 4	44.2	93.6
Tumor 5	0	0
Tumor 6	0	50
Tumor 7	56.4	124.2
Tumor 8	45.7	40.6
average	22.88	60.03
standard dev	25.03	49.05
p value	0.077	

E)
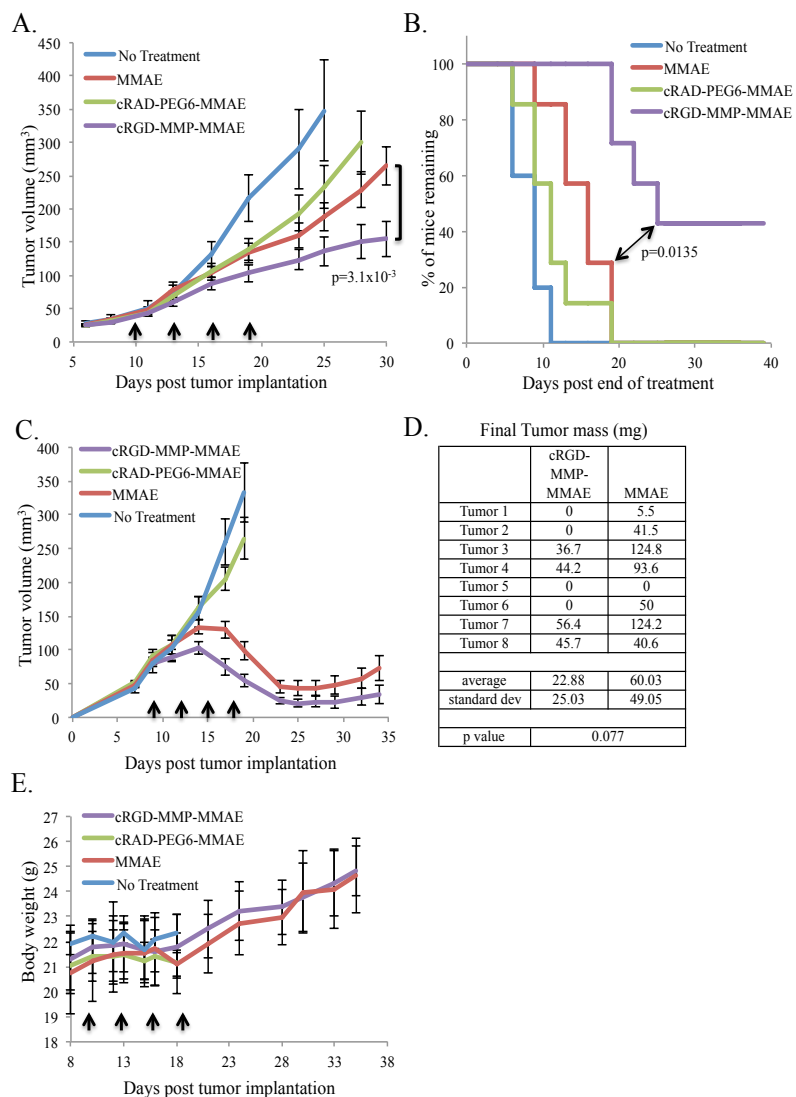
Figure 4.7 Targeting of MMAE with cRGD-MMP-ACPPs significantly improved therapeutic efficacy. A) Mice were injected with 7.5×10^5 MDA-MB-231 cells in Matrigel in both the left and right mammary fat pads. When tumors were ~50mm³, animals were divided into treatments groups of n=7. Mice either received no treatment, or the therapeutic dose of 6.5 nanomoles of MMAE, cRGD-MMP-MMAE or cRAD-PEG6-MMAE, which is equivalent to 0.2mg/kg auristatin. Mice were treated every three days for a total of 4 doses, as indicated by the black arrows, and tumor volumes were measured at regular intervals. Growth curves represent the average tumor volume and the error bars are SEM, statistics were performed using a students paired t-test. B) Kaplan-Meier survival curve beginning the first day post therapy. Animals were sacrificed once a tumor grew to a diameter of $\geq$ 10mm. Statistical analysis was performed using SigmaPlot's log-rank survival. C) Mice were injected with 7.5×10^5 MDA-MB-231 cells in Matrigel in both the left and right mammary fat pads. When tumors grew to approximately 80mm³ animals were divided into treatments groups of n=4. Mice either received no treatment, or therapeutic dosed of 10 nanomoles of MMAE, cRGD-MMP-MMAE or cRAD-PEG6-MMAE, which is equivalent to 0.32mg/kg auristatin. Mice were treated every three days for a total of 4 doses, as indicated by the black arrows. D) Table of all the final tumor masses for the mice treated with either cRGD-MMP-MMAE or MMAE. Statistics were done using a student's paired t-test. E.) Animal weights for each of the mice from panel C. Lines are the average weight with error bars representing the standard deviations. Dates of therapeutic injections are noted with black arrows.

4.5. Discussion

The combination of integrin and MMP targeting was successful at amplifying tumor targeting beyond levels attained by either mechanism alone. This synergy was possible because the two targeting moieties did not disturb one another's activity. The attachment of cyclic (RGDfK) near the substrate site resulted in a minute decrease in peptide cleavage rates when incubated with recombinant MMP-2. Furthermore, having the ACPP appended to the integrin binding peptide had no impact on cRGD's affinity for $\alpha_v\beta_3$. It would be interesting to monitor peptide cleavage kinetics in a more biological context, possibly a cell-based assay, to determine if the association of $\alpha_v\beta_3$ and MMP-2 improves cleavage rates. It is clear from cell culture experiment that dual targeting drastically in improves uptake. Cellular fluorescence of cRGD-MMP was superior to just the building blocks, cRGD-Cy5 and MMP-ACPP, as well as control peptides where integrin, enzyme or both targeting strategies were knocked down.

When tested in tumor bearing mice, the cRGD-MMP peptide had significantly higher tumor fluorescence, tumor:background contrast and uptake compared to its controls. The differences between the various peptides were more pronounced when comparing fluorescent intensity measurements for the tumor as opposed to the SUV values. A factor that may contribute to this discrepancy is the error introduced into the SUV calculations because tissue homogenates are of different opacities. Some tumors from the mammary fat pads are infused with more adipose tissue than others and a high fat content causes the homogenates to be significantly more "cloudy". This filters the fluorescent signal, leading to artifacts in the calculated SUV value. Because there is a wide spectrum of fat incorporation, this variable to hard to control for.

Imaging peptide fluorescence on a histological scale supported the gross fluorescent data. Cross sections of tumors with cRGD-MMP injected mice not only had substantially more peptide fluorescence, but the labeling was distributed throughout the tumor. With just MMP targeting, the fluorescence was localized to the edges of tumor and once the enzymatic targeting was disabled, tumor signal dropped significantly. To build upon this data, it would be interesting to visualize peptide cleavage in live tumors. Work is currently underway to accomplish this; a Cy5-Cy7 FRET probe has been designed such that proteolysis results in a change in fluorescent emission. This spectral shift will be monitored with in the tumors using two photon confocal laser microscopy. A similar approach was just used successfully applied to investigate the reduction of folate conjugates in mouse kidneys (Yang, Kularatne et al. 2012).

There is also a resent report that combines legumain protease activation and integrin targeting to deliver MMAE (Liu, Bajjuri et al. 2012). This paper focuses on how the prodrug formulation increases in therapeutic window for MMAE, showing reduction in primary tumor volume and metastatic burden using three times the maximum tolerated dose of MMAE alone. The therapy experiments do not have peptide controls and primarily compare animal data for prodrug-MMAE with mice that are not receiving treatment. In order to accurately compare this technology to the construct presented in this report, more information needs to be obtained about cRGD-MMP toxicity. Currently cRGD-MMP has only been tested at sub-lethal doses of MMAE, allowing for comparison of pretargeted drug with the parent drug. At these doses, the tumor responses were similar to those reported in Lui et al. If elevated doses of cRGD-MMP do not cause toxicity,

there is a possibility that $\alpha_v\beta_3$-MMP2 targeting could lead to cancer remission in even larger treatment groups.

4.6. Acknowledgments

The dissertation author would like to thank:

Dr. Elamprakash Savariar for synthesis of all the peptide used in this chapter and for assistance with experimental design. Heather Glasgow for performing the integrin-binding assay. Dr. Mike Whitney for his thoughtful discussion and help with experimental design. Perla Arcaira for maintenance of the various cell lines, preparing tumor cell injections, performing some of the tumor cell injection and for animal husbandry.

Chapter 4, in part, is currently being prepared for submission for publication of the material. Crisp, J.L.; Savariar E.N.; Glasgow, H.; Whitney, M.; Tsien R.Y. The dissertation author was the primary author of this material.

CHAPTER 5: Targeting of Clinically Approved Nanoparticles with Activatable Cell Penetrating Peptides; Doxorubicin Liposomes

5.1. Abstract

The attachment of activatable cell penetrating peptides (ACPPs) to clinically approved therapeutic nanoparticles provides an excellent platform to test ACP targeting for enhanced drug efficacy. ACPPs utilize the enzymatic activity associated with cancer invasion and metastasis to selectively unleash a very efficient mechanism for drug retention and cellular uptake. The aim of this chapter is to demonstrate the therapeutic potential of ACPPs by testing them against untargeted particles and control peptides in the context of doxorubicin loaded liposomes. The incorporation of ACPPs into these nanoparticles is fairly simple and the synthesis is robust, enabling large yields. The formulation, validation and extensive *in vivo* testing of ACPP targeted doxorubicin liposomes will be described. Initial results were very promising, but in the attempt to further validate ACPPs, the results began to show minimal differences between treatment groups. The possible reasons for this loss of efficacy will be discussed as well as what future directions should be pursued.

5.2. Introduction

The primary objective of ACPP based therapeutics is to design a molecule or particle that can take advantage of the enzymatic activation and amplification that ACPPs

can provide in areas of tumor invasion and metastasis. To prove that a targeting agent works, it is important to show that ACPP drug conjugates are more effectively than free drugs or the untargeted configurations. To further validate the ACPP targeting mechanism, it must also be demonstrated that the cleavable version of the peptide is more effective than it's uncleavable counterpart. While ACPPs with the addition of cyclic RGD were able to enhance the therapeutic efficiency of monomethyl auristatin E (MMAE) (Chapter 4), it's the extreme potency of this drug that made it a viable candidate for peptide targeting. Unfortunately, the inerrant toxicity of ACPPs makes them impracticable carriers for a majority of chemotherapeutics (Aguilera, Olson et al. 2009).

One niche where ACPP targeting has the potential to be successful is the addition of the peptide to established therapeutic nanoparticles. This eliminates many of the variables of drug design, such as selecting the proper therapeutic agent, linker and polymer chemistry, and provides a solid platform to build upon. One obvious candidate is the liposomal formulation of doxorubicin known as Doxil, which is FDA approved for use in multiple forms of cancer (Muggia, Hainsworth et al. 1997; Gordon, Fleagle et al. 2001; Park 2002). Doxil greatly improved the delivery of doxorubicin and reduced the cardiac toxicity associated with a high cumulative dose of free drug (Orditura, Quaglia et al. 2004).

The clinical approval of Doxil was a result of nearly 30 years of research in the field of liposome technology. Doxil is essentially a rigid liposome with a high concentration of doxorubicin at its core and an outer coating of polyethylene glycol (peg). This peg coating extends the plasma half-life to approximately 50 hours, an increase from

times as short as a few minutes for liposomes without it, by masking the drug from the reticuloendothelial system (Blume and Cevc 1990; Klibanov, Maruyama et al. 1990; Gabizon, Catane et al. 1994). Another major breakthrough was the ability to concentrate doxorubicin inside the liposome using an ammonium sulfate gradient (Lasic, Ceh et al. 1995). Other salt gradients can be used for doxorubicin loading and some can trigger drug release upon a reduction in pH, however these formulations suffer from reduced stability (Fritze, Hens et al. 2006). Other factors can also affect liposome stability and pharmacokinetic properties, such as lipid composition, particle size and storage buffer. To keep these variables constant, it was decided go forward with a formulation that mimicked that of clinical Doxil and focus on varying ACPP incorporation.

The concept of appending doxorubicin liposomes with targeting agents has had extensive academic investigation with variable success. A popular approach is to add antibodies or antibody fragments to the outer surface of the liposome. These antibodies target particular antigens on the surface of cancer cells, one example is Her2, a receptor that is unregulated in certain breast cancers (Laginha, Moase et al. 2008). Other approaches include folaic acid (Gabizon, Shmeeda et al. 2004), vascular ligands (Pastorino, Di Paolo et al. 2008), integrin ligands (Xiong, Huang et al. 2005; Murphy, Majeti et al. 2008) and the attachment of tumor homing peptides (Chang, Chiu et al. 2009). Some of these targeting mechanisms had such promising results that they are currently in clinical trials. Although these successes are noted, there is promise that ACPP targeting could out preform previous strategies because its enzymatic activation provides amplification, which could be superior to the stoichiometric binding of the exiting targeting moieties.

5.3. Methods

5.3.1. ACPP-lipid conjugates

Peptieds were synthesized as previously described in (Aguilera, 2009). Briefly, to generate DSPE-ACPP-Cy5: e_9-OPLGC(Me)AG-r_9-c and e_9-(Peg$_2$)$_2$-r_9-c were synthesized by solid phase fmoc chemistry and purified by high performance liquid chromatography (HPLC). Peptides were reacted with 1,2-distearoyl-sn-glycero-3-phosphoethanolamin-N-[maleimide(polyethylene glycol)-2000] (DSPE-Peg(2000)-maleimide) (Avanti Polar Lipids) in dimethylforamide (DMF) with N-methyl morpholine (NMM), and the reaction was monitored by HPLC. When near complete, Cy5-NHS (GE Life Sciences) ester was added to the mixture the conjugation was monitored by HPLC. After completion of synthesis the DSPE-ACPP-Cy5 was purified by HPLC.

For the second round of Lipid-ACPP synthesis, the peptide was first reacted with Cy5-NHS in the presence of 10 molar equivalents of N-hydroxy-sulfo-succinimide to prevent a cross reaction of the NHS ester with the free thiol on the peptide. The peptide was then purified by HPLC before reacting with DSPE-Peg-(2000)-maleimide.

5.3.2. Synthesis of ACPP containing doxorubicin liposomes

Liposomes were synthesized as previously described in (Aguilera 2009). Briefly, liposomes were formed from a lipid cake with 11:7:1 proportions of hydrogenated soy phosphatidyl choline, cholesterol, and 1,2-distearoyl-sn-glycero-3-phosphoethanolamin-N-[methoxy(polyethylene glycol)-2000] (DSPE-Peg(2000)) (Avanti Polar lipids) on a 30μmole of lipid scale (Fritze, Hens et al. 2006; Murphy, Majeti et al. 2008). For ACPP coated liposomes, various mole ratios of DSPE-ACPP-Cy5 to DSPE-Peg(2000) were

achieved before cake formation. The lipid cake was hydrated in a buffer containing 250mM ammonium sulfate, 50mM sucrose and 0.33mg/ml histidine at pH 6.5, heated to 60°C, and bath sonication to form multilamellar vesicles. This solution weas then probe sonicated for 2 minutes to generate small unilamellar vesicles (SUV). The SUVs were extruded a minimum of 20 times through a 0.2μm and then a 0.1μm membrane filter (Whatman) at 60-65°C using a mini-extruder (Avanti Polar Lipids). After extrusion, buffer exchanged was performed using a sephadex G25 (Sigma-Aldrich) column to clear all the extra liposomal ammonium sulfate. The liposomes, now in 300mM sucrose 2mg/mL histidine buffer at pH 6, were incubated with 15mgs of doxorubicin for 1 hour at 60°C. Size exclusion chromatography using sepharose CL-4B column (Sigma-Aldrich) removed all excess doxorubicin and the eluted liposomes were stored at 4°C. To determine the drug concentration, liposomes were disrupted with 1.5% trition-X solution and bath sonicated, then the doxorubicin concentration was calculated with the Beer-Lambert law by measuring by absorbance and using 11,500 M-1cm-1 as the extinction coefficient.

5.3.3. Enzymatic cleavage of ACPP-liposomes

Doxorubicin liposomes with 3% OPLGC(Me)AG-lipid were diluted in 300mM sucrose buffer containing 20mM Tris at pH 7.4. Active MMP-9 (Calbiochem) was spiked into the liposomes to a final concentration of 50nM and the reaction was placed in a 37°C incubator. Aliquots were taken at various time points and mixed with 2X tricine sample buffer (Life Technologies) and heated to 90°C for 60 seconds. Samples were then run on 10-20% tricine gradient gels (Life Technologies) and imaged on Maestro (CRI) using 620/20 nm excitation and 670/20 nm emission filters.

5.3.4. Imaging of doxorubicin in cells treated with ACPP
liposomes

HT1080 cells were plated on 96-well glass bottom plates and treated with various liposome formulations at a concentration of 50μM doxorubicin for 25 minutes in serum free media. The cells were then washed 3 times over 30 minutes with serum containing media and imaged for doxorubicin fluorescence by confocal microscopy (Zeiss, LSM 5 Live) using 488 nm laser and 550 LP emission filters. Doxorubicin uptake was quantitated on Zeiss software by drawing a region over the cell and recording the average fluorescent intensity.

5.3.5. Animal studies for testing ACPP doxorubicin liposomes

Mice were injected subcutaneously with 1×10^6 cells in the right and or left mammary fat pads to produce xenograft tumors. HT1080 cells were injected into athymic nu/nu mice and 4T1.2, PyMT 8119 and PyMT 230 cells were injected into mice with analogous genetic backgrounds. Once tumors became 50-150 mm^3, mice were injected intravenously (IV) with vehicle, doxorubicin liposomes, or ACPP coated doxorubicin liposomes at a dose of 3mg/kg of doxorubicin. Mouse tumor measurements were taken with calipers and weights were recorded at regular intervals. For most experiments mice were injected with multiple doses, and the timing of those doses depended on the tumor growth curves. When tumor volumes reached near maximum, as stipulated in the UCSD IACUC protocol, the animals were sacrificed and tumors were weighed and imaged. Explora Biolabs performed the experiments in Figure 2 and Figure 5 A and B.

For metastasis experiments $5\text{x}10^5$ cells were injected IV and allowed to seed in the lugs for 4 weeks prior to the first administration of drug. To evaluate therapeutic affect, lungs were harvested, fixed with paraformaldehyde and stained with Carmine solution. To quantitate the percent of lung metastases, histological sections were generated and the area of each metastatic nodule was calculated, summed and divided by the total area of the lung section. This was done for three independent sections for each of the 5 lobes of the lungs for each of the mice in the treatment group.

5.3.6. Quality control analysis for ACPP doxorubicin liposomes

Samples at 1mM doxorubicin concentration were subject to size exclusion HPLC (Agilent) followed by dynamic light scattering (Wyatt). Light scattering provided particle size, distribution, and density in particles/ml. These samples were collected and the Cy5 fluorescence was measured on a plate reader (Tecan). The fluorescent counts were compared to a calibration curve to determine the Cy5 concentration. With the knowledge of liposome and Cy5 concentrations for a given sample, the Cy5 molecules per liposome (essentially the ACPP concentration per liposome) could be calculated.

5.3.7. Blood clearance of ACPP doxorubicin liposomes

Doxorubicin liposomes were injected into mice at a dose of 3mg/kg. At various time points after injection the tails were clipped and approximately 50μL of blood was collected into heparinized tubes and immediately centrifuged to separate the blood contents. Plasma was aspirated from the tubes and diluted into 1.5% triton-X solution and bath sonicated. Doxorubicin fluorescence was measured and used to monitor liposome clearance.

5.3.8. Doxorubicin uptake in tumors

Mice harboring HT1080 xenografts were injected with the therapeutic dose of doxorubicin liposomes and tumor were harvested 24 hours after injection. Tumors were homogenized in 70% ethanol 0.3N HCl and doxorubicin was extracted over night at 4°C. Samples were then centrifuged and the supernatants were aspirated and analyzed for doxorubicin fluorescence.

5.4. Results

5.4.1. Synthesis and *in vitro* characterization of ACPP targeted Doxorubicin liposomes

To generate doxorubicin targeted liposomes the ACPP first had to be attached to a pegylated lipid. The was done by synthesizing peptides with the sequence of NH_2-e_9-OPLGC(Me)AG-r_9-c-$CONH_2$ and reacting Cy5 to the N terminus and a DSPE-Peg(2000) to the C terminal cysteine residue. While Cy5 is not required for tumor therapy, it is a useful tool for *in vitro* characterization and quality control analysis. Liposomes were made in house with the composition of 11:7:1 hydrogenated soy phosphatidylcholine (HSPC), cholerterol, and DSPE-Peg(2000) to mimic the formulation of pharmaceutical Doxil. Liposomes were synthesized with varying concentrations of DSPE-ACPP-Cy5 by adding different molar ratios of the lipid-ACPP at the first stage of preparation. For the subsequent experiments, % ACPP refers to the molar percent of DSPE-peg(2000)-ACPP that was included in the formulation. Dynamic light scattering confirmed that ACPP

containing particles had a similar size distribution as their untargeted counterparts, with an average diameter (z-average) of ~130 nm (data not shown.)

The peptide was oriented such that upon enzymatic cleavage the Cy5-e$_9$ portion would dissociate, leaving the activated poly arginine to facilitate uptake of the liposome into cells (Figure 5.1 A). To ensure that the ACPP was present on the surface of the particle and still accessible for enzymatic cleavage, liposomes were incubated with MMP-9 at 37°C and peptide cleavage was monitored by gel electrophoresis (Figure 5.1 B). Over half of the peptide had been cleaved after a 1 hour incubation, but some intact peptide was still detectable after an overnight incubation. One explanation for this could be that not all of the ACPPs face out to the external surface of the liposome; therefore some of the peptide is never exposed to the protease.

Next, liposomes were treated on HT1080 cells in culture to determine if addition of the targeting peptide could enhance drug uptake (Figure 5.1 C). Liposomes with varying molar percentages of ACPP were incubated on cells for 25 minutes, the treatments were removed, and cells were washed and imaged with confocal microscopy to visualize doxorubicin fluorescence. The amount of drug present in the cells increased significantly as the percentage of ACPP increased. Liposomes were present in the cell predominantly as small punta, presumably in endocytic vesicles, but some of the drug had managed to escape those vesicles and was detectable in the nuclei. This is an important observation, as endosome escape is critical for chemotherapeutic activity (as discussed in Chapter 4). Cells treated with liposomes containing a control mpeg peptide had levels of doxorubicin fluorescence similar to that of untargeted liposomes, validating

that the enhanced drug uptake was in fact due to enzymatic dependent targeting (Figure

5.1 D and E).
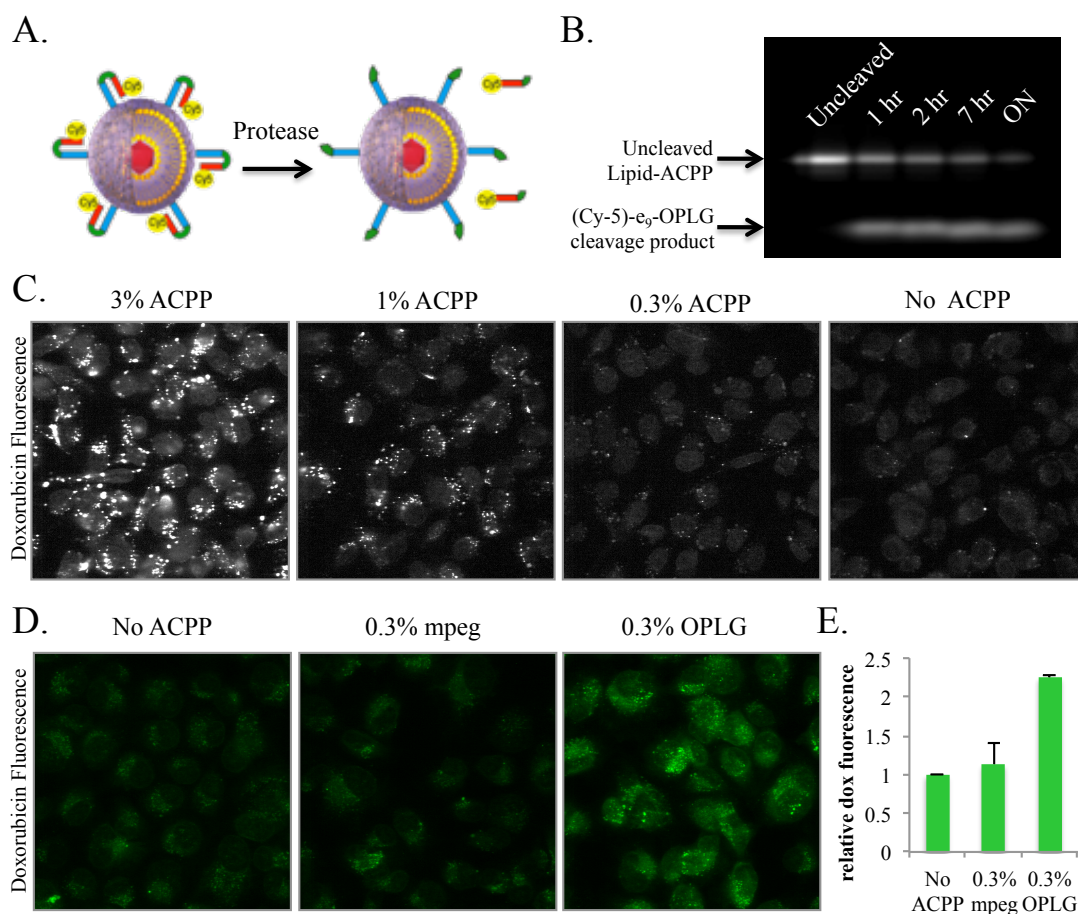
Figure 5.1 *In vitro* characterization of ACPP targeted liposomes. A) Schematic representation of ACPP coated liposomes, protease cleavage yields and activated CPP that facilitates uptake of the liposome into adjacent tissue. Image of liposome adapted from Ortho Biotech. B) Gel electrophoresis of ACPP coated liposomes after incubation with MMP-9. Top band is intact lipid-ACPP and the bottom band is the Cy5-e$_9$-OPLG cleavage product. ON is short for over night. C) Treatment of HT1080 cells in culture with 50μM doxorucin liposomes with varying amounts of MMP cleavable ACPP incorporated. Cells were dosed for 25 minutes at 37°C, then washed prior to confocal imaging. Liposome uptake was monitored with doxorubicin fluorescence. D) Comparison of cellular uptake for untargeted, uncleavable and MMP cleavable ACPP liposomes. E) Quantitation of doxorubicin uptake for liposomes with No ACPPs or 0.3% of either uncleavble control or MMP cleavable peptide. Uptake was calculated by drawing a region around each cell in a tretment group and measuring the average flurescent intensity. Data represent three individual experiments done under the same experimental conditions.

5.4.2. Early therapy experiments: when ACPP targeting worked

Preliminary *in vivo* results were reported in the dissertation of Dr. Todd Aguilera but will be summarized here to lay the groundwork for the data presented in this chapter. While high molar percentages of ACPP were very effective at increasing the drug uptake on cancer cells in culture, the same was not the case in animal studies. Mice treated with a single dose of 0.3% MMP-ACPP liposomes had substantially smaller tumor than those treated with either 3% MMP-ACPP or untargeted liposomes. In fact, untargeted doxorubicin liposomes performed better than 3% MMP-ACPP liposomes.

With multiple *in vivo* results demonstrating the effectiveness of ACPP targeting, experiments were expanded to include two additional variables: a further reduction in the molar percentage of ACPPs and the addition of an uncleavable peptide ($Cy5-e_9-(Peg_2)_2-r_9-c$). Liposomes were made with 0.3% and 0.1% ACPP-DSPE with both test and control peptides. Eight HT1080 tumor-bearing mice were injected with 3mg/kg equivalents of doxorubicin liposomes on days 8 and 22 post tumor cell injection (Figure 5.2 A). The 0.1% MMP ACPP group was the most efficacious, with over a 4-fold reduction in average tumor volume when compared to untargeted liposomes. In addition, the MMP targeted ACPPs were superior to their uncleavable counterparts at both molar concentrations. Mice treated with the uncleavable ACPP liposomes also had smaller tumors compared to the untargeted liposomes, this could be a result of the "breathing" in the peptide's hairpin structure, therefore generating some inherent activity even in the absence of proteolysis. On day 32 of the experiment, mice were sacrificed and the tumors were removed and weighed (Figure 5.2 B). Both the 0.3% and 0.1% MMP cleavable ACPP groups had significantly lower tumor masses with a $p<0.05$. By the end of the

experiment, mice in all of the treatment groups, including the untargeted vehicle, had

begin to loose weight (data not shown). There was no evidence that this weight loss was

due to the drug treatments or the presence of the ACPP. Hematological analysis showed

minimal variance between treatment groups except the platelet count for the 0.1%

cleavable and uncleavable mice were lower than the vehicle group (data not shown).
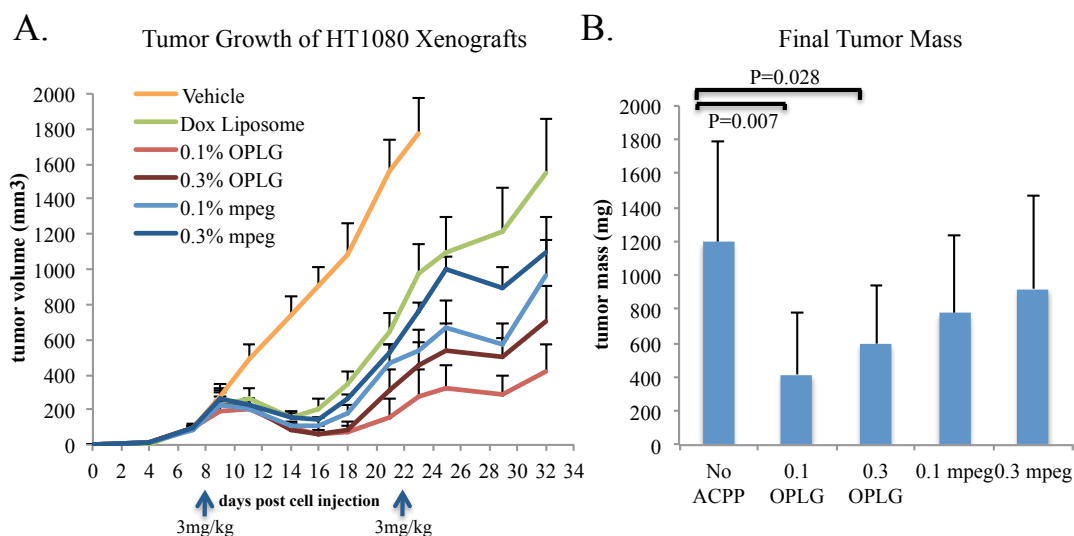
Figure 5.2 Reducing the molar percentage of ACPPs has a greater therapeutic effect and MMP cleavable ACPPs are superior to uncleavable control peptides. A) Eight athymic nu/nu mice (per treatment group) harboring HT1080 tumors were injected with liposomes at a dose of 3mg/kg doxorubicin on days 8 and 22 post tumor cell injections. Tumor volumes were monitored at regular intervals using calipers. MMP cleavable ACPPs were more effective than the uncleavable control peptide or the untargeted drug. B) Upon completion of the experiment, mice were sacrificed and the tumors were harvested and weighed to compare final tumor mass. Tumors from mice treated with MMP cleavable ACPP targeted liposomes had significantly less mass than those treated with the untargeted drug.

The next study moved beyond treatment of primary tumors to determine if ACPP

targeting could help reduce metastatic burden in the lungs. Because the formation of

spontaneous pulmonary metastases from primary tumors is rare in a majority of mouse

models, an experimental metastasis model was chosen. Breast cancer cells derived from

the transgenic polyoma middle T (PyMT) model were selected so the experiment could

be conducted in immunocompetent animals. PyMT 230 cells ($5x10^5$) were injected intravenously and allowed to circulate in the blood stream, eventually seeding in the lungs. On days 28 and 52 post tumor cell injection, mice were dosed with 3mg/kg doxorubicin equivalent of either untargeted or 0.1% MMP cleavable ACPP liposomes. Metastatic nodules were permitted to grow until day 52 when the mice were sacrifice and the lungs were harvested. Each lobe of the lung was removed, fixed with paraformaldehyde and stained with carmine before imaging. Representative images for each of the treatment groups are presented in Figure 5.3 A. The metastases appear as dark purple nodules in the lung parenchyma. From whole lobe images it is obvious that doxorubicin liposome treatments significantly reduced metastatic burden over the vehicle group, and that ACPP targeting resulted in further reductions in both the number of nodules and also the size.

To confirm these observations, lungs were sectioned and tumor burden was quantified on a histological level. Three sections from each of the 5 lobes of the lung for every mouse in the experiment were imaged and processed to determine the % lung area with metastasis (Figure 5.3 B). With this analysis the difference between the treatment groups became quite significant, with over a 3-fold reduction in metastatic area from untargeted to 0.1% MMP-ACPP liposomes. When stratifying the data based on the area of the nodules, it is clear that at the smaller size there are fewer mets with ACPP targeting and that targeting prevented the formation of larger metastatic lesions (Figure 5.3 C).

A. No ACPP liposomes   0.1% ACPP liposomes   Sucrose- Vehicle

B.

C.
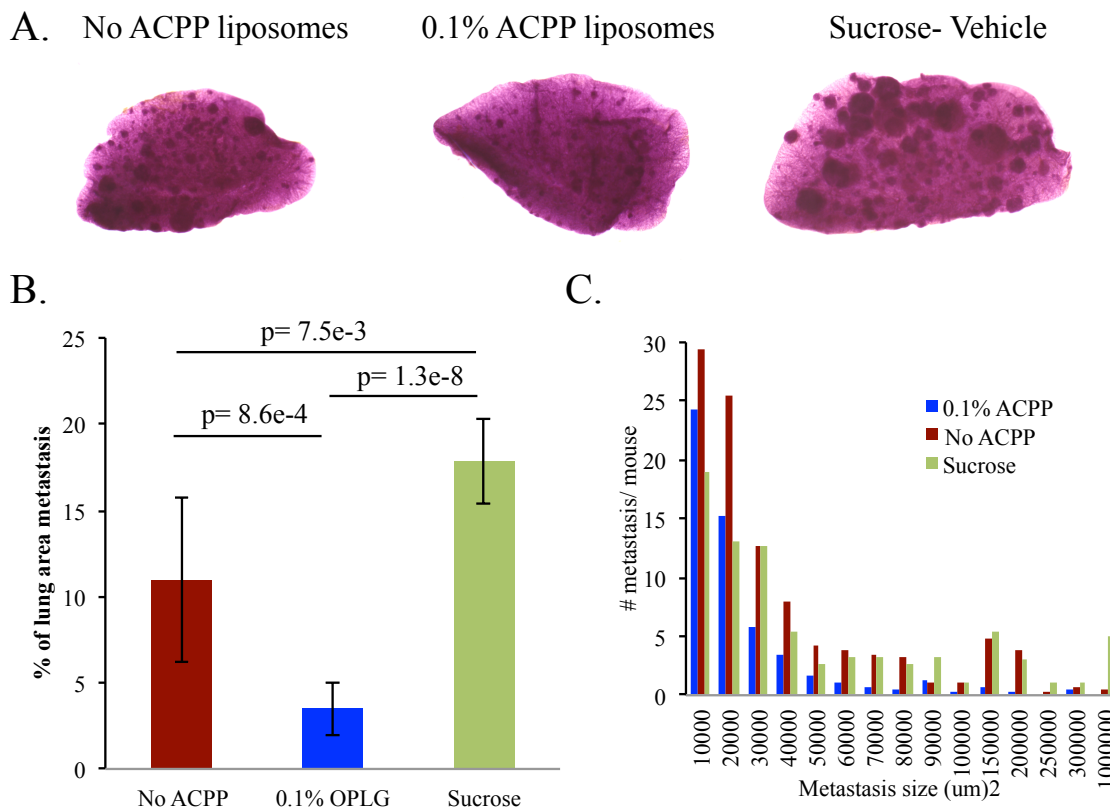
Figure 5.3 ACPP targeting of doxorubicin liposomes significantly reduced metastatic burden in the lungs of mice injected with PyMT 230 breast cancer cells. A) Mice were injected intravenously with $5x10^5$ PyMT 230 breast cancer cells and cells seeded in the lungs to generate a model of pulmonary metastasis. Doxorubicin liposomes were injected at 3mg/kg doxorubicin on days 28 and 35 after tumor cell injection. Mice were sacrificed on day 52 and all 5 lobes of the lungs were harvested fixed in paraformaldehyde then stained with carmine. These are representative lobes for each treatment group, which had an n=5. B) Metastatic burden was quantified by taking 3 histological sections from each of the five lobes of the lungs for each of the mice in the experiment. The area of each cancerous lesion was measured and summed for each section, then divided by the total area of the lung section to calculate % of lung area metastasis. C) Data was stratified by the metastasis size to compare the # of metastases in the various size groups for each of the treatments.

Liposome synthesis, while not mentally taxing, can be very time consuming and labor intensive. One way to bypass the de novo synthesis is to incorporate the DSPE-ACPP into clinically available Doxil. This is accomplished by simply incubating the lipid-peptide conjugate with Doxil at 60°C for 1hour. Size exclusion chromatography removed any extraneous lipid-ACPP and incorporation was confirmed by monitoring Cy5 fluorescence. Mice with HT1080 tumors were injected with ACPP targeted Doxil at

a dose of 3mg/kg doxorubicin (Figure 5.4 A). Interestingly, with this nanoparticle the

higher molar percent ACPP was more efficacious, with the 0.1% ACPP performing

worse than the untargeted drug. While the results for both tumor volume and tumor mass

make 0.3% ACPP Doxil appear to be very effective (Figure 5.4 A and B), it is important

to note that the treatment group lost one animal on September 18th and another on

September 21st due to tumor ulceration. This ulceration was not due to drug treatment,

but the result of the tumor growing into the skin instead of being confined to the fat pad.

Because the larger tumors in the treatment groups were the ones to ulcerate, the data is a

somewhat misrepresentative. This experiment was still considered positive because on

September 18th, before any of the tumors had been excluded, there was a difference in

average tumor volume between the Doxil and 0.3% OPLG treatment groups.
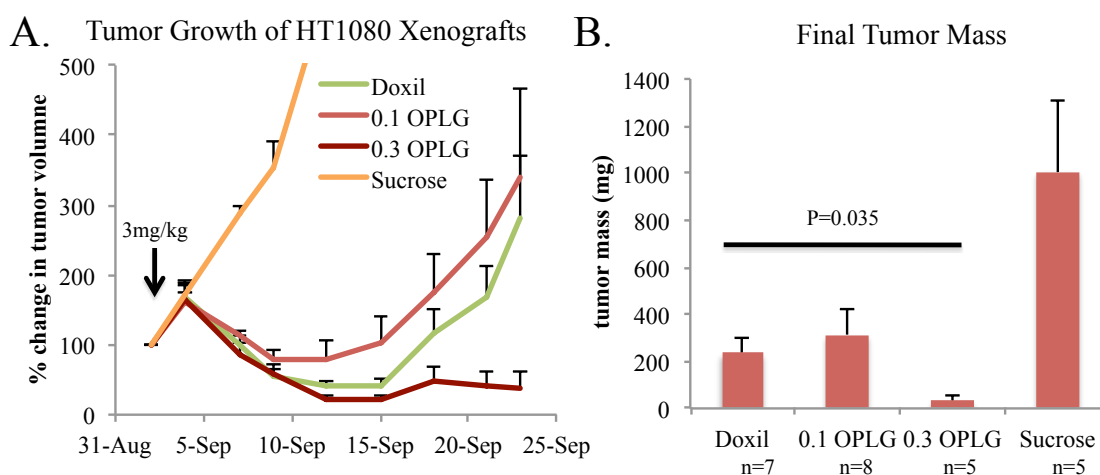
Figure 5.4 Incorporation of DSPE-peg(2000)-ACPP into clinical Doxil reduced average tumor size of HT1080 xenografts. A) Four mice were injected with HT1080 cells in both the left and right mammary fat pads for a total of eight tumors per treatment group. Mice were dosed with 3mg/kg doxorubicin as noted by the black arrow. A single dose of 0.3% OPLG targeted Doxil was very effective at shrinking tumors, and only one dose was given because as the tumors began to grow back they started to ulcerate. Note that the 0.3% OPLG lost two tumors on September 21st (mouse was sacrificed) and one more tumor on September 23rd so the final tumor count was n=5. The untargeted group also lost a tumor to ulceration on September 23rd therefore the experiment was terminated. B) Tumors that had not lost mass due to ulceration were harvested and the weight was recorded. There was statistical significance between the Doxil and the 0.3 OPLG treatment groups, but since the larger tumors in the 0.3 OPLG group were the ones to ulcerate, this data is misrepresentative..

5.4.3. ACPP targeting started to fail in the HT1080 model

While the lung metastasis and Doxil studies mentioned previously were on going, the HT1080 primary tumor model was revisited in order to determine what percentage of ACPP gave the best therapeutic effect. In all previous studies with this model, lowering the molar percentage of ACPPs, improved the drug performed, therefore homemade liposomes with 0.03% and 0.01% MMP-ACPP were tested (Figure 5.5A). The results of this study were disturbing because the untargeted liposomes were now significantly more effective than any of the ACPP targeted liposomes, and there was no apparent trend in ACPP percentage and average tumor volume. It was hypothesized that the No ACPP and 0.1% MMP-ACPP samples had been mislabeled before they were given to Explora Biolabs, since swapping those treatment groups would generate data that was congruent with all the previous studies. Unfortunately, none of the injectates remained at the end of the study so the data had to be taken at face value.

The experiment was then repeated with MMP-ACPP liposomes having molar percentages ranging from 0.3%-0.01% in half log dilutions, as well as 0.1% mpeg ACPP liposomes as a uncleavable control (Figure 5.5 B). ACPP targeting was again out performing the untargeted liposomes, but it was the uncleavble control group that had the smallest average tumor volume. With this experiment there was only a single dose of drug given on day 9, which could help explain why the treatment groups were not as stratified as previous results.
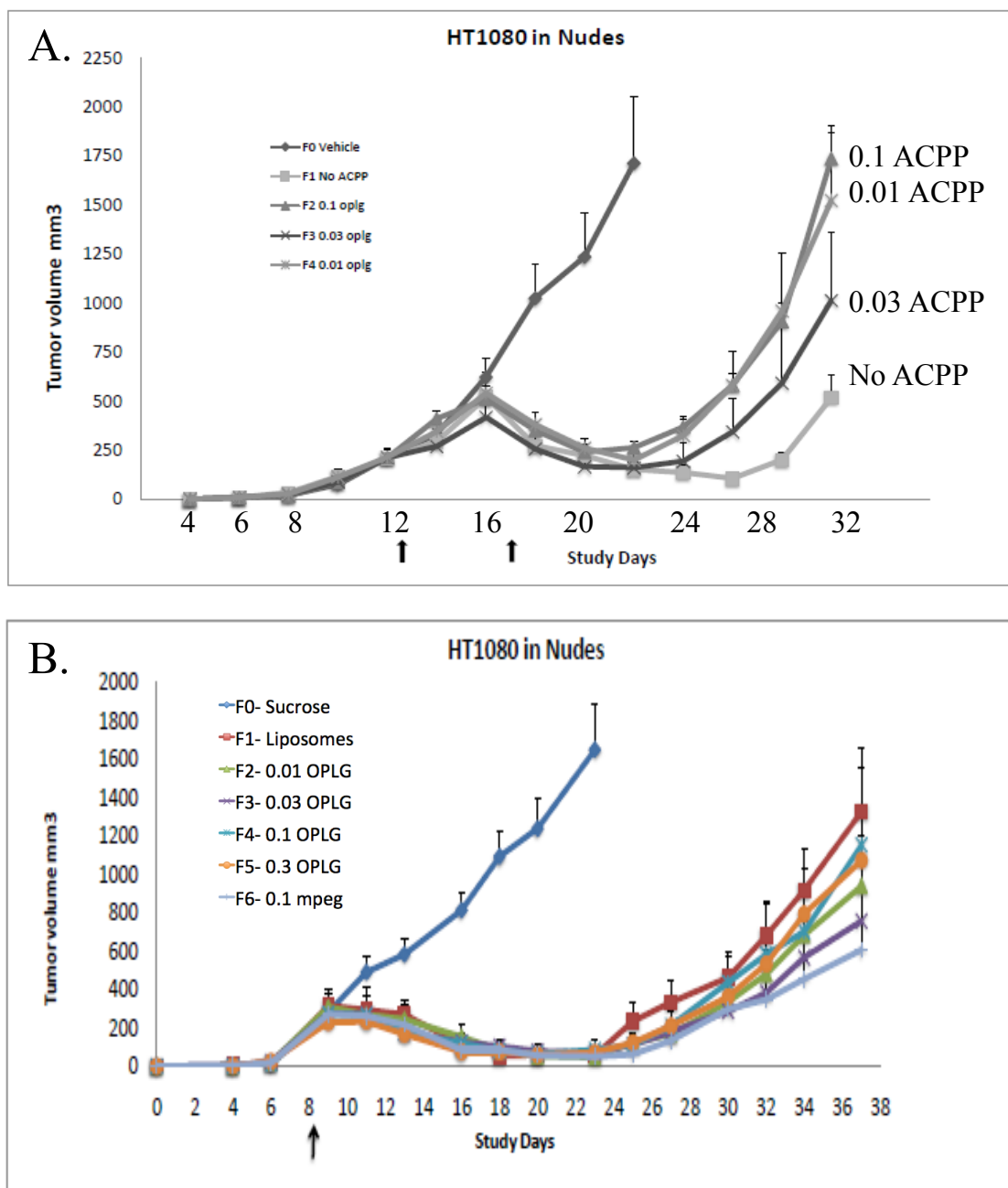
Figure 5.5 ACPP targeting of doxorubicin liposomes begins to fail in the HT1080 xenograft model. A) Eight mice per treatment group were injected in one of the mammary fat pads with 1x10^{6} HT1080 fibrosarcoma cells. Liposomes were dosed at 3mg/kg doxorubicin on days 13 and 18 after tumor cell injection and tumor volume was monitored at regular intervals. B) Eight mice per treatment group were injected in one of the mammary fat pads with 1x10^{6} HT1080 fibrosarcoma cells. Liposomes were dosed at 3mg/kg doxorubicin on day 8 after tumor cell injection and tumor volume was monitored at regular intervals.

5.4.4. Minimal success with ACPP targeting in syngeneic breast cancer models

ACPP targeted liposomes were tested in a few syngeneic breast cancer models including 4T1.2, PyMT 8119 and PyMT 230. Primary tumors derived from the 4T1.2 cell line were sensitive to doxorubicin liposome therapy. Tumors shrank significantly after treatment and the average tumor volume remained low for all of the groups that received drug (Figure 5.6 A). Once the tumors began to grow back, the 0.1% mpeg-ACPP had the fastest growth rate, but there was no difference between the untargeted and 0.1% OPLGC(Me)AG-ACPP liposome groups. This cell line was also used to generate experimental lung metastases for therapeutic studies. Animals were dosed twice with a 3mg/kg equivalents of doxorubicin and lungs were harvested and processed in the same manner at the PyMT 230 experiment previously mentioned. While the treatment groups with 0.1% and 0.3% MMP cleavable ACPPs had a lower metastatic burden (Figure 5.6 B), the differences were not statistically significant from the untargeted control group.

ACPP targeting was also tried in two different cell lines generated by our collaborator Dr. Lesley Ellies. Dr. Ellies' isolated tumor initiating cell lines from the PyMT model, which give rise to both luminal and basal-EMT tumors. The PyMT 8119 cell line produces basal-EMT tumors that have a relatively fast growth rate and elevated expression of MMPs (data not shown). These tumors however were fairly resistant to doxorubicin chemotherapy, and groups that had been treated with the various forms of doxorubicin liposomes had tumor growth curves similar to the vehicle mice (Figure 5.6 C). PyMT 230 cells generate tumors with a luminal phenotype, and these tumors have

slower growth rates but are sensitive to doxorubicin therapy. Previous data with this cell line in the lung metastasis model had shown a significant reduction is metastatic burden with ACPP targeting (Figure 5.3), so it was decided to try targeted therapy with primary tumors. Mice were dosed with 3mg/kg equivalents of doxorubicin on days 8 and 19 after tumor cell injection and tumors were permitted to grow until day 56 (Figure 5.6 D). Liposomes targeted with 0.3% MMP cleavable ACPPs had a significant reduction in tumor volume over the untargeted drug (p=$1.4x10^{-4}$ using a students t-test). The 0.1% MMP cleavable ACPP liposomes had a small therapeutic effect compared to the untargeted group, but there was no difference compared to 0.1% mpeg group. Finally, Doxil with DSPE-ACPP incorporation was tested in PyMT 230 primary tumors (Figure 5.6 E). In this study the 0.1% MMP-ACPP Doxil showed no effect when compared Doxil alone, whereas the 0.3% MMP-ACPP Doxil significantly reduce the tumor volume but the 0.1% mpeg control had similar effects.
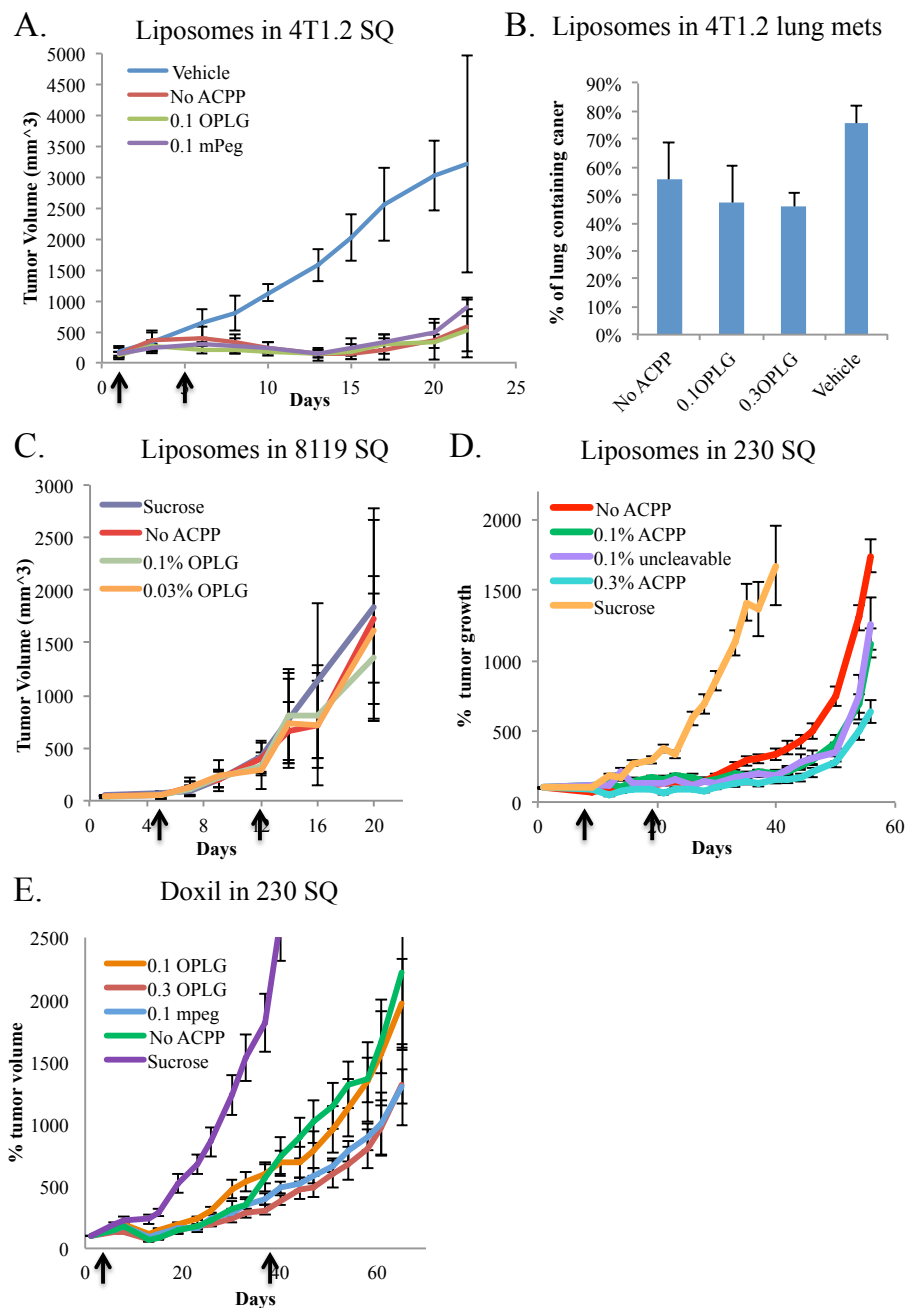
Figure 5.6 Performance of ACPP targeted doxorubicin liposomes in various syngeneic breast cancer models. For each of the tumor growth curves in this figure, the injected dose of doxorubicin was 3mg/kg and the timing of the doses is designated by black arrows along the x-axis. A) 4T1.2 primary tumors after treatment with doxorubicin liposomes. B) $5x10^5$ 4T1.2 cells were injected in the tail vein and seeded in the lungs. Mice were dosed with doxorubicin liposomes and the lungs were harvested, fixed in paraformaldehyde and stained with carmine. Metastatic burden was quantified by using histological sections. C) Mice were injected with $5x10^5$ PyMT 8119 cells into the left and right mammary fat pads and dosed with liposomes on days 5 and 12 after tumor cell injection. D) Mice were injected with $1x10^6$ PyMT 230 cells into the left and right mammary fat pads and subsequently dosed with liposomes on days 8 and 19 after tumor cell injection. E.) Mice were injected with $1x10^6$ PyMT 230 cells into the left and right mammary fat pads and treated with ACPP targeted Doxil on days 9 and 38 after tumor cell injection.

5.4.5. Blood clearance and doxorubicin tumor uptake

The plasma half life and doxorubicin uptake into HT1080 tumors was measured for MMP cleavable ACPP targeted liposomes using doxorubicin fluorescence. The blood half-life for the liposomes is approximately 10 hours, with a fast initial clearance and a slower clearance as time after injection increased (Figure 5.7 A). By 56 hours after injection doxorubicin was almost undetectable in the blood. The addition of ACCPs to the surface of the liposomes did not impact the rate at which the particles were cleared from circulations. To quantitate tumor uptake, tumors were harvested 24 hours after liposome injection and the doxorubicin was extracted from tumor homogenates. The addition of 19 targeting peptides to the particle surface was able to increase the amount of drug found in the tumor by nearly 33% over the untargeted control with $p=0.046$ (Figure 5.7 B). By 72 hours after injection the levels of doxorubicin in the tumors was not detectable over tissue autofluorescence (data not shown).
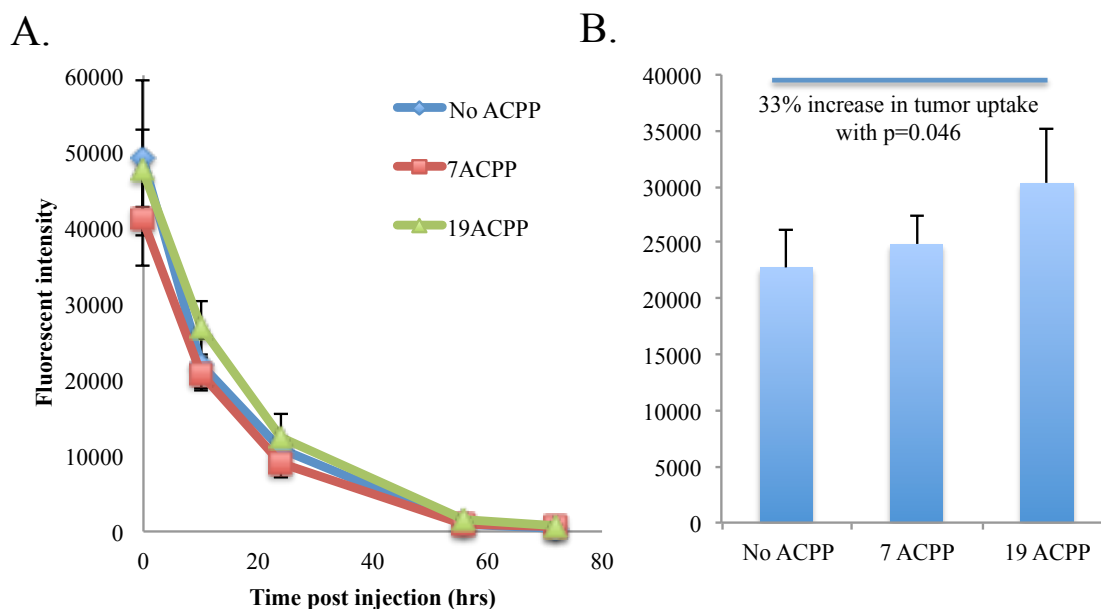
Figure 5.7 MMP cleavable ACPP targeting of doxorubicin liposomes does not alter clearance of the particle from the blood but does increase tumor uptake at 24 hours post injection. A) Mice were injected with the therapeutic dose of doxorubicin liposomes and blood samples were collected at various time points for up to 72 hours. Blood collected in heparinized tubes was immediately centrifuged to collect plasma. The liposomes within the plasma were disrupted with a 1.5% triton-X solution and doxorubicin fluorescence was used to monitor clearance. B) Mice harboring HT1080 xenografts were injected with 3mg/kg doxorubicin equivalent of liposomes and tumors were harvested 24 hours after drug injection. Tumors were homogenized in an acidic ethanol solution and doxorubicin was extracted into that solution overnight at 4°C. The tissue homogenate was centrifuged and the level of doxorubicin fluorescence in the tumor supernatant was used to compare liposome uptake.

5.4.6. Liposome quality control

As more experiments began to produce inconclusive results, the need for more stringent liposome quality control became apparent. The first variable to examine was the stability of the lipid-ACPP, which had been stored in water at 4°C for nearly 10 months by the end of the experiments presented in Figure 5.6. HPLC analysis revealed the presence of two absorbance peaks in the Cy5 wavelength (642-658nm) and it was clear that the DSPE-peg(2000)-ACPP had begun to degrade (Figure 5.8 A, third panel). It is

unknown when this began to occur, but this peptide could no longer be used for therapeutic testing.

Dr. Elamprakash Savariar, an experienced nanoparticle chemist and post doctoral fellow in our lab, synthesized a new lipid-ACPP construct. The same peptide sequence and DSPE-peg(2000)-maleimide were used, but the method with which the conjugate was synthesized differed from the first round. Dr. Aguilera had reacted the ACPP with both the lipid-maleimide and Cy5 NHS ester in a one pot reaction, whereas Dr. Savariar first reacted the peptide with Cy5, purified the fluorescently labeled peptide then reacted that product with the DSPE-peg(2000)-maleimide. The second method of synthesis, while more time consuming, is superior to the first because it ensured that all the lipid-ACPP conjugate is fluorescently labeled. With the first synthesis method, it is not possible to remove any unlabeled lipid-ACPP in the final purification step (using size exclusion HPLC). A sample HPLC trace is given for the second DSPE-peg(2000)-ACPP in Figure 5.8 B.

A.

Impurity

B.

Cy5 based impurities developed here with old sample
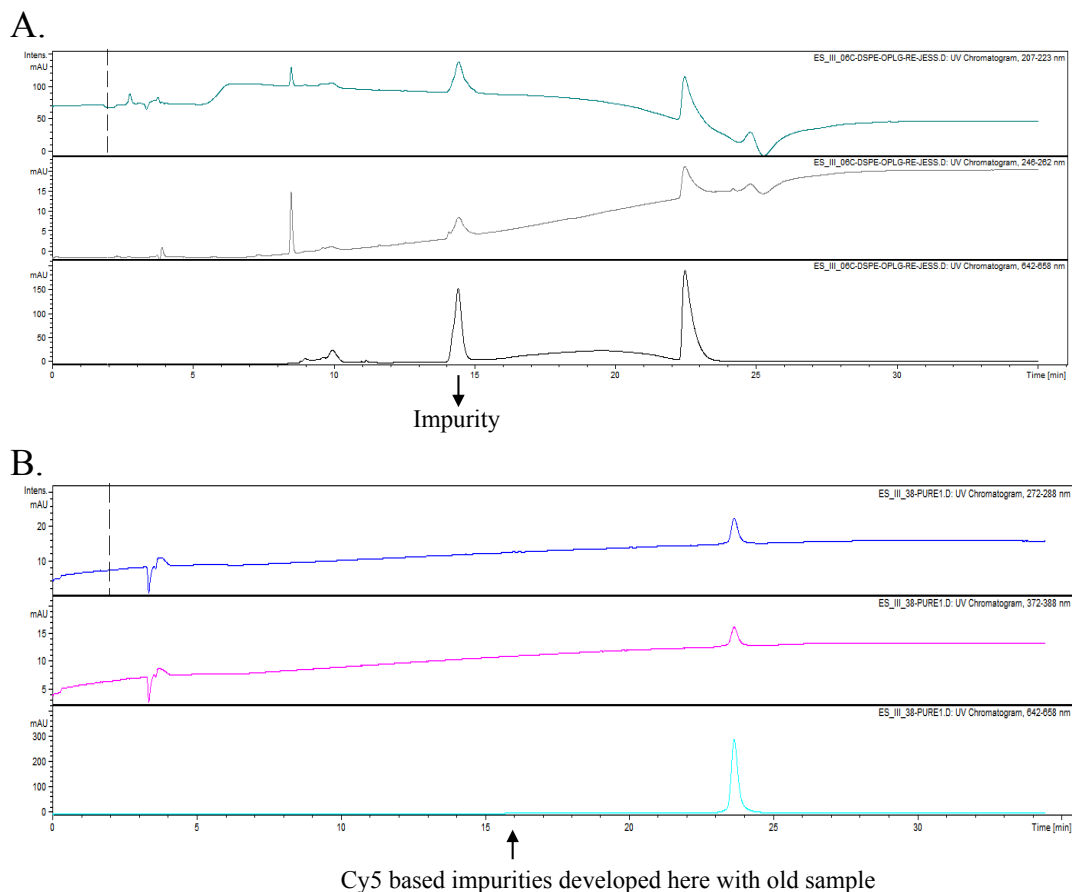
Figure 5.8 HPLC of the DSPE-peg(2000)-ACPP constructs. A) Absorbance traces from an HPLC run performed with a size exclusion column of the first synthesis of DSPE-peg(2000)-ACPP (MMP cleavable). The top panel is absorbance from 207- 223nm, the middle panel is absorbance in the wavelengths of 246-262nm and the bottom panel is Cy5 absorbance in the range of 642-658nm. The presence of two distinct peaks in the bottom panel and multiple peaks in the above panels are evidence of the peptide degredation. B) Absorbance traces from a similar HPLC run performed with the second synthesis of DSPE-peg(2000)-ACPP. The panel absorbance ranges are the same as listed above. Note that there is only one peak in all of the monitored wavelengths, attesting to the purity of the lipid-peptide conjugate.

The next variable that needed to be addressed was determining the number of ACPPs that were incorporated into the liposomes. For every batch of liposome synthesis the concentration of the ACPP-lipid was confirmed and the same molar ratio of peptide was added, yet the incorporation of peptide was not always constant between batches or between the cleavable and uncleavable peptides (Table 5.1). For experimental results to be comparable, the number of ACPPs should be documented.

Dynamic light scattering was used in the original syntheses to measure the hydrodynamic radius of the liposomes and confirm a mono disperse population, but new equipment acquired in the lab made it possible to determine particle density as well. With this information, the number of ACPPs per liposome could be calculated. Briefly, liposome preparations at 1mM doxorubicin were injected into an HPLC with a size exclusion column where the absorbance at 490nm (doxorubicin) and 650nm (Cy5) were recorded (Figure 5.9 A). The liposomes eluted from the column into a Wyatt dynamic light scattering machine that provided both the radius of the liposomes and the density in particles/ml. The samples were collected from the Wyatt and transferred to a plate reader where the Cy5 fluorescence was measured and compared to a calibration curve to determine the Cy5 concentration (Figure 5.9 B). With the knowledge of doxorubicin concentration, Cy5 concentration and particle density, the doxorubicin loading and number of ACPPs per particle could be calculated (Figure 5.9 C).

For all applicable experiments, the number of ACPPs per liposome was calculated and is reported in Table 5.1. Depending of the synthesis, the 0.1% MMP cleavable ACPP ranged from 7-21 ACPPs per liposome, the 0.3% MMP cleavable ranged from 21-39 ACPPs and the 0.1% mpeg had between 7-8 peptides. When analysis was done on liposomes made with the new lipid-ACPP (synthesized by Dr. Savariar), the number of ACPPs per particle increased significantly, with 25 peptides for 0.1% OPLGC(Me)AG, 93 ACPPs for the 0.3% OPLGC(Me)AG, 52 peptide for the 0.1% mpeg and 110 ACPPs for the 0.3 % mpeg. This QC protocol was developed after the initial *in vivo* studies so it is not known how these numbers compare to the targeted liposomes that yielded the promising data.
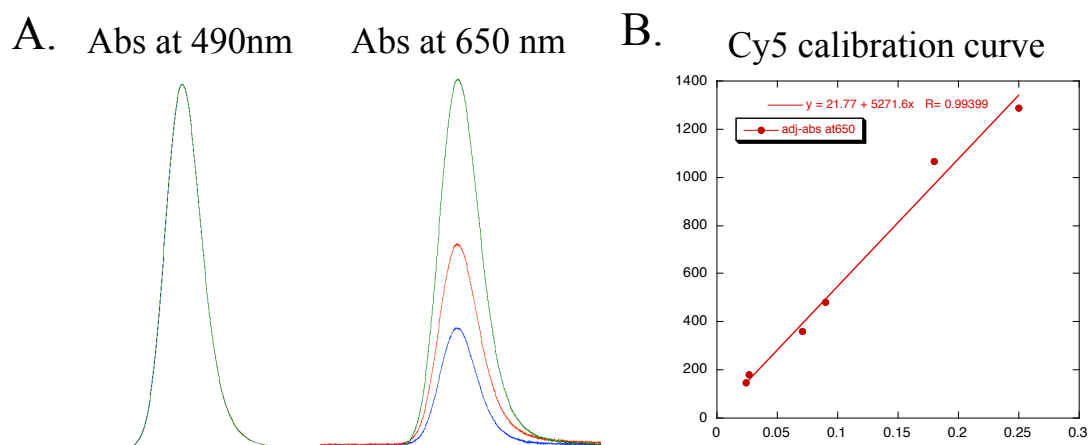
Figure 5.9 Quality control protocol to determine the doxorubicin loading and number of ACPPs incorporated and the into the liposomes. A) Overlay of absorbance traces from HPLC size exclusion runs for No ACPP, Low ACPP and High ACPP samples. Each of the three samples had the same doxorubicin concentration, as evident by the absorbanceat 490nm, and the varying amount of Cy5 are represented by the different levels of absorbance at 650nm. There is some backgorund absorbance in the 650nm range from the doxorubicin. B) Calibration curve to convert the Cy5 fluorescence of liposome samples collected from the HPLC run into the concentration of Cy5, which is the concentraion of ACPP. C) Sample data table that can be generated from the HPLC-size exclusion-dynamic light scattering procss. Dynamic light scattering provides the particle radius and the particle density. The doxorubicin concentration is known prior to analysis and can be used to calculate the doxorubicin loading. The Cy5 concentration of each sample is determined using the calibration curve and is used to calculate the # ACPPs/particle.

5.4.7. Liposomes targeted with the second synthesis of ACPP-lipid were not able to reproduce previous results

Primary tumor and lung metastases experiments were repeated with the PyMT 230 model using the new lipid-ACPP with both clinical Doxil and and well-characterized home made liposomes. With the clinical Doxil, there was no reduction in average tumor volume with ACPP targeting (Figure 5.10 A). The 0.1% cleavable ACPP had a higher average tumor volume for the duration of the experiment, and the 0.3% MMP cleavable, No ACPP and 0.1% mpeg performed the best with almost identical tumor growth curves. It is important to note that the new lipid-ACPP caused the Doxil to form large aggregates upon heating and could incorporate into the liposome at room temperature. This was not observed with the first peptide, which required heating for incorporation and never led to issues with solubility.

Liposomes were then synthesized de novo with the new lipid ACPP and tested in both the primary tumor and metastasis model with the PyMT 230 cell line. Again, there was no significant difference in the tumor growth curves for the various liposome formulations (Figure 5.10 B). Finally, the experimental lung met experiment was repeated with the inclusion of the negative control peptide (Figure 5.10 C). With this experiment the mice were dosed with drugs on days 30 and 37 post tumor cell injection and the lungs were harvested on day 42. There was an error in the timing of this experiment and the mice were sacrificed 10 days earlier than in the first experiment, which could explain why the overall tumor burden in this cohort of lungs was relatively low. Liposome therapy was able to reduce the amount lug metastases when compared to

the vehicle group, but again there was no observable difference between targeted and untargeted drug. There is the possibility that the treatment groups could have stratified if given the proper time to grow.
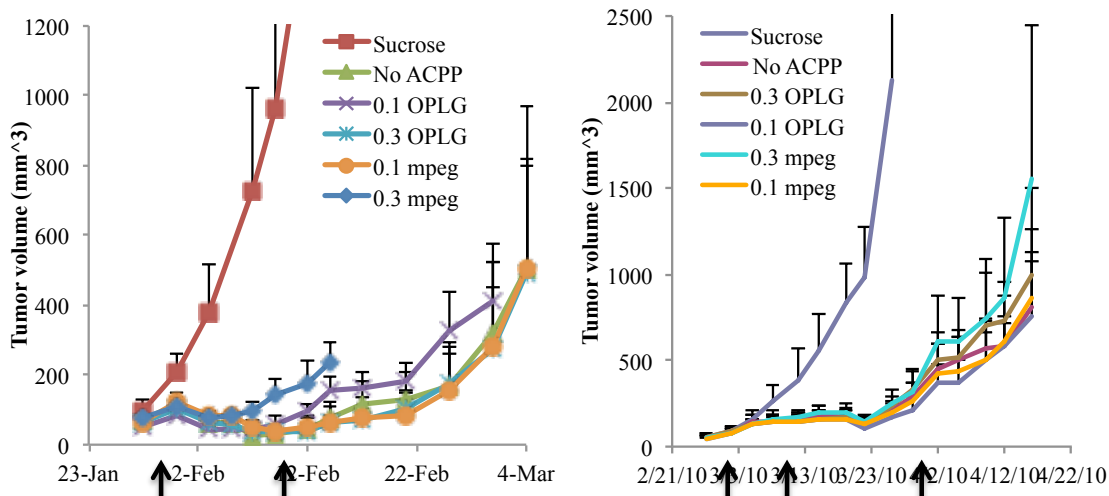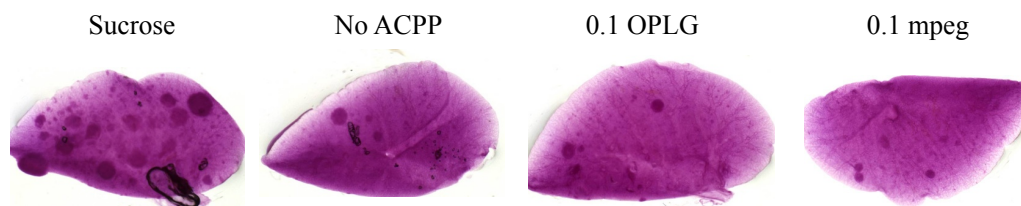
Figure 5.10 Failure to replicate previous experimental results with new lipid-ACPP conjugate in PyMT 230 breast cancer models. For each of these panels the second synthesis of the lipid ACPP was used. A) Doxil targeting was accomplished by incubating the DSPE-peg(2000)-ACPP with the liposome formulation at room temperature for 1 hour prior to animal injections. Mice harboring PyMT 230 syngeneic breast tumors were injected with various forms of Doxil at 3mg/kg equivalents of doxorubicin as indicated by the black arrows. Tumor volumes were monitored at regular intervals. B) Homemade doxorubicin liposomes were injected into mice with PyMT 230 tumors as indicated by the black arrows. C) Mice were injected intravenously with 5x10^5 PyMT 230 cells and the cancer cells were alllowed to seed in the lungs. Doxorubicin liposomes were administered on days 30 and 37 post tumor cell injections and the mice were sacrificed on day 43. Lungs were harvested, fixed with paraformaldehyde and stained with carmine. Representative images for mice from each of the treatment groups are shown.

5.4.8. Summary of all in vivo experiments using ACPP targeted liposomes

Presented in this section is a table summarizing all of the therapy experiments performed with ACPP targeted liposomes. The abbreviations in the table include the following, BSB: Basic Sciences Building, TA-pep: first lipid-ACPP synthesized by Dr. Aguilera, ES-pep: second lipid-ACPP synthesized by Dr. Savariar, Agg: aggregated, cl: MMP cleavable ACPP, uncl: mpeg uncleavable ACPP, SQ: subcutaneous tumor cell injections, Mets: experimental metastasis model, inj: injections.

Table 5.1 Summary of all the *in vivo* experiments with ACPP targeted doxorubicin liposomes

Exp date/ locations	Peptide syntheis/ preparation	Route/ Cell line	Dose/ # inj	ACPP/Lipo	Results	Figure reference
3/2009; Stein	TA-pep; home lipos	SQ HT1080s	3mg/kg, 1 inj		0.3%<1%<No ACPP	TA thesis
4/2009; Explora	Ta-pep; home lipos; agregated inj 1	SQ HT1080s	3mg/kg, 2 inj		Agg ACPPs worse, 2nd inject 0.3% best	TA thesis
4/2009; Stein	TA-pep; home lipo; Agg vs no	SQ HT1080s	3mg/kg, 1inj		0.3% NoAgg<No ACPP< 0.3% Agg	TA thesis
6/2009; Explora	TA-pep; home lipo; 0.3 & 0.1% w mpeg	SQ HT1080s	3mg/kg, 2 inj		0.1% Cl<0.3% Cl< 0.1% uncl< 0.3% uncl < No ACPP	Figure 5.2 A and B
9/2009; BSB	TA-pep, home lipos	Mets 230s	3mg/kg, 2 inj		0.1% cl < No ACPP < NT, % lung area mets sig	Figure 5.3
9/2009 stein	TA-pep; Doxil	SQ HT1080s	3mg/kg, 1 inj		0.3 cl < No ACPP = 0.1 cl, sig 0.3 vs no, some died may miss rep data	Figure 5.4
7/2009; Explora	TA-pep; home lipo; lower than 0.1%	SQ HT1080s	3mg/kg, 2 inj	0.1 cl= 4.2, 0.03 cl=1.4	No ACPP< 0.03 cl< 0.1 cl= 0.01cl	Figure 5.5 A
10/2009; Explora	TA-pep; home lips	SQ HT1080s	3mg/kg, 1 inj	0.01 cl= 1, 0.03 cl 2.4, 0.1cl =6.7, 0.3 cl =39	0.1uncl< 0.3 cl< 0.1cl < 0.03cl< 0.01 cl < No ACPP	Figure 5.5 B
9/2009; BSB	TA-pep; home lipos; 0.1 cl and uncl	SQ 4T1.2	3mg/kg, 2inj		No ACPP= 0.1cl<0.1 uncl, all similar and small	Figure 5.6 A
9/2009; BSB	TA-pep; home lipos; 0.1 cl and 0.3 cl	Mets 4T1.2	3mg/kg, 2inj		0.3 cl< 0.1cl< No ACPP, not sig but trend	Figure 5.6 B
9/2009; BSB	TA-pep; home lipos; 0.3 and 0.1%	SQ 8119s	3mg/kg, 2inj		All about the same, 8119 cells not sensitive to liposomes	Figure 5.6 C
9/2009; BSB	TA-pep; home lipos	SQ 230s	3mg/kg, 2 inj	0.1%=19; 0.3%=38; 0.1% uncl 8.2	0.3% cl<0.1cl = 0.1 uncl < No ACPP, tumors grew slow, sig difference 0.3 to No ACPP.	Figure 5.6 D
10/2009; BSB	TA-pep, Doxil	SQ 230s	3mg/kg, 2 inj	0.1 cl=7; 0.3 cl =21 ; 0.1 uncl =7	0.3cl= 0.1 uncl < 0.1 cl = No ACPP	Figure 5.6 E
1/2010; stein	Elam-pep; Doxil	SQ HT1080s	3mg/kg, 2 inj		0.3 cl< doxil < 0.1 cl	Figure 5.8 A
2/2010; BSB	Elam-pep; home lipo	SQ 230s	3mg/kg, 3 inj	0.1 cl =25, 0.3 cl 93, 0.1 uncl = 52, 0.3 uncl= 110	0.1 cl =No ACPP = 0.1 uncl, 0.3 cl < 0.3 uncl	Figure 5.8 B
4/2010, BSB	Elam-pep; home lipo	Met 230s	3mg/kg, 2 inj	0.1 cl =25, 0.3 cl 93, 0.1 uncl = 52, 0.3 uncl= 110	No obvious difference	Figure 5.8 C

5.5. Discussion

Using ACPPs to target therapeutic nanoparticles is a challenging goal, one that was met with mixed success. The addition of ACPPs to the surface of doxorubicin liposomes was able to enhance cellular uptake in culture in an enzyme dependent manner. Also, many of the *in vivo* experiments had promising results, demonstrating that ACPPs could enhance therapeutic efficacy. As experiments began to fail, quality control analysis did uncover that the lipid-ACPP construct had begun to degrade. There were also distinct differences in the first and second syntheses of the lipid-ACPP in how they incorporated into Doxil and the extent that they integrated into the homemade liposomes. How much of negative data can be attributed to these variable is unknown.

During this process a lot of knowledge was gained that can be built upon to try and progress ACPPs on the therapeutic front. A rather surprising result was that a high molar percentages, >1%, there was a significant decrease in the ability of ACPPs to help reduce tumor volume over the untargeted drug. It easy to hypothesize that increasing the number of ACPPs would lead to greater nonspecific uptake in organs such as the liver, thus accelerating clearance and limiting the plasma half-life. Experiments were performed using Calcein liposomes with up to 3% ACPP and no differences in the blood clearance were detected (data not shown). It was also demonstrated in many experiments that the 0.3% ACPP liposomes performed better than the 0.1%, meaning that lower numbers are not always better. From this we can reason that there must be a "sweet spot" with the number of peptides attached and it will be important in future studies to determine what the optimal count for targeting molecules is. Because of this, a protocol was developed to accurately determine ACPP incorporation. While the same amount of

lipid-ACPP was added during liposome synthesis, the number of ACPPs that coated the liposome surface varied from one synthesis to another. While these variations were never more than two fold, experimental results demonstrated that even those subtle differences could have a large impact on drug performance.

One potential drawback to using doxorubicin liposomes is that the particle size is large. Doxil is around 100nm in diameter and the synthesized liposomes were between 120-130nm. There have been claims that with particles of this size targeted probes do not accumulate in grafted tumors to any greater extent than untargeted ones (Goren, Horowitz et al. 1996). However, certain groups have demonstrated that their targeting mechanism enhanced therapeutic effect (Kirpotin, Drummond et al. 2006; Bartlett, Su et al. 2007) and the attachment of ACPPs to liposomes led to a 33% increase in the levels of doxorubicin in the tumor. There is also the possibility that while the absolute level of drug may not increase much due to our peptides, the CPP will facilitate retention of the particle in the tumor tissue as well as uptake into the cancer cells and surrounding stromal cells. And an increase in subcellular doxorubicin concentration should result in enhanced efficacy.

An immense amount of effort was put into targeting doxorubicin liposomes and due to of the lack of reproducible results, this project will probably never be published outside of this dissertation. When moving forward with targeted therapeutics, there are many variables that can be modified in order to find the optimal configuration. The main one to focus on is a reduction in particle size. Liposomes are known to have efficient "passive" targeting for tumors because of the leaking vasculature and lack of sufficient lymphatic drainage known as the enhanced permeability and retention (EPR) effect

(Matsumura and Maeda 1986; Maeda, Wu et al. 2000; Greish 2007). The optimal particle

size for accumulation due to EPR is less than 200nm (Hobbs, Monsky et al. 1998;

Moghimi, Hunter et al. 2001) and greater than 70nm (Litzinger, Buiting et al. 1994). The

liposomes in this study were within this size range, and it could be the effectiveness of

EPR that led to the lack of differences between the treatment groups in some of the

studies performed. Furthermore, in many pathological situations, such as the formation of

micrometastases, the vascular endothelium remains unaffected and there is no

opportunity to take advantage of EPR. To validate a targeting mechanism it may be better

to work in a model where EPR is not so prevalent or with particle sizes that are no so

amenable to it. Other options to consider would be to add additional targeting moieties,

similar to the data presented in Chapter 4, or to change the drug in the core of the

liposome, similar to the nanogels introduced by Dr. David Cheresh's lab (Murphy, Majeti

et al. 2011)

5.6. Acknowledgments

The dissertation author would like to thank:

Dr.Todd Aguilera for his pioneering of ACPP targeted therapeutic studies. There

was near equal contribution with Dr. Aguilera and the dissertation author in the early

studies presented in this chapter. The dissertation author continued on with liposome

testing after Dr. Aguilera defended his thesis and left the lab. Dr. Lelsey Ellies for

providing the PyMT 230 and PyMT 8119 cell lines as well as performing a majority of

the tumor cell injections with those models. Kevin Kao for tumor measurements and for

histological analysis with the lung metastases. Dr. Elamprakash Savariar for synthesis of

lipid-ACPP constructs as well as helping to generate the QC protocol and performing the

dynamic light scattering analysis. Perla Arcaira for maintenance of cell lines and animal husbandry. And finally, Dr. Stephen Howell for providing the means for us to procure extra Doxil from the patient clinic at Moore's Cancer Center.

CHAPTER 6: Parallel *in Vivo* and *in Vitro* Selection Using Phage Display Identifies Protease-dependent Tumor-targeting Peptides

Parallel *in Vivo* and *in Vitro* Selection Using Phage Display Identifies Protease-dependent Tumor-targeting Peptides*[S]

Mike Whitney‡, Jessica L. Crisp§, Emilia S. Olson‡¶, Todd A. Aguilera‡¶, Larry A. Gross‡‖, Lesley G. Ellies**, and Roger Y. Tsien‡§‖[1]

From the Departments of ‡Pharmacology, §Chemistry and Biochemistry, and **Pathology, the ‖Howard Hughes Medical Institute, and the ¶Medical Scientist Training Program, University of California at San Diego, La Jolla, California 92093

We recently developed activatable cell-penetrating peptides (ACPPs) that target contrast agents to *in vivo* sites of matrix metalloproteinase activity, such as tumors. Here we use parallel *in vivo* and *in vitro* selection with phage display to identify novel tumor-homing ACPPs with no bias for primary sequence or target protease. Specifically, phage displaying a library of ACPPs were either injected into tumor-bearing mice, followed by isolation of cleaved phage from dissected tumor, or isolated based on selective cleavage by extracts of tumor *versus* normal tissue. Selected sequences were synthesized as fluorescently labeled peptides, and tumor-specific cleavage was confirmed by digestion with tissue extracts. The most efficiently cleaved peptide contained the substrate sequence RLQLKL and labeled tumors and metastases from several cancer models with up to 5-fold contrast. This uniquely identified ACPP was not cleaved by matrix metalloproteinases or various coagulation factors but was efficiently cleaved by plasmin and elastases, both of which have been shown to be aberrantly overexpressed in tumors. The identification of an ACPP that targets tumor expressed proteases without rational design highlights the value of unbiased selection schemes for the development of potential therapeutic agents.

Molecular targeting of contrast and therapeutic agents to tumors is a fundamental goal of cancer research and treatment. Targeting based on tumor-specific molecules has largely relied on binding of antibodies, peptides, or vitamins to antigens or receptors expressed at high levels on tumor cells or their associated vasculature. The drawback to such mechanisms is that they rely on stoichiometric binding that lacks amplification, so either the target must be very highly expressed, or the readout must be extremely sensitive. Activatable cell-penetrating peptides (ACPPs)[2] are a new strategy in which enzymatic amplification drives *in vivo* accumulation of peptide-conjugated cargo within tissues containing active extracellular proteases (1–6). An ACPP consists of three domains: a polycationic cell-penetrating peptide (7–9), a cleavable linker, and a polyanionic inhibitory domain. Before cleavage of the linker, the polyanion pairs with the polycation and prevents cell adhesion and internalization; after cleavage, the polyanion dissociates, unleashing the cell-penetrating peptide to adhere immediately to adjacent cells, followed by cellular internalization. The first ACPPs were designed to be activated by matrix metalloproteinases (MMPs), which are frequently up-regulated in tumors and play a crucial role in extracellular matrix degradation, tissue invasion, and metastasis (10–15). Although an MMP-activated ACPP has been shown to effectively target tumors *in vivo*, this rational design of an ACPP is limited by the availability of known protease substrates and the tissue specific expression of the target protease. For instance, there is currently no known peptide substrate that is perfectly selective for MMPs, and no MMP is exclusively expressed in tumors. Therefore, to improve the applicability of ACPPs, it is important to explore other classes of proteases and substrates with methods that might provide greater specificity and flexibility than *a priori* design.

Previously, phage display technology has been used extensively *in vitro* to identify peptides, proteins, and antibodies based on specific binding or catalytic activity (16–18). In addition, phage display has been used *in vivo* to identify linear or circularized peptides that stoichiometrically bind and accumulate in tumors, synovium, and vascular tissues (19, 20). In this report, we have used phage display to identify peptides that accumulate within tumors *in vivo* as a result of proteolytic modification. This method identifies novel protease substrates that are cleaved within tumors without bias for class of protease or specific substrate sequence. To examine the efficacy of this approach, we performed parallel *in vivo* and *in vitro* selections with phage displaying a library of unique ACPPs. For *in vivo* selection, phage were injected into tumor-bearing mice followed by isolation of cleaved phage from homogenized tumors. For *in vitro* selection, phage were sequentially exposed to normal *versus* tumor tissue extract, followed by isolation of uncleaved or cleaved phage, respectively. Phage selected ACPPs were resynthesized as fluorescently labeled peptides, injected into tumor-bearing mice, and shown to accumulate

within primary and metastatic tumors in a protease-dependent manner.

EXPERIMENTAL PROCEDURES

Phage Library Preparation and Selection—A phage library was generated by PCR, using 5′-primer ggccaagagctccatcatcat-catcatcatctc, 3′-primer ggccagactagtccgtcgccgtcgccgtcg, and oligonucleotide template ccatcatcatcatcatcatctcgaggaggaggag-gaggaggaggaggagnnknnknnknnknnknnkcggcgacggcgacggcga-cggcgacggactag, where n denotes any nucleotide and k indicates a mixture of g and t. PCR was performed for 25 cycles with 52 °C annealing and standard reaction conditions. PCR products were digested with restriction enzymes SpeI and SacI for directional cloning into pComb M13 phage expression vector (17). The phage library contained 5×10^6 primary transformants, which were converted to infectious phage using helper phage superinfection. Phage libraries were then titered by infection of XL1blu cells and plated on ampicillin plates. For *in vitro* selections, 10^9 phage were incubated for 3 h at 37 °C with mixed liver/kidney tissue extracts equivalent to 2% (2 mg of each tissue per 100 μl). Ni^{2+}-NTA-agarose (Qiagen) was added and incubated for 15 min, followed by three washes with PBS. The Ni^{2+}-NTA-agarose coupled to the uncleaved phage was then exposed to 2% tumor tissue extract at 37 °C for 3 h. Unbound cleaved phage were eluted from the Ni^{2+}-NTA with PBS and plated on XL1blue *E. coli* to recover phage. For *in vivo* selections, 10^9 phage in 100 μl of PBS were injected into the tail veins of 10–13-week-old transgenic mice that had 5–15-mm mammary tumors due to expression of PyMT driven by the long terminal repeat of mouse mammary tumor virus. Tumors were excised and homogenized in PBS in the presence of protease inhibitor containing 100 μM 4-(2-aminoethyl)-benzenesulfonyl fluoride-HCl, 80 nM aprotinin, 5 μM bestatin, 1.5 μM E-64, 2 μM leupeptin hemisulfate, and 1 μM pepstatin A (EMD Biosciences mixture III). Uncleaved phage were removed by absorption with Ni^{2+}-NTA-agarose, and cleaved phage from the supernatant were reamplified and reinjected into different PyMT tumor-bearing mice.

Peptide Synthesis and Fluorophore Labeling—Peptides were either obtained from the W. M. Keck Facility Small Scale Core (Yale University, New Haven, CT) or synthesized in our laboratory on a Perceptive Biosystems Pioneer automatic peptide synthesizer using standard protocols for Fmoc solid-phase synthesis. All peptides were of the general format N terminus-(D-glutamyl)$_9$-(6-aminohexanoyl)-(6-amino acid cleavage site)-(D-argininyl)$_9$-(either Cy5-D-cysteinamide or ϵ-(fluorescein-5(6)-carbonyl)-L-lysinamide) (see supplemental Fig. 1 for complete details). Carboxyfluorescein-labeled peptides were generated by Fmoc synthesis with Lys-5(6)-carboxyfluorescein and were acetylated at the N terminus. Albumin-reactive peptide, Mal-e$_9$-ahx-RLQLK(Ac)L-r$_9$-c(Cy5)-NH$_2$, was generated by reacting 3-maleimidopropionic acid pentafluorophenyl ester (Molecular Biosciences) with the free N terminus of Cy5-labeled peptide (see supplemental Fig. 1 for detailed structures of all peptides). The negative control maleimide (Mal) peptide had -NH(CH$_2$CH$_2$O)$_2$CH$_2$CO-, an uncleavable (mpeg) linker (4), in place of the 6-aminohexanoyl and sub-

strate sequence. All Cy5-labeled peptides were purified to greater than 95% purity using C-18 reverse phase HPLC with a 20–50% acetonitrile gradient in 0.1% TFA and the mass was confirmed by mass spectrometry.

In Vitro Peptide Cleavage—Tissue extracts were generated by dissecting fresh tissue and gently homogenizing in PBS, while on ice, to minimize the release of intracellular proteases. Homogenates were then microcentrifuged at $14,000 \times g$ for 1 min, and supernatants were recovered and used for *in vitro* testing. All cystic fluids were aspirated with a 28-gauge syringe from surgically exposed mammary tumors of PyMT mice containing fluid filled nodules. *In vitro* cleavages were done with 5 μM peptide in 20 μl of PBS containing 1 μM ZnCl$_2$ plus 2 μl of 20% tissue extract (20 mg of tissue homogenate per 100 μl) or 2 μl of undiluted cystic fluid, followed by incubation at 37 °C. Aliquots were removed at time intervals from 20 min to 18 h with data being shown for the 2-h time point. For cleavage with purified enzymes, a 50 nM concentration of each enzyme was incubated with 5 μM peptide in the manufacturer's recommended buffer for 4 h. Enzymes and inhibitors were obtained from commercial sources in their active form (a complete table of enzymes and inhibitors is shown in supplemental Fig. 2). Tricine sample buffer was added, and treated peptides were boiled for 1 min prior to electrophoresis on 10–20% Tricine acrylamide gels (Invitrogen). Gels were quantitatively imaged on a UVP Biospectrum AC imaging system with external Biolite light source with excitation at 628 ± 20 nm and emission at >700 nm. Quantitation of enzyme cleavage was done using UVP Biospectrum software.

For mass spectrometry determination, each peptide was purified from homogenized cell extract by two steps of reverse phase HPLC. A 30-μl sample of 5 μM ACPP digested with tissue extract for 2 h was diluted to 2.5 ml with solvent A, which contained 2% acetonitrile and 0.14% trifluoroacetic acid. Samples were immediately injected into a Dionex BioLC HPLC system. The autosampler (Gilson model 231) had a 2-ml sample loop, so two 1-ml injections were used for each HPLC chromatogram. The column was a protein C4 from Vydac with a 4.6-mm inner diameter and 25-cm length. The column temperature was 35 °C, and the flow rate was 0.8 ml/min. After an 11-min delay (12% solvent B) for the injections, the gradient was from 12 to 56% solvent B (90% acetonitrile, 0.08% trifluoroacetic acid) in 11 min, followed by a 3-min step of 80% B. The peak eluted at 20 min. Detection was by fluorescence (Dionex RF2000 fluorescence detector, excitation at 640 nm, and emission at 680 nm), and the peak was collected with a Gilson FC203 fraction collector.

For the second step of reverse phase HPLC, the fraction was reconcentrated to 200 μl by centrifuge evaporation (Savant SpeedVac) and then diluted to 600 μl with solvent A again. A Michrom Magic HPLC system was used for liquid chromatography-mass spectrometry, and the column output was detected by a Jasco 920 fluorescence detector and an LTQ Orbitrap XL mass spectrometer. A Michrom sample loop microtrap was used to preconcentrate the entire 600-μl sample for injection. The column was a 1-mm inner diame-

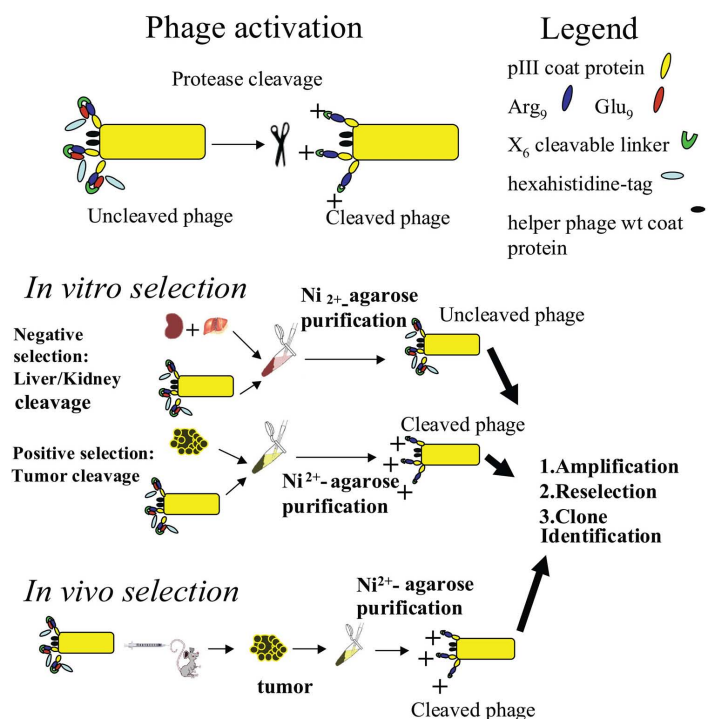*Identification of Protease-dependent Tumor-targeting Peptides*

FIGURE 1. **Parallel *in vivo* and *in vitro* selection with phage display identifies cleavage sequences for protease-dependent tumor targeting.** *In vitro*, an M13 phage was generated with a diverse population of ACPPs (5×10^6) presented on the surface of the phage Selection was initiated with 10^9 phage, as determined by the number of colony-forming units after superinfection with helper phage and plating on 100 μg/ml ampicillin plates. All secondary *in vitro* selection was initiated by incubating 10^9 with 2% liver/kidney tissue extracts at 37 °C for 3 h. Uncleaved phage selected for resistance to liver/kidney cleavage and therefore less likely to be efficiently cleaved in that tissue were then purified by presence of their hexahistidine tag and exposed to tumor tissue extract for 3 h. Cleaved phage in which the hexahistidine tags were removed by protease cleavage were then collected and reamplified prior to additional selection cycles. Because each phage may have more than one ACPP and associated hexahistidine tag, every ACPP must be cleaved to provide enrichment after purification. Representative phage were sequenced after each round of selection. *In vivo*, phage (10^9 in 100 μl of PBS) were injected into PyMT tumor-bearing mice. After 5 h, mice were sacrificed, and tumors were removed and homogenized to recover phage within the tumor tissue. Phage that had lost their hexahistidine tags due to cleavage within the tumor cells were purified away from uncleaved phage that might be contained in circulating blood at the time of collection. Selected phage were reamplified and iteratively selected in another tumor-bearing mouse, with at least 10^8 phage being used for each additional round of selection.

ter, 15-cm Michrom C18AQ, and the fluorescence detector settings were similar to those in the first step. The solvents, column temperature, and gradient were also similar, and the flow rate was 80 μl/min. The MS was set for ~0.5-s scans with the high resolution Orbitrap from 400 to 2000 *m/z*. The entire column output went into the mass spectrometer without splitting, using the electrospray interface.

In Vivo Testing of Peptides—For each tumor model, Cy5-labeled peptide was injected intravenously via the tail vein. Mice were imaged at time intervals up to 6 h using a Maestro imager (CRI Inc.) with excitation at 640 ± 24 nm, emission at >700 nm. For *in vivo* testing, we used either PyMT mice with spontaneous progressive mammary tumors or nude mice

with 5–7-mm MDA-MB-435 clone M4A4 (gift of D. Tarin, UCSD) xenograft tumors generated by subcutaneous injection of 10^6 tumor cells into the mammary fat pads (mice 5–8 weeks of age; Charles Rivers Laboratories). Animals were anesthetized with a 1:1 mixture of 80 mg/kg ketamine and 5 mg/kg midazolam, weighed, and injected with 100 μl of 100 μM free peptides or 100 μl of 30 μM albumin-reactive peptide. After imaging, the animals were euthanized with isoflurane, and tissues were harvested and weighed for standardized uptake values (SUVs). To measure SUVs, 30 mg of each tissue was added to 100 μl of Tris buffer (pH 7.6) with 1% SDS. The tissue was homogenized, heated to 85 °C for 10 min, microwaved for 10 s, centrifuged at 20,500 $\times$ *g* for 15 min, and imaged on the Maestro imager. Four sets of tissue-specific standards (tumor, liver, kidney, and muscle from non-injected animals, added to known amounts of ACPP and processed as above) were used to calibrate fluorescence intensity in terms of peptide concentration. Tissue-specific standards were necessary because different tissues vary in their ability to quench or conceal Cy5 fluorescence. From this calibration, the quantity of peptide in 30 mg of tissue for each organ was calculated. SUVs were calculated as the molality of peptide in the tissue divided by the total injected dose as mol/kg of body weight. In previous experiments with the MMP-cleavable ACPP, SUVs determined using this method were similar to SUVs determined using technetium chelates (1, 4–6, 21). Means are given ± S.D.; statistical significance of differences was determined by two-tailed *t* tests.

To generate mice with lung metastases, 5×10^5 4T1 tumor cells (ATCC) were injected into the tail veins of BALB/c mice 8 days prior to injection with imaging agent. Lungs were removed and imaged either 6 or 48 h postinjection, depending on the peptide construct. Average fluorescent intensity was determined for metastatic lung nodules and compared with adjacent non-malignant tissue or lungs from a tumor-bearing animal that had no lung metastases. We analyzed nine selected regions of 80–200 pixels of each type of tissue, and all tissues were imaged using identical parameters.

RESULTS

In order to generate a phage library displaying ACPPs, amino acid sequences of the format $Met-His_6-E_9-X_6-R_9$ (where X_6 represents 6 randomized amino acids) were fused to the N terminus (0–4 copies per phage) of a truncated form of the M13 phage gIII coat protein (17, 22). This library contained 5×10^6 putative protease cleavage sites as determined by primary colony-forming units after helper phage infection and dispersal on plates containing antibiotics. This represents about 8% of the potential diversity of 6.4×10^7 for X_6. The X_6 region of the library was generated using NNK(G/T) degenerate oligonucleotides. A hexahistidine motif was added at the N terminus to allow separation by immobilized metal affinity chromatography of unmodified phage from phage whose peptides had been cleaved releasing the hexahistidine tag.

In vivo selections were performed by injecting a library of phage displaying recombinant ACPPs intravenously into PyMT mice (Fig. 1). This transgenic breast cancer model produces spontaneous heterogeneous tumors, which can be cystic and will progress to metastasis in older animals (23–25). Six hours after injection, animals were sacrificed, and their tumors were dissected out and homogenized in the presence of protease inhibitors to prevent secondary cleavage of contained phage. Uncleaved phage in the tumor vasculature or nonspecifically localized to tumor at the time of dissection were removed by absorption with Ni^{2+}-NTA-conjugated agarose. This purification step was necessary because, as previously reported, phage particles can be retained for long periods in tissues even in the absence of any selection (26). Purified phage that had been cleaved within the mouse were reamplified and injected into different PyMT tumor-bearing mice. This selection was continued for seven iterative cycles with 10–15 individual phage clones being sampled by DNA isolation and sequencing after each round of selection. Five sequences, RLQLKL, RTRYED, RIPLEM, QFDEPR, and TSAVRT, were each isolated multiple times during the *in vivo* selection (Table 1).

For *in vitro* selection, the ACPP phage library was pre-exposed to extracts of liver and kidney, tissues that typically have high nonspecific uptake of drugs and imaging agent, to allow cleavage by proteases contained within these extracts. Ni^{2+}-agarose was then used to isolate uncleaved phage that had retained their hexahistidine tags. These preselected phage were then exposed to PyMT tumor extracts and selected for peptide cleavage and loss of their hexahistidine tags. Isolated phage were reamplified and subjected to six additional rounds of both negative (no liver/kidney cleavage) and positive (tumor cleavage) selection, with representative phage being isolated and sequenced after each round. This *in vitro* selection identified five sequences isolated in the *in vivo* selection scheme as well 15 additional sequences (Table 1). Only one sequence, RLQLKL, was identified in duplicate in both the *in vivo* and *in vitro* selection schemes.

To test if isolated peptides corresponding to the phage-selected sequence could be proteolytically cleaved by tumor tissue extracts, 14 of the 21 selected phage sequences were syn-

TABLE 1

Phage sequences identified by *in vivo* or *in vitro* selection and cleavage of derived peptides by PyMT tumor tissue extracts

All phage sequences that were identified in at least duplicate from either the *in vivo* or *in vitro* selection are listed. No duplicate phage were identified in either screen prior to the third round of selection. Crude peptides of the format acetyl-e_9-ahx-X_6-r_9-(L-lysine 5(6)-carboxyfluorescein) were synthesized for all phage sequences that were identified three or more times independently. Peptides with internal cysteine residues were excluded because dimerization in protease digest buffer complicated analysis. The percentage of cleavage of crude peptides was determined by digesting 5 μM synthetic peptides with 2% tumor tissue extracts (1 mg of gently homogenized tissue in 50 μl of PBS with 1 mM $ZnCl_2$). Quantitation of peptide cleavage was done using gel electrophoresis after a 16-h digestion at 37 °C. The percentage of cleaved *versus* uncleaved peptide was determined using UVP imaging software. Four peptides with 6-amino acid cleavage sequences RLQLKL, RTRYED, GMMYRS, and RWRTNF were cleaved >90% after the 16-h digest. These four peptides were therefore prioritized for further study, which included resynthesis and labeling with a longer wavelength Cy5 fluorophore to facilitate *in vivo* testing. NT, not tested.

Cleavage site (X_6)	*In vivo* number isolated	*in vitro* number isolated	Cleavage of e_9-X_6-r_9 peptide by tumor extract
			%
RLQLKL	2	11	>90
RTRYED	3		>90
RIPLEM	3		<10
QFDEPR	3		<10
TSAVRT	2		NT
GLWQGP		7	~20
QCTGRF	1	5	NT
LPGMMG		5	~20
DVGTTE		5	No cleavage
TDLGAM		5	No cleavage
GMMYRS		4	>90
DSNAES		4	No cleavage
ITDMAA	1	3	~20
RWRTNF		4	>90
WRPCES	1	2	NT
WRNTIA		3	~50
IDKQLE		3	<5
FMEIET		3	<5
HEVVAG		2	NT
GGHTRQ		2	NT
INGKVT		2	NT

thesized as peptides in the format acetyl-e_9-(ahx)-X_6-r_9-5(6)-carboxyfluorescein-labeled L-lysinamide using solid-phase synthesis (for complete structures, see supplemental Fig. 1). The (ahx) denotes 6-aminohexanoyl, a flexible linker that is included in ACPPs to give the cleavable X_6 domain the ability to adopt a more extended conformation within the protease cleavage domain. The polyglutamate and polyarginine segments consisted entirely of D-amino acids (denoted by lowercase letters) in order to maximize their resistance to proteolysis *in vivo*. Four peptides, containing X_6 = RLQLKL, RTRYED, GMMYRS, and RWRTNF, were cleaved >80% by tumor tissue extract after 16-h digestions at 37 °C (Table 1).

These top four peptides were resynthesized in the format H_2N-e_9-(ahx)-X_6-r_9-(Cy5-labeled D-cysteinamide), followed by purification to greater than 95% for *in vitro* and *in vivo* testing. Each of these peptides was tested for differential cleavage by tumor *versus* mixed liver/kidney tissue extracts after a 2-h digestion compared with the 16-h digestion shown in Table 1 (Fig. 2A). All four peptides were cleaved >50% by tumor tissue extract, with RLQLKL being the most rapidly cleaved, >90% after 4 h (full time course not shown). Each peptide except for GMMYRS showed increased cleavage by tumor extract relative to mixed liver/kidney extracts. A control peptide with all D-amino acids, X_6 = rlqlkl, was not cleaved by any of the tissue extracts.

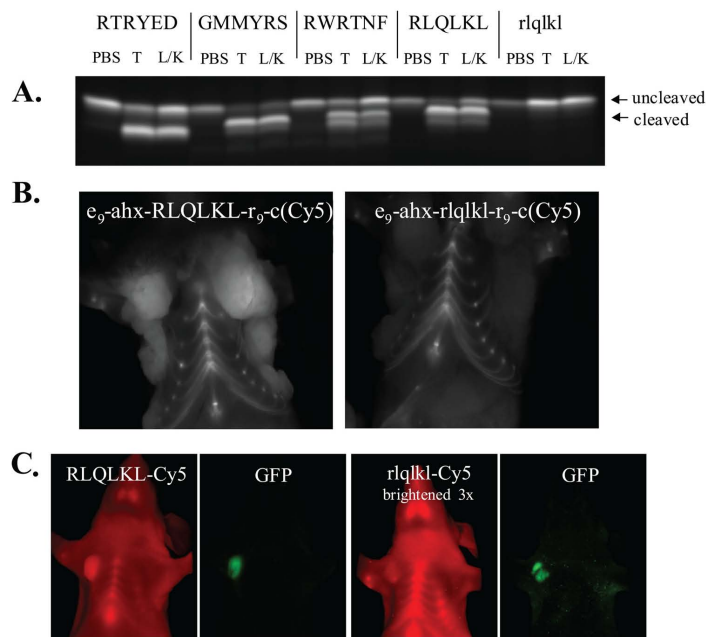*Identification of Protease-dependent Tumor-targeting Peptides*

FIGURE 2. *A, in vitro* characterization of five Cy5-labeled ACPPs containing RTRYED, GMMYRS, RWRTNF, RLQLKL, and rlqlkl at the protease cleavage site. Uppercase and lowercase letters denote L- and D-amino acids, respectively. For each reaction, 5 μM ACPP was incubated with either 2% tumor or 2% liver/kidney tissue extracts at 37 °C for 2 h (compared with 16 h; Table 1). Cleavage was detected by electrophoresis on 16% Tricine acrylamide gels. RLQLKL, RTRYED, and RWRTNF ACPPs were more efficiently cleaved by tumor extract *versus* liver/kidney extracts (see ratio of cleaved to uncleaved). Of these, RWRTNF showed the greatest differential cleavage by tumor *versus* liver/kidney extracts. As expected, the all-D-rlqlkl peptide showed no cleavage under any of the tested conditions. *B, in vivo* characterization of tumor uptake on mice injected with Cy5-labeled ACPPs. PyMT tumor-bearing mice were imaged 6 h after injection with 100 μl of a 100 μM concentration of either the protease-cleavable ACPP NH$_2$-e$_9$-(ahx)-RLQLKL-r$_9$-c-(Cy5)-NH$_2$ (*left*) or the uncleavable all D-amino acid control peptide NH$_2$-e$_9$-(ahx)-rlqlkl-r$_9$-c(Cy5)-NH$_2$. Images with skin removed are shown because they highlight the variability of the labeling throughout the tumor. Skin-off images also eliminate artifacts that sometime appear due to incomplete shaving of the animal or nicks that occur during shaving. Skin-on images are shown for comparison in supplemental Fig. 2. Tissues were removed post mortem for SUV determination. *C,* nude mice with MDA-MB-435 M4A4 xenografts expressing GFP were injected with either RLQLKL ACPP (*far left*) or control rlqlkl peptide (*middle right*), 100 μl of 100 μM in each case. The RLQLKL ACPP gave visible contrast in tumors that were confirmed by imaging GFP fluorescence. Mice injected with rlqlkl peptide showed no tumor contrast in the Cy5 channel (*middle right*), although the tumor was clearly visible by GFP (*far right*). All images were taken 6 h after injection, in live animals with skin on, using identical settings on the Maestro imager. Images for rlqlkl peptides were brightened 3-fold to illustrate the lack of contrast for tumor compared with surrounding tissue for the uncleavable control.

($n = 3$) with $p = 0.014$. The decreased tumor accumulation in the mice injected with the uncleavable D-amino acid probe of identical molecular weight and hydrophobicity strongly suggests that tumor uptake is dependent on protease susceptibility rather than nonspecific adhesion or enhanced vascular permeability of tumors. This ratio of 3 between protease-sensitive and relatively insensitive peptides compares with a ratio of 3.6 for our previous ACPP, in which X_6 = PLGLAG and targets matrix metalloproteinases (1). PLGLAG ACPP had SUV values of 0.51 ± 0.05 ($n = 5$) *versus* 0.14 ± 0.06 ($n = 5$), $p < 0.01$, for its D-amino acid control. As with all free peptide ACPPs, there is labeling of cartilaginous portions of the anterior ribcage (4, 5). One advantage of RLQLKL ACPP *versus* PLGLAG ACPP is that skin uptake was significantly less, improving contrast during noninvasive visualization in live animals (see supplemental Fig. 3 for images).

To explore whether RLQLKL ACPP could be used as a contrast agent for tumor models other than the PyMT mice, Cy5-labeled RLQLKL ACPP and its all-D-amino acid control were tested in mice bearing MDA-MB-435 M4A4 human xenografts. This tumor model (also known as M14 melanoma (27)) was stably transfected with GFP for unambiguous identification of xenograft *versus* host tissue. Tumors of mice injected with the RLQLKL ACPP showed far red (Cy5) fluorescence, which co-localized with the GFP fluorescence (Fig.

In order to compare *in vivo* tumor labeling, these four Cy5-labeled ACPPs were separately injected intravenously into PyMT mice with spontaneous mammary tumors. Six hours postinjection, mice were imaged by fluorescence to show contrast of tumor compared with adjacent normal tissue. The most striking visual contrast for tumor uptake was obtained from mice injected with the RLQLKL ACPP (Fig. 2B). Consistent with this high visual contrast, the SUVs in the tumor, defined as the molality of Cy5 in the specific tissue divided by the molality of the injected dose for the total weight of the animal, was the highest for the RLQLKL ACPP at 0.39 ± 0.14 ($n = 8$). This compared with the uncleavable all-D-amino acid peptide, rlqlkl ACPP, which had a SUV of 0.13 ± 0.03

2C). Mice injected with the uncleavable D-amino acid (rlqlkl) control showed much less Cy5 fluorescence within the tumors, which were still clearly visible by GFP fluorescence. Tumor SUVs 6 h after injection were also significantly higher for the RLQLKL ACPP 0.70 ± 0.27 ($n = 6$) compared with 0.34 ± 0.16 ($n = 6$) for rlqlkl control peptide ($p = 0.022$).

To characterize the protease activity responsible for tumor uptake, the effect of various protease inhibitors on tissue extract mediated cleavage of RLQLKL ACPP was tested. Unfortunately, cleavage of RLQLKL ACPP by crude tissue extracts is quite resistant to inhibition by protease inhibitors, which may be due to high protease activity in tissue extracts or the multiplicity of proteases released upon tissue disruption. We there-

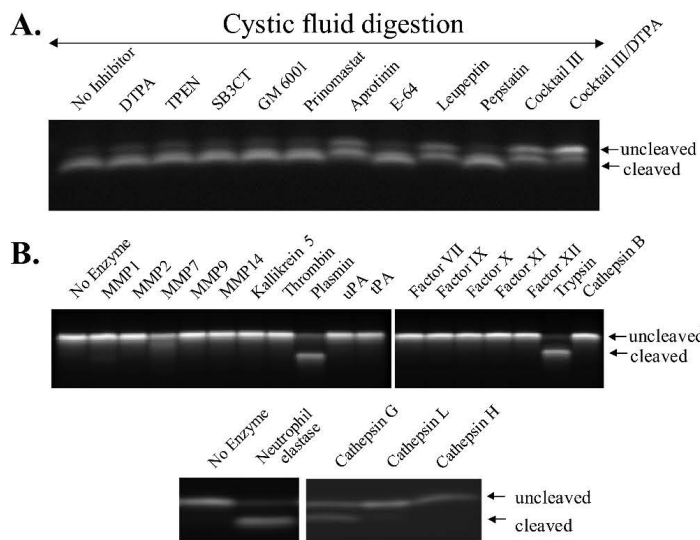**A.** Cystic fluid digestion

B.

FIGURE 3. **Effects of enzymes and inhibitors on cleavage of the RLQLKL ACPP *in vitro*.** *A*, cleavage of 5 μM Cy5-labeled RLQLKL ACPP for 2 h with 2% cystic fluid obtained from PyMT tumors, in the absence of inhibitor or with 5 mM Ca-DTPA, 50 μM TPEN, 18 μM SB3CT (43), 50 nM GM6001 (also tested at 1 μM and no inhibition; data not shown), 0.26 μM prinomastat, 150 nM aprotinin, 10 μM E-64, 100 μM leupeptin, 1 μM pepstatin A, Calbiochem mixture III (diluted 1:1000), mixture III + DTPA. All inhibitors were used at the manufacturers' recommended concentrations, which should inhibit $\geq$95% of the target enzymes' activity. *B*, cleavage of RLQLKL ACPP for 2 h with 50 nM MMP-1, MMP-2, MMP-7, MMP-9, MMP-14, kallikrein 5, thrombin, plasmin, urokinase plasminogen activator, tissue plasminogen activator, factor VIIa, factor IXa, factor Xa, factor XIa, factor XIIa, trypsin (cathepsins B, G, L, and H), and neutrophil elastase. The percentage of cleavage measured with UVP software was 93.0 $\pm$ 2.9% for trypsin, 79.0 $\pm$ 2.8% for neutrophil elastase, 77.9 $\pm$ 2.1% for plasmin, 60% $\pm$ 2.3% for cathepsin G, 23.4 $\pm$ 2.5% for MMP7, 9.7 $\pm$ 1.1% for MMP1, and less than 3% for all other enzymes tested, including hepsin, enterokinase, and prostate-specific antigen (supplemental Fig. 4). MMP-8, MMP-13, matriptase, urokinase, and legumain also showed no cleavage (data not shown). Trypsin and trypsin-2 cleavage of various ACPP are also shown in supplemental Fig. 4.

fore switched to cystic fluid obtained from fluid-filled nodules of PyMT tumors because this fluid probably contained proteases that had been secreted by adjacent tumor tissue and was less likely than tumor extracts to be contaminated with intracellular proteases. The use of similar tumor cystic fluids (although obtained from pancreatic and not mammary tumors) for cancer protease profiling has been reported elsewhere (28, 29). Cystic fluid cleaved RLQLKL ACPP similarly to tumor tissue extracts, and this cleavage was partially inhibited by two serine protease inhibitors, aprotinin and leupeptin (Fig. 3*A*). This inhibitor profile supported the involvement of a serine protease in the *in vivo* cleavage and tumor uptake of RLQLKL ACPP.

Cleavage of RLQLKL ACPP was further investigated using a panel of candidate proteases. The serine proteases plasmin, trypsin, and neutrophil elastase were the only enzymes found to efficiently cleave RLQLKL ACPP (Fig. 3*B* and supplemental Fig. 4). Each of these proteases has been reported to be up-regulated in cancers. There was also minimal cleavage of RLQLKL ACPP by cathepsin G, MMP-1, MMP-7, and MMP12, which at times was only visible upon gel overexposure. MMPs are not likely to be responsible for *in vivo* tumor uptake because they exhibit low cleavage rates.

Additionally, cleavage by cystic fluid was unaffected by MMP-specific inhibitors (GM6001, SB3CT, prinomastat) and Zn^{2+} chelators (DTPA and TPEN). Plasmin has been reported to be associated with tumor vasculature, and urokinase plasminogen activator is known to be preferentially activated in PyMT tumors (30–32). The plasmin-specific inhibitor serpin F2/α_2-antiplasmin, however, did not inhibit the protease activity of cystic fluid or tumor extract on RLQLKL ACPP, although it did inhibit plasmin cleavage, as expected (Fig. 4*A*). This result indicated that plasmin was probably not responsible for tumor extract cleavage or *in vivo* uptake of RLQLKL ACPP. Another candidate protease for *in vivo* cleavage of RLQLKL ACPP, trypsin, is normally produced by the pancreas as a zymogen (trypsinogen) and is later modified into its active form by enterokinase. Trypsin and trypsin-like protease expression has been reported in malignant non-pancreatic cells and has been shown to stimulate cancer cell growth in culture and in nude mice (33–36). However, trypsin cleavability correlated poorly with *in vivo* uptake because trypsin, unlike elastase, efficiently cleaved RTRYED and GMMYRS ACPPs, but these peptides showed little fluorescence contrast in tumors relative to adjacent normal tissue (data not shown). Elastase, a component of breast milk, has been reported to be expressed in breast cancer cell lines and has been implicated as a factor in both the prognosis and progression of breast cancer (37–39). Although this protein is expressed ubiquitously, high circulating levels of its natural inhibitor α_1-antitrypsin (up to 50 μM) prevent its activity in the bloodstream. We found that α_1-antitrypsin inhibited the protease activity of cystic fluid and was also the only inhibitor tested that significantly inhibited tumor extract-dependent cleavage of RLQLKL ACPP (Fig. 4*B*, *top*). This inhibition increased as the concentration of tumor extract was reduced from 2 to 0.25%. Additionally, both the highly related pancreatic form of elastase and leukocyte elastase (ELA-2 from a different source) effectively cleaved RLQLKL ACPP.

To further characterize the proteolytic cleavage and means of tumor uptake of RLQLKL ACPP, mass spectrometry was used to compare the proteolytic cleavage products produced by exposure to liver, kidney, and tumor extracts to those produced after cleavage by plasmin, trypsin, and elastase

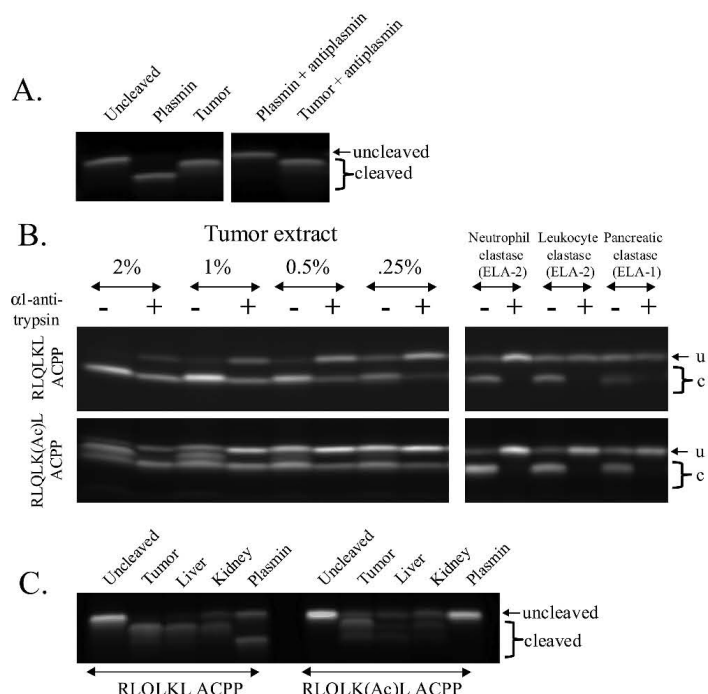*Identification of Protease-dependent Tumor-targeting Peptides*

FIGURE 4. *A*, cleavage of 5 μM Cy5-labeled RLQLKL ACPP by plasmin and tumor extract with and without plasmin-specific inhibitor F2/α2-antiplasmin. *B*, cleavage of 5 μM Cy5-labeled RLQLKL or RLQLK(Ac)L ACPP with varied amounts of tumor extract (2.0 to 0.25%), neutrophil/leukocyte elastase (ELA-2, two sources) or pancreatic elastase (ELA-1) in the presence or absence of 60 μM α1-antitrypsin. *C*, comparison of RLQLK(Ac)L ACPP with parent RLQLKL ACPP. For each reaction, 5 μM purified Cy5-labeled peptide was incubated with either 2% tumor, 2% liver, or 2% kidney tissue extracts or 50 nM plasmin at 37 °C for 2 h. Cleavage was detected by electrophoresis on 16% Tricine acrylamide gels.

KLr$_9$c-(Cy5), supporting elastases as a good target enzyme for *in vivo* tumor uptake of RLQLKL ACPP.

To improve tumor-selective cleavage of RLQLKL ACPP, a modified version was generated in which the ϵ-amino group of lysine was acetylated. We hypothesized that because lysine is the site of cleavage by liver extracts and the non-target enzymes trypsin and plasmin, acetylation at this residue should increase tumor selectivity by reducing off-target cleavage. Indeed, this new RLQLK(Ac)L ACPP was not cleaved by plasmin, although it was efficiently cleaved by tumor extracts (Fig. 4C). As predicted, cleavage of this acetylated ACPP by liver and kidney tissue extracts was also significantly reduced compared with the parent RLQLKL ACPP, thereby further enhancing selectivity for tumor cleavage. Interestingly, tumor extract cleavage of RLQLK(Ac)L ACPP produced two bands by electrophoresis gel analysis (Fig. 4B, *bottom*). The generation of one of these bands upon digestion with tumor extract could be efficiently inhibited by the addition of α_1-antitrypsin, whereas production of a lower molecular weight cleavage product showed little or no inhibition. This further supported elastase as a target enzyme but highlights the presence of at least one additional protease within tumor extracts that can cleave and potentially enhance tumor uptake of RLQLK(Ac)L ACPP. The presence of neutrophil elastase within PyMT tumor extracts was confirmed by Western blot analysis (supplemental Fig. 6). Mass spectrometry was used to analyze cleavage products produced by tumor extract in the presence and absence of α_1-antitrypsin, but variability between tumor extract preparations, incomplete inhibition, and heterogeneity of cleavage products prevented the identification of a specific cleavage product that was inhibited by α_1-antitrypsin. We were, however, able to confirm that as with RLQLKL ACPP, cleavage of RLQLK(Ac)L ACPP by tumor extracts or elastases produced the same major product, K(Ac)Lr9c-(Cy5) (supplemental Fig. 5).

To test *in vivo* uptake, Cy5-labeled RLQLK(Ac)L ACPP was injected into PyMT tumor-bearing mice. This optimized ACPP was taken up in tumors to levels equal to or slightly greater than the unmodified parent RLQLKL ACPP (SUV = 0.39 ± 0.14 (n = 8) for RLQLKL and 0.48 ± 0.04 (n = 3) for RLQLK(Ac)L, p = 0.33), supporting the hypothesis that elastase but not plasmin could be responsible for tumor uptake in the PyMT model

(supplemental Fig. 5). The cleavage products produced by tissue extract cleavage are inherently variable, depending on time of digest, batch, and concentration of tissue extract. However, it was determined that cleavage of RLQLKL ACPP by either kidney or tumor extracts produced in differing ratios three detectable cleavage products, corresponding to (LKLr$_9$c-(Cy5), KLr$_9$c-(Cy5), and Lr$_9$c-(Cy5)). KLr$_9$c-(Cy5) was the most abundant cleavage product after treatment with tumor extracts, whereas each of the three cleavage products was represented about equally when cleaved by kidney. In contrast, cleavage by liver produced only one product Lr$_9$c-(Cy5), which suggests that liver cleavage was due to different endoproteases from kidney and tumor or alternatively that liver was much more efficient at removing leucine and/or lysine from either LKLr$_9$c-(Cy5) or KLr$_9$c-(Cy5). Digestion of RLQLKL ACPP with either plasmin or trypsin produced the single cleavage product Lr$_9$c-(Cy5), suggesting that these enzymes may be responsible for liver but not tumor cleavage. In contrast, like tumor extract, cleavage by either pancreatic or neutrophil elastase produced as their major product

A. Free peptide-skin off (6 hrs post injection)   Carrier attached peptide (48 hours post injection)
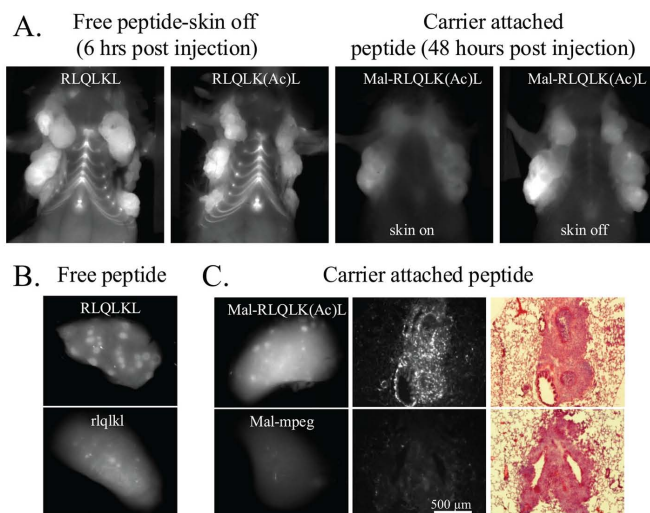

B. Free peptide   C. Carrier attached peptide

FIGURE 5. *A, in vivo* characterization of tumor uptake on mice injected with Cy5-labeled RLQLK(Ac)L ACPP and albumin-reactive Mal-e$_9$-(ahx)-RLQLK(Ac)L-r$_9$-c(Cy5)-NH$_2$ ACPP compared with parent RLQLKL ACPP. PyMT tumor-bearing mice were imaged 6 h after injection with 10 nmol of either H$_2$N-e$_9$-(ahx)-RLQLKL-r$_9$-c-(Cy5)-NH$_2$ (*left*) or H$_2$N-e$_9$-(ahx)-RLQLK(Ac)L-r$_9$-c-(Cy5)-NH$_2$ PyMT tumor-bearing mouse imaged 48 h after injection with 3 nmol of Mal-e$_9$-(ahx)-RLQLK(Ac)L-r$_9$-c(Cy5)-NH$_2$ (*right*) (complete structures diagrammed in supplemental Fig. 1). Skin-off images are shown for free peptide (*left*), and skin-off/skin-on images are shown for albumin-reactive peptide (*right*). Tissues were removed post mortem for SUV determination. *B*, detection of PyMT lung metastases and seeded lung tumors with various ACPPs. PyMT tumor mice were injected with free peptide RLQLKL ACPP. Lungs were removed and imaged 6 h postinjection. Lung metastases were seen as distinct fluorescent spots compared with adjacent tissue, within the lungs (*top*). Fluorescent spots were verified to be metastasis by hematoxylin/eosin staining (supplemental Fig. 4). Lungs from animals injected with uncleavable control rlqlkl ACPP show much less distinct fluorescent spots (*bottom*). Metastases were confirmed to be of similar size. *C*, lungs from mice that had been generated by seeding 4T1 tumor cells into lungs 10 days prior to injection of contrast agent. Mice were injected with either Mal-RLQLK(Ac)L ACPP (*top row*) or an uncleavable Mal-mpeg-ACPP (*bottom row*) and imaged. Lungs were then sectioned, and serial sections were either imaged for Cy5 fluorescence or used for hematoxylin/eosin staining. Bright fluorescence in the *top center* was from a single metastatic nodule.

(Fig. 5*A, top left*). In addition to improved specificity, acetylation of the RLQLKL ACPP simplifies attachment of dyes or other functional groups to the N-terminal amine of the peptide by blocking cross-reactivity to the lysine within the protease cleavage site.

To increase tumor-specific uptake relative to background tissues, RLQLK(Ac)L ACPP was additionally modified by conjugating a maleimide (Mal) group to the N-terminal amine, thereby generating an albumin-reactive peptide (40, 41). The rapid covalent attachment of this thiol-reactive peptide, Mal-RLQLK(Ac)L ACPP, to a cysteine on serum albumin increases the molecular size of the imaging agent, thereby increasing the blood circulation time while decreasing renal and synovial filtration. The albumin-reactive ACPP was injected into PyMT tumor-bearing mice and imaged 48 h postinjection before and after skin removal. Tumor to non-tumor contrast was 5.1-fold for the Mal-RLQLK(Ac)L ACPP, compared with less than 3-fold for free peptide RLQLK(Ac)L ACPP (Fig. 5*A*). SUVs were 2.3 ± 0.6 (*n* = 3) for the albumin-reactive ACPP compared with 0.48 ± 0.04 (*n* = 3) for free peptide RLQLK(Ac)L ACPP. Background labeling of cartilage and bone was also greatly

decreased, consistent with previously reported data for macromolecule-conjugated ACPPs (5).

In addition to identifying primary tumors, RLQLKL ACPP was used for the detection of lung metastases in PyMT mice. These spontaneous lung metastases (which occur sporadically in older animals) were clearly visible as bright fluorescent spots compared with adjacent normal lung tissue (Fig. 5*B, top*). These zones were confirmed as metastases by hematoxylin and eosin staining of paraffin-embedded sections (supplemental Fig. 6). Lungs from similar animals without metastases (also from animals with primary tumors) were uniformly dim (supplemental Fig. 6) and were 4.2-fold (*p* < 0.01) less bright than metastatic nodules on average. Nonmalignant tissue adjacent to metastases appeared brighter than tissue from lungs with no metastases, possibly because some of the fluorescence from metastases scattered into adjacent lung tissue or because some protease-secreting cells, protease, or cleaved peptide spread from the metastasis into the surrounding tissue. For comparison, the rlqlkl control peptide showed much reduced contrast compared with the RLQLKL ACPP (Fig. 5*B, bottom*). The small amount of contrast observed for metastasis from mice that had been injected with rlqlkl ACPP may be due to the differential cell density of lung metastasis *versus* normal lung tissue. Unfortunately, lung metastases were present in only a fraction of PyMT tumor-bearing mice, so data were obtained from only a few animals.

To further study the labeling of metastases by RLQLK(Ac)L ACPP, a new experimental lung metastasis model was generated by injecting 4T1 tumor cells intravenously and allowing them to seed in the lungs. Lungs from mice that had been injected with either Mal-RLQLK(Ac)L ACPP or uncleavable Mal-mpeg-ACPP were removed and imaged. Again, the cleavable probe highlighted fluorescent nodules, which were confirmed by hematoxylin and eosin staining to be metastases (Fig. 5*C, top row*). The uncleavable control showed little or no uptake in metastases (Fig. 5*C, bottom row*). Lung sections viewed at higher magnification showed that the fluorescence from the albumin-reactive cleavable ACPP was distributed throughout the metastatic nodules and originated from numerous 10–50-μm punctae, which could represent labeling of individual or small clusters of cells. These results conclusively demonstrated specific labeling of lung metastases with this newly identified elastase-cleavable ACPP.

Identification of Protease-dependent Tumor-targeting Peptides

DISCUSSION

Phage display identified the RLQLKL ACPP as a promising new tool that has the ability to detect protease activity in tumors and could be used to direct therapeutic or imaging agents to cancer cells *in vivo*. This selected ACPP was modified using a non-native amino acid, N^ϵ-acetyl-lysine, to further enhance its enzyme selectivity and specific tumor uptake. Modification of the lysine residue within the protease cleavage site facilitates attachment to a large molecular weight carrier, such as albumin. Further modification of our current best substrate RLQLK(Ac)L ACPP by genetic or synthetic iteration around the RLQLKL cleavage sequence (*e.g.* holding some residues constant while exhaustively varying the remainder) could provide additional optimization. *In vivo* properties could be further modulated by attachment to other high molecular weight carriers for improved pharmacokinetics or increased valency of the ACPP to enhance tissue specific uptake.

In addition, because this method identifies a specific ACPP cleavage sequence (in this case RLQLKL and the acetylated derivative), traditional biochemical techniques, including inhibitor and enzyme assays, extraction methods, or activity-based protease profiling (42), can be used to identify the target protease(s). We have used these techniques to characterize the cleavage of RLQLKL ACPP and demonstrate cleavage by multiple serine proteases. We then generated an improved, acetylated substrate that was still efficiently cleaved by tumor extracts and elastases but had reduced cleavage by liver and kidney and was not cleaved by plasmin. Based on this and other presented data showing expression of elastase in PyMT tumors and inhibition of protease activity in tumor extracts by α_1-antitrypsin and prior reports of elastase expression in breast cancers, we postulate that elastases are probably responsible for a major part of tumor uptake of RLQLKL ACPPs in PyMT tumors. Despite this claim, the identification of one specific protease that is responsible for 100% of cleavage and tumor uptake of any specific ACPP may not be possible because cleavage and tumor uptake probably results from a plurality of proteases present in the extracellular matrix of tumors. Additionally complicating the one enzyme-targeted mechanism is that peptide substrates and inhibitors that are exquisitely specific to a single protease remain a biochemical challenge. Interestingly, the identification of a protease substrate that is cleaved by multiple proteases could be expected based on the presented selection strategy that identified phage modified by extracellular enzymes expressed by tumors that probably contained more than one protease. Validation of this possibility for *in vivo* substrate cleavage by a multiplicity of proteases and utilizing this as a tool for synergistic multiprotease tumor targeting would represent a novel mechanism for targeting cancers and other tissues.

To highlight the technical improvements in the novel phage selection strategy presented here, it must be compared with prior *in vivo* phage selections. Previously published *in vivo* phage selection strategies relied almost entirely on tissue-specific binding, whereas the selection scheme presented here represents a novel use of phage display as an unbiased way to identify sites of *in vivo* enzymatic activity, in this case protease activity within tumors. Our strategy includes selection for covalent modification of the targeting sequence and not simply binding to the target tissue. Exclusive reliance on such tissue binding and localization for selection has the problem that phage particles have been shown to be nonspecifically retained in tissues for ≥ 24 h after *in vivo* injection (26). Future selections using our new strategy could become more elaborate by targeting specific intracellular compartments, either by including subcellular fractionation in the recovery step or by selecting for a compartment-specific biochemical modification, such as phosphorylation or biotinylation.
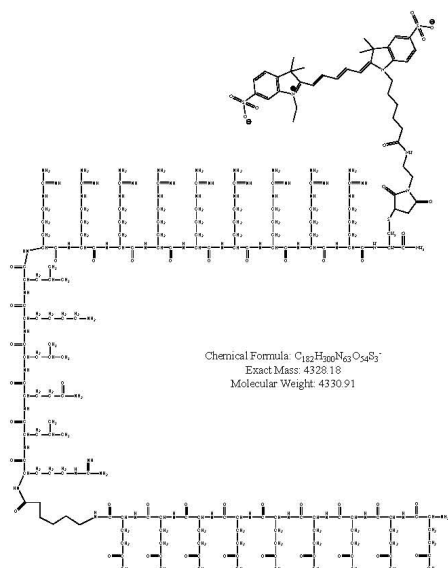
REFERENCES

1. Jiang, T., Olson, E. S., Nguyen, Q. T., Roy, M., Jennings, P. A., and Tsien, R. Y. (2004) *Proc. Natl. Acad. Sci. U. S. A.* **101**, 17867–17872
2. Goun, E. A., Shinde, R., Dehnert, K. W., Adams-Bond, A., Wender, P. A., Contag, C. H., and Franc, B. L. (2006) *Bioconjug. Chem.* **17**, 787–796
3. Zhang, Y., So, M. K., and Rao, J. H. (2006) *Nano Lett.* **6**, 1988–1992
4. Aguilera, T. A., Olson, E. S., Timmers, M. M., Jiang, T., and Tsien, R. Y. (2009) *Integrative Biology* **1**, 371–381
5. Olson, E. S., Aguilera, T. A., Jiang, T., Ellies, L. G., Nguyen, Q. T., Wong, E. H., Gross, L. A., and Tsien, R. Y. (2009) *Integrative Biology* **1**, 382–393
6. Olson, E. S., Jiang, T., Aguilera, T. A., Nguyen, Q. T., Ellies, L. G., Scadeng, M., and Tsien, R. Y. (2010) *Proc. Natl. Acad. Sci. U. S. A.* **107**, 4311–4316
7. Gammon, S. T., Villalobos, V. M., Prior, J. L., Sharma, V., and Piwnica-Worms, D. (2003) *Bioconjug. Chem.* **14**, 368–376
8. Rothbard, J. B., Kreider, E., VanDeusen, C. L., Wright, L., Wylie, B. L., and Wender, P. A. (2002) *J. Med. Chem.* **45**, 3612–3618
9. Wright, L. R., Rothbard, J. B., and Wender, P. A. (2003) *Curr. Protein Pept. Sci.* **4**, 105–124
10. Bremer, C., Bredow, S., Mahmood, U., Weissleder, R., and Tung, C. H. (2001) *Radiology* **221**, 523–529
11. Bremer, C., Tung, C. H., and Weissleder, R. (2001) *Nat. Med.* **7**, 743–748
12. La Rocca, G., Pucci-Minafra, I., Marrazzo, A., Taormina, P., and Minafra, S. (2004) *Br. J. Cancer* **90**, 1414–1421
13. Ratnikov, B. I., Deryugina, E. I., and Strongin, A. Y. (2002) *Lab. Invest.* **82**, 1583–1590
14. Sounni, N. E., Janssen, M., Foidart, J. M., and Noel, A. (2003) *Matrix Biol.* **22**, 55–61
15. Talvensaari-Mattila, A., Pääkkö, P., and Turpeenniemi-Hujanen, T. (2003) *Br. J. Cancer* **89**, 1270–1275
16. Atwell, S., and Wells, J. A. (1999) *Proc. Natl. Acad. Sci. U.S.A.* **96**, 9497–9502
17. Barbas, C. F., 3rd, Kang, A. S., Lerner, R. A., and Benkovic, S. J. (1991) *Proc. Natl. Acad. Sci. U.S.A.* **88**, 7978–7982
18. Kridel, S. J., Sawai, H., Ratnikov, B. I., Chen, E. I., Li, W., Godzik, A., Strongin, A. Y., and Smith, J. W. (2002) *J. Biol. Chem.* **277**, 23788–23793
19. Laakkonen, P., Akerman, M. E., Biliran, H., Yang, M., Ferrer, F., Karpanen, T., Hoffman, R. M., and Ruoslahti, E. (2004) *Proc. Natl. Acad. Sci. U.S.A.* **101**, 9381–9386
20. Mi, Z., Lu, X., Mai, J. C., Ng, B. G., Wang, G., Lechman, E. R., Watkins, S. C., Rabinowich, H., and Robbins, P. D. (2003) *Mol. Ther.* **8**, 295–305
21. Thie, J. A. (2004) *J. Nucl. Med.* **45**, 1431–1434
22. Sidhu, S. S. (2001) *Biomol. Eng.* **18**, 57–63
23. Guy, C. T., Cardiff, R. D., and Muller, W. J. (1992) *Mol. Cell. Biol.* **12**, 954–961
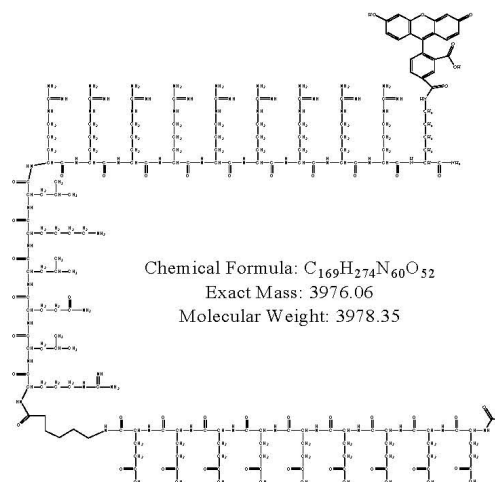24. Lin, E. Y., Jones, J. G., Li, P., Zhu, L., Whitney, K. D., Muller, W. J., and

Pollard, J. W. (2003) *Am. J. Pathol.* **163**, 2113–2126

25. Maglione, J. E., Moghanaki, D., Young, L. J., Manner, C. K., Ellies, L. G., Joseph, S. O., Nicholson, B., Cardiff, R. D., and MacLeod, C. L. (2001) *Cancer Res.* **61**, 8298–8305

26. Zou, J., Dickerson, M. T., Owen, N. K., Landon, L. A., and Deutscher, S. L. (2004) *Mol. Biol. Rep.* **31**, 121–129

27. Lacroix, M. (2008) *Int. J. Cancer* **122**, 1–4

28. Alles, A. J., Warshaw, A. L., Southern, J. F., Compton, C. C., and Lewandrowski, K. B. (1994) *Ann. Surg.* **219**, 131–134

29. Sperti, C., Pasquali, C., Guolo, P., Polverosi, R., Liessi, G., and Pedrazzoli, S. (1996) *Cancer* **78**, 237–243

30. Cuevas, B. D., Winter-Vann, A. M., Johnson, N. L., and Johnson, G. L. (2006) *Oncogene* **25**, 4998–5010

31. Danø, K., Behrendt, N., Høyer-Hansen, G., Johnsen, M., Lund, L. R., Ploug, M., and Rømer, J. (2005) *Thromb. Haemost.* **93**, 676–681

32. Sabapathy, K. T., Pepper, M. S., Kiefer, F., Möhle-Steinlein, U., Tacchini-Cottier, F., Fetka, I., Breier, G., Risau, W., Carmeliet, P., Montesano, R., and Wagner, E. F. (1997) *J. Cell Biol.* **137**, 953–963

33. Koivunen, E., Saksela, O., Itkonen, O., Osman, S., Huhtala, M. L., and Stenman, U. H. (1991) *Int. J. Cancer* **47**, 592–596

34. Koshikawa, N., Hasegawa, S., Nagashima, Y., Mitsuhashi, K., Tsubota, Y., Miyata, S., Miyagi, Y., Yasumitsu, H., and Miyazaki, K. (1998) *Am. J. Pathol.* **153**, 937–944

35. Miyata, S., Koshikawa, N., Higashi, S., Miyagi, Y., Nagashima, Y., Yanoma, S., Kato, Y., Yasumitsu, H., and Miyazaki, K. (1999) *J. Biochem.* **125**, 1067–1076

36. Paju, A., Vartiainen, J., Haglund, C., Itkonen, O., von Boguslawski, K., Leminen, A., Wahlström, T., and Stenman, U. H. (2004) *Clin. Cancer Res.* **10**, 4761–4768

37. Desmedt, C., Ouriaghli, F. E., Durbecq, V., Soree, A., Colozza, M. A., Azambuja, E., Paesmans, M., Larsimont, D., Buyse, M., Harris, A., Piccart, M., Martiat, P., and Sotiriou, C. (2006) *Int. J. Cancer* **119**, 2539–2545

38. Foekens, J. A., Ries, C., Look, M. P., Gippner-Steppert, C., Klijn, J. G., and Jochum, M. (2003) *Cancer Res.* **63**, 337–341

39. Yamashita, J. I., Ogawa, M., Ikei, S., Omachi, H., Yamashita, S. I., Saishoji, T., Nomura, K., and Sato, H. (1994) *Br. J. Cancer* **69**, 72–76

40. Kratz, F., Müller-Driver, R., Hofmann, I., Drevs, J., and Unger, C. (2000) *J. Med. Chem.* **43**, 1253–1256

41. Kratz, F., Warnecke, A., Scheuermann, K., Stockmar, C., Schwab, J., Lazar, P., Drückes, P., Esser, N., Drevs, J., Rognan, D., Bissantz, C., Hinderling, C., Folkers, G., Fichtner, I., and Unger, C. (2002) *J. Med. Chem.* **45**, 5523–5533

42. Jessani, N., Liu, Y., Humphrey, M., and Cravatt, B. F. (2002) *Proc. Natl. Acad. Sci. U.S.A.* **99**, 10335–10340

43. Brown, S., Bernardo, M. M., Li, Z. H., Kotra, L. P., Tanaka, Y., Fridman, R., and Mobashery, S. (2000) *J. Am. Chem. Soc.* **122**, 6799–6800

Supplemental Figure 1. Structures of Cy5 and
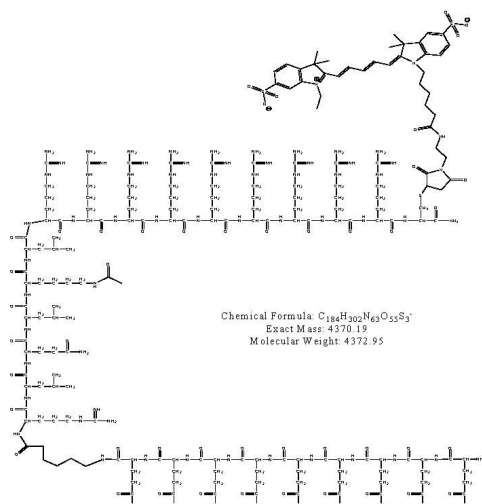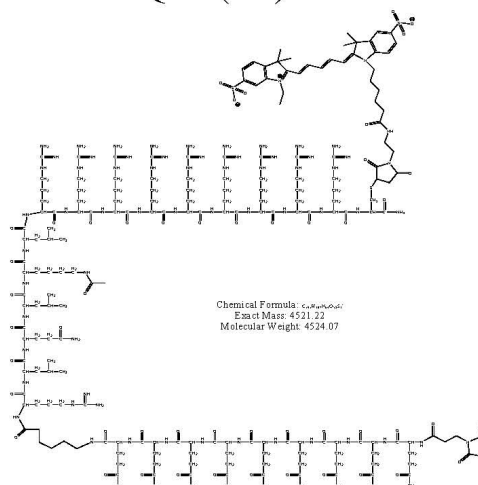Carboxyfluorescein labeled RLQLKL ACPPs

Cy5 labeled RLQLKL ACPP

Chemical Formula: $C_{182}H_{300}N_{63}O_{54}S_3^-$
Exact Mass: 4328.18
Molecular Weight: 4330.91

Carboxyfluorescein labeled RLQLKL ACPP

Chemical Formula: $C_{169}H_{274}N_{60}O_{52}$
Exact Mass: 3976.06
Molecular Weight: 3978.35

Cy5 labeled RLQLK(Ac)L ACPP

Chemical Formula: $C_{184}H_{302}N_{63}O_{55}S_3^-$
Exact Mass: 4370.19
Molecular Weight: 4372.95

Maleimide-Cy5 RLQLK(Ac)L ACPP

Chemical Formula: $C_{...}H_{...}N_{...}O_{...}S_{...}$
Exact Mass: 4521.22
Molecular Weight: 4524.07

# Supplemental Figure 2. Table of Enzymes and Inhibitors

- **Enzymes**
- **Cathepsin B human EMD/Calbiochem Cat # 219362**
- **Cathepsin G human EMD/Calbiochem Cat # 219373**
- **Cathepsin H human EMD/Calbiochem Cat # 219404**
- **Cathepsin L human EMD/Calbiochem Cat # 219402**
- **Coagulation Factor VII human EMD/Calbiochem Cat # 219367**
- **Coagulation Factor IX human EMD/Calbiochem Cat # 233279**
- **Coagulation Factor X human EMD/Calbiochem Cat # 233282**
- **Coagulation Factor XI human EMD/Calbiochem Cat # 233480**
- **Coagulation Factor XII human EMD/Calbiochem Cat # 233490**
- **Enterokinase R and D systems Cat # 1185-SE**
- **rhHepsin R and D systems Cat # 4775-SE**
- **Kallekrein 5 R and D systems Cat # 1108-SE**
- **Leukocyte elastase (human) Sigma Cat # E8140**
- **MMP1 EMD/Calbiochem Cat # PF067**
- **MMP2 R and D systems Cat # 902MPM**
- **MMP7 EMD/Calbiochem Cat # 444270 active human**
- **MMP9 EMD/Calbiochem Cat # PF024 human recombinant**
- **MMP12 Sigma Cat # M9695**
- **MMP14 R and D systems 918MP**
- **Neutrophil elastase EMD/Calbiochem Cat # 324681**
- **Pancreatic elastase- Sigma E7885 (porcine pancrease)**
- **Plasmin-human recombinant EMD/Calbiochem Cat # 527622**
- **PSA EMD/Calbiochem Cat # 539834**
- **Thrombin human EMD/Calbiochem Cat # 605190**
- **tPA –human EMD/Calbiochem Cat # 612200**
- **Trypsin bovine pancrease EMD/Calbiochem Cat # 650200**
- **Trypsin 2 recombinant human R and D systems Cat # 3586SE**
- **uPA-urokinase-human urine EMD/Calbiochem Cat # 67112**

- **Inhibitors**
- **Alpha2-antiplasmin- EMD/Calbiochem Cat # 178221**
- **Alpha1-antitrypsin- EMD/Calbiochem Cat # 178251**
- **Aprotinin bovine EMD/Calbiochem Cat # 616370**
- **Cocktail III EMD/Calbiochem Cat # 539134**
- **Cocktail III/DTPA**
- **DTPA- EMD/Calbiochem Cat # 288130**
- **E-64 EMD/Calbiochem Cat # 324890**
- **GM 6001- EMD/Calbiochem Cat # 364205 20pm for 9, 500pm for2**
- **Leupeptin EMD/Calbiochem Cat # 108975**
- **Pepstatin EMD/Calbiochem Cat # 516481**
- **Prinomastat** Gift from Pfizer
- **SB3CT-Calbiochem-(no current Cat #)**
- **TPEN- EMD/Calbiochem Cat # 616394**

Supplemental Figure 3. RLQLKL (left) has decreased skin uptake relative to previously published MMP activatable ACPP (middle). An animal injected with the all-D amino acid rlqlkl ACPP is also shown (right). Images highlight to ability to visualize tumor uptake of the ACPPs with skin on and how remaining hair can affect images.

RLQLKL-ACPP   PLGLAG-ACPP   rlqlkl-ACPP
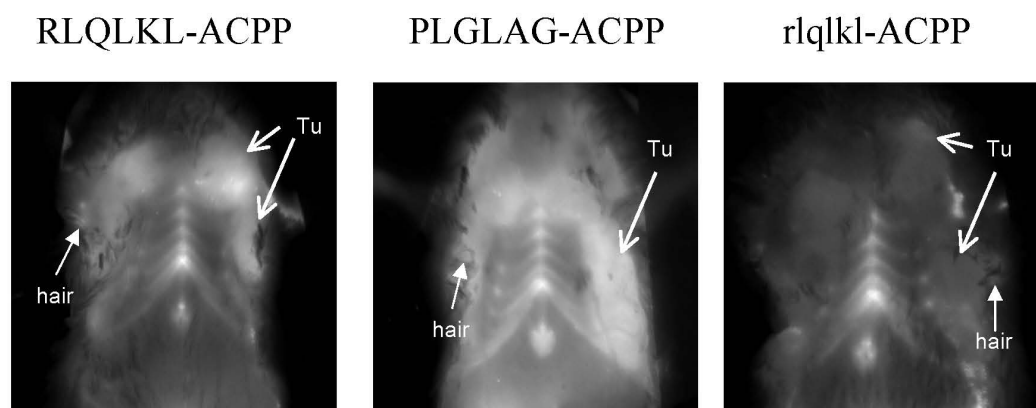
Legend Supplemental Figure 3. Imaging of live mice which were injected with Cy5 labeled ACPP. Comparisons are shown for live animals injected with an ACPP with cleavage sites corresponding to either RLQLKL or the previously published MMP activated ACPP with cleavage site of PLGLAG. Also shown is the control animal injected with the all D-amino acid rlqlkl ACPP. Mice were injected with 100μl of 100μM ACPP and imaged 6 hours post injection. Hair was partially removed using NAIR hair removal lotion. RLQLKL has less skin uptake likely due to lack of enzymes that cleave this sequence within this tissue which enhances tumor contrast when imaging live animals. Both images were taken using identical capture settings. Tu denotes tumor.

Supplemental Figure 4. Trypsin,trypsin-2, hepsin, prostate specific antigen (PSA), enterokinase and plasmin digestion of ACPP substrates
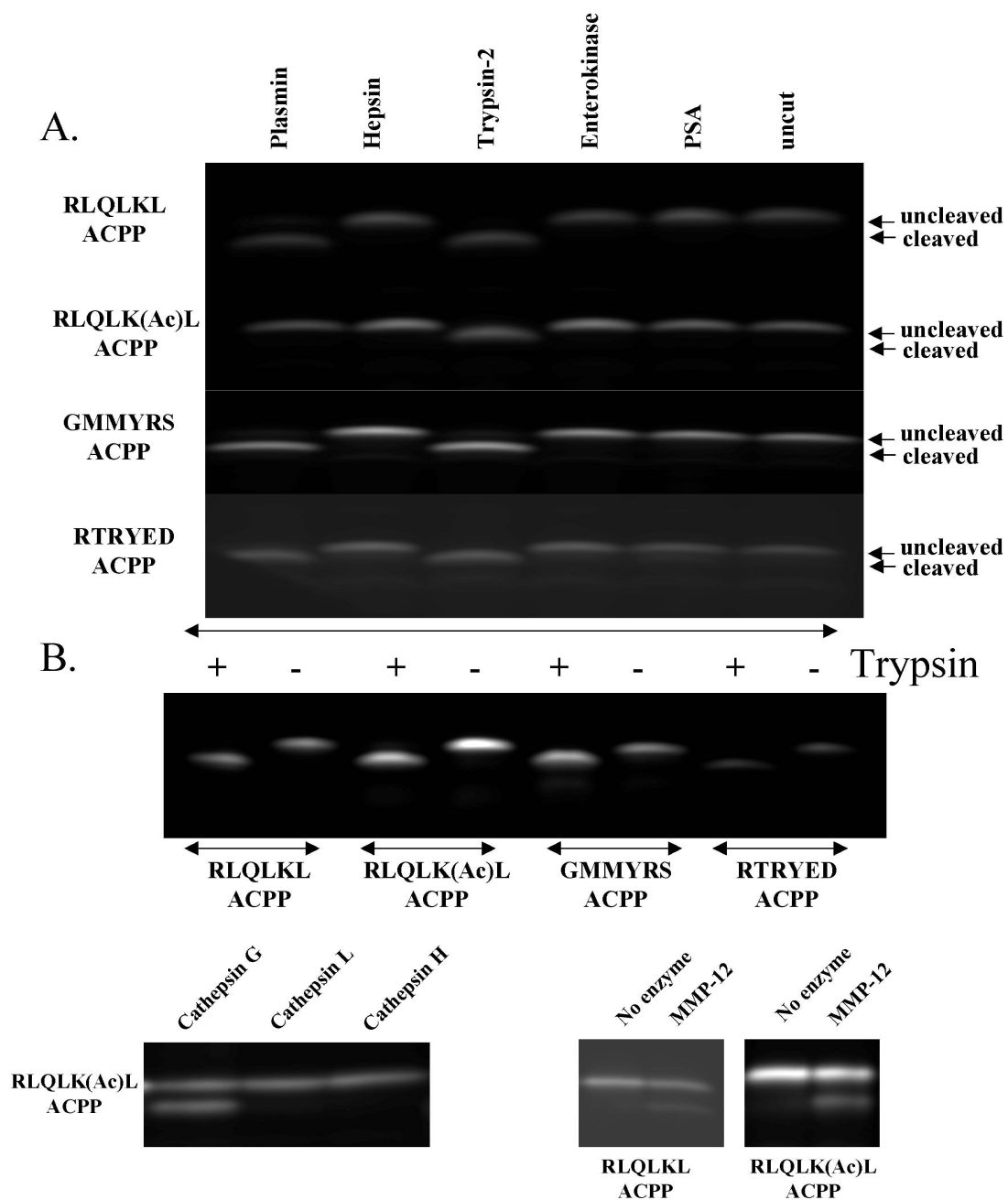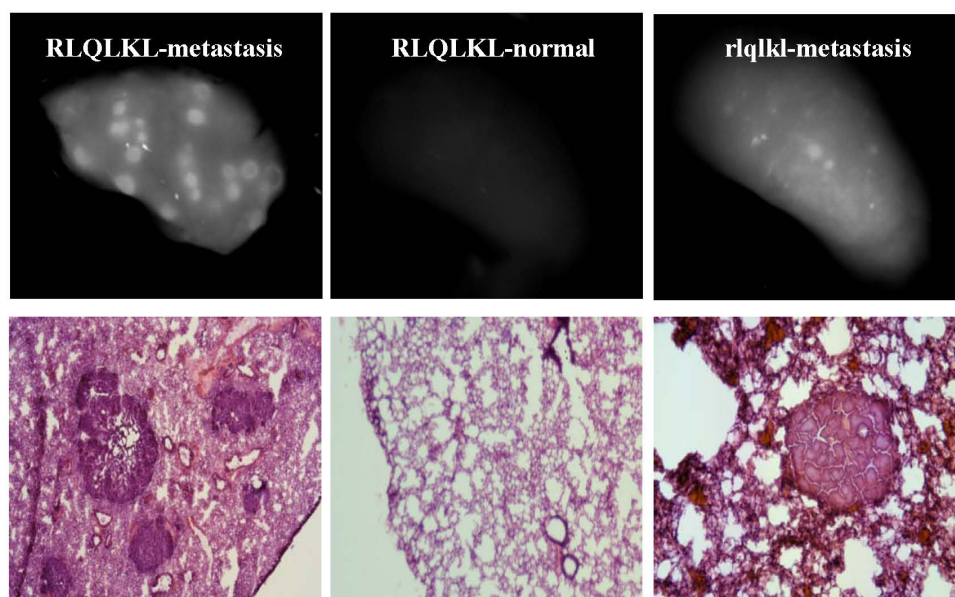
Supplemental Figure 5. Summary of Cy5 labeled cleavage products detected by Mass Spectrometry

RLQLKL ACPP	Plamin	Trypsin	P.elastase	N.elastase	tumor	liver	kidney
Lr9c(Cy5+18)	1	1	1		3	1	1
KLr9c(Cy5+18)			2	1	1		1
LKLr9c(Cy5+18)					2		1
RLQLK(ac)L							
Lr9c(Cy5+18)	nt	nt			2	nt	nt
K(Ac)Lr9c(Cy5+18)	nt	nt	1	1	1	nt	nt
QLK(Ac)Lr9c(Cy5+18)	nt	nt	2			nt	nt

Legend Supplemental Figure 5. For mass spectrometry determination each peptide was purified from homogenized cell extract by two steps of reverse phase HPLC. A 30 ul sample of 5 uM ACPP digested with tissue extract for 2 hours was diluted to 2.5 ml with solvent A, which contained 2% acetonitrile and 0.14% trifluoroacetic acid. Signal intensities from each peak isolated by mass spectrometry were compared to determine relative abundance of various cleavage products. Intensities were ranked so the most abundant cleavage product(s) were ranked as 1 and the least abundant 3. If intensities varied by less than 50% they were given the same rank. (nt=not tested)

Supplemental Figure 6.

A. Elastase western (Rabbit polyclonal) with PyMT tumor extracts

102 KD

39 KD

22 KD

Elastase=26 KD
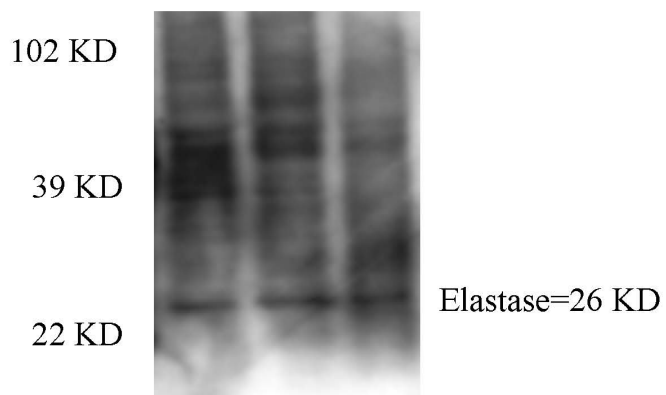
B. Lungs from an animal with PyMT tumors but without lung metastases (middle panels) show little fluorescence contrast with 4.2 fold decreased fluorescent intensity ($p < 0.01$) compared to metastatic nodules (left panels). Representative hematoxylin/eosin sections for each lung are shown below the fluorescent image.

RLQLKL-metastasis   RLQLKL-normal   rlqlkl-metastasis

6.1. Acknowledgements

This chapter is a reprint of the work as it appears in Journal of Biological Chemistry, published May 2010:

The dissertation author was secondary author on this material and contributed to experimental design, execution of experiments, interpretation of data, generation of figures and editing of manuscript.

The dissertation author would like to thank:

Dr. Mike Whitney for mentoring me as I worked with him on this project. Dr. Todd Aguilera and Dr. Emilia Olson for training me to work with animals and teaching me the basic protocols for tumor model generation and fluorescent imaging with whole animals and tissue sections. Dr. Larry Gross for performing all mass spectroscopy analysis that helped to rationally evolve the peptide sequence. Dr. Tao Jiang for training with peptide synthesis and purification. Evangeline Moss, Timothy Salazar and Perla Arcaira for their assistance with animal husbandry, cancer models and the processing of tissues for SUV calculations.

CHAPTER 7: ACPPs selectively target macrophages in metastatic lungs

7.1. Abstract

Tumor associated macrophages (TAMs) have several pro-tumorigenic functions including promotion of angiogenesis, matrix remodeling, suppression of adaptive immune responses, and resistance to chemotherapy. High macrophage density has been associated with poor patient prognosis in a number of human studies. Because of this, macrophages are a prime target for cancer imaging and therapeutic intervention. Activatable cell penetrating peptides (ACPPs) provide a novel means of targeting activated macrophages by utilizing the enzymes they upregulate. The peptide sequence RLQLK(Ac)L is a substrate for MMP-12, macrophage metalloelastase, and ACPPs with that cleavage site selectively label macrophages in lungs of mice with breast cancer metastases. ACPP uptake only occurs in advanced metastatic disease and requires cleavage of the RLQLK(Ac)L substrate. Analysis is currently underway to determine the activation state of these macrophages in hopes that this peptide can provide selective targeting of TAMs in future therapeutic studies.

7.2. Introduction

Macrophages, once thought to be involved in anti-tumor immunity, are now being implicated in all the various stages of tumorgenesis from initiation to metastasis. Clinical data makes a strong argument that macrophages promote tumor growth, one meta

analysis in 2002 reported that over 80% of studies show a positive correlation between macrophage density and poor patient prognosis (Bingle, Brown et al. 2002). Later studies only corroborated that claim in thyroid, lung, and hepatocellular cancers (Chen, Lin et al. 2005; Ryder, Ghossein et al. 2008; Zhu, Zhang et al. 2008). Although, there are some cases where high macrophage density is associated with a favorable outcomes but those are in the minority (Lewis and Pollard 2006).

Macrophages are a diverse group of cells that can be divided into subpopulations based on their anatomical location and functional phenotype. The spectrum of macrophage activation has taken on the 1/2 nomenclature similar to that of the helper T cell immune response. M1, or classically activated, macrophages mediate host defenses from a variety of protozoan bacteria and viruses and have roles in antitumour immunity. M2, or alternatively activated, macrophages have an anti-inflammatory function and moderate wound healing (Qian and Pollard 2010; Murray and Wynn 2011). Tumor associated macrophages (TAMs) are similar to the prototypic polarised M2 population in both gene expression and function. They have been associated with several pro-tumorigenic functions such as angiogenesis, matrix remodeling, suppression of adaptive immune responses, and resistance to chemotherapy (Sica, Schioppa et al. 2006; De Palma and Lewis 2011)

Because of this, macrophages are a prime candidate for therapeutic intervention. By simultaneously targeting both proliferating tumor cells and terminally differentiated macrophages, the success rate of both diagnosis and treatment could significantly improve over standard therapies that just target tumor cells. A recent publication found that immune suppressive activity in the tumor microenvironment was hindering the

therapeutic effect of antibodies against αOX40, a member of the Tumor Necrosis Factor (TNF) receptor family. When this treatment was combined with an inhibitor to arginase-1, a protein mediator of the M2 phenotype, therapeutic efficacy was restored (Gough, Killeen et al. 2012). Another report found that treating mice with liposomes containing siRNA against CCR2, a chemokine receptor used by inflammatory macrophages, significantly reduced the volume of EL4 lymphoma xenograft tumors and decreased the number of TAMs in the tumor by 54% (Leuschner, Dutta et al. 2011).

ACPPs provide a novel mechanism for targeting inhibitors of macrophage function to sites of cancer by utilizing the enzymes that TAMs express. The RLQLKL substrate sequence was discovered from an *in vivo* phage display selection in polyoma middle T (PyMT) mice (Whitney, Crisp et al. 2010). This peptide sequence and the acetylated derivative, RLQLK(Ac)L, are substrates for various elastases including MMP-12, known as macrophage metalloelastase. Elevated levels of this enzyme have been associated with poor prognosis in patients with hepatocellular carcinoma and overexpression of MMP-12 has also been found in patients with lung cancer (Qu, Du et al. 2009; Ng, Qi et al. 2011). This chapter focuses on targeting macrophages with the RLQLK(Ac)L ACPP in lungs of mice with experimental models of breast cancer metastasis. Macrophage uptake of this peptide was only found in animals with advanced metastatic disease, and required enzymatic cleavage of the substrate.

7.3. Methods

7.3.1. Peptide synthesis

Peptides were synthesized as previously described in Chapter 6. Peptides used in this chapter have the sequence: maleimide-$(CH_2)_3$-$CONH_2$-e_9-*x*-RLQLK(Ac)L-r_9-c(Cy5) and maleimide-$(CH_2)_3$-$CONH_2$-e_9-$(peg_2)_2$-r_9-c(Cy5).

7.3.2. In vivo testing

To generate experimental lung metastases, $5x10^5$ syngeneic breast cancer cells (PyMT 8119 and PyMT 5944 GFP+) were injected intravenously into the tail vein of black-6 mice. Cells circulated in the blood stream until they eventually seeded in the lungs and generated metastatic nodules. Mice were sacrificed anywhere from 3-18 days after tumor cell injection.

7.3.3. Lung imaging

7.3.3.1. Whole lung imaging

Twenty-four hours after maleimide peptide injections, mice were sacrificed and the chest cavity and trachea were exposed. The lungs were inflated via the trachea using a 1ml syringe and an 18-gauge needle. The syringe was filled with a 1:1 mixture of phosphate buffered saline (PBS) and O.C.T. Compound (Tissue-Tek). After the lungs were filled, the syringe and needle were removed and the trachea was clamed. The trachea was then cut above the clamp and the clamp was used to help resect the lungs. Lungs were imaged on the Maestro (CRI) using either the 620/22nm excitation, 670/20nm emission for Cy5 or 466/44 nm excitation and 525/20nm emission filters for green fluorescent protein (GFP).

7.3.3.2. Lung sections

Lungs inflated with PBS:OCT were placed in a cryo-mold cassette and submerged in OCT prior to being flash frozen with liquid nitrogen. Lung tissue was cut in 10μm sections on a cryostat (Leica) then mounted on either a super frost ++ slide or a glass coverslip. For the initial images in Figure 4.1, tissue sections were mounted on the super frost slides and permitted to dry prior to imaging on the Lumar stereoscope (Zeiss) using the Cy5 filter set. For images in Figure 4.2, Lung sections were mounted on super frost slides, fixed with 4% paraformaldehyde (PFA) for 60 seconds at room temperature, washed and coversliped just prior to imaging. For images in Figure 4.3, lung sections were mounted onto a glass coverslip and imaged while frozen as described in the methods section of Chapter 3.

7.3.3.3. Confocal imaging *ex vivo*

Immediately after the lungs were inflated and harvested from the mouse they were placed in a glass bottom-imaging disk and transferred to the microscope. The trachea remained clamped to keep the lung volume as constant as possible during imaging. Lungs were imaged on a 5-Live line scanning confocal microscope (Zeiss) using an excitation laser of 488 nm with an emission filter of 500-525nm to visualize GFP and a 635nm laser with a 650nm long pass filter to image Cy5. Z stacks were taken with a z step of 1μm and images are displayed as maximum projections.

7.3.4. Immunohistochemistry

10μm sections of frozen lung tissue were mounted on to super frost slides and fixed with 4% PFA for 60 seconds at room temperature. Sections were washed 3 times in

PBS and blocked with 10% normal goat serum (Invitrogen) for 30-60 minutes at room temperature. The slides were tilted to allow a majority of the serum to run off, but leaving a thin film over the tissue section. Primary antibodies, Neutrophil 7-4 FITC (Abcam, ab53453), CD86 [FA-11] (Abcam, ab53444) and CD 163 (Santa Cruz, sc-33560) were diluted 1:100 in PBS, placed on the tissue and then allowed to incubate overnight at 4°C in the dark within a humidified chamber. Primary antibodies were removed and the sections were washed 3X for 20 minutes each at room temperature in PBS with slight agitation. For Neutrophil 7-4, coverslips were mounted using Prolong Gold antifade reagent (Life Technologies) prior to imaging. For CD 68 and CD 163, the tissue sections were blocked again with goat serum for 20 minutes at room temperature before application of the secondary antibody. Secondary antibodies (for CD 68: Rabbit pAb to Rat IgG FITC , Abcam, ab6730 and for CD 163: Goat pAb to Rabbit IgG, Santa Cruz, sc-2012) were diluted 1:500 in PBS and incubated for 2-3 hours at room temperature. Sections were washed 3 times for 20 minutes each with PBS and slight agitation and coverslips were mounted with Prolong Gold. Imaging was done on the 5-Live line scanning confocal microscope (Zeiss) using an excitation laser of 488nm with an emission filter of 500-52nm to visualize FITC and a 635nm laser with a 650nm long pass filter to image Cy5.

7.3.5. Lung digestion and FACS sorting

Mice harboring PyMT 5944 GFP+ lung metastases were injected with 3 nanomoles of maleimide-RLQLK(Ac)L ACPP 15 days after tumor cell injection. Twenty-four hours after peptide injected the mice were sacrificed and the chest cavity was exposed. The animal was then profused with 20ml of PBS through the left ventricle.

Blanching of the liver and lung tissue was observed. The lungs were then inflated via the trachea with the collagenase buffer containing 1mg/ml collagenease (Sigma, C-9891), 2mg/ml Soybean anti trypsin (Sigma, T6522), 1 pill per 10ml of EDTA-free complete inhibitor tablets (Roche) in 20mM HEPES buffered DMEM with no phenol-red (CellGrow). After lung inflation, they were harvested from the animal and each lobe was chopped into cubes ranging from 1-3 mm^3. Lung pieces were incubated in 10 ml of the collagenase buffer described above with significant agitation for 1-3 hours. This solution was then filtered twice prior to fluorescence associated cell sorting (FACS). Lungs were sorted on a FACS Diva (BD Biosciences) and gating was based on Cy5 fluorescence, emission filter of 675/20 nm.

7.4. Results

7.4.1. Cellular labeling by maleimide-RLQLK(Ac)L ACPP is enzyme dependent and only occurs in metastatic lungs

Identifying metastases is important for cancer staging and the ability to target them provides hope for future therapeutic development. Therefore, the capacity of maleimide-RLQLK(Ac)K ACPP to identify cancerous nodules in metastatic lungs was investigated. The maleimide version of the ACPP is thiol reactive and forms a covalent attachment with albumin upon IV injection. Experimental lung metastasis models were chosen because the formation of spontaneous metastases from mice with primary breast tumors, while preferable, takes many weeks to generate and is not reliable. Therefore, mice were inoculated with cancer cells via the tail vein and either 10 days (4T1.2) or 13

days (PyMT 8119) post were dosed with albumin reactive ACPPs. From fluorescent images of whole lung lobes it is clear that the elastase cleavable Mal-RLQLK(Ac)L peptide has significantly higher fluorescence than the uncleavable, mpeg control peptide in both cancer models (Figure 7.1). With 4T1.2 cells, the peptide can distinguish individual metastatic nodules within the lungs with up to 4-fold contrast to surrounding tissue. Staining with the PyMT 8119 model is not as defined as with 4T1.2, but there are distinct regions of elevated fluorescence.
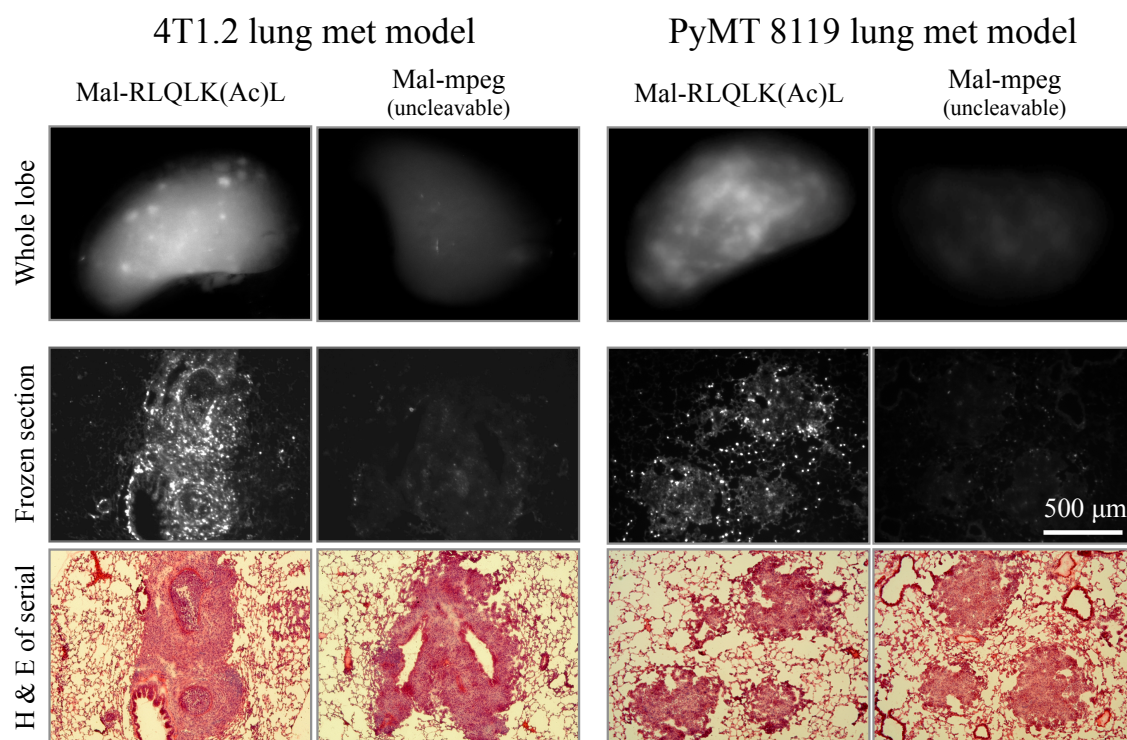
Figure 7.1 Differential labeling of lung metastases with Mal-RLQLK(Ac)L ACPP. Mice were injected via the tail vein with 5×10^5 syngeneic breast cancer cells, either 4T1.2 or PyMT 8119. Ten to thirteen days after tumor cell injection, the mice were dosed with 3 nanomoles Cy5 labeled peptide, either Mal-RLQLK(Ac)L or Mal-$(peg_2)_2$, the uncleavable control. Twenty-four hours after peptide injection, animals were sacrificed and the lungs were harvested. Representative images of a lung lobe are presented in the top row of the figure for both tumor models and both peptides that were tested. The lobes were then frozen and sectioned to image Cy5 fluorescence on a histological level. Representative fluorescent images of lung sections are presented in the middle row with corresponding images of hemotoxylin/esosin stained tissue sections in the bottom row.

To confirm that the enhanced fluorescence coincided with areas of metastasis, lungs were sectioned and imaged on a histological scale. With the 4T1.2 model, the ACPP was distributed throughout the metastatic nodules and had numerous puncta between 10-50μM in diameter that had high peptide uptake, accounting for a majority of the fluorescent signal. In contrast, the metastatic nodules in the PyMT 8119 lungs showed only moderate peptide uptake, especially when compared to bright punctate staining that appeared in the lung parenchyma surrounding the cancer. Because this labeling had such high contrast, what appeared to be single cell resolution and was due to enzymatic cleavage, further studies were done to better characterize it.

The next round of experiments with mal-RLQLK(Ac)L in the PyMT 8119 lung metastasis model confirmed that the bright spots were in fact single cells and that these cells only light up when a high tumor burden was present. The ACPP was administered to naïve mice that had never been injected with cancer cells, mice where cancerous lesions had only begun to form, or mice with an established metastatic burden (Figure 9.2 A-C). Fluorescence punctate was only visible in the lung sections of mice with advanced disease and this fluorescence was confirmed to be cellular with the co-staining of Hoescht, a nuclear marker. Again, lungs of mice that were injected with the negative control peptide were devoid of any fluorescent signal when imaged using the same parameters (Figure 7.2 D). Representative hemotoxylin/eosin (H&E) stained lung sections are presented to help define what "low" and "high" tumor burden are (Figure 7.2 E and F). In panel E, the yellow arrow indicates a region with small tumor growth.

Closer inspection of these images revealed that the Cy5 fluorescence was only present in the cytoplasmic region of the cells and was excluded from the nucleus. This

tissue was not fixed prior to freezing, therefore the cellular membranes could have been compromised allowing the peptide signal to diffuse during freezing or the thawing process that mounts the tissue onto the slide. Because of this, no claim can be made as to the exact sub-cellular location, i.e in the cytoplasm versus confined to vesicles. It is presumed that the peptide is sequestered in some cellular compartment because typically once CPPs are released in the cytoplasm of living cells, they immediately translocate to the nucleus.
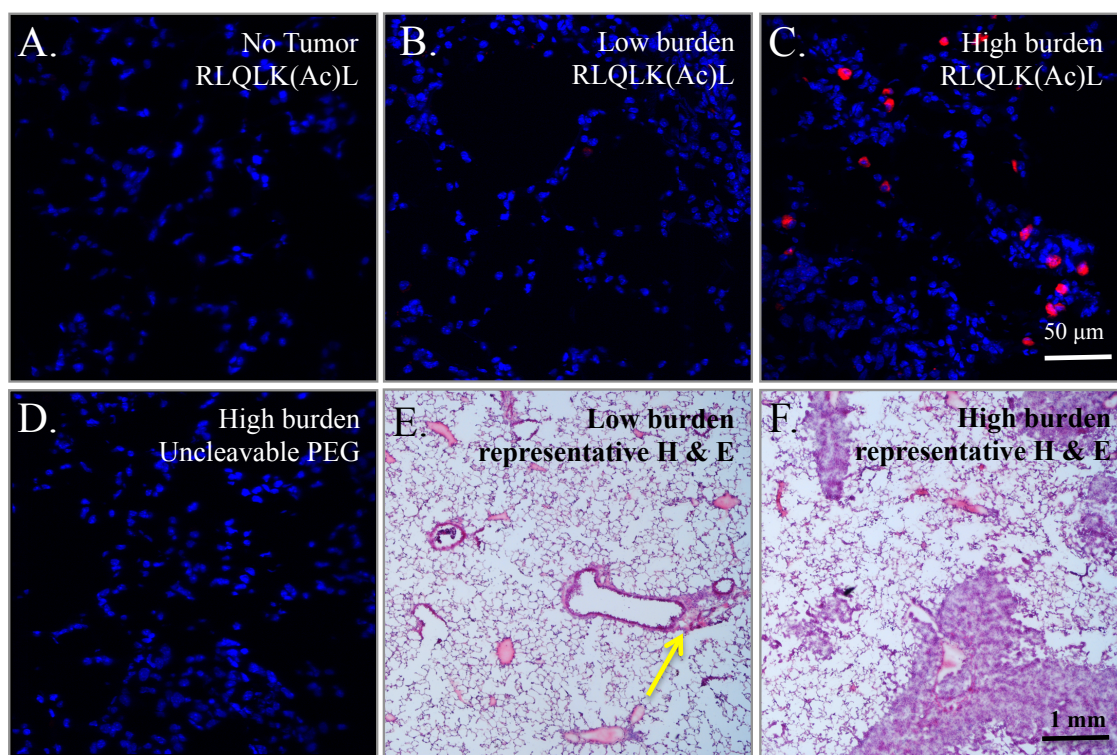
Red: Cy-5, Blue: Hoechst nuclear stain

Figure 7.2 Uptake of mal-RLQLK(Ac)K by cells in the lung parenchyma is enzyme dependent and only occurs in mice with advanced metastatic disease. A-C) Maleimide-RLQLK(Ac)L ACPP was administered to naïve (A), mice where cancerous lesions had only begun to form (B), or mice with an established metastatic burden (C). Twenty-four hours after peptide injection, mice were sacrificed and the lungs were harvested and frozen. Sections were mounted onto imaging slides, fixed with 4% PFA and rinsed with PBS containing Hoescht prior to imaging. D) Maleimide-(peg$_2$)$_2$ control peptide was injected into a mice with high 8119 tumor burden and 24 hours later the lungs were harvested and processed as described above. E-F) Representative H&E images of tumor sections from the same lung set as presented in B and C to demonstrate what low (E) and high (F) tumor burden mean.

The question arose as to whether the labeled cells were native to the lungs, some form of infiltrating immune cell from the host animal or individual cancer cells that were present in the parenchyma. To test the theory that the ACPP was being taken up by single cancer cells, the model was changed to a PyMT 5944 cell line that stably expresses GFP. PyMT 5944 GFP+ is similar to PyMT 8119 in that they both have a basal-epithelial mesenchymal transition (EMT) phenotype (Sarrio, Rodriguez-Pinilla et al. 2008).

PyMT 5944 GFP+ cells were injected into the tail vein of mice and allowed to grow in the lungs for various time periods prior to administration of the mal-RLQLK(Ac)L ACPP. Whole lung images reveal the appearance of fluorescent metastatic nodules (Figure 7.3 left column) as early as 3 days post injection and progressing to heavy disease 8 days thereafter. ACPP fluorescence on the whole lung scale increased with progressing tumor burden; peptide labeling started around day six and improved drastically by day 13 (Figure 7.3 middle column). Comparing the GFP and Cy5 images for whole lungs from days 9 and 13, there is some elevation in Cy5 fluorescence that co-localizes with GFP signal, but the contrast is not impressive because the levels of Cy5 in the background are high.

Lungs from each time point were sectioned and imaged to first determine if this cancer model had the same ACPP cellular labeling phenomenon and subsequently establish if those cells were cancerous (Figure 7.3 right column). The cellular uptake of Cy5 does not begin to take place until day 9 after tumor cell injection, when metastatic growth appears to encompass a large portion of the lung volume. As the cancer is allowed to persist, the number of Cy5 labeled cells also increases. From these images it is clear that the GFP and Cy5 fluorescence do not overlap. While there is some level of Cy5

fluorescence in the tumor nodules, the cells with the highest peptide uptake are not GFP labeled cancer cells

Lungs from mice 13 days post PyMT 5944 GFP+ cell inoculation and injected with ACPP were imaged *ex vivo* with confocal microscopy to analyze peptide distribution in live tissue. The window of time to perform this type of imaging is small, so the lungs went immediately from the animal to the microscope stage. Lungs were inflated prior to harvesting and remained clamped; therefore the only portion of tissue that could be viewed was the outer surface of the lung. Figure 7.4 shows one field of view that has examples of both a metastatic nodule as well and the peptide labeled cells. Again, it is clear that the Cy5 fluorescent cells do not posses any GFP fluorescence (Figure 7.4 B). Examining the peptide uptake around the metastasis is more interesting because there is some diffuse uptake throughout the small tumor but around the margins there are cells that have high peptide uptake but are not GFP positive (Figure 7.4 C).

| Whole lung GFP | Whole lung Cy5 | Frozen tissue section |

Un-injected

3 days post

Zoom 2X and brightened 10X

6 days post

9 days post

13 days post

Green: GFP tumor   Red: Cy5 ACPP
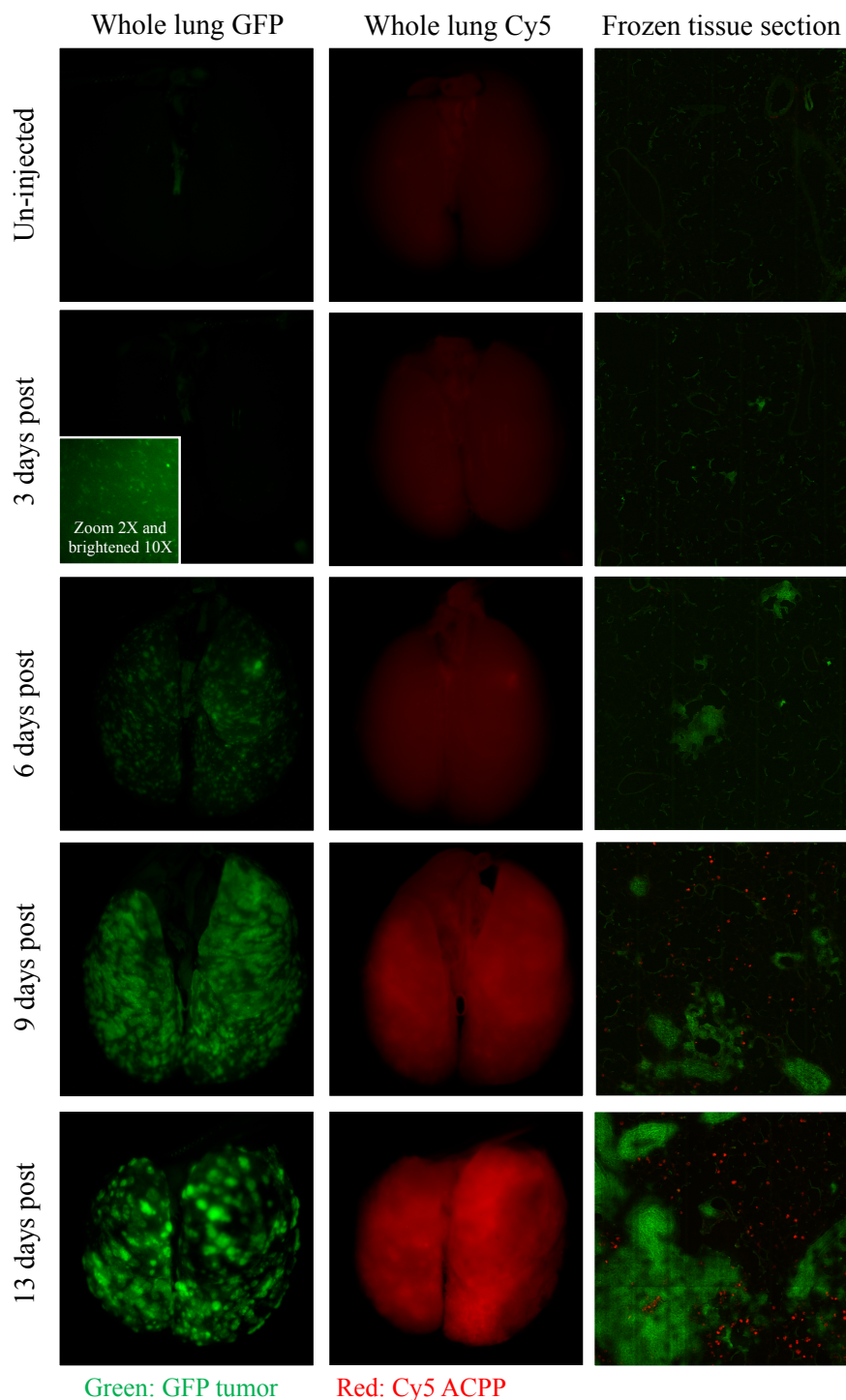
Figure 7.3 Time course of metastatic development and corresponding imaging with mal-RLQLK(Ac)L peptide. 5×10^5 PyMT 5944 breast cancer cells that stably express green fluorescent protein (GFP) were injected intravenously into black-6 mice. At various time points after tumor cell injection mice were dosed with 3 nanomoles of mal-RLQLK(Ac)L-Cy5 and sacrificed 24 hours later. Lungs were harvested and imaged for both GFP (left column) and Cy5 (middle column) fluorescence. Lung lobes were then flash frozen and sectioned to look at Cy5 and GFP cancer cell fluorescence (right column) on a histological level. All images within a column are scaled equally.
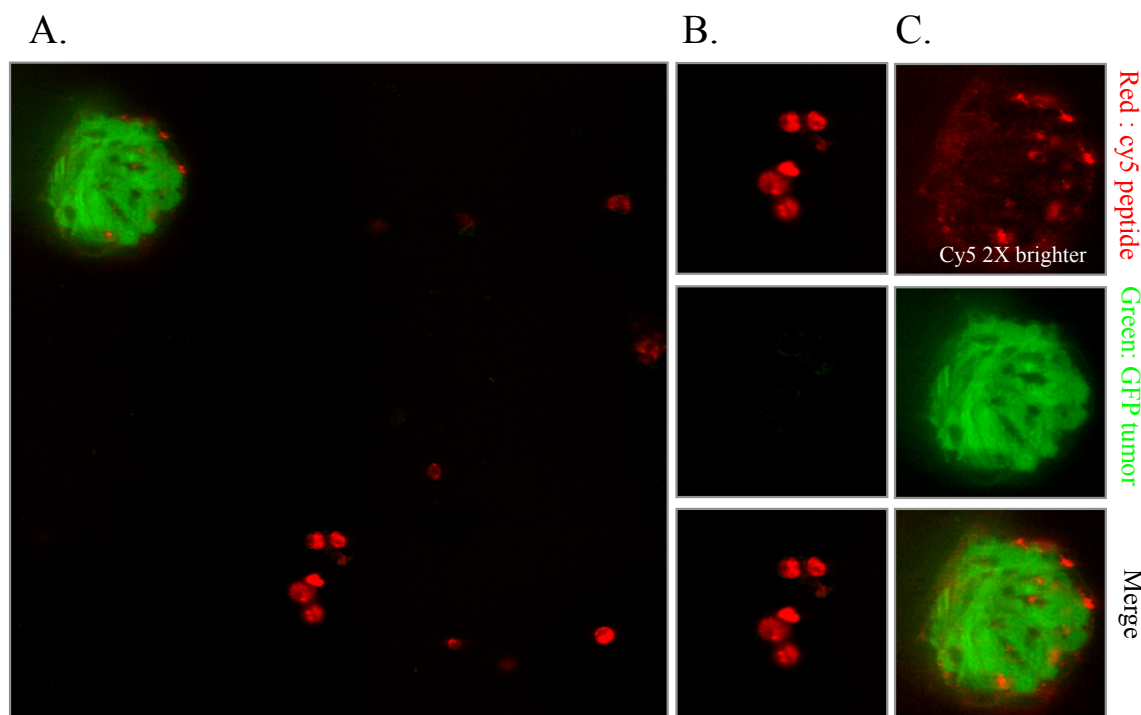
Figure 7.4 *Ex vivo* imaging of lungs harboring PyMT 5944 GFP+ metastases confirm that mal-RLQLK(Ac)L is not labeling single cancer cells within metastatic lungs. A) Mice harboring PyMT 5944 GFP+ lung metastases were injected with maleimide-RLQLK(Ac)L ACPP. 24 hours after peptide injection the mice were sacrificed and the lungs were harvested and transferred into a glass-bottom imaging dish. The outer surface tissue of the lungs was imaged using a Zeiss 5-live line scanning laser confocal microscope. Z stacks were collected and images are reconstructed maximum projections. B-C) The Cy5 and Fluorescein components of the image above were split to help visualize both peptide an GFP cancer cell fluorescence for regions with either ACPP labeled cells (B) or metastasis (C).

7.4.2. Maleimide RLQLK(Ac)L ACPP identifies macrophages in metastatic lungs

RLQLKL and the acetylated derivative are substrates for serine proteases,

including neutrophil elastase and MMP-12, also known as macrophage metalloelastase.

Therefore neutrophils and macrophages were two of the candidates for cell type

identification using immunohistochemistry (IHC). Neutrophil 7/4 antibody was selected

for neutrophil identification because it recognizes a polymorphic antigen that is expressed

by polynuclear cells but it absent on resident tissue macrophages (Hirsch and Gordon

1983; Li, Huang et al. 2010). When tissues sections from mice harboring PyMT 8119

metastases were subjected to IHC, neutrophils could be identified in the lungs, but the

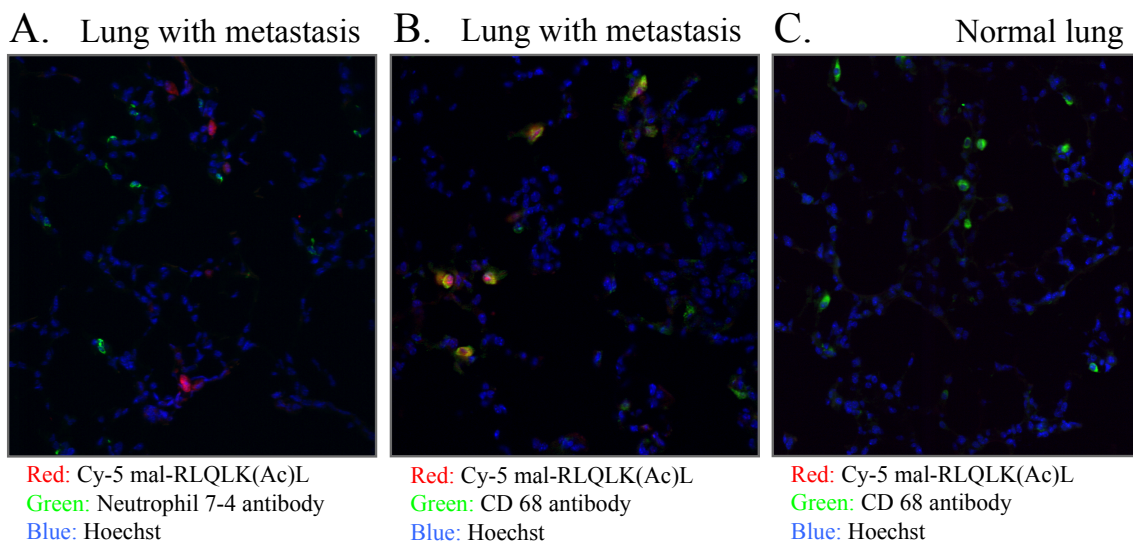antibody signal did not co localize with the peptide fluorescence (Figure 7.5 A).

A. Lung with metastasis	B. Lung with metastasis	C. Normal lung
Red: Cy-5 mal-RLQLK(Ac)L Green: Neutrophil 7-4 antibody Blue: Hoechst	Red: Cy-5 mal-RLQLK(Ac)L Green: CD 68 antibody Blue: Hoechst	Red: Cy-5 mal-RLQLK(Ac)L Green: CD 68 antibody Blue: Hoechst

Figure 7.5 Immunohistochemistry identifies ACPP targeted cells as macrophages and not neutrophils. A-B) Lungs from mice harboring PyMT 8119 experimental lung metastases were injected with mal-RLQLK(Ac)L ACPP prior to tissue harvesting and freezing. Frozen sections were prepared at a thickness of 10μm and incubated with primary antibodies against either Neutrophil 7/4 (A) or CD 68 (B), a macrophage marker. After completion of the IHC protocol, sections were coversliped with True Gold containing a nuclear stain, Hoechst, and imaged with confocal microscopy. C) Cancer free mice were injected with mal-RLQLK(Ac)L ACPP and lungs were harvested as controls for IHC procedures. Frozen sections from these lungs were also probed with primary antibodies against CD 68 and imaged for Cy5, antibody and nuclear fluorescence.

Next, similar tissue sections were probed with an antibody for CD 68. CD 68 is a

membrane-anchored glycoprotein that binds low-density lipoproteins and is highly

expressed by blood monocytes and tissue macrophages (Holness and Simmons 1993). It

is a common marker in IHC for macrophages but it is also known to be present on

lymphocytes, fibroblasts, endothelial cells and some tumor cell lines (Murray and Wynn

2011; Shabo and Svanvik 2011). Images of tissue sections incubated with the CD 68

antibody showed significant co-localization with Cy5 fluorescence (Figure 7.5 B)

demonstrating that the ACPP was getting cleaved and endocytocyed by macrophages.

Sections of lungs from normal mice that had been injected with the mal-RLQLK(Ac)K

ACPP were positive for CD 68 (Figure 7.5 D) with no visible Cy5 fluorescence.

CD 68 IHC was also performed on lung sections with PyMT 5944 GFP+

metastases (Figure 7.6). The same FITC labeled secondary antibody was used without

worry of spectral interference because it was previously observed that GFP fluorescence

did not survive 4% PFA fixation. Again, CD 68 co-localized with Cy5 ACPP

fluorescence. With the PyMT 8119 model there is almost complete co-registration of the

two fluorescent signals whereas with the PyMT 5944 GFP+ lungs there are CD68

positive cells that lack Cy5 fluorescence. It is also important to note that not all cells have

the same level up Cy5 uptake. This could be due to differing levels of enzyme secretion

in the macrophages, which hints at various types or degrees of macrophage activation.

Alternatively, it could simply be a product of variable access to blood flow and therefore

peptide substrate.
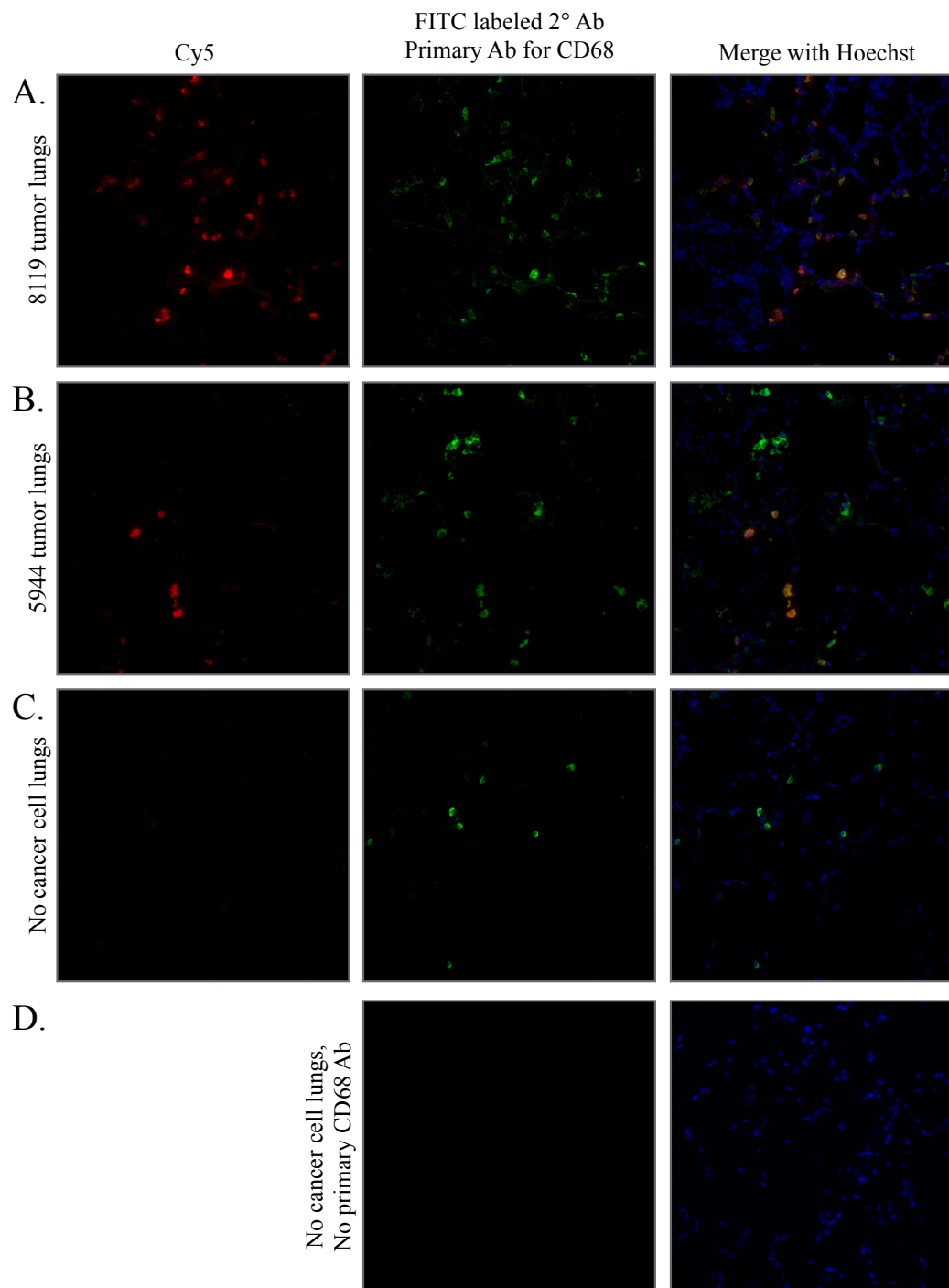
Figure 7.6 Immunohistochemistry for CD 68 confirms macrophage labeling by mal-RQLK(Ac)L ACPP in multiple tumor models. A-C) Lung sections from mice harboring PyMT 8119 lung metastases (A), PyMT 5944 GFP+ lung metastases (B) or normal mice never injected with cancer cells (C) and dosed with mal-RLQLK(Ac)L, were probed with a primary antibody against CD 68, then a fluorescein conjugated secondary antibody against the primary IgG and finally co-stained with a nuclear stain, Hoescht. D) As a control, normal lungs were incubated with the FITC conjugated secondary antibody in the absence of the primary CD 68 antibody.

7.4.3. Further characterization of macrophages to determine activation state

Once the macrophage identity was confirmed, efforts went into determining the activation state. Because the peptide was not taken up by resident macrophages in normal lungs, it was assumed that the high metastatic burden elicited an immune response that initiated the recruitment and activation of macrophages to the region. There is a wide spectrum of macrophage activation ranging from the classically activated macrophages (M1) that are "pro-inflammation" and "anti-tumor" to the alternatively activated macrophage (M2) that are thought be "pro-tumorigenic" (Sica, Schioppa et al. 2006; Murray and Wynn 2011). If the mal-RLQLK(Ac)L ACPP is preferentially taken up by M2 macrophages, this peptide could be a valuable tool in therapeutic strategies that target tumor associated macrophages.

CD 163 is a scavenger receptor for haptoglobin–hemoglobin complexes and is proposed in the literature as a marker for alternatively activated macrophages (Komohara, Hirahara et al. 2006; Komohara, Hasita et al. 2011; Kurahara, Shinchi et al. 2011). Its expression is induced by interleukin (IL)-6, IL-10, and glucocorticoid (Sulahian, Hogger et al. 2000; Schaer, Boretti et al. 2001) and it is down regulated by classical macrophage activators such as lipopolysaccharide and interferon-g (Buechler, Ritter et al. 2000). IHC was performed on frozen lung tissue sections from mice with PyMT 8119 metastases that were dosed with mal-RLQLK(Ac)L ACPP. There were regions in the tissue sections where the antibody staining and the peptide fluorescence overlapped (Figure 7.7 A) but there were also regions in the lungs where the two signals had no co-registration (Figure

7.7 B). Sections from mice with normal lungs also had positive signal for CD 163,

demonstrating that this antibody is not sufficient to identify alternatively activated

macrophages. For all IHC results presented in this chapter, the proper negative controls

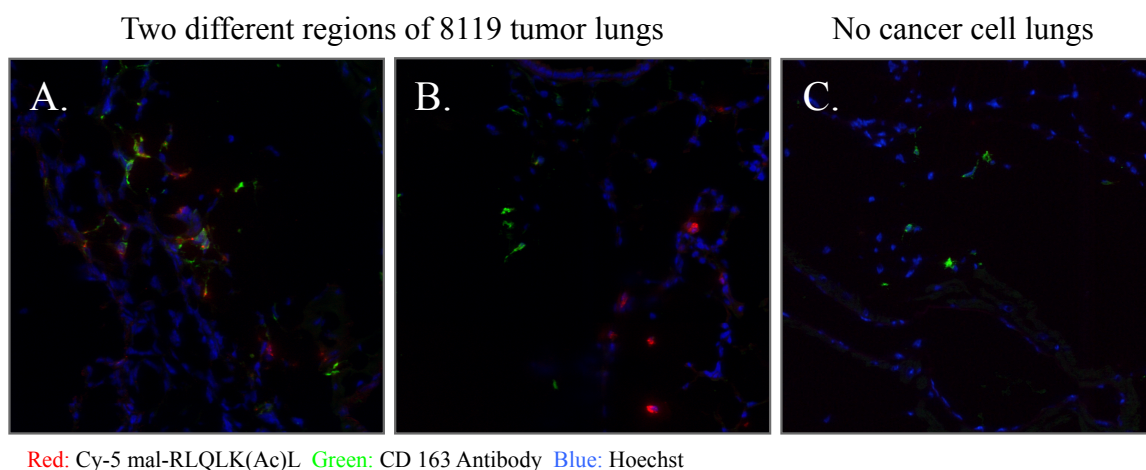(i.e. no primary antibody) were performed, even if the data is not shown.

Two different regions of 8119 tumor lungs   No cancer cell lungs

Red: Cy-5 mal-RLQLK(Ac)L Green: CD 163 Antibody Blue: Hoechst

Figure 7.7 Immunohistochemistry for CD 163 is inconclusive for identifying alternatively activated macrophages. A-C) Lung sections from mice harboring PyMT 8119 lung metastases (A,B), or normal mice never injected with cancer cells (C) and dosed with mal-RLQLK(Ac)L were probed with a primary antibody against CD 163 and then a fluorescein conjugated secondary antibody against the primary IgG and finally co-stained with a nuclear stain, Hoescht.

To confirm macrophage activation and distinguish a phenotype, more rigorous

analysis (beyond IHC with a single antibody) needs to be done. RT-PCR can be

performed to measure mRNA expression of a multitude of inflammatory cytokines and

enzymes. These levels can then be compared to resident alveolar macrophages or cells

that have been purposely activated with classical triggers. Before any of this can be done,

ACPP labeled cells must first be isolated from lung tissue. Therefore, lungs from mice

harboring PyMT 5944 GFP+ metastases and injected with mal-RLQLK(Ac)L ACPP

were digested with collagenase to form a cellular suspension. This suspension was

filtered and subjected to fluorescent associated cell sorting (FACS) to isolate the Cy5

positive cells. Sample histograms, population plots and fluorescent images for the lung homogenates and the isolated cell population are presented in Figure 7.8.

From this data is it clear that the Cy5 cells are a minority population in the lung suspension but they can be isolated. As techniques, such as profusion of the lung to remove blood products, are introduced to the protocol, the macrophage density and sorting efficiency are improving. This approach, while very time consuming, is superior to using an antibody and bead pull down method because with this stagey RT-PCR will only be done on cells that have high levels of ACPP uptake. And as the procedure for preparing the lung homogenates improves, the collection window for Cy5 fluorescence can be narrowed even farther to begin to investigate why some macrophages have higher peptide uptake than others. A collaboration with Dr. Shweta Joshi in the lab of Dr. Patrick Durden at UCSD is currently underway to begin RT-PCR analysis on the collected cells. This lab is also interested in macrophage activation in metastatic lungs.
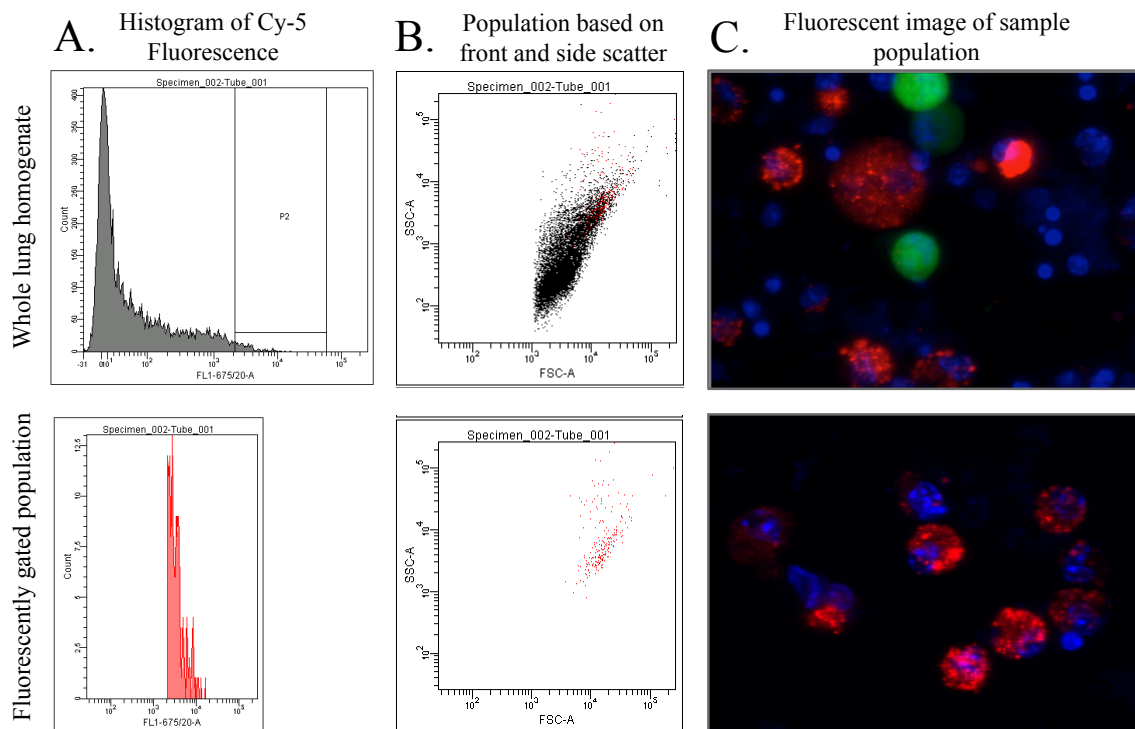
Figure 7.8 FACS based on Cy5 fluorescence isolates the labeled macrophage population from lung homogenates for future RT-PCR analysis. A) Histogram of event counts as a function of Cy5 fluorescence; top panel is for the whole lung homogenate and the bracketed portion represents the population that was collected, bottom panel is the histogram for the sorted population. B) Scatter plot of events based on front and side scatter that gives a representation of cell size; top panel is for whole lung homogenate, bottom panel is for sorted population. C) Representative fluorescent images of live cells from whole lung homogenates (top) and the sorted population (bottom). Red is the Cy5 labeled peptide, Green is GFP expressing tumor cells and blue is Hoescht nuclear stain.

7.5. Discussion

The maleimide RLQLK(Ac)L ACPP has exciting potential for imaging and therapeutic intervention with tumor associated macrophages. Macrophage uptake of this peptide is highly specific, has substantial optical contrast, occurs only when a tumor burden is present and is a function of enzyme cleavability. The next step is to characterize the macrophages responsible for peptide uptake and determine if they have a pro-tumorigenic (M2) phenotype. FACS protocols have been established that can

successfully isolate the ACPP positive cells and RT-PCR can be performed to look at mRNA expression of a multitude of inflammatory cytokines and enzymes. The expression pattern can then be compared to resident alveolar macrophages or cells that have been purposely activated with classical triggers.

Another interesting observation is that ACPP labeling varies among different tumor cell types. With 4T1.2 metastases, maleimide RLQLK(Ac)L had the highest peptide uptake in the tumor nodules, and macrophages in the parenchymal regions were not detectable. The nodules did have bright puncta, which could indicate that the peptide is labeling macrophages that have infiltrated into the cancer. Also, lungs that were riddled with B16-F10 melanoma metastases did not demonstrate RLQLK(Ac)L ACPP uptake, with almost no detectable fluorescence when imaged using the same conditions as those for PyMT 8119 and PyMT 5944 lungs (data not shown). This hints at the possibility of differential macrophage activation for different tumor models. Similar to how high macrophage density is correlated with poor patient prognosis for some types of cancer but can indicate better patient survival in others. A lot of work needs to be done before this hypothesis can be substantiated, but if this is in fact the case, the RLQLK(Ac)L ACPP could be a valuable tool for studying cancer biology with respect to macrophage activation.

In addition to imaging macrophage activity, the hope is to eventually use macrophage targeting with ACPPs to introduce novel therapies. There is now the possibility of combination targeting, where cRGD-MMP ACPPs (described in Chapter 4) deliver chemotherapeutics to the cancer cells while RLQLK(Ac)L ACPPs attack the tumor promoting macrophages. RLQK(Ac)L ACPPs could also be used to target

liposomes loaded with molecules designed to kill the macrophages, or modulators, such as inhibitors and siRNA, that could potentially reprogram the cells to a classically activated phenotype.

7.6. Acknowledgements

The dissertation author would like to thank:

Dr. Lesley Ellies for providing the PyMT 8119 and PyMT 5944 GFP cell lines. Perla Arcaira for culturing and maintaining these cell lines, as well as preparing cells for animal injections. Qing Xiong for peptide synthesis and running the FACS machine that really is a DIVA. Dr. Beth Freidman for assistance with immunohistochemistry protocols. Dr. Mike Whitney for thoughtful discussion.

CHAPTER 8: Fluorescent peptides highlight peripheral nerves during surgery in mice

Fluorescent peptides highlight peripheral nerves during surgery in mice

Michael A Whitney[1], Jessica L Crisp[2], Linda T Nguyen[3], Beth Friedman[1], Larry A Gross[4], Paul Steinbach[4], Roger Y Tsien[1,2,4] & Quyen T Nguyen[3]

Nerve preservation is an important goal during surgery because accidental transection or injury leads to significant morbidity, including numbness, pain, weakness or paralysis. Nerves are usually identified by their appearance and relationship to nearby structures or detected by local electrical stimulation (electromyography), but thin or buried nerves are sometimes overlooked. Here, we use phage display to select a peptide that binds preferentially to nerves. After systemic injection of a fluorescently labeled version of the peptide in mice, all peripheral nerves are clearly delineated within 2 h. Contrast between nerve and adjacent tissue is up to tenfold, and useful contrast lasts up to 8 h. No changes in behavior or activity are observed after treatment, indicating a lack of obvious toxicity. The fluorescent probe also labels nerves in human tissue samples. Fluorescence highlighting is independent of axonal integrity, suggesting that the probe could facilitate surgical repair of injured nerves and help prevent accidental transection.

Accidental transection or injury of nerves during surgery can lead to significant patient morbidity including chronic pain or permanent paralysis. Thin or buried nerves are particularly difficult to distinguish and are therefore the most likely to be damaged during surgical procedures.

Identification of motor nerves before direct exposure is currently dependent on electromyographic (EMG) monitoring[1–3], in which a stimulating electrode is inserted and distal muscle twitches are monitored. EMG is not an imaging technique, so even if a nerve has been identified in one location, there is no visual guidance for how far from the stimulation site the nerve lies. Furthermore, EMG identifies only motor pathways, not sensory fibers such as the first two divisions of the trigeminal nerves, the cochleovestibular nerve or the neurovascular bundle surrounding the prostate gland[4,5], where nerve injury during radical prostatectomy leads to significant urinary incontinence and erectile dysfunction[6]. Finally, EMG fails if axonal or neuromuscular transmission is temporarily blocked distal to the recording site by nerve compression, trauma, tumor invasion, local anesthetics or neuromuscular blockers. Although there are developing technologies for *in vivo* nerve visualization such as optical coherence tomography[7] or laser confocal microscopy[8], these technique have focused on the visualization of the optic or other superficial nerves and may not be generally applicable for viewing nerves in a surgical setting.

Current methods for nerve labeling during surgery depend on retrograde or anterograde tracing of individual axonal tracts using fluorescent dyes[9–12]. The dyes are applied either to the innervation target and travel in a retrograde fashion to label the innervating nerve fibers or directly to identified nerves and label nerve fibers in both anterograde and retrograde directions. Local injections have the drawback of only labeling one nerve fiber tract at a time and that axonal labeling is limited. Axonal transport is relatively slow and it can take days to label a single human nerve. Furthermore, the direct injection of fluorescent dyes contaminates the surgical site with excess fluorescent dyes and may be damaging to the target organs or nerve of interest.

In this study, we describe the development of peptides by phage display[13] that preferentially bind to peripheral nerve tissue compared to adjacent non-nerve tissue after systemic administration.

We used *in vitro* selection with either excised murine peripheral nerves or purified myelin basic protein (MBP) and *in vivo* selection where phage were injected into living mice and nerves were harvested for phage isolation. From the *in vitro* selection against MBP, a single phage with its variable sequence coding for the peptide TYTDWLNFWAWP (NP39) was identified (**Supplementary Fig. 1**).

The *in vitro* selection against excised peripheral nerves yielded three sequences that were repeatedly observed. Of 14 specific phage sequences at the end of seven rounds of selection, 5 coded for NTQTLAKAPEHT (NP41), 3 for KSLSRHDHIHHH (NP40) and 2 for DFTKTSPLGIH (NP42). The remaining phage sequences were each represented only once (**Supplementary Fig. 1**). The *in vivo* selection did not yield any duplicated phage after eight rounds of selection, perhaps because vigorous washing to remove mechanically entangled or loosely bound phage is not possible in a live animal. One sequence selected *in vivo*, AHHNSWKAKHHS (NP38), was chosen for further testing because it contained multiple histidines reminiscent of NP40. Both NP40 and NP38 have been previously identified in various phage selection schemes for binding to proteins (scFV, GST-FLAS-DRD) or hepatoma cell lines, which could indicate that these peptides either bind nonspecifically to proteins or cells or alternatively that they bind to substrates common to both screens[14–17].

[1]Department of Pharmacology, University of California at San Diego, La Jolla, California, USA. [2]Department of Chemistry and Biochemistry, University of California at San Diego, La Jolla, California, USA. [3]Division of Otolaryngology-Head and Neck Surgery, University of California at San Diego, La Jolla, California, USA. [4]Howard Hughes Medical Institute, University of California at San Diego, La Jolla, California, USA. Correspondence should be addressed to Q.T.N. (quyennguyen@ucsd.edu).

Figure 1 Whole-body survey of nerves in mice (*n* = 3) 4 h after injection with 450 nmoles of FAM-NP41. (**a,b**) Brachial plexus. Reflectance image (**a**) showing left brachial plexus (arrow). Smaller branches (~50–100 µm) are easily seen (arrowheads) with fluorescence labeling (**b**) but not in reflectance image. (**c,d**) Sciatic nerve. Reflectance image (**c**) showing right sciatic nerve (arrow). Many more small branches (~50–100 µm) are seen (arrowheads) with fluorescence imaging (**b**) compared to reflectance. (**e,f**) Phrenic nerve. Reflectance image (**e**) showing left phrenic nerve (arrow) descending from the mediastinum to innervate the diaphragm. Note that the nerve is seen as a single linear fluorescent structure (arrow, **f**) compared to the bundle of nerve and connective tissue seen with reflectance (arrow, **e**). Arrowhead points to an intercostal nerve which is easily seen with fluorescence but not with reflectance. (**g,h**) Dorsal cutaneous nerves.
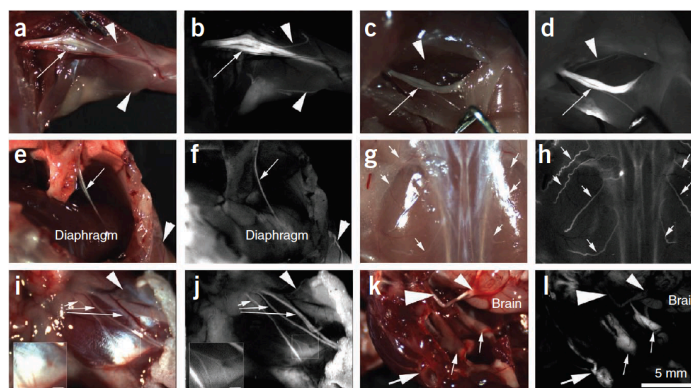
Reflectance image (**g**) showing the dorsal musculature. Fluorescence imaging highlights the dorsal intercostal nerves (arrows, **h**) that are not easily seen with reflectance. (**i,j**) Facial nerve. Main facial nerve branches (arrows) are easily seen with both reflectance (**i**) and fluorescence (**j**). However, a small branch of nerve arborization (arrowhead) leading to the upper face can be distinguished from surrounding tissue with fluorescence but not with reflectance. Insert shows arborizations (~50 µm diameter) of the lower division of the facial nerve that can be easily seen with fluorescence labeling. (**k,l**) Dorsal view of skull base. Reflectance image (**k**) showing left facial nerve (large arrow) wrapping around the ear, trigeminal nerves (small arrows), optic nerves (large arrowhead) and optic chiasm (small arrowhead). Fluorescence image (**l**) shows fluorescence labeling of the facial and trigeminal nerves (peripheral nervous system) but not the optic nerves and chiasm (central nervous system). Scale bar (**a–l**), 5 mm; inserts (**i** and **j**), 1 mm.

Sequences NP38, 40, 41, 42 and a control peptide containing the shared amino acids in random order were similarly synthesized as fluorescein-5(6)-carbonyl group (FAM) conjugates on a C-terminal lysinamide. To test nerve binding affinity *in vivo* of each of the identified sequences, we injected FAM-labeled peptides intravenously into living mice and evaluated the contrast between nerve and muscle 2–4 h after injection. The sequence identified through *in vitro* selection against MBP (NP39) and the sequence identified through the *in vivo* selection (NP38) did not have significant nerve-to-muscle contrast and both showed high-background binding to the surrounding nonneural tissue. The peptide sequence identified most often in *in vitro* selection against excised nerves NP41 had the best nerve to nonnerve contrast. The other two sequences, NP40 and NP42, identified through this same selection strategy also yielded some nerve-to-muscle contrast, although less than that of NP41 (**Supplementary Table 1**). A systemic survey of animals injected with FAM-NP41 revealed that all peripheral nerves and their arborizations (including nerve branches as small as 50 µm in diameter) were brightly labeled, including motor pathways, and sensory nerves such as the first two divisions of the trigeminal nerves (**Fig. 1**). The central nervous system did not appear to take up any fluorescence, perhaps because the peptide did not cross the blood-brain barrier.

To evaluate the kinetics of peptide nerve binding *in vivo*, we imaged sciatic nerves and surrounding nonnerve tissue in mice before and after intravenous administration of FAM-NP41. Before administration of the peptide, there was little contrast between the nerve (small yellow arrowheads) and surrounding nonnerve tissue (**Supplementary Fig. 2a**). Within seconds after intravenous administration of FAM-NP41, fluorescence could be seen leaking from capillaries (arrows) associated with the sciatic nerves (insert, **Supplementary Fig. 2b**). Nerve fluorescence peaked at 10 min after administration (**Supplementary Fig. 2c**) and declined thereafter to a plateau (**Fig. 2a**). Muscle fluorescence was highest immediately after intravenous administration of the peptide, with a half-life of ~20 min (*n* = 5, **Fig. 2a**). Serum half-life was calculated at ~10 min (*n* = 5, **Fig. 2b**). Useful contrast

between nerve and surrounding tissue developed by 2 h after injection (*n* = 5, **Fig. 2c** and **Supplementary Fig. 2e**) and lasted several hours (**Fig. 2a,c** and **Supplementary Fig. 2e,f**), reaching seven- to tenfold by 4–5 h (*n* = 5, **Fig. 2c**). By 24 h after injection, all visible staining had disappeared (*n* = 20). Intravenous injection of the mirror-image peptide with all D-amino acids showed nerve staining at the level of carboxyfluorescein alone (**Supplementary Fig. 3**). The nerve-to-surrounding tissue contrast ratio was correlated with the amount of peptide administered over the range of 15 to 5,000 nmoles per mouse (**Fig. 2d**).

We attempted topical application of FAM-NP41 to label mouse sciatic nerves *in vivo*, however, incomplete wash-out of probe and residual fluorescence due to the probe infiltrating into tissue pockets led to the appearance of linear structures that could be mistaken for nerve fibers.

To evaluate the localization of NP41 binding within nerves, we injected peptide into thy1-YFP transgenic mice whose axons were genetically encoded with YFP under a neuron-specific promoter[18]. To avoid spectral overlap with YFP and to allow imaging deeper in tissues, we replaced FAM with the deep red fluorophore Cy5. Cy5-NP41 precisely labeled nerves that expressed YFP and correlated with nerve fibers as seen in brightfield imaging (**Fig. 3a–c**). No nerve-to-muscle contrast was detected in mice injected with unconjugated Cy5 (**Supplementary Fig. 4a**).

To confirm that changing the fluorophore does not change nerve distribution of NP41, we imaged frozen cross-sections of nerves from mice that had been injected with either 150 nmols FAM-NP41 or Cy5-NP41. Imaged cross-sections showed that labeling was comparable using the two fluorophores (**Supplementary Fig. 4b,c**). To determine if the NP41 was labeling axons, we imaged 3–5 µm cryosections of nerves from thy1-YFP animals treated with Cy5-NP41. Cy5-NP41 localized to the epineurium of the nerves with some labeling of the perineurium and endoneurium, but did not colocalize with either myelin or axons (**Fig. 3d–i**).

To evaluate the ability of NP41 to highlight nerve branches that were buried within tissue, we compared visibility of standard white light reflectance and fluorescent images of Cy5-NP41 and YFP-labeled axons.
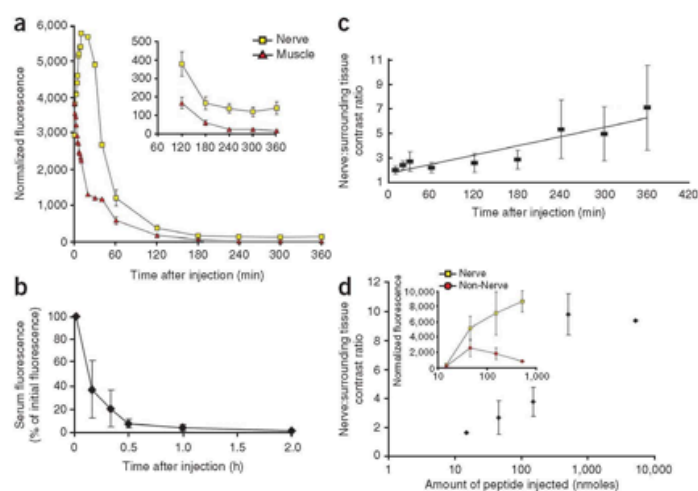
LETTERS

Cy5-NP41 (**Fig. 3c**, insert arrows) was better than brightfield (**Fig. 3a**, insert) or YFP (**Fig. 3b**, insert) at highlighting nerves that were branching deep into muscle. Nerve branches not on the surface were essentially invisible with reflectance imaging (long arrow, arrowheads, **Fig. 4a**). However, these buried branches can be visualized with Cy5-NP41 (arrowheads and long arrow, **Fig. 4b**) and YFP (arrowheads, **Fig. 4c**).

We also assessed the visibility of nerve branches covered by breast cancer tumor in syngeneic graft models[19,20]. For this evaluation we co-administered Cy5-labeled dendrimer conjugates of activatable, cell-penetrating peptides (ACPPs), which highlight tumor margins and FAM-NP41 (refs. 19,20). As shown, nerve branches that descend into the tumor become invisible with reflectance imaging (arrowhead, **Fig. 4d**); however, these buried branches could be visualized, with FAM-NP41 (arrowhead, **Fig. 4e**) protruding into the tumor which has been labeled with Cy5 dendrimer (**Fig. 4f**). The ACPP marks the tumor to be excised, whereas the NP41 highlights the nerve tissue whose preservation is most essential.

Mice showed no change in behavior or activity after injections of 15–5,000 nmoles of FAM-NP41 or 75–300 nmoles Cy5-NP41.

In addition, mice that had been injected with 15 nmoles ($n = 2$), 45 nmoles ($n = 2$), 150 nmoles ($n = 2$), 450 nmoles ($n = 2$), 5,000 nmoles ($n = 1$) showed no significant weight changes or morbidity through 8 weeks of monitoring compared to uninjected mice ($n = 2$). In addition, injection of 150 nmoles of FAM-NP41 had no effect on the shape, amplitude or latency of compound muscle action potential[21] (**Supplementary Fig. 5**), indicating NP41 has no acute effect on peripheral nerve conduction or neuromuscular transmission.

To evaluate the biodistribution of the peptide after systemic administration, organs were harvested from mice intravenously injected with 150 nmoles FAM-NP41 or Cy5-NP41 and fluorescence uptake was evaluated. The majority of the fluorescence accumulated in the kidney and was excreted into the urine. Liquid chromatography–electrospray mass spectrometry of the urine gave different peaks from normal mouse urine spiked with intact FAM-NP41 or Cy5-NP41, indicating that the injected peptides had been efficiently metabolized. The major fluorescently labeled species identified by matrix-assisted laser desorption/ionization mass spectrometry were cysteinamide-Cy5

Figure 3 Cy5-NP41 (acetyl-SHSNTQTLAKAPEHTGC-(Cy5)-amide) labeling of sciatic nerve in Thy1-YFP transgenic mice. (**a**) Low-power brightfield view of left exposed sciatic nerve. Inset shows magnified view of central boxed region. (**b**) Same nerve as in **a** with YFP fluorescence (pseudocolored yellow) superimposed on the brightfield image, showing transgenic expression of YFP in axons. (**c**) Same nerve as in **a** and **b** viewed with Cy5 fluorescence (pseudocolored cyan for maximal contrast during live surgery) superimposed on the brightfield image, showing nerve labeling with Cy5-NP41. Arrows in **b** and **c** point to thin buried nerve branches that are better revealed by the long-wavelength Cy5 fluorescence than by brightfield reflectance or shorter-wavelength YFP fluorescence. There is some nonspecific labeling of skin (asterisk) and cut edges of muscle (arrowhead) by Cy5-NP41. Fortunately, such nonspecific labeling hardly ever has the filamentous appearance of nerves, so an experienced surgeon can usually distinguish nonspecific from specific targets. (**d**) Low magnification longitudinal section showing myelin within the sciatic nerve using differential interference contrast (DIC), pseudocolored blue. (**e**) Same nerve as in **d** showing axoplasmic YFP pseudocolored green (arrows). (**f**) Same nerve as in **d** and **e**, showing Cy5-NP41 labeling (pseudocolored red) of epineurium (arrows) and endoneurium (arrowheads). (**g**) Composite image of **d**, **e** and **f** showing that NP41 labeling does not colocalize with either myelin or axoplasm. (**h–k**) Cross-sectional images corresponding to panels **e–g**.
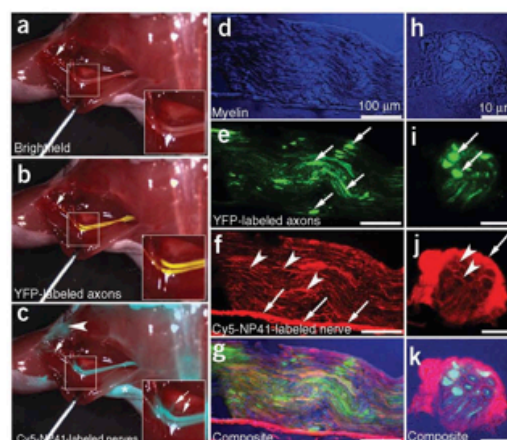
Figure 4 NP41 can highlight buried nerve branches invisible by standard illumination. (a–c) Right facial nerve and its arborizations in a thy1-YFP mouse treated with Cy5-NP41, viewed by (a) white light reflectance, (b) Cy5 fluorescence (pseudocolored cyan) overlaid on reflectance and (c) YFP fluorescence (pseudocolored yellow), also overlaid on reflectance. The short arrow marks a nerve branch visible by all three imaging modes. The arrowheads point to branches that are difficult to differentiate from muscle fascia in reflectance, but clearly distinguishable in both fluorescence images. The long arrow indicates a deeply buried branch visible only by Cy5-NP41 due to the better penetration of far-red wavelengths. (d–f) Left sciatic nerve (arrow) and its arborization in a mouse with a syngeneic 8119 mammary tumor graft[17,18], viewed by (d) white light reflectance, (e) FAM fluorescence 2 h after intravenous injection of NP41 (150 nmoles) (pseudocolored cyan, overlaid on reflectance) and (f) Cy5 fluorescence (pseudocolored green, overlaid on reflectance) from conjugates of activatable cell-penetrating peptides and dendrimers (ACPPDs). The large arrowheads in d and e point to a nerve branch buried under tumor, visible only by FAM fluorescence. Small arrowheads in f denote tumor. See Supplementary Video 1.
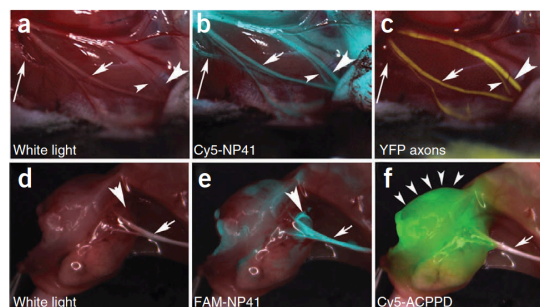
and lysinamide-FAM from mice injected with Cy5-NP41 or FAM-NP41, respectively. Small fractions of successive fragments of NP41 starting from the C terminus were also recovered, suggesting that the entire peptide had been sequentially degraded from the N terminus (Supplementary Fig. 6c,d). In contrast, in urine from mice injected with control all D-amino acid FAM-NP41, the full-length peptide was recovered intact (Supplementary Fig. 6e).

In addition to labeling healthy nerves during nontrauma related surgery, the ability to label and identify severed or injured nerves is also of considerable clinical utility. Such, visualization of injured or severed nerves could guide procedures such as rejoining severed nerves leading to better prognosis after injury. In the cases of injury involving motor nerves, EMG may fail because severed nerves typically lack functionality. Direct labeling could also prove useful when EMG detection does not work because swelling or inflammation leads to short-term loss of nerve conduction. Nerve labeling by FAM-NP41 was 100% of contralateral intact nerve immediately and 1 d after crush injury, decreased by 40% at day 3 and was back to 100% 7 d after injury (Supplementary Fig. 7a–f,j). Because we detected a transient decrease in uptake upon crush injury, we tested if this effect could potentially be due to a temporary decrease in blood flow to the nerve tissue thereby inhibiting uptake. As predicted, nerve devascularization (by intentional injury to the feeding vessels before peptide administration) greatly diminished subsequent uptake of FAM-NP41 (Supplementary Fig. 7g,h).

To evaluate whether NP41 could highlight human as well as mouse nerves, freshly resected recurrent laryngeal nerves and adjacent muscle obtained from patients undergoing total laryngectomy were incubated with FAM-NP41. Selective binding of FAM-NP41 to nerves as compared to adjacent muscle was observed (Supplementary Fig. 8a,b). Histological examination of tissue sections showed that the fluorescence was concentrated in the connective tissue surrounding the nerve, that is, epineurium, perineurium and endoneurium (Supplementary Fig. 8c–h), similar to the binding pattern in murine nerves. Although we cannot administer NP41 to human subjects without much further testing and regulatory approval, these ex vivo tests provide preliminary evidence that NP41 could cross-react with human nerves.

The method of systemic injection of fluorescently labeled peptides to label nerves overcomes some of the major disadvantages of currently available fluorescent tracers, which provide only localized labeling, have low signal-to-noise ratio and require preoperative lead time incompatible with most surgical procedures.

Our peptide localizes predominantly to nerve-associated connective tissue and not to myelin or axonal membranes, which may explain why there were no pharmacological or toxic effects observed in our preliminary toxicity assessments. We achieve good contrast of all nerves in

the body including motor and sensory nerves within 2–3 h compared to tracers that have to be transported in an anterograde or retrograde direction and can require days to label. Contrast from our systemically injected peptides lasts several hours, which would be long enough for most typical operations. A probe of this sort could potentially be further optimized to minimize wash-out time allowing the agents to be provided intravenously within minutes before skin incision. We believe that eventually the use of fluorescently labeled probes for nerve visualization will be routine and will decrease the incidence of inadvertent injury during surgery and may improve identification and repair of nerves after trauma thereby leading to improved patient prognosis.

We were able to detect nerve arborizations as small as 50 μm, which is at least one order of magnitude smaller than most surgically relevant nerves in the human body. In addition, the peptide is cleared within 24 h and completely metabolized, which should reduce the chance of side effects. We would like to optimize NP41 and are therefore using a variety of methods to identify the molecular target(s) to which peptide NP41 binds. The identification of a specific target may allow setting up specific binding assays or using crystallographic information to determine structure-activity relationships and optimize NP41.

Even in the absence of a defined target, we can optimize for nerve affinity, decrease binding to negative tissues, shift fluorescence to longer wavelengths and modify pharmacology to improve contrast of NP41 or related molecules for improved in vivo imaging of nerves.

The minimal murine doses of NP41 used in vivo are currently equivalent to 1–3 g for a 70 kg person. This is within clinical dosing parameters for antibiotics, which are routinely given at such doses two to three times daily for systemic infections; intravenous immunoglobulins may be given in doses up to 150–300 g for a 70 kg person. As pharmacokinetic clearance is substantially slower in humans compared to mice, similar contrast may be achieved using a lower dose of NP41 or related contrast agent although slower pharmacokinetics may increase lead time required before surgery. In addition to improving affinity/specificity of NP41 the attachments of macromolecular carriers or other controlled released formulation may be required to optimize this contrast agent for potential clinical use.

METHODS

Methods and any associated references are available in the online version of the paper at http://www.nature.com/naturebiotechnology/.

Note: Supplementary information is available on the Nature Biotechnology website.

LETTERS

1. Gantz, B.J. Intraoperative facial nerve monitoring. Am. J. Otol. Nov., (Suppl.), 58–61 (1985).
2. Davis, W.E., Rea, J.L. & Templer, J. Recurrent laryngeal nerve localization using a microlaryngeal electrode. Otolaryngol. Head Neck Surg. 87, 330–333 (1979).
3. Miller, M.C. & Spiegel, J.R. Identification and monitoring of the recurrent laryngeal nerve during thyroidectomy. Surg. Oncol. Clin. N. Am. 17, 121–144 (2008).
4. Walz, J., Graefen, M. & Huland, H. Basic principles of anatomy for optimal surgical treatment of prostate cancer. World J. Urol. 25, 31–38 (2007).
5. Walz, J. et al. A critical analysis of the current knowledge of surgical anatomy related to optimization of cancer control and preservation of continence and erection in candidates for radical prostatectomy. Eur. Urol. 57, 179–192 (2010).
6. Kübler, H.R. et al. Impact of nerve sparing technique on patient self-assessed outcomes after radical perineal prostatectomy. J. Urol. 178, 488–492 (2007).
7. Zhivov, A., Blum, M., Guthoff, R. & Stachs, O. Real-time mapping of the subepithelial nerve plexus by in vivo confocal laser scanning microscopy. Br. J. Ophthalmol. 94, 1133–1135 (2010).
8. Zysk, A.M., Nguyen, F.T., Oldenburg, A.L., Marks, D.L. & Boppart, S.A. Optical coherence tomography: a review of clinical development from bench to bedside. J. Biomed. Opt. 12, 051403 (2007).
9. Kobbert, C. et al. Currents concepts in neuroanatomical tracing. Prog. Neurobiol. 62, 327–351 (2000).
10. Richmond, F.J.R. et al. Efficacy of seven retrograde tracers, compared in multiple-labelling studies of feline motoneurones. J. Neurosci. Methods 53, 35–46 (1994).
11. Marangos, N., Illing, R., Kruger, J. & Laszig, R. In vivo visualization of the cochlear nerve and nuclei with fluorescent axonal tracers. Hear. Res. 162, 48–52 (2001).
12. O'Malley, M. et al. Fluorescent retrograde axonal tracing of the facial nerve. Laryngoscope 116, 1792–1797 (2006).
13. Pasqualini, R. & Ruoslahti, E. Organ targeting in vivo using phage display peptide libraries. Nature 380, 364–366 (1996).
14. Shtatland, T., Buettler, D., Kossodo, M., Pivovarov, M. & Weissleder, R. PepBank—a database of peptides based on sequence text mining and public peptide data sources. BMC Bioinformatics 8, 280 (2007).
15. Berger, S., Bannantine, J.P. & Griffin, J.F.T. Autoreactive antibodies are present in sheep with Johne's disease and cross-react with mycobacterium avium subsp. Paratuberculosis antigens. Microbes Infect. 9, 963–970 (2007).
16. Kim, G.S. et al. Suppression of receptor-mediated apoptosis by death effecter domain recruiting domain binding peptide aptamer. Biochem. Biophys. Res. Commun. 343, 1165–1170 (2006).
17. Jiang, Y. et al. Targeting of hepatoma cell and suppression of tumor growth by a novel 12mer peptide fused to superantigen TSST-1. Mol. Med. 12, 81–87 (2006).
18. Feng, G. et al. Imaging neuronal subsets in transgenic mice expressing multiple spectral variants of GFP. Neuron 28, 41–51 (2000).
19. Olson, E.S. et al. Activatable cell penetrating peptides attached to nanoparticles: dual probes for fluorescence and magnetic resonance imaging of proteases in vivo. Proc. Natl. Acad. Sci. USA 107, 4311–4316 (2010).
20. Nguyen, Q.T. et al. Surgery with molecular fluorescence imaging using activatable cell penetrating peptides decreases residual cancer and improves survival. Proc. Natl. Acad. Sci. USA 107, 4317–4322 (2010).
21. Osuchowski, M.F., Teener, J. & Remick, D. Noninvasive model of sciatic nerve conduction in healthy and septic mice: reliability and normative data. Muscle Nerve 40, 610–616 (2009).

ONLINE METHODS

All experiments on mice were performed under protocol approved by the University of California San Diego Institutional Animal Care and Use Committee.

Peptide selection with phage display. Phage display screens were used for *in vitro* selection of peptides binding to excised murine nerves or purified MBP and for an *in vivo* selection screen in which the phage library was injected in the tail vein of mice followed by dissection of nerve tissue and isolation of phage. For the *in vitro* selection, an m13 phage library expressing random 12-amino-acid sequences on the N terminus of gIII (New England Biolabs) were processed through two parallel *in vitro* selections for binding to either purified MBP or to excised murine nerves. In the selection against MBP, phage expressing a library of peptides were selected through multiple cycles for binding to biotinylated MBP, using avidin agarose to isolate selected phage. Specifically, the phage library was mixed with biotinylated MBP and allowed to bind for 1 h. Avidin agarose was added and incubated for an additional hour. Nonbinding phage were removed by washing the agarose three times with PBS solution and the supernatant was plated for titer and amplification for subsequent cycles. This process was repeated five times; once repeat sequences appeared, these were synthesized for affinity testing.

In the selection against excised murine nerves, phage from the same library as the selection against MBP were isolated based on differential binding to excised murine nerves and not to adjacent muscles and fat tissue. Phage were processed through multiple cycles of selection, with representative phage being isolated and sequenced after each cycle. Specifically, for positive selection using nerve tissue, nerve tissue was dissected/washed and mixed with a phage library. After incubation, the mixture (containing mostly intact nerves with phage particles that had variable affinity for nerves) was centrifuged and the pellet washed with PBS. The pellet was homogenized and plated for titering and reamplification. For negative selection using nonnerve tissues, nonnerve tissues (muscle and fat) were dissected from normal mice and incubated with the phage library obtained from the positive selection. After the incubation period, the mixture was centrifuged and the supernatant plated for titer and sequencing. Once individual sequences started to appear repetitively, these were resynthesized as peptides for affinity testing.

For the *in vivo* selection, the same phage library as for the *in vitro* selections was injected in the tail vein of mice followed by dissection of nerve tissue and isolation of phage. In each case isolated phage were reamplified and reinjected to iterate each selection step up to 8 times. Specifically, phage were injected into wild-type mice. Following a binding/washout period of 2–4 h, the mice were euthanized and nerve tissue (sciatic, brachial plexus, cranial nerves) dissected, washed and homogenized. Homogenates were plated for titering and re-amplified for subsequent injections. Sample phage were sequenced after each round of selection. Once repeat sequences appeared, they were synthesized for affinity testing.

Peptide synthesis and fluorophore labeling. Peptides were either synthesized in our laboratory on an Agilent Prelude peptide synthesizer using standard protocols for fluorenylmethoxycarbonyl (Fmoc) solid-phase synthesis or made by AnaSpec. All peptides were acetylated at the N terminus and labeled on the C terminus by (either (Cy5-l-cysteinamide or ε-(fluorescein-5(6)-carbonyl)-L-lysinamide) (**Supplementary Fig. 3**). Carboxyfluorescein labeled peptides were generated by Fmoc synthesis with ε-(fluorescein-5(6)-carbonyl)-L-lysinamide. Cy5 labeling was done after cleavage from the synthesis resin by reacting the thiol group of the L-cysteinamide with Cy5 mono-maleimide (GE Healthcare). Peptides were purified to >95% purity using C-18 reversed phase high-performance liquid chromatography (HPLC) with a 20–50% acetonitrile gradient in 0.1% trifluoroacetic acid and confirmed by mass spectrometry.

Testing of nerve binding with fluorescently labeled peptides. Wild-type albino C57BL6 (Jackson Laboratory) or SKH1 (Charles River Laboratories) mice were treated intravenously with 150 nmoles of fluorescently labeled NP41 by tail vein injection. Following a 2–4 h wash-out period for FAM-NP41 or 5–6 h for Cy5-NP41, mice were anesthetized with ketamine and midazolam (80 mg/kg intraperitoneally), a skin incision was made over the dorsal surface of the hind legs and the sciatic nerves exposed bilaterally. Nerves were imaged

using a Zeiss Lumar fluorescent dissecting microscope or a custom-made surgical fluorescence imaging system based on an Olympus dissecting microscope. Carboxyfluorescein and YFP were imaged with 450–490 nm excitation and 500–550 nm emission. Cy5 was imaged with 590–650 nm excitation and 663–738 nm emission.

Time course of nerve binding. Female 8-week-old SKH1 mice were anesthetized with ketamine and midazolam and a skin incision was made over the dorsal surface of the hind legs and the sciatic nerves exposed. A preinjection image was taken a dissecting microscope (Lumar Zeiss) and a monochrome CCD camera (Coolsnap). The mice were injected intravenously with 150 nmoles of FAM-NP41. Sequential fluorescence images were obtained as described above: 450–490 nm excitation and 500–550 nm emission, exposure 15 ms–5s. For quantification, integrated intensity was determined using ImageJ for nerve regions and compared to adjacent muscle or other nonnerve tissue. We analyzed 5–10 selected regions of 40 × 40 pixels of each type of tissue and all tissues were imaged using identical parameters. Background was subtracted using a measurement with identical settings in a region with no mouse and values were averaged.

Dose response of peptide binding. Female 8-week-old SKH1 mice (average weight 25 g) were treated with varying amounts of FAM-NP41 ranging from 15–5,000 nmoles. After a 2-h wash-out period, mice were euthanized and sciatic nerves exposed. Nerves and adjacent nonnerve tissue were delineated with Image J and relative fluorescence was measured. Quantification of fluorescence was then performed after subtraction of dark current and normalizing to uninjected specimens. For the mice injected with 5,000 nmoles of NP41, we found that background fluorescence was still very high at 2 h, making the contrast ratio low even though the absolute nerve fluorescence was very high. The skin incision on these mice was repaired and the mice allowed to awaken from anesthesia. At 6 h after initial NP41 administration, the mice were euthanized and the sciatic nerves exposed and analyzed as above.

Nerve labeling in tumor model. Syngeneic tumor grafts were generated in the laboratory with 8119 murine mammary adenocarcinoma cells[19]. We injected 1×10^6 cells intramuscularly into the left flank of albino C57BL/6 mice (Jackson Laboratory). Tumor isografts were monitored until tumor size was ~1 cm in largest diameter (~7–10 d). Cy5-ACPPD (2 nmoles)[19] and FAM-NP41 (150 nmoles) were administered through tail vein injection 48 and 2–3 h, respectively, in the same animal before imaging.

Toxicity and motor function. Female 8-week-old SKH1 mice (average weight 25 g) were treated with varying amounts of FAM- NP41 ranging from 15 to 5,000 nmoles. Generalized activity, behavior and weight gain were evaluated after single intravenous injection of 15–5,000 nmoles of FAM-NP41 on a daily basis for 3 d after injection. Thereafter, the mice were monitored three times per week for 8 weeks. We found that generalized activity, behavior and weight gain were similar between NP41-treated and control mice.

Nerve conduction studies. Maximal compound muscle action potential amplitude (CMAP) and nerve conduction latency were measured. Briefly, control female 8-week-old SKH1 mice and mice treated with FAM-NP41 were anesthetized with ketamine-midazolam and placed in a prone position. CMAP potentials were evoked (Grass stimulator) with stimulating electrode (Medtronics) placed 2 mm lateral to the midline. The recording electrode was an ear-clip electrode (Life-tech.com) placed on the digits of the hind foot and the reference electrode was placed on the heel of the foot. Maximal CMAPs were generated by gradually increasing the stimulation (5–10 V, 1 pulse per second, paired, 0.5–2 s duration) until a maximal, artifact-free tracing was obtained. The CMAP traces were captured on a digital oscilloscope (Tektronic). Nerve conduction latency was measured from the beginning of the stimulation to the start of the upslope. CMAP amplitude was measured from the start of the upslope to the peak. Data were analyzed using two-tailed Student's *t*-test.

Peptide metabolism. For liquid chromatography-mass spectrometry (LC-MS), each mouse urine sample was diluted and analyzed by reversed-phase HPLC with a 1 mm inner diameter, 15 cm length Higgins PLRP-S C18

column. The outlet from the HPLC (Michrom Magic with UV detector) was connected through a Jasco 920 fluorescence detector to the electrospray interface of a LTQ Orbitrap XL mass spectrometer. A 2 μl sample of mouse urine was diluted to 80 μl with solvent A, 0.1% formic acid in water. The HPLC had a 130 μl sample loop. The column temperature was 40 °C and the flow rate was 80 μl/min. After a 4 min delay (2% solvent B) for the injection, the gradient was 2 38% solvent B (0.1% formic acid in acetonitrile) in 37 min, followed by a 5 min step of 90% B. The pure peptide diluted from stock solution eluted at ~24 min. UV absorbance (single wavelength, 215 nm), fluorescence and mass spectral chromatograms were collected simultaneously for each LC-MS run. FAM and Cy5 fluorescences were measured at excitation/emission wavelength settings of 480/510 and 640/680 nm respectively. The fluorescence detector flow cell volume was 5 μl. The Orbitrap was set for 5 s scans with 30,000 resolution from 100 to 1,800 m/z. The entire HPLC output went into the mass spectrometer without splitting.

Effect of nerve injury on labeling. Wild-type mice were anesthetized and the left sciatic nerve exposed and crushed with microforceps for 3–5 s. Muscular contractions during the crush and immediately afterwards were monitored to ensure uniformity of the injury. The skin incision was then closed and mice returned to their cages to recover. At varying times after crush injury, FAM-NP41 (150 nmoles) was administered intravenously. After wash-out for 2–3 h, mice were anesthetized, bilateral sciatic nerves exposed and fluorescent images obtained. Nerve and adjacent muscle fluorescence were measured using ImageJ software by measuring standardized boxed regions. Crushed and contralateral control nerve fluorescence were compared for each animal.

Human nerve labeling. Recurrent laryngeal nerves and adjacent muscle obtained from patients undergoing total laryngectomy for laryngeal cancer at the time of surgery were incubated with FAM-NP41 at 50 μM for 15 min and washed three times in saline for 15 min each. The nerve and muscle segments were then placed on a black nonfluorescent plate and imaged (Maestro, CRI). The nerve segments were then embedded in Tissue-Tek, frozen and cryosectioned. We then imaged 7–10 μm cryosections with standard fluorescence microscopy. Adjacent sections were stained with hematoxylin and eosin (H&E) and imaged by transmitted light.
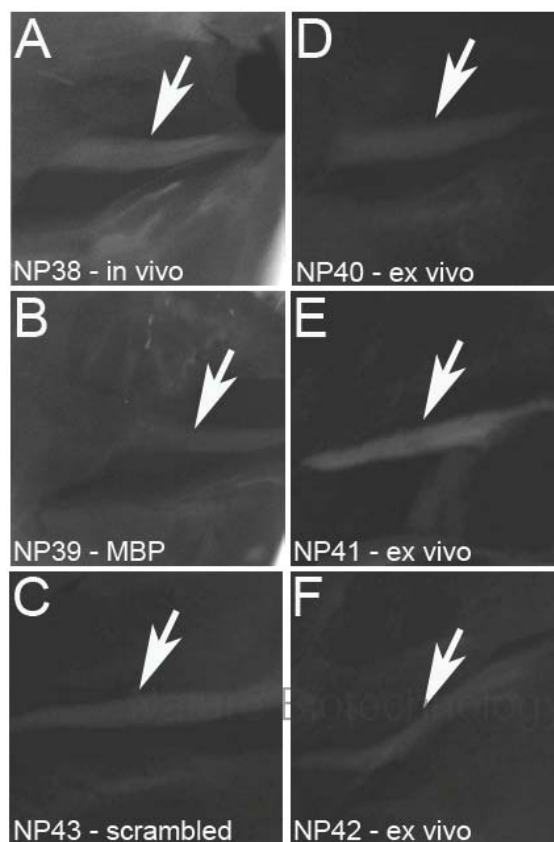
Figure S1. Nerve binding affinity of FAM-labeled peptides. A-F. Fluorescence images of exposed sciatic nerves in living mice 2-3 hours following administration of 20 nmoles of (A) FAM-NP38 (B) FAM-NP39 (C) FAM-NP43 (D) FAM-NP40 (E) FAM-NP41 and (F) FAM-NP42. Labels "in-vivo", "MBP", "ex vivo" indicate mode of phage selection. "Scrambled" denotes a control containing similar amino acids as found in the selected phage but in random order.

Table S1.

Table 1. Peptides selected from phage display screen

Selection strategy	Peptide sequence	Name	Nerve/Muscle contrast
In vivo	AHHNSWKAKHHS	NP38	1.8
In vitro against MBP	TYTDWLNFWAWP	NP39	1.4
In vitro against excised nerves	KSLSRHDHIHHH	NP40	1.9
	NTQTLAKAPEHT	NP41	3.8
	DFTKTSPLGIH	NP42	1.5
Control random sequence	STARDLWPHGKE	NP43	1.3

When these peptides were chemically resynthesized, acetyl-SHS was added at the N-terminus to mimic the context within the phage display backbone, and G was added at the C terminus to provide a flexible linker between the dye and the peptide.
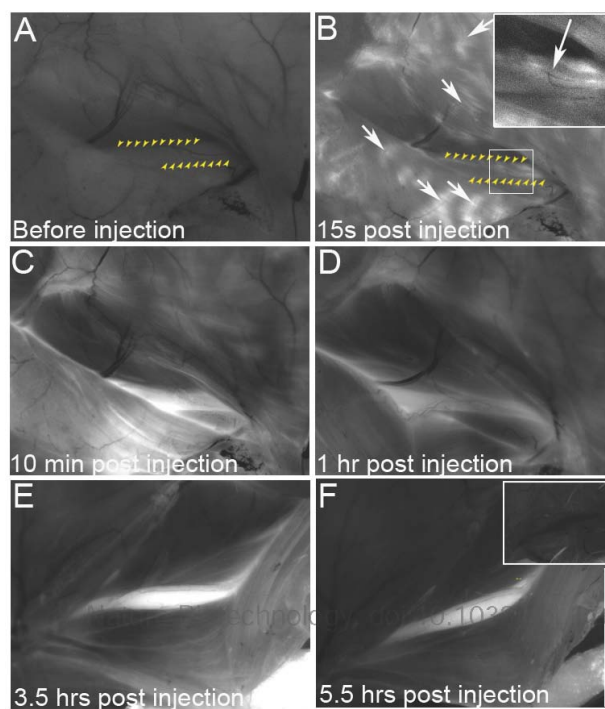
Figure S2. Fluorescence images of sciatic nerves and surrounding non-nerve tissue in living mice (n=2). Prior to administration of 150 nmoles FAM-NP41 (A), there was little contrast of the nerve (arrowheads) in relation to surrounding non-nerve tissue. Within seconds following intravenous injection of FAM-NP41 (B), the fluorescence could be seen leaking from capillaries (arrows), including capillaries associated with the sciatic nerves (insert). Nerve to surrounding tissue contrast gradually increases fromless than 1.5 fold at 10 minutes post injection (C) increasing linearly from 1 hour (D), 3.5 hours (E), and reaching a maximum of 6.9±3.7 at ~5.5 hours post injection and is completely gone by 24 hours (insert) (F). This gradual increase in nerve to muscle contrast highlights how NP41 washes out faster from non-nerve tissue compared to sciatic nerve. Scale bar = 5mm.
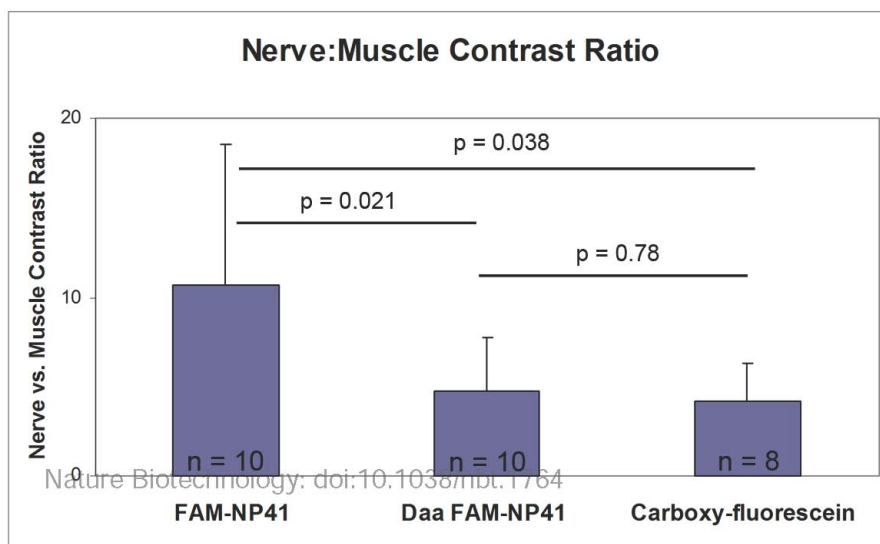
Figure S3. Intravenous injection of control FAM-NP41 with all-d amino acids showed reduced nerve binding to the level of carboxy-fluorescein alone.
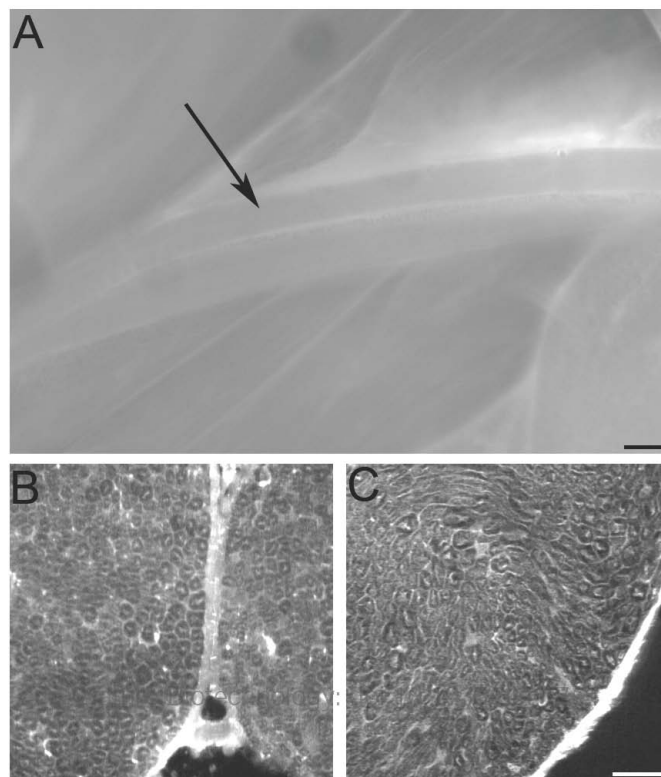
Figure S4. A. Fluorescence image of sciatic nerve (arrow) 4.5 hours after injection of 150nmoles of unconjugated Cy5 showing no nerve to surrounding tissue contrast (scale bar = 1mm). Fluorescence image of 5 μm section from sciatic nerve 4.5 hours after injection of 150nmoles FAM-NP41 (B) or 150nmoles of Cy5-NP41 (C). scale bar = 100 μm.
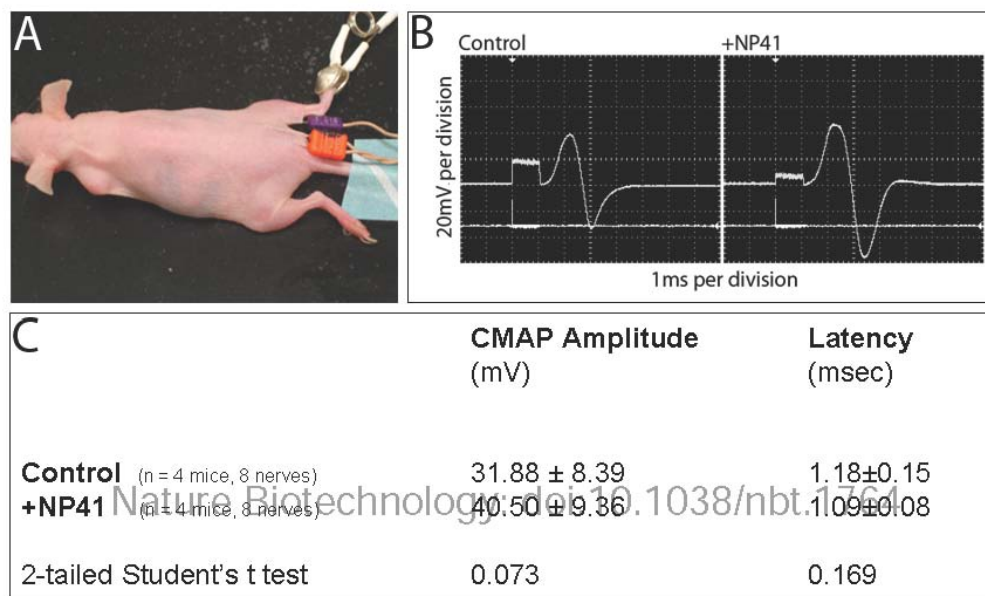
Figure S5. Nerve conduction studies. A. Compound muscle action potentials (CMAP) were evoked with stimulating electrodes (orange) placed 2 mm lateral to the midline. The recording electrode was an ear-clip electrode placed on the digits of the hind foot and the reference electrode (purple) was placed on the heel of the foot. B. Representative CMAP tracing for control (left panel) and FAM-NP41-treated (right panel) animals. C. Tabulated CMAP amplitude and latency, showing that there is no significant difference between the control and NP41-treated nerves by 2-tailed Student's t test.
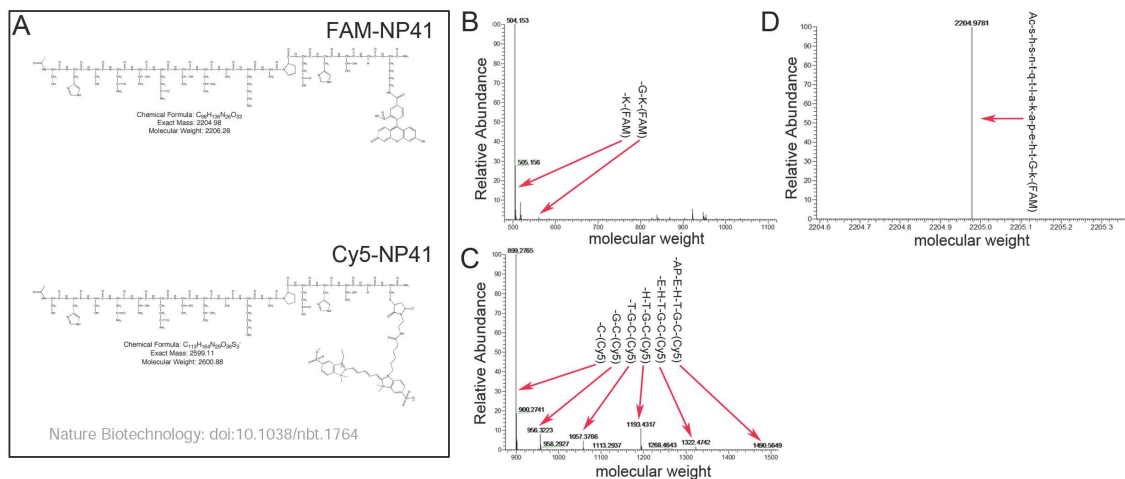
Figure S6. The major fluorescently labeled species identified from mouse urine following treatment with FAM-NP41 (A) or Cy5-NP41 (B) were lysinamide-FAM (C) or cysteinamide-Cy5 (D) respectively. Small fractions of successive fragments of NP41 starting from the C terminus were also recovered, suggesting that the entire peptide had been degraded (C-D). In contrast, analysis of urine samples from mice treated with control all-d amino acid NP41 resulted in the recovery of the entire intact sequence (E).
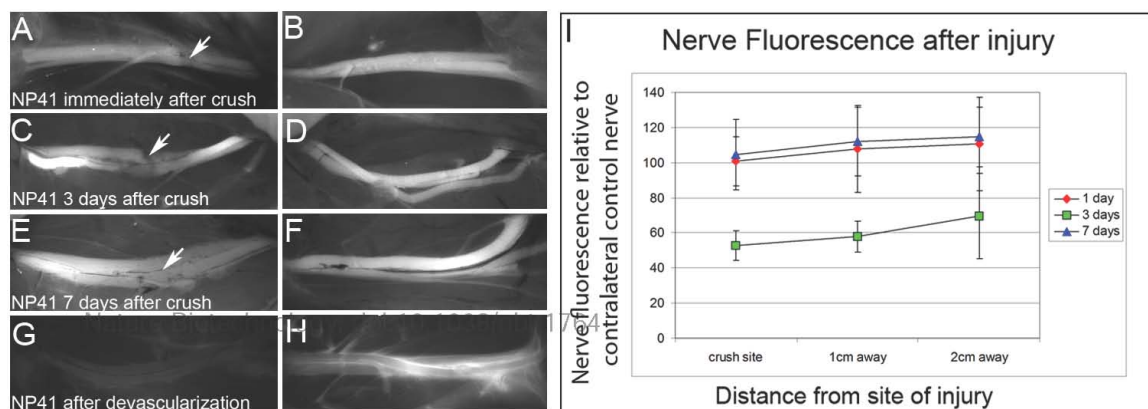
Figure S7. Nerve labeling with FAM-NP41 is diminished at 3 days following injury but recovers by 7 days after injury. A-H, Representative sciatic nerves in which FAM-NP41 was injected a few minutes (A), 3 days (C), or 7 days after crushing (E) or after devascularization (G) Images taken 2-3 hours after injection of peptide. Panels B, D, F, and H show the control uninjured nerves contralateral to A, C, E, and G respectively. I. Graph showing that a) nerve fluorescence does not significantly diminish as a function of distance from crush site and b) nerve fluorescence is significantly diminished by day 3 (n = 3) but recovers to equality with contralateral control nerve by day 7 (n = 2) after crush (Occasionally, nerve labeling immediately at the site of injury was slightly diminished compared to nerve labeling several centimeters away from the site of injury (A) but this observation was highly variable and not statistically significant (I).
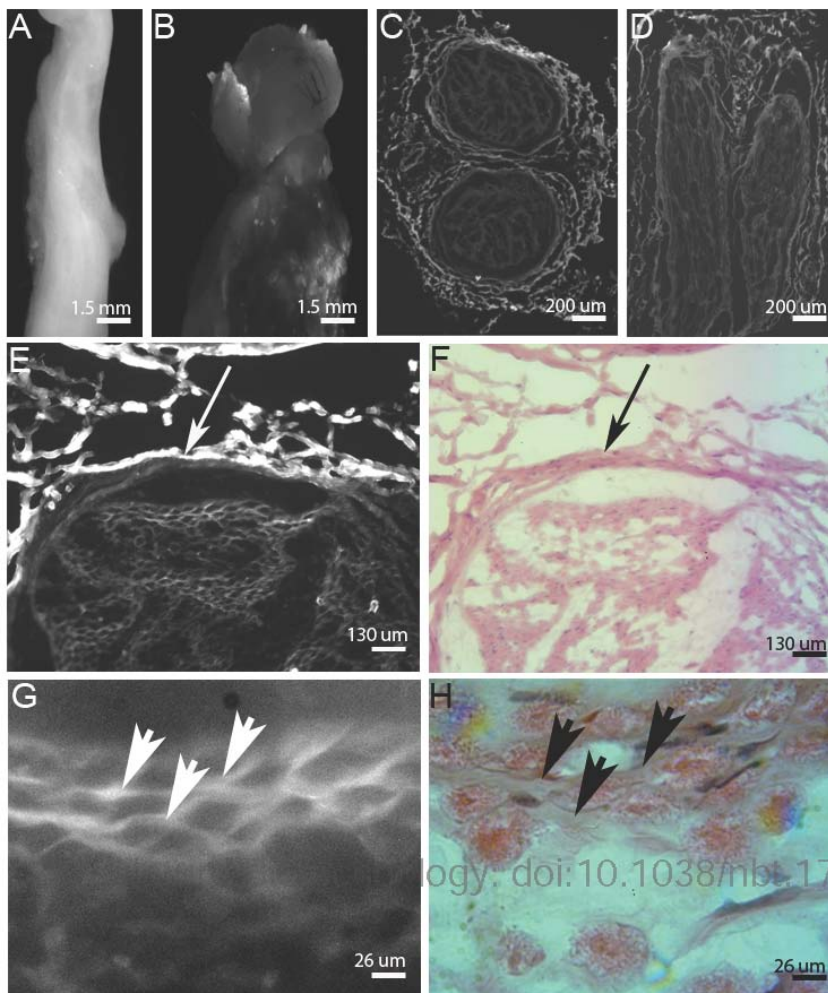
Figure S8. Human nerve labeling with FAM-NP41. Fluorescence images at matching

gain settings of (A) recurrent laryngeal nerve and (B) adjacent muscle freshly resected

from patient undergoing total laryngectomy after labeling with FAM-NP41. Fluorescent

photomicrograph of human nerve in cross-section (C) and longitudinal section (D). High-

power fluorescent and H&E cross sections of human nerve showing staining of

epineurium (arrow,E, F) and endoneurium (arrowhead,G, H).

8.1. Acknowledgements

This chapter is a reprint of the work as it appears in Nature Biotechnology, published February 2011.

The dissertation author was secondary author on this material and contributed to experimental design, execution of experiments, interpretation of data and editing of manuscript.

The dissertation author would like to thank:

Dr. Mike Whitney and Dr. Quyen Nguyen for performing the phage screen that generated the peptide sequences we tested. Dr. Whitney for peptide for synthesis. Dr. Nguyen for performing *in vivo* imagining and collaboration with the pharmacokinetic studies. Dr. Beth Friedman for the confocal microscopy on tissue sections and training with tissue sectioning, imaging and staining. Dr. Larry Gross for mass spectroscopy analysis on peptide metabolites. Paul Steinbach for the numerous hours he devoted to developing new ways of imaging tissue sections and for engineering the fluorescence guided surgery equipment. Dr. Linda Nguyen for nerve injury experiments and investigating peptide binding to human nerve tissue.

CHAPTER 9: Evolution of the Nerve Homing Peptide and Discovery of New Sequences with Enhanced Nerve Fluorescence

9.1. Abstract

The preservation of peripheral nerves is a main goal of any surgical procedure because accidental transection leads to significant patient morbidity and nerve regeneration is slow and often incomplete. Previous work from our lab generated fluorescently labeled nerve-homing peptides whose sequences were discovered from a phage display selection with mouse peripheral nerves. The best peptide that arose from that screen was NP 41. Many attempts were made to improve nerve selectivity and enhance nerve:background contrast. These include modifications to the amino acid sequence, addition of polyethylene glycol and trying to improve peptide avidity by making multimeric probes. Unfortunately, none of these approaches were successful. To increase peptide signal penetration through tissue, the fluorophore was changed from fluorescein to red shifted dyes ranging from tetramethyl rhodamine to IR800, but an inverse trend between fluorophore wavelength and nerve contrast was observed. Moving beyond NP 41, new peptide sequences resulting from phage display cross selections against myelin basic protein and excised nerve tissue were tested. NP 124 was discovered, which had similar contrast to NP 41 but a significant increase in nerve fluorescence. Finally, a phage selection was done against excised human nerve tissue that provided the sequence for HNP 301, which possessed significant nerve contrast when tested in rodents. It is hypothesized that because this peptide was identified for its affinity

to human nerves, it will be have a greater potential to bind human nerves when this technology is translated to the clinic.

9.2. Introduction

Peripheral nerve preservation is a critical goal of any surgical procedure because accidental transection leads to significant patient morbidity. Also, nerve regeneration is slow and often incomplete. Surgeons typically identify peripheral nerves based on their relationship to nearby structures as well as their appearance as white, elongated fibers. However, identification based on physical criteria can be challenging, especially in cases of tumor involvement, inflammation, infection, or in surgical fields that have been previously operated on.

Current techniques for nerve labeling primarily depend on tracing individually identified axonal tracts with fluorescent dyes (Richmond, Gladdy et al. 1994; Kobbert, Apps et al. 2000; Marangos, Illing et al. 2001; O'Malley, Wittkopf et al. 2006). The dyes are either applied to the target and travel in a retrograde fashion to label the innervating nerve fibers, or are applied directly to the identified nerves and label the nerve fibers both anterogradely and retrogradely. Some issues with thse methods are: a minimal number of nerves can be labeled simultaneously, there is limited accumulation of fluorescent dyes along the axonal tracts, and retrograde transport is relatively slow, on the order of millimeters per day.

Chapter 8 describes fluorescently labeled nerve-homing peptides that were derived using phage display selection with mouse peripheral nerves (Pasqualini and Ruoslahti 1996; Whitney, Crisp et al. 2010). These nerve-binding peptides are superior to

the imaging methodologies described above primarily because systemic delivery allows all peripheral nerves in the body to be labeled. Also, nerve fibers are clearly delineated in the context of adjacent non-neural structures, the binding of the peptides occurs quickly, and visualization of peripheral nerves can be accomplished within hours.

Even with these advantages, there are still issues that need to be addressed. The first is determination of the binding target. While it was observed that the peptide localizes to connective tissue, such as the epineurium and perineurium, the exact molecular target remains a mystery. This chapter will introduce a strategy to identify those proteins using chemical cross-linking, mass spectroscopy and bioinformatics (Deutsch, Lam et al. 2008; Leitner, Walzthoeni et al. 2010). Sequence modifications were used to try and determine what portion of the peptide is required for nerve affinity. Finally, chemical conjugations were done in attempts to improve the peptide' sensitivity and avidity. Another option is to move beyond the original sequence with new selection strategies.

Because the intended clinical application of nerve-homing peptides is in human patients, a phage selection was performed to find unique peptide sequences that bound to human nerves. It is hypothesized that because these peptides were identified for their affinity to human tissue, following administration into human patients, these probes will be more likely to bind human nerves compared to sequences that were selected against rodent nerves.

9.3. Methods

9.3.1. Peptide synthesis

Peptides were synthesized, labeled and purified as previously described in Chapter 8. For generating the cross-linking version of NP 41 that is discussed in section 9.4.2, the standard NP 41 was synthesized with an addition cysteine and biocytin (lysine conjugated to biotin, Anaspec) on the C terminal side. Hydrazine-peg$_2$-maleimide was reacted with the free thiol on the cysteine to generate the complete peptide. To generate NP 41 AcK, the lysine residue was reacting with acetic anhydride or an fmoc version of the modified amino acid (Anaspec) was incorporated during synthesis. NP 41 FAM-dimer was made by synthesizing NP 41 FAM with an additional cysteine residue on the C terminus and allowing two of the peptides to form a disulfide bond. The peg$_{11}$ dimer peptide was made in a similar fashion but instead of forming a disulfide bond, a peg$_{11}$ linker was inserted using thiol-maleimide chemistry. Cy5 bis NP 41 is a result of reacting two NP 41 peptides, with C terminal cysteines, with a bis-maleimide-Cy5 (GE LifeSciences). The G2 dendrimer (Dnanotech) was reacted with 3 molar equivalents of NP 41 and molar equivalent of Alex 647. The peptide (C-terminal cysteine) was attached via an aldehyde group (introduced through a maleimide cross-linker) to peg$_4$ylated G2 dendrimer labeled via the amines with a hydrazine (using Solulink chemistry). The unreacted hydrazines were capped with a peg$_4$-aldehyde. Finally, all of the dyes mentioned in section 9.4.4 were either purchased (Tetramethyl Rhodamine, Texas Red: Life Technologies, Cy5: GE Life Sciences, IR-800 CW: Licor) with maleimide

functional groups, or synthesized with a maleimide moiety by Dr. Stephen Adams (Methylene Blue and Resofrufin).

9.3.2. In vivo animal imaging

Sciatic nerve imaging and contrast ratio quantitation were performed as previously described in Chapter 8. The standard imaging protocol was 150 nanomole dose with a circulation time of 4 hours. Mice were placed under heavy anesthesia, to a point where they were not responsive to a foot pinch, and the sciatic nerves were exposed and imaged on a Lumar stereoscope (Ziess) using the fluorescein filter set. Minor variations to this protocol were made depending on the peptide construct, but those will be noted in the results section.

9.3.3. Two-photon confocal imagining

Mice were injected with 150 nanomoles of FAM labeled NP 41 and sacrificed 3 hours post injection. The skin on the cheek of the animal was removed and facial nerves were imaged in the context of their surrounding tissues on an Olympus FluoView[TM] FV1000MPE Multiphoton Laser Scanning Microscope using a 20X dipping water objective.

9.3.4. Cross linking of peptide to nerve tissue

Mice were injected with 200 nanomoles of NP41-FAM-hydrazine-biotin and sacrificed 1 hour post injection. Sciatic nerves were harvested and placed in 2mM KIO_4 in PBS at pH 5.5 for 1 hour in the dark. Nerves were then washed 3 times in water and snap frozen in liquid nitrogen before being shipped on dry ice to our collaborator in

Germany. For imaging experiments, nerves were washed overnight at 4 C in water prior to visualization on the Maestro (CRI).

9.3.5. Tissue sectioning, imaging and staining

Cryosections of sciatic nerves were processed, imaged and dyed as previously described in Chapter 3 and Chapter 8.

9.3.6. Human nerve phage selection

Two M13 phage libraries were used, with either 7 or 12 random amino acid sequences expressed on the N-terminus of the gIII coat protein. (New England Biolabs) Selections were based on phage binding to freshly resected or frozen human nerves. Phage libraries were incubated with human nerve homogenate, centrifuged, and the pellets were washed, rehomogenized and plated for phage tittering and re-amplification. Each library went through up to 7 rounds of positive selection (for greater detail on selection strategy refer to Chapter 8). Negative selections were also performed by incubating the phage library with muscles and fat tissue in between rounds of positive selection. After each round, sample plaques were chosen for sequence analysis. Once the sequences began to converge, the selection was stopped and the sequences with the most repeats were converted to synthetic peptides.

9.4. Results

9.4.1. Peptide contrast varies with type of anesthesia

It was observed with NP 41 that nerve contrast varied depending on how the mice were anesthetized. For most of the studies presented in the previous chapter mice were

anesthetized with a 50μL intraperitoneal (IP) injection of a 1:1 mixture of ketamine and midazolam (KM). This rendered the mice unconscious for 30-45 minutes after peptide injection but they were awake for over an hour prior to imaging. When this method was temporarily unavailable, the mice were put under using a vaporizer that administered a low percentage of isofluorane. The mice were only anesthetized for a short time during peptide injection and then permitted to wake up almost immediately after. It was observed that nerve contrast and absolute fluorescence were significantly lower than previously reported.

This led to an experiment that measured both nerve and muscle fluorescence under various forms and durations of anesthesia (Figure 9.1). Mice were either given i) one IP injection of KM and permitted to wake up once the drug wore off, ii) given IP injections of KM every 45-70 minutes to maintain unconsciousness for the 4 hour duration, iii) subjected to isofluorane only during peptide injection and allowed to wake up immediately after, or iv) kept under with isofluorane for the duration of the experiment. Each treatment group included 3 mice with two sciatic nerves, for a total of 6 data points. Sciatic nerves were exposed and imaged in the context of the surrounding muscle and those images were processed with ImageJ to measure the integrated fluorescent intensity (Figure 9.1 A). From this data it is clear that allowing the mice to wake up immediately after injection reduced the nerve fluorescence, and the best nerve:muscle contrast is observed with just a single dose of KM (Figure 9.1 B). Interestingly, there is more variability in keeping the mice under for 4 hours with isofluorane when compared to KM (Figure 9.1 C).
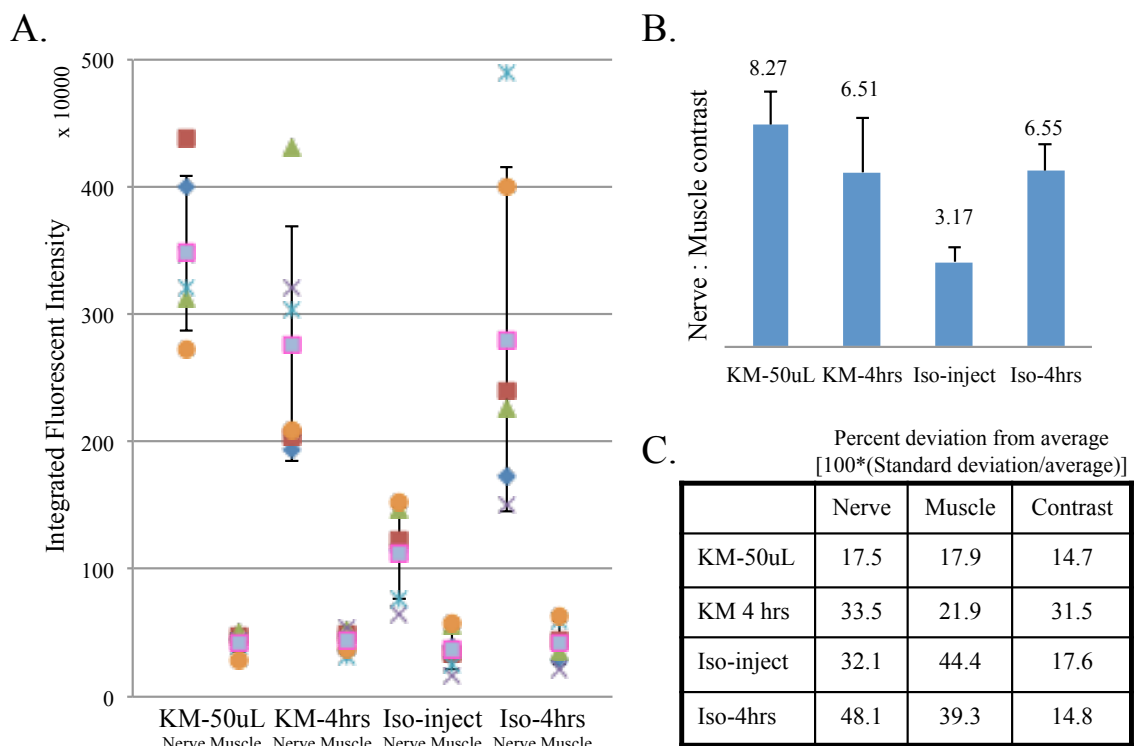
A.

B.

C.

	Nerve	Muscle	Contrast
KM-50uL	17.5	17.9	14.7
KM 4 hrs	33.5	21.9	31.5
Iso-inject	32.1	44.4	17.6
Iso-4hrs	48.1	39.3	14.8

Percent deviation from average
[100*(Standard deviation/average)]

Figure 9.1 NP 41 labeling of sciatic nerves varies depending on the method of anesthesia used during peptide injection. A) SKH mice were put under with various forms of anesthesia, either ketamine:midazolam or isofluorane, and kept asleep until the drugs naturally wore off or for the four hour duration of the imaging experiment. Sciatic nerves were exposed and imaged, and the nerve and muscle fluorescence was measured with ImageJ. These fluorescent measurements are presented as a scatter plot. B) Nerve to muscle contrast ratios were calculated for each of the sciatic nerves, data is presented as the average and standard deviation. C) The percent deviation from the average was calculated for the nerves, muscle and contrast ratio for each of the treatment groups.

9.4.2. Progress in determining the ligand for NP-41

Histological sections of sciatic nerves from mice injected with NP 41 suggest that

the peptide binds to connective, but is excluded from the axon and myelin (Chapter 8,

Figure 3). To validate these observations facial nerves were imaged with 2-photon

microscopy immediately post mortem (Figure 9.2). NP 41 was imaged using the

appropriate laser settings and second harmonic generation (Mohler, Millard et al. 2003)

was used to visualize collagen fibers and the striations in muscle tissue (Figure 9.2 A).

This method of imaging confirmed the binding of the peptide to the epineurium and

perineurium in a live and in-tact nerve. This image also shows labeling of what appears to

be elastin, it is still unclear if this fluorescence is due to peptide binding or

autofluorescence of the fibers (Konig, Schenke-Layland et al. 2005; Schenke-Layland,

Riemann et al. 2005). In the subset of the image that is presented in Figure 9.2 B, it is

clear that the peptide is excluded from the axonal space and does not appear to bind to
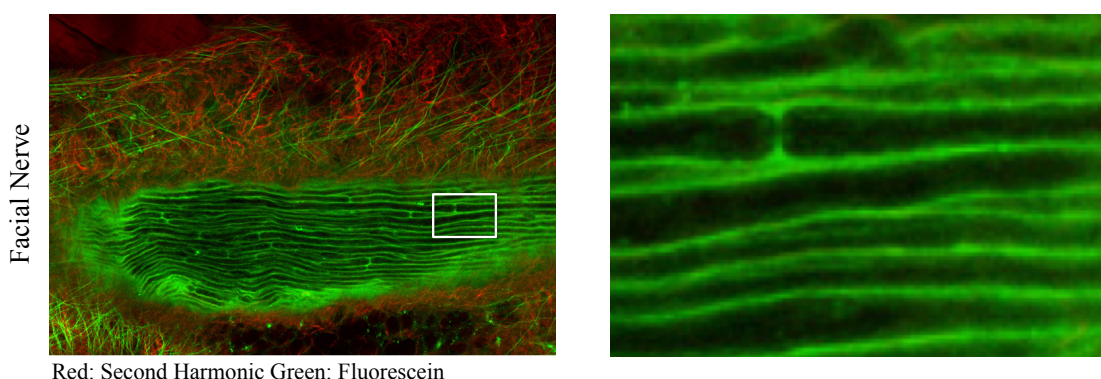
myelin.

Red: Second Harmonic Green: Fluorescein

Figure 9.2 Two-photon microscopy of facial nerves confirms that NP 41 binds to the epineurium and perineurium. Left panel: an SKH mouse was injected with 150 nanomoles of NP 41 FAM and the facial nerves were resected immediately post mortem and imaged with two-photon microscopy. NP 41 is represented in green and second harmonic generation in red. Right panel: increased magnification of the region outlined by the white box on the left

Beyond visualizing where the peptide binds, it is important to know what the

binding target is. To accomplish this, a version of NP 41 was synthesized with a

fluorescein, hydrazine and biotin near the C terminus (Figure 9.1 A). The purpose of

these functional groups is to cross link (via hydrazine) the fluorescently labeled peptide

to its *in vivo* binding target and isolate (via biotin) the peptide-target conjugate from

nerve homogenates. Mass spectroscopy then will be used to determine what biomolecules

are attached to the peptide (Leitner, Walzthoeni et al. 2010). Before this is possible, it

must be established that the additional functional groups do not interfere with peptide

binding or localization. NP 41 and the trifunctional NP 41 were injected into mice in

parallel and the sciatic nerves were harvested after 1 hour and frozen for cryosectioning and confocal microscopy. Images of nerve sections reveal that both versions of the peptide have higher fluorescent signal in the epineurium (Figure 9.5 B) with varying amounts of fluorescence in the perineuriem. NP 41 has higher peptide signal in the perineurium, but the nerve cross section is more longitudinal than that of the trifunctional NP 41 (Figure 9.5 C), which could explain the differences in signal because more of the perineurium is exposed.

Since the addition of the hydrazine and biotin did not significantly impact peptide binding, the next step was to perform the cross linking reaction. The trifunctional peptide was injected into mice at a higher does of 200 nanomoles, and sciatic nerves were harvested after 1 hour and immediatly placed in a sodium periodate solution to facilitate the reaction between the hydrazine and any glycoproteins in close proximity. Some of the nerve fragments were put in water as a control. Even after extensive washing, nerve tissue incubated in the sodium periodate solution retained significantly more fluorescence than those placed in water (Figure 9.3 D). Samples prepared for mass spectroscopy were washed after sodium periodate treatment then flash frozen in liquid nitrogen and sent to our collaborator, Andreas Frie at the Institute of Molecular Systems Biology in Zurich, for processing.
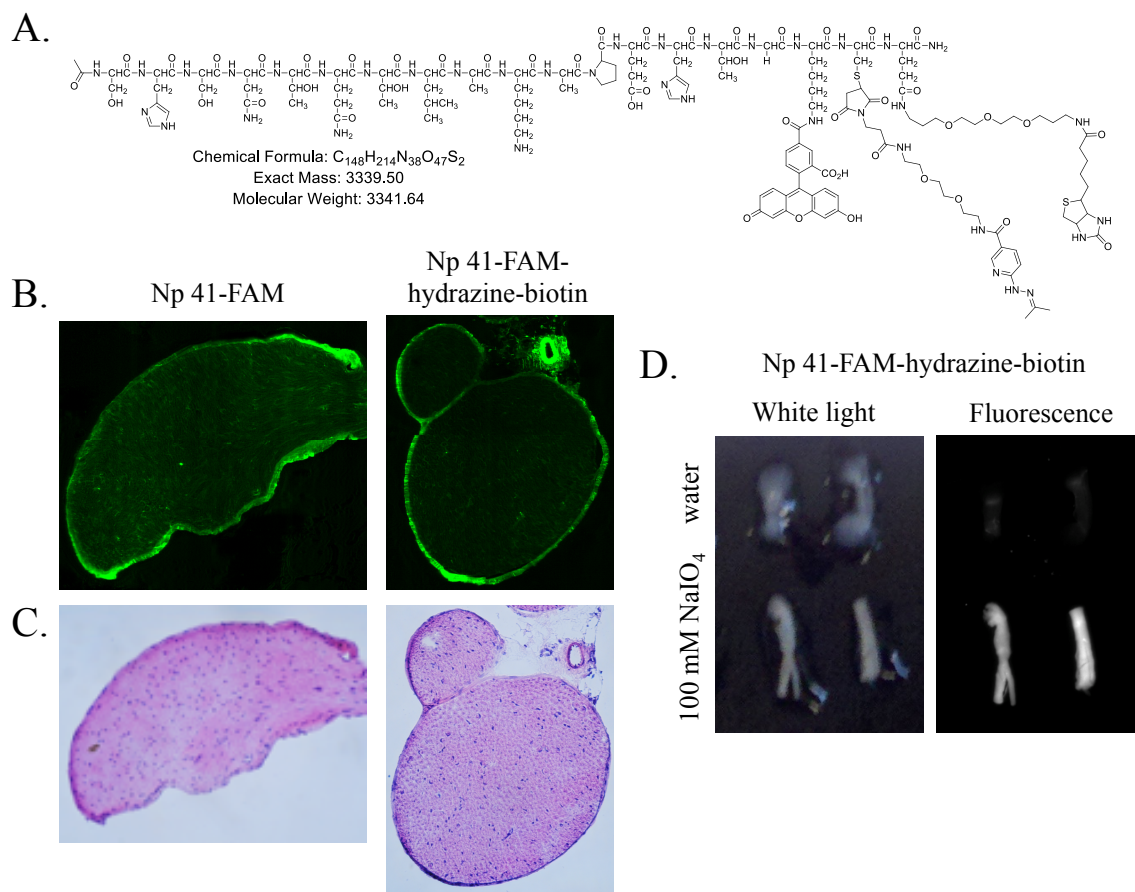
Figure 9.3 Determining the *in vivo* target of NP 41. A) Structure of the tri function NP 41, the fluorescein allows for visualization of the peptide, the hydrazine with cross react with amines on any neighboring proteins once placed in a sodium periodate solution and the biotin is used to isolate the peptide-target out of nerve homogenates. B) NP 41 FAM and the trifunction NP 41 were injected into mice in parallel and sciatic nerves were resected, frozen and imaged to examine peptide localization. C) Periodate dependence on nerve cross-linking was tested by incubating sciatic nerves from mice injected with the trifuntional NP 41 in either 100mM $NaIO_4$ for 1 hour at 25 C or water and then washing the nerves overnight at 4 C prior to imaging fluorescein fluorescence.

9.4.3. Modifications in peptide sequence and conjugation

A library of peptides was synthesized based on the original sequence of NP 41.

This library included peptides that had simple point mutations, or deletions ranging from

a single amino acid to six residues from either the N or C termini. The purpose of this

screen was two-fold; the first was to learn what portions of the peptide are important for

nerve binding and the second was to find the smallest peptide that still generates

substantial nerve contrast. There is hope that one day this peptide will be translated into clinical use, therefore the cost of peptide synthesis must be considered. The peptides in this screen are listed in Table 9.1 and are named NP 101-NP 120.

Table 9.1 Sequence modifications to NP 41

Name	Peptide Sequence	Modification	Affect on contrast
NP 41	Ac-SHSNTQTLAKAPEHTGK(FAM)-CONH2		
NP 101	Ac-K(FAM)NTQTLAKAPEHTGK-CONH2	N term label, no SHS, additional K on C term	None
NP 102	Ac-K(FAM)NTQTLAKAPEHTK-CONH2	N term label, no SHS, no G, additional K on C term	Slight improvement
NP 103	Ac-K(FAM)SHSNTQTLAKAPEHTK-CONH2	N term label, no G, additional K on C term	Worse
NP 104	Ac-K(FAM)SHSNTQTLAKAPEHTGK-CONH2	N term label, additional K on C term	None
NP 111	Ac- SHSNTQTLAKAPEHT-ahx-K(FAM)-CONH2	changed linker from Glycine to ahx	Worse
NP 112	Ac-SNTQTLAKAPEHTGK(FAM)-CONH2	removed SH from N term	Worse
NP 113	Ac-TQTLAKAPEHTGK(FAM)-CONH2	removed SHSN from N term	Worse
NP 114	Ac-TLAKAPEHTGK(FAM)-CONH2	removed SHSNTQ from N term	None
NP 115	Ac-SHSNTQTLAKAPEHK(FAM)-CONH2	removed TG from C term	Slight improvement, high variability
NP 116	Ac-SHSNTQTLAKAK(FAM)-CONH2	removed PEHTG from C term	Worse
NP 117	Ac-NTQTLAKAPEHGK(FAM)-CONH2	removed SHS from N term and T from C term	None
NP 118	Ac-NTQTLAKAPEGK(FAM)-CONH2	removed SHS from N term and HT from C term	None
NP 119	Ac-SHSNTQTLARAPEHTGK(FAM)-CONH2	changed the internal Lysine to Arginine	None
NP 120	Ac-NTQTLAKAPEH-ahx-K(FAM)-CONH2	removed SHS from N term and TG from C term	None

These peptides were injected into SKH mice at a dose of 150 nanomoles and nerves were exposed for imaging three hours after peptide injection. These images were used to calculate the nerve to muscle contrast ratio for each of the modified peptides (Figure 9.4) and the results of the modifications are also briefly summarized in the

preceding table. Removing SH or SHSN from the N terminus reduced nerve contrast yet removing SHSNTQ from had no impact of nerve contrast. Removing the G residue from the C terminal side of the peptide or changing it to an aminohexanoic linker negatively impacted peptide performance. Furthermore, the elimination of PEHTG from the C terminus also diminishes contrast yet removing the H, HT, or the TG (along with the N term SHS) had no effect on nerve labeling. From this data, it is hard to conclude with any confidence what amino acids can safely be removed.
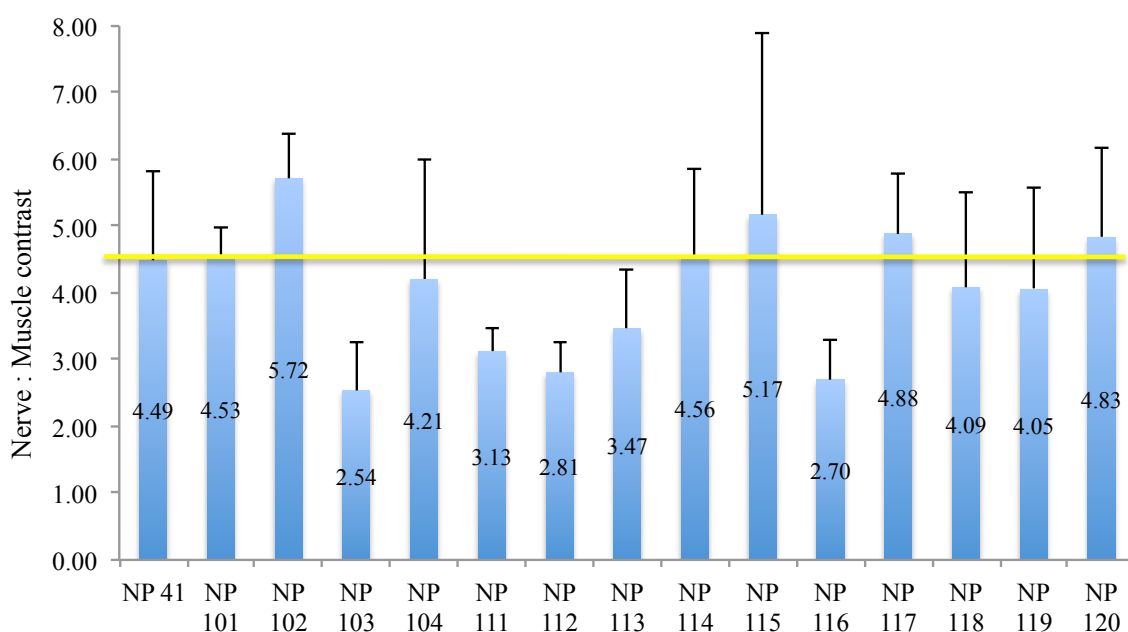

Figure 9.4 Nerve to muscle contrast ratios for peptides NP 41 though NP 120. Mice were injected with 150 nanomoles of fluorescein labeled peptide three hours prior exposure of the sciatic nerve. Fluorescent images were used to determine the nerve to muscle contrast ratios. (N=3 mice for each peptide)

The next step in improving the peptide sensitivity and nerve to muscle contrast is trying various chemical and structural modifications. The easiest way to modify NP 41 is to conjugate molecules via the reactive amine on the N terminus. One hindrance to this chemistry is the primary amine on the internal lysine of the peptide, therefore the residue was capped with acetic anhydride to render it unreactive. This capped version of the

peptide, NP 41 AcLys had similar contrast and nerve binding as the unmodified peptide (Figure 9.5 A and B).

Nerve binding was then assessed for NP 41 AcLys with various lengths of peg attached to the N terminus. The addition of peg_2 and peg_4 reduced nerve contrast by increasing the amount of probe in the muscle (Figure 9.5 C). With the longer peg_{12}, the images were saturated with the same exposure time, indicating significantly higher peptide retention. These peptides were then tested at a later timepoint of 4.5 hours. The longer washout decreased the muscle fluorescence for both the peg_2 and peg_4 but the nerve signal also went down proportionally, resulting in a net decrease in contrast. The peg_{12} NP 41 at 4.5 hours had similar contrast to the unpegylated NP 41 at 2 hours and had an overall higher fluorescent signal.
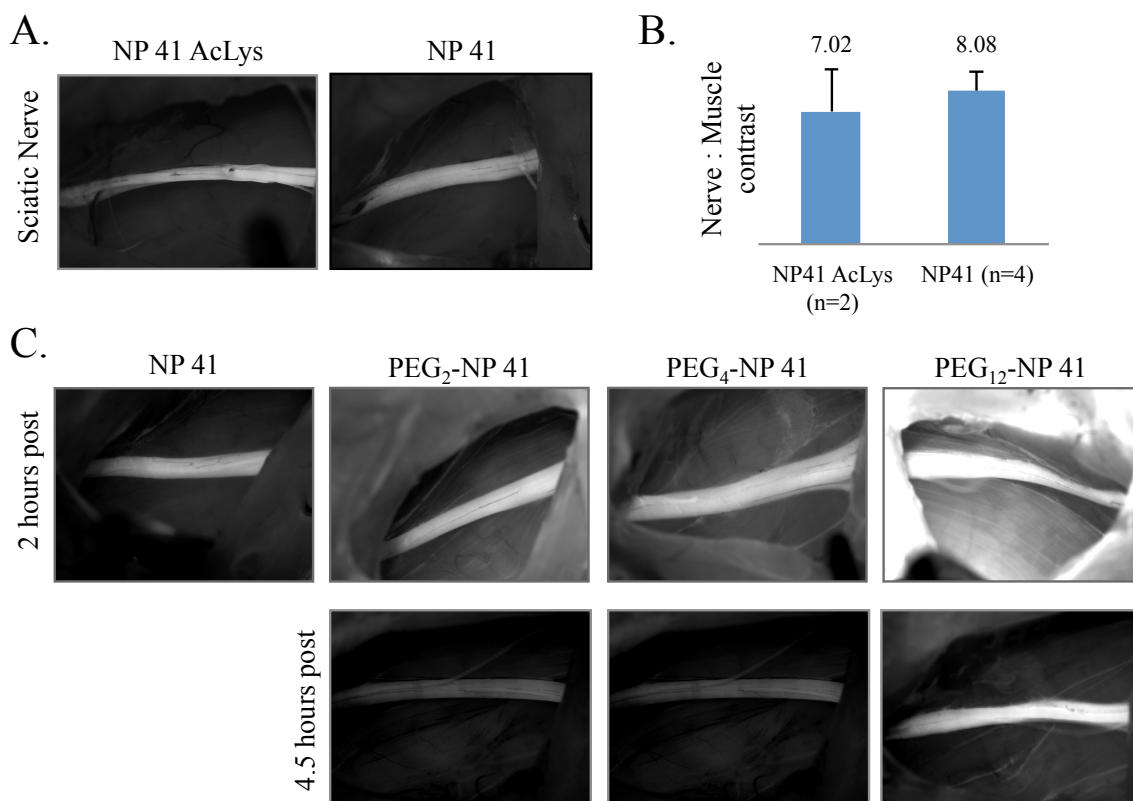
Figure 9.5 Capping of NP 41's internal lysine and subsequent conjugation of various sized peg chains to the N terminus. A) Mice were injected with 150 nanomoles of either NP 41 FAM or NP 41 FAM AcLys and the sciatic nerves were exposed to image peptide labeling. B) Nerve to muscle contrast was calculated for the two peptides, n is the number of mice and each mouse has two sciatic nerves. C) NP 41 AcLys was reacted with peg_2, peg_4 or peg_{12} via the free amine on the N terminus. Peptide were injected into SKH mice at a dose of 150 nanomoles and allowed to circulated for 2 hours prior to sciatic nerve imaging. D) The pegylated peptides were injected into mice at the same dose as in (C) but the time point for imaging was extended to 4.5 hours after injection.

Another method to increase nerve labeling is to improve the avidity of the peptide for its target; this is done by using multiple copies of the peptide in a single molecular construct. Several forms of dimeric peptides were synthesized as well as a generation two (G2) dendrimeric nanoparticle (Figure 9.6 A). Two fluorescein versions of the dimeric peptide were tested, the first is simply two NP 41 FAM peptides linked via a disulfide bond and the second has two NP 41 FAM peptides conjugated through a peg_{11} linker. Neither dimeric peptide was successful at improving nerve contrast and the results were

worse than the monomer (Figure 9.5 B). Similar strategies were attempted with NP 41

labeled with the far-red dye Cy5 or an analogous Alexa 647 (Figure 9.5 C) and similar

results were obtained. The dimeric peptide formed by reacting two NP 41 peptides with a

bis maleimide Cy5 had no improvement in contrast over the monomeric peptide. A

generation two dendrimer that had three molar equivalents of NP 41 peptide and one

equivalent of Alexa 647 also showed no enhancement in nerve contrast. Plasma clearance

of NP 41 Cy5 and the G2 dendrimer version were monitored and both constructs had

similar half lives of approximately 10 minutes, with most of the probe being cleared by
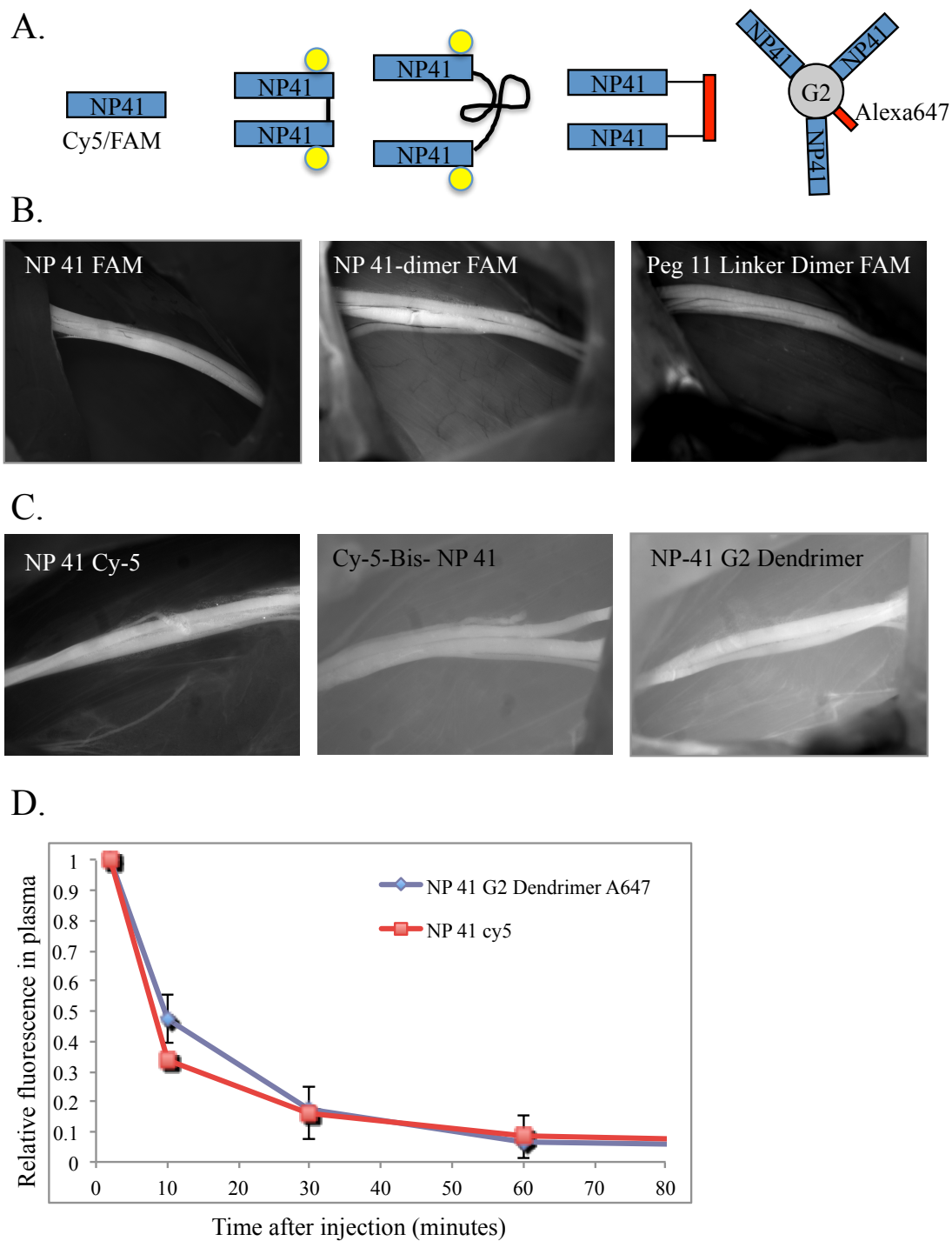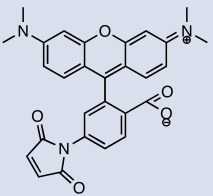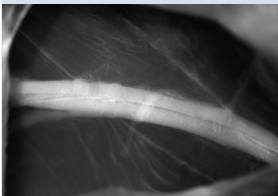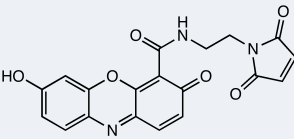
60 minutes post injection (Figure 9.6 D).
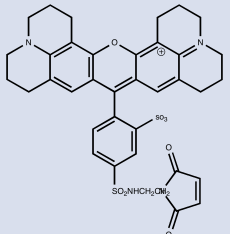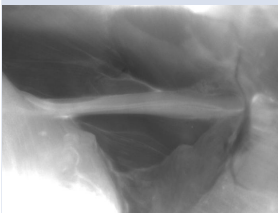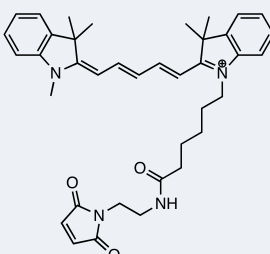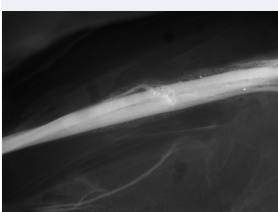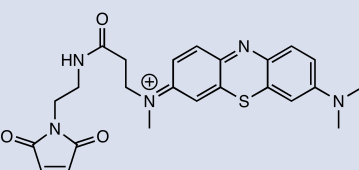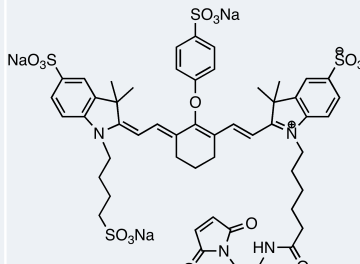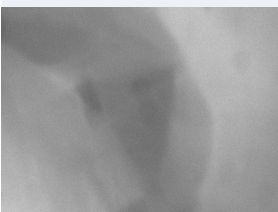
Figure 9.6 Using dimeric peptides and small nanoparticles with multiple peptide copies to improve NP 41 avidity for its target resulted in diminished nerve contrast. A) Cartoon representations of the various peptide constructs that were tested. B) Images of sciatic nerves taken two hours after mice were injected with 150 nanomoles of NP 41 FAM, NP 41-dimer FAM or NP 41-peg $_{11}$ dimer FAM. C) Images of sciatic nerves taken three to four hours after mice were injected with 150 nanomoles of NP 41 Cy5, Cy5 bis NP 41 or NP 41 G2 dendrimer (Alexa 647). D) Plasma clearance of NP 41-cy5 and the G2 dendrimer with NP 41 and Alexa 64

9.4.4. Farther red fluorophores reduce or diminish nerve peptide contrast

To detect small nerves that are not on the surface of the surgical bed, it is important that the nerve peptide be labeled with a dye that can better penetrate through tissue. For fluorescence imaging *in vivo*, red shifted and near infrared (NIR) dyes have less competition from tissue autofluorescence and less absorption by hemoglobin (Frangioni 2003). NP 41 was synthesized with a C terminal cysteine that was reacted with a variety of dyes with excitation wavelengths ranging from 550-777nm. All of the dyes that were tested are listed in Table 9.2 with their name, structure, excitation and emission wavelengths, as well as a representative image from *in vivo* labeling of a sciatic nerve. Tetramethyl rhodamine and Cy5 gave the best contrast, but the images required windowing. The nerve was distinguishable with resorufin and texas red but once the excitation wavelength moved beyond 670nm, as with methylene blue and IR800 CW, no nerve contrast was detectable.

Table 9.2 Summary of all red fluorophores that were conjugated to NP 41 and tested for nerve contrast *in vivo*. Note that the units for dose are nanomoles and each image is scaled to maximize contrast

Name	Structure	Ex.	Em.	Dose Time/ point	Representative image of sciatic nerve
Tetramethyl-rhodamine (TAMRA) Maleimide		550	570	150/ 3hrs	
Resorufin Maleimide		576	580	75/ 4hrs	
Texas Red C₂ Maleimide		595	615	150/ 3hr	
Cy-5 Maleimide		650	670	150/ 4hrs	
Methylene Blue Maleimide		670	688	150/ 2 and 4 hrs	
IR800 CW Malemide		777	789	150/ 3hrs	

9.4.5. Screen with new nerve peptide sequences

Modifications to NP 41 did not enhance peptide binding or nerve contrast; therefore results from the screen performed in Chapter 8 were revisited. The final rounds from both the *in vitro* screens, one against myelin basic protein (MBP) and the other against excised mouse nerves, were put through one more round of selection. This time the results from the final round of the MBP screen were selected against excised nerves and vise versa. Sample plaques from both the pools were sequenced and the corresponding synthetic peptides are listed in Table 9.3. There were no repeats in the sequences, but even with the lack of enrichment it was decided to continue with *in vivo* testing.

Table 9.3 Sequence results from last round of cross selection with *in vitro* screens against myelin basic protein and excised mouse nerves

Name	Peptide Sequence
NP 121	Ac-K(FAM)VAPTKAPLHSPSG-CONH2
NP 122	Ac-K(FAM)NNLKTGTSAPTGG-CONH2
NP 123	Ac-K(FAM)HKTAQWPFIAFRG-CONH2
NP 124	Ac-K(FAM)RLTNAPAYQAPAG-CONH2
NP 125	Ac-K(FAM)MQNPLNGKPGRG-CONH2
NP 126	Ac-K(FAM)THYSRSLTDGTRG-CONH2
NP 127	Ac-K(FAM)YPSPNRPPNLTNG-CONH2

The new nerve peptides, NP 121-NP 127, were subjected to the standard *in vivo* imaging protocol and the contrast for sciatic nerve to surrounding muscle was determined

(Figure 9.7 A). NP 122, NP 124 and NP 125 all had contrast ratios that were superior to NP 41. When looking at the raw data for fluorescent intensities of the nerve and muscle (Figure 9.7 B) as well as the images of the sciatic nerves (Figure 9.7 C), it is clear that NP 124 had the highest overall fluorescence, so it was selected for further characterization.
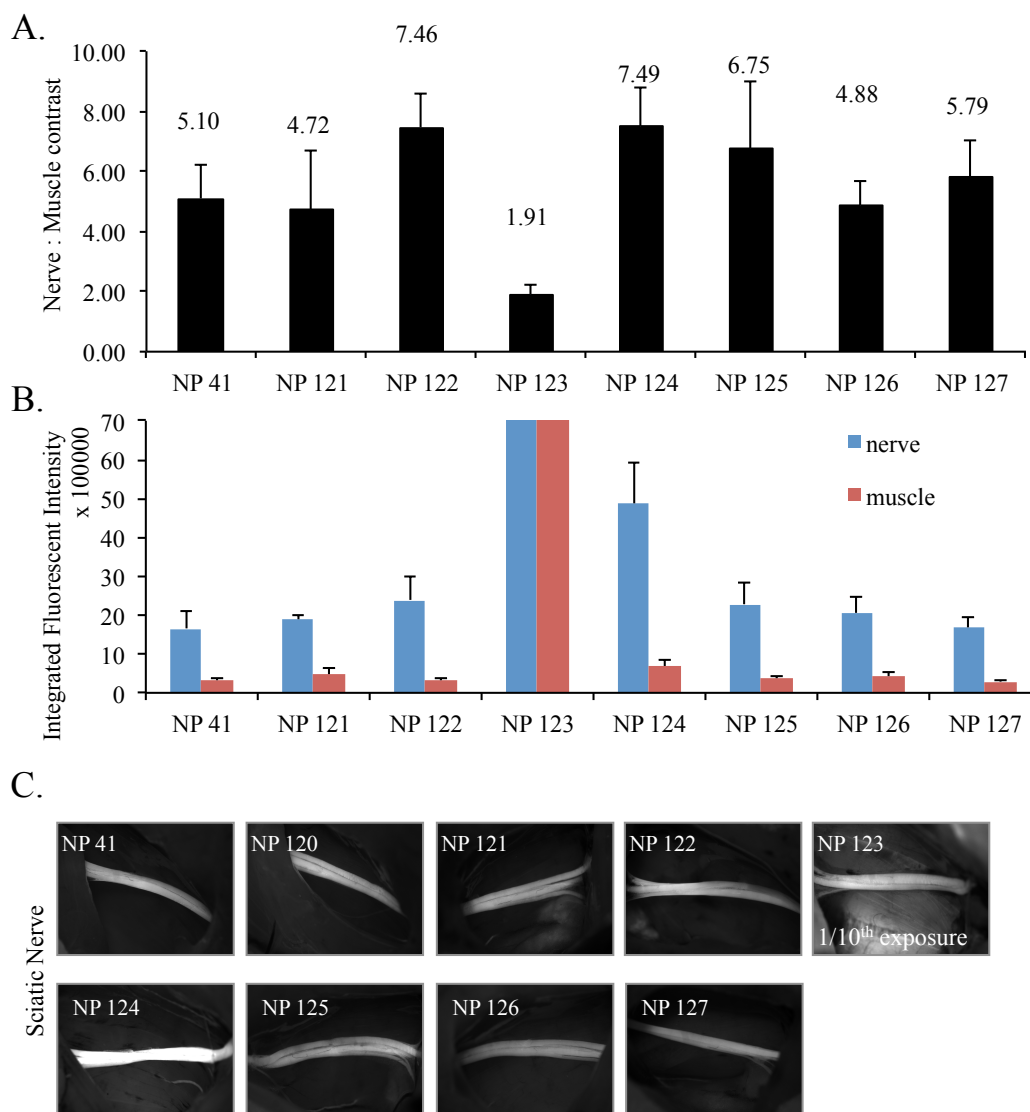
Figure 9.7 *In vivo* nerve contrast for screen of new peptide sequences 121-127. A) Nerve to muscle contrast ratios for NP 121-NP 127 compared to the original NP 41 peptide. B) Fluorescent intensity values of both the nerve (blue) and muscle (red) for NP 41 and NP 121-NP 127. Note that NP 123 was significantly brighter and surpassed the scale on the y-axis. C) Representative images of NP 41 and NP 121-127 taken two hours after 150 nanomole injection of fluorescein labeled peptide. All images are taken with the same filter set, exposure time and scaling with the exception of NP 123, which had a 1/10th the exposure time.

Nerve contrast, overall fluorescence and histological localization were compared for NP 41 and NP 124. Both peptides were a result of the X12 library but NP 41 retained the phage sequence SHS on the N terminus and was labeled with K(FAM) on the C terminal side. NP 124 omits the SHS and the K(FAM) was placed on the N terminal side. (The change in fluorophore arrangement was a result of problems with the solid phase peptide synthesis, the traditional TGR resin was on backorder and the substitute resin aggregated when K(FAM) was the first amino acid conjugated to it.) When comparing the twelve amino acid sequences (NP 41: NTQTLAKAPEHT and NP 124: RLTNAPAYQAPA), NP 41 has a net zero charge (the K and E cancel each other out) and NP 124 has a net positive charge (R) and both have some tertiary structure that is influenced by proline residues. Overall, NP 124 has more hydrophobic amino acids with over half the sequence comprised of alanine, leucine, tyrosine and proline. Neither peptide had issues with solubility, both being stable in aqueous solutions at concentrations over 2mM.

When compared *in vivo*, NP 124 is significantly brighter than NP 41 in both the nerve and the muscle (Figure 9.8 A). The fluorescent signal of NP 124 is more variable than that of NP 41, yet interestingly, NP 41 has more variation in the nerve to muscle contrast ratio (Figure 9.8 B). Sample images of the sciatic nerves are presented in Figure 9.8 C. Fluorescein imaging of nerve cross sections demonstrate that the two peptides have similar localization to the connective tissue of the epineurium and perineurium, with NP 124 having superior peptide staining in the perineurium (Figure 9.8 D).
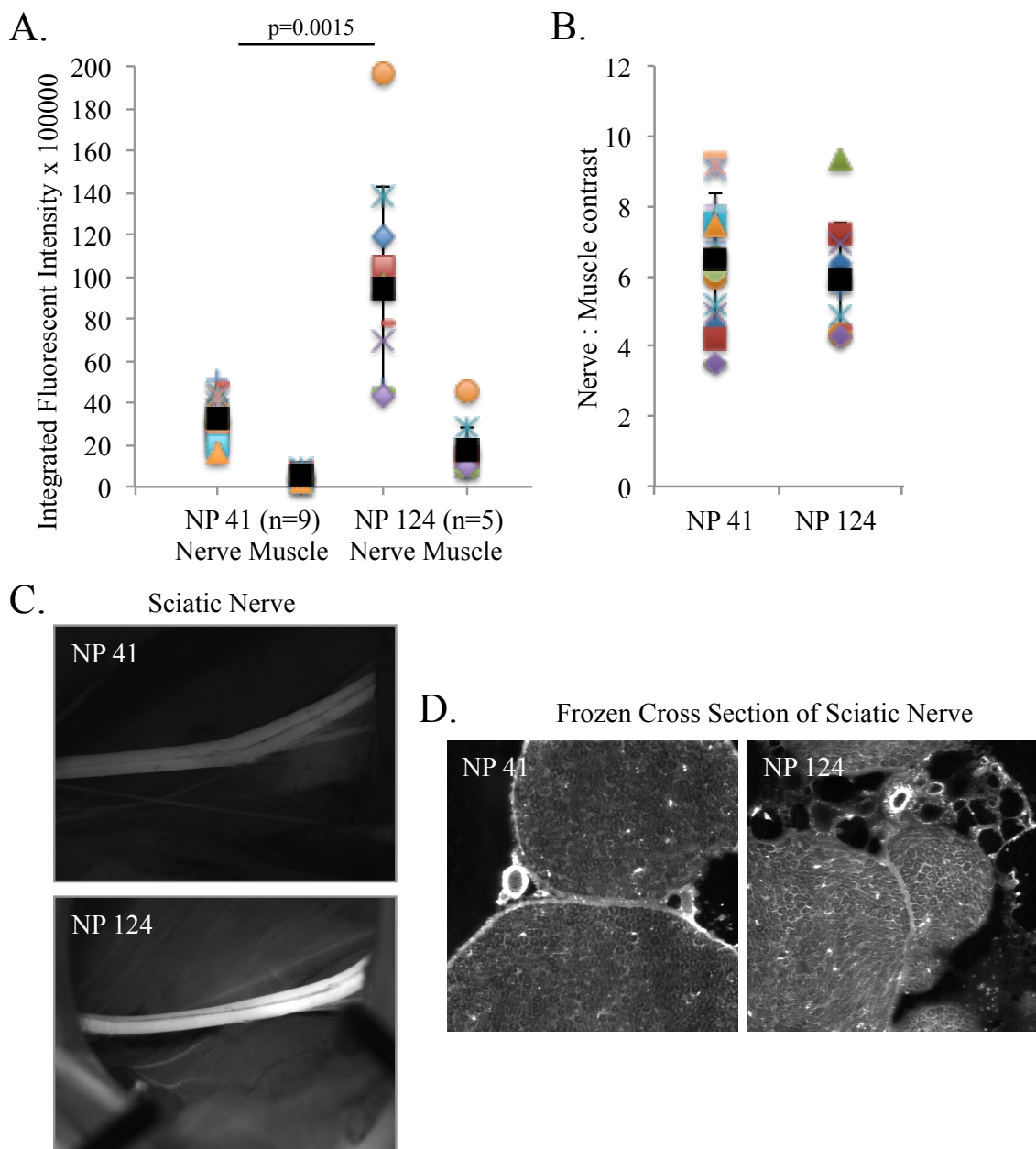
Figure 9.8 *In vivo* comparison of NP 41 and NP 124. A) Scatter plot presenting for NP 41 and NP 124 nerve and muscle fluorescence. The large black square is the average value with the bars representing the standard deviation. N denotes with number of mice tested with each mouse having two muscle and nerve values. B) Scatter plot for the nerve to muscle contrast ratios. The large black square represents the average value and the number of data point is the same as that provided in (A). C) Representative images of the sciatic nerve taken two hours after 150 nanomole peptide injection. D) Confocal images of 10μm sections of excised sciatic nerves.

9.4.6. Phage selection with human nerve tissue

With the goal that nerve peptide technology will translate into the clinic and be used during surgery in human patients, a phage selection strategy was designed to identify peptide sequences that preferentially bound to human nerve tissue. Dr. Mike Whitney and Rachael Levin used m13 phage libraries that expressed either 7 or 12 random amino acids on the N terminus of their coat proteins. These libraries were exposed to either freshly resected or frozen human nerve homogenates and there was sequence enrichment after five round of selection. These sequences were synthesized as fluorescein labeled peptides and are presented in Figure 9.9 A. The peptides were tested *in vitro* and had preferential binding to human nerve over muscle/fat tissue (data not shown). They were then injected into mice and successfully labeled the sciatic nerve with 6-7 fold contrast to surrounding tissue (Figure 9.9 B). The fluorescent intensities were measured and HNP 301 provided the highest nerve fluorescence (Figure 9.9 C), therefore this peptide has been selected for future pre-clinical development.

A.

Name	Peptide Sequence
HNP301	FAM-SHSSEFPRSWDMETNG-CONH2
HNP303	FAM-SHSMLPSVLDG-CONH2
HNP305	FAM-SHSTMKTLSLG-CONH2

B.

Sciatic Nerve

C.
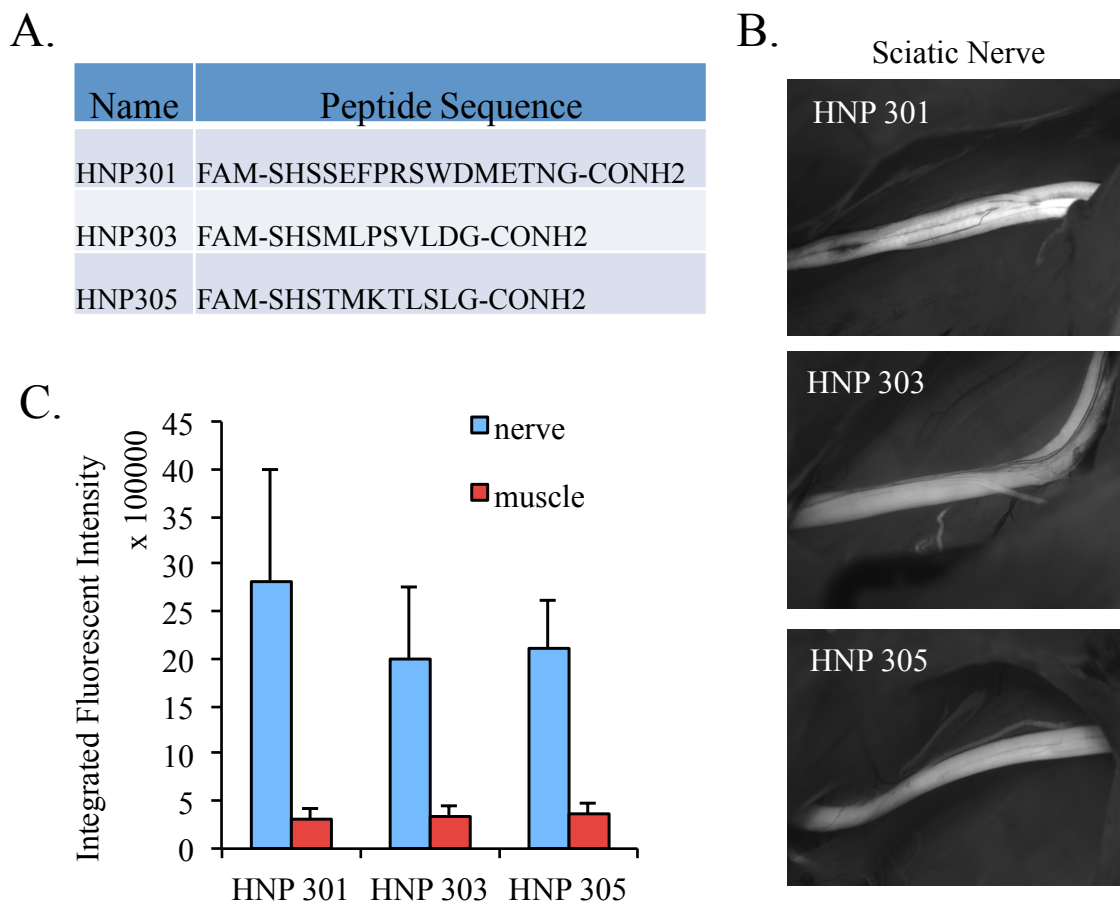
Figure 9.9 Results of phage selection with human nerve tissue. A) Sequences from the selection against human nerve tissue were made as synthetic fluorescein labeled peptides. B) Peptides were injected into SKH mice at a dose of 150 nanomoles and the sciatic nerve was exposed and imaged two hours later. C) Fluorescent intensities were measure for both the nerve and surrounding muscle, data is presented as the average and standard deviation with an n=3 mice.

9.5. Discussion

Preservation of peripheral nerves is one of primary goals of any surgical procedure and fluorescently labeled nerve-homing peptides provide a novel tool to help accomplish that. Nerve peptide41 (NP-41), with the sequence Ac-SHSNTQTLAKAPEHTGK(FAM)-CONH$_2$, provided the best nerve contrast of all the peptides that resulted from the phage display selection described in Chapter 8. Numerous

attempts were made to improve that sequence, but rational ligand optimization is much easier when the molecular target is known. For NP 41, it is clear that the peptide binds to connective tissue, but the exact protein target is still a mystery. Affinity columns were made by immobilizing NP 41, and nerve homogenates were passed through those columns to identify binding partners, but the experimental results were inconclusive. One reason for this could be that the peptide has low affinity for its target(s). When imaging nerve cryosections, the addition of any aqueous media resulted in an almost immediate diffusion of the peptide. This is what led to the development of frozen section imagining, so that the nerve tissue remained frozen and never had to be processed prior to analysis.

The current attempt to identify binding partners is the development of a trifunction peptide that can cross-link to the target protein after systemic injection. The functionality of the construct also facilitates isolation from nerve homogenates. This work is collaboration with Andreas Frie at the Institute of Molecular Systems Biology in Zurich. He will be using mass spectroscopy on the digested nerve samples to determine what protein fragments are covalently linked to the trifunctional NP 41 peptide. The sequence information from these protein fragments will in turn identify the target protein(s).

In lieu of target identification, manipulations were made to the peptide sequence and structure to try to increase nerve binding and contrast. Regrettably, most of these modifications failed to enhance nerve labeling and resulted in diminished contrast. The peptide library that included point mutations and sequence deletions gave no clear indication that certain residues were required while others could be eliminated. The various combinations of deletions gave an unpredictable pattern of peptide performance,

suggesting that the tertiary structure of the peptide generates affinity and not necessarily the specific amino acid sequence. This could also help explain why the mulitermic probe constructs were unsuccessful. Having multiple peptides in close proximity to one another or conjugating them on a large carrier could alter their conformation or make the active portion of the peptide inaccessible.

Attempts to shift the fluorophore wavelength to the far red and infrared also resulted in diminished contrast. One reason is that fluorescein provides additional contrast for light colored tissues, and nerves are distinctly white. As discussed in Chapter 4, tissues and organs with pigmentation can obstruct light, especially in the green wavelengths. Although, only a portion of NP 41 contrast is a result of the inherent properties of FAM because peptides conjugated to TAMRA and Cy5 provided significant nerve labeling. When those dyes were injected systemically as just naked fluorophores, no nerve contrast was observed.

Moving beyond NP-41, phage selection strategies was used to find new and improved nerve homing sequences. The cross selection of the final rounds from the *in vitro* screens described in Chapter 8 resulted in one peptide sequence, NP 124, that had superior nerve fluorescence. The peptide also had higher background staining, giving it a nerve:muscle contrast ratio similar to that of NP 41. But this peptide has potential to improve surgical applications because greater peptide fluorescence allows for nerve visualization in settings where the number of photons for fluorophore excitation is limited and permits shorter exposure times, which is imperative for generating real-time images to help guide the surgeon. Finally, a phage display selection was performed against human nerve tissue. Of the 7 sequences that were enriched, only three of them generated

FAM labeled peptides that were soluble at high enough concentrations for systemic injection. Of those three peptides, HNP 301 had the best nerve fluorescence and contrast when testing in mouse models. This peptide has also been tested in rats and was able to identify peripheral nerves, including motor, sensory and autonomic nerves. Because this peptide was selected for its ability to bind human nervous tissue, it is hypothesized that following systemic injection into human patients, this peptide will be more likely to identify nerves compared to sequences that were selected with rodent nerves.

9.6. Acknowledgements

CHAPTER 10: Conclusion

One of the main goals of this body of work was to improve ACPP targeting such that the platform could be moved towards therapeutic applications. This included modifications to the substrate sequence and peptide structure, attachment of the ACPP to carrier molecules, and investigating various forms of cargo release upon endocytosis. Optical imaging with fluorescent dyes was used to screen the various ACPP and CPP adaptations and provided a quantifiable readout. From this work, is was observed that small increases in the molecular weight of the probe can significantly reduced cartilage binding, but do little to improve the delivery of the peptide to the liver and kidneys. When the peptide is attached to large carriers, the biodistribution and tumor uptake are drastically improved, but the targeting mechanism can be overshadowed by EPR. A novel phage display screen was performed to find substrate sequences that targeted tumors with no prior bias to amino acid sequence or target enzyme. This resulted in the identification of RLQLKL and its acetyled derivative. The RLQLKL ACPP had significant optical contrast for tumors and identified spontaneous and experimental metastases in the lungs. Further characterization of the RLQLK(Ac)L probe revealed that it is marker for macrophages under the appropriate conditions and may be a valuable tool for identifying tumor associated macrophages *in vivo*.

The ACPP modification that yielded the best results was the addition of cyclic-RGD, a common ligand for integrins that are overexpressed in neovasculature. Synergistic targeting of integrins and MMPs significantly enhanced tumor contrast and peptide uptake and provided the first results where ACPP targeted improved the efficacy

of a chemotherapeutic. With this peptide construct, release of monomethyl auristatin E was facilitated by cleavage of a peptide linker designed for lysosomal proteases. Another mode of drug release presented in this dissertation is disulfide bond reduction. This mechanism was found to successfully release cargo molecules from the CPP upon endocytosis when incubated in culture, but the disulfide bond is not stable in plasma during *in vivo* testing.

Early results with doxorubicin liposomes demonstrated promise for ACPP targeting of therapeutic nanoparticles. Now that the proper quality control protocols are in place, it is necessary to restart the *in vivo* therapeutic studies to truly determine if ACPPs can help increase the efficacy of drugs that are already in use in the clinic. But since doxorubicin liposomes are quite prevalent in the literature of molecular targeting, it would be advantageous to take what was learned from the Doxil studies and apply it to other novel nanoparticle formulations.

Finally, nerve-homing peptides were found through phage display selection techniques that generate significant nerve contrast when administered systemically and imaged in a surgical setting. Currently, nerve peptides are able to produce contrast ratios greater than 7 and can identify nerves as small as 50μm in diameter. These probes will eventually be combined with ACPPs to help navigate tumor resection during fluorescent-guided surgery. The combination of all the molecularly targeted peptides presented in this body of work can facilitate the identification of cancer *in vivo*, increase the efficacy of chemotherapeutics and will hopefully lead to improvements in early detection and tumor resection, which are the ultimate cures for cancer.

REFERENCES:

Adams, S. R. T., R. Y. (2006). Imaging the influx of cell-penetrating into the cytosol of individual cells. Handbook of Cell-Penetrating Peptides 2nd Edition. U. Langel**:** 505-512.

Aguilera, T. A. (2009). Activatable Cell Penetrating Peptides and their use in Clinical Contrast Agent and Therapeutic Development. phd Thesis, University of California San Diego.

Aguilera, T. A., E. S. Olson, et al. (2009). "Systemic in vivo distribution of activatable cell penetrating peptides is superior to that of cell penetrating peptides." Integr Biol (Camb) **1**(5-6): 371-381.

Alley, S. C., N. M. Okeley, et al. (2010). "Antibody-drug conjugates: targeted drug delivery for cancer." Curr Opin Chem Biol **14**(4): 529-537.

Andersson, M. K., M. Enoksson, et al. (2009). "The extended substrate specificity of the human mast cell chymase reveals a serine protease with well-defined substrate recognition profile." Int Immunol **21**(1): 95-104.

Arias, J. L. (2011). "Drug delivery strategies in targeting cancer: current concepts and future developments." Curr Drug Targets **12**(8): 1094-1095.

Arunachalam, B., U. T. Phan, et al. (2000). "Enzymatic reduction of disulfide bonds in lysosomes: characterization of a gamma-interferon-inducible lysosomal thiol reductase (GILT)." Proc Natl Acad Sci U S A **97**(2): 745-750.

Atkinson, J. M., R. A. Falconer, et al. (2010). "Development of a novel tumor-targeted vascular disrupting agent activated by membrane-type matrix metalloproteinases." Cancer Res **70**(17): 6902-6912.

Austin, C. D., X. Wen, et al. (2005). "Oxidizing potential of endosomes and lysosomes limits intracellular cleavage of disulfide-based antibody-drug conjugates." Proc Natl Acad Sci U S A **102**(50): 17987-17992.

Bajjuri, K. M., Y. Liu, et al. (2011). "The legumain protease-activated auristatin prodrugs suppress tumor growth and metastasis without toxicity." ChemMedChem **6**(1): 54-59.

Bartlett, D. W., H. Su, et al. (2007). "Impact of tumor-specific targeting on the biodistribution and efficacy of siRNA nanoparticles measured by multimodality in vivo imaging." Proc Natl Acad Sci U S A **104**(39): 15549-15554.

Bibby, D. C., J. E. Talmadge, et al. (2005). "Pharmacokinetics and biodistribution of RGD-targeted doxorubicin-loaded nanoparticles in tumor-bearing mice." Int J Pharm **293**(1-2): 281-290.

Bingle, L., N. J. Brown, et al. (2002). "The role of tumour-associated macrophages in tumour progression: implications for new anticancer therapies." J Pathol **196**(3): 254-265.

Bisby, R. H., C. Mead, et al. (2000). "Active uptake of drugs into photosensitive liposomes and rapid release on UV photolysis." Photochem Photobiol **72**(1): 57-61.

Blewitt, M. G., L. A. Chung, et al. (1985). "Effect of pH on the conformation of diphtheria toxin and its implications for membrane penetration." Biochemistry **24**(20): 5458-5464.

Blume, G. and G. Cevc (1990). "Liposomes for the sustained drug release in vivo." Biochim Biophys Acta **1029**(1): 91-97.

Brooks, P. C., R. A. Clark, et al. (1994). "Requirement of vascular integrin alpha v beta 3 for angiogenesis." Science **264**(5158): 569-571.

Brooks, P. C., S. Stromblad, et al. (1996). "Localization of matrix metalloproteinase MMP-2 to the surface of invasive cells by interaction with integrin alpha v beta 3." Cell **85**(5): 683-693.

Buechler, C., M. Ritter, et al. (2000). "Regulation of scavenger receptor CD163 expression in human monocytes and macrophages by pro- and antiinflammatory stimuli." J Leukoc Biol **67**(1): 97-103.

Burtea, C., S. Laurent, et al. (2008). "Contrast agents: magnetic resonance." Handb Exp Pharmacol(185 Pt 1): 135-165.

Chambers, A. F. and L. M. Matrisian (1997). "Changing views of the role of matrix metalloproteinases in metastasis." J Natl Cancer Inst **89**(17): 1260-1270.

Chang, D. K., C. Y. Chiu, et al. (2009). "Antiangiogenic targeting liposomes increase therapeutic efficacy for solid tumors." J Biol Chem **284**(19): 12905-12916.

Chen, J. J., Y. C. Lin, et al. (2005). "Tumor-associated macrophages: the double-edged sword in cancer progression." J Clin Oncol **23**(5): 953-964.

Cheung, J. C., P. Kim Chiaw, et al. (2009). "A novel method for monitoring the cytosolic delivery of peptide cargo." J Control Release **137**(1): 2-7.

Chipman, S. D., F. B. Oldham, et al. (2006). "Biological and clinical characterization of paclitaxel poliglumex (PPX, CT-2103), a macromolecular polymer-drug conjugate." Int J Nanomedicine **1**(4): 375-383.

Cho, K., X. Wang, et al. (2008). "Therapeutic nanoparticles for drug delivery in cancer." Clin Cancer Res **14**(5): 1310-1316.

Ciofani, G., C. Riggio, et al. (2009). "A bi-modal approach against cancer: magnetic alginate nanoparticles for combined chemotherapy and hyperthermia." Med Hypotheses **73**(1): 80-82.

Cole, N. B. and J. G. Donaldson (2012). "Releasable SNAP-tag probes for studying endocytosis and recycling." ACS Chem Biol **7**(3): 464-469.

Collins, D. S., E. R. Unanue, et al. (1991). "Reduction of disulfide bonds within lysosomes is a key step in antigen processing." J Immunol **147**(12): 4054-4059.

Console, S., C. Marty, et al. (2003). "Antennapedia and HIV transactivator of transcription (TAT) "protein transduction domains" promote endocytosis of high molecular weight cargo upon binding to cell surface glycosaminoglycans." J Biol Chem **278**(37): 35109-35114.

Conti, P., M. L. Castellani, et al. (2007). "Role of mast cells in tumor growth." Ann Clin Lab Sci **37**(4): 315-322.

Couvreur, P. and C. Vauthier (2006). "Nanotechnology: intelligent design to treat complex disease." Pharm Res **23**(7): 1417-1450.

Darby, N. J., R. B. Freedman, et al. (1994). "Dissecting the mechanism of protein disulfide isomerase: catalysis of disulfide bond formation in a model peptide." Biochemistry **33**(25): 7937-7947.

De Palma, M. and C. E. Lewis (2011). "Cancer: Macrophages limit chemotherapy." Nature **472**(7343): 303-304.

Derossi, D., G. Chassaing, et al. (1998). "Trojan peptides: the penetratin system for intracellular delivery." Trends Cell Biol **8**(2): 84-87.

Deutsch, E. W., H. Lam, et al. (2008). "Data analysis and bioinformatics tools for tandem mass spectrometry in proteomics." Physiol Genomics **33**(1): 18-25.

DiPaola, R. S., J. Rinehart, et al. (2002). "Characterization of a novel prostate-specific antigen-activated peptide-doxorubicin conjugate in patients with prostate cancer." J Clin Oncol **20**(7): 1874-1879.

Dubowchik, G. M. and R. A. Firestone (1998). "Cathepsin B-sensitive dipeptide prodrugs. 1. A model study of structural requirements for efficient release of doxorubicin." Bioorg Med Chem Lett **8**(23): 3341-3346.

Duncan, R., P. Kopeckova-Rejmanova, et al. (1987). "Anticancer agents coupled to N-(2-hydroxypropyl)methacrylamide copolymers. I. Evaluation of daunomycin and puromycin conjugates in vitro." Br J Cancer **55**(2): 165-174.

Dyduch, G., K. Kaczmarczyk, et al. (2012). "Mast cells and cancer: enemies or allies?" Pol J Pathol **63**(1): 1-7.

Erickson, H. K., P. U. Park, et al. (2006). "Antibody-maytansinoid conjugates are activated in targeted cancer cells by lysosomal degradation and linker-dependent intracellular processing." Cancer Res **66**(8): 4426-4433.

Falnes, P. O. and S. Olsnes (1995). "Cell-mediated reduction and incomplete membrane translocation of diphtheria toxin mutants with internal disulfides in the A fragment." J Biol Chem **270**(35): 20787-20793.

Falnes, P. O. and K. Sandvig (2000). "Penetration of protein toxins into cells." Curr Opin Cell Biol **12**(4): 407-413.

Fanale, M. A., A. Forero-Torres, et al. (2012). "A phase I weekly dosing study of brentuximab vedotin in patients with relapsed/refractory CD30-positive hematologic malignancies." Clin Cancer Res **18**(1): 248-255.

Feener, E. P., W. C. Shen, et al. (1990). "Cleavage of disulfide bonds in endocytosed macromolecules. A processing not associated with lysosomes or endosomes." J Biol Chem **265**(31): 18780-18785.

Francisco, J. A., C. G. Cerveny, et al. (2003). "cAC10-vcMMAE, an anti-CD30-monomethyl auristatin E conjugate with potent and selective antitumor activity." Blood **102**(4): 1458-1465.

Frangioni, J. V. (2003). "In vivo near-infrared fluorescence imaging." Curr Opin Chem Biol **7**(5): 626-634.

Fritze, A., F. Hens, et al. (2006). "Remote loading of doxorubicin into liposomes driven by a transmembrane phosphate gradient." Biochim Biophys Acta **1758**(10): 1633-1640.

Gabizon, A., R. Catane, et al. (1994). "Prolonged circulation time and enhanced accumulation in malignant exudates of doxorubicin encapsulated in polyethylene-glycol coated liposomes." Cancer Res **54**(4): 987-992.

Gabizon, A., H. Shmeeda, et al. (2004). "Tumor cell targeting of liposome-entrapped drugs with phospholipid-anchored folic acid-PEG conjugates." <u>Adv Drug Deliv Rev</u> **56**(8): 1177-1192.

Gao, Z., H. D. Fain, et al. (2004). "Ultrasound-enhanced tumor targeting of polymeric micellar drug carriers." <u>Mol Pharm</u> **1**(4): 317-330.

Giepmans, B. N., S. R. Adams, et al. (2006). "The fluorescent toolbox for assessing protein location and function." <u>Science</u> **312**(5771): 217-224.

Gordon, A. N., J. T. Fleagle, et al. (2001). "Recurrent epithelial ovarian carcinoma: a randomized phase III study of pegylated liposomal doxorubicin versus topotecan." <u>J Clin Oncol</u> **19**(14): 3312-3322.

Goren, D., A. T. Horowitz, et al. (1996). "Targeting of stealth liposomes to erbB-2 (Her/2) receptor: in vitro and in vivo studies." <u>Br J Cancer</u> **74**(11): 1749-1756.

Gough, M., N. Killeen, et al. (2012). "Targeting macrophages in the tumor environment to enhance the efficacy of alphaOX40 therapy." <u>Immunology</u>.

Gradishar, W. J. (2006). "Albumin-bound paclitaxel: a next-generation taxane." <u>Expert Opin Pharmacother</u> **7**(8): 1041-1053.

Greish, K. (2007). "Enhanced permeability and retention of macromolecular drugs in solid tumors: a royal gate for targeted anticancer nanomedicines." <u>J Drug Target</u> **15**(7-8): 457-464.

Guo, X., F. Cui, et al. (2011). "Investigation of a new injectable thermosensitive hydrogel loading solid lipid nanoparticles." <u>Pharmazie</u> **66**(12): 948-952.

Haag, R. and F. Kratz (2006). "Polymer therapeutics: concepts and applications." <u>Angew Chem Int Ed Engl</u> **45**(8): 1198-1215.

Hallahan, D., L. Geng, et al. (2003). "Integrin-mediated targeting of drug delivery to irradiated tumor blood vessels." <u>Cancer Cell</u> **3**(1): 63-74.

Herter, S., D. E. Piper, et al. (2005). "Hepatocyte growth factor is a preferred in vitro substrate for human hepsin, a membrane-anchored serine protease implicated in prostate and ovarian cancers." <u>Biochem J</u> **390**(Pt 1): 125-136.

Hilgenbrink, A. R. and P. S. Low (2005). "Folate receptor-mediated drug targeting: from therapeutics to diagnostics." <u>J Pharm Sci</u> **94**(10): 2135-2146.

Hirsch, S. and S. Gordon (1983). "Polymorphic expression of a neutrophil differentiation antigen revealed by monoclonal antibody 7/4." <u>Immunogenetics</u> **18**(3): 229-239.

Hobbs, S. K., W. L. Monsky, et al. (1998). "Regulation of transport pathways in tumor vessels: role of tumor type and microenvironment." Proc Natl Acad Sci U S A **95**(8): 4607-4612.

Holmgren, A. and F. Aslund (1995). "Glutaredoxin." Methods Enzymol **252**: 283-292.

Holmgren, A. and M. Bjornstedt (1995). "Thioredoxin and thioredoxin reductase." Methods Enzymol **252**: 199-208.

Holness, C. L. and D. L. Simmons (1993). "Molecular cloning of CD68, a human macrophage marker related to lysosomal glycoproteins." Blood **81**(6): 1607-1613.

Hood, J. D. and D. A. Cheresh (2002). "Role of integrins in cell invasion and migration." Nat Rev Cancer **2**(2): 91-100.

Hooper, J. D., L. Campagnolo, et al. (2003). "Mouse matriptase-2: identification, characterization and comparative mRNA expression analysis with mouse hepsin in adult and embryonic tissues." Biochem J **373**(Pt 3): 689-702.

Hwang, C., A. J. Sinskey, et al. (1992). "Oxidized redox state of glutathione in the endoplasmic reticulum." Science **257**(5076): 1496-1502.

Jabaiah, A. and P. S. Daugherty (2011). "Directed evolution of protease beacons that enable sensitive detection of endogenous MT1-MMP activity in tumor cell lines." Chem Biol **18**(3): 392-401.

Jensen, K. S., R. E. Hansen, et al. (2009). "Kinetic and thermodynamic aspects of cellular thiol-disulfide redox regulation." Antioxid Redox Signal **11**(5): 1047-1058.

Jensen, P. E. (1995). "Antigen unfolding and disulfide reduction in antigen presenting cells." Semin Immunol **7**(6): 347-353.

Jiang, T., E. S. Olson, et al. (2004). "Tumor imaging by means of proteolytic activation of cell-penetrating peptides." Proc Natl Acad Sci U S A **101**(51): 17867-17872.

Jones, R. A., C. Y. Cheung, et al. (2003). "Poly(2-alkylacrylic acid) polymers deliver molecules to the cytosol by pH-sensitive disruption of endosomal vesicles." Biochem J **372**(Pt 1): 65-75.

Kalli, K. R., A. L. Oberg, et al. (2008). "Folate receptor alpha as a tumor target in epithelial ovarian cancer." Gynecol Oncol **108**(3): 619-626.

Kameyama, S., M. Horie, et al. (2007). "Acid wash in determining cellular uptake of Fab/cell-permeating peptide conjugates." Biopolymers **88**(2): 98-107.

Karmali, P. P., V. R. Kotamraju, et al. (2009). "Targeting of albumin-embedded paclitaxel nanoparticles to tumors." Nanomedicine **5**(1): 73-82.

Keir, C. H. and L. T. Vahdat (2012). "The use of an antibody drug conjugate, glembatumumab vedotin (CDX-011), for the treatment of breast cancer." Expert Opin Biol Ther **12**(2): 259-263.

Kellogg, B. A., L. Garrett, et al. (2011). "Disulfide-linked antibody-maytansinoid conjugates: optimization of in vivo activity by varying the steric hindrance at carbon atoms adjacent to the disulfide linkage." Bioconjug Chem **22**(4): 717-727.

Kirpotin, D. B., D. C. Drummond, et al. (2006). "Antibody targeting of long-circulating lipidic nanoparticles does not increase tumor localization but does increase internalization in animal models." Cancer Res **66**(13): 6732-6740.

Klibanov, A. L., K. Maruyama, et al. (1990). "Amphipathic polyethyleneglycols effectively prolong the circulation time of liposomes." FEBS Lett **268**(1): 235-237.

Kobbert, C., R. Apps, et al. (2000). "Current concepts in neuroanatomical tracing." Prog Neurobiol **62**(4): 327-351.

Komohara, Y., H. Hasita, et al. (2011). "Macrophage infiltration and its prognostic relevance in clear cell renal cell carcinoma." Cancer Sci **102**(7): 1424-1431.

Komohara, Y., J. Hirahara, et al. (2006). "AM-3K, an anti-macrophage antibody, recognizes CD163, a molecule associated with an anti-inflammatory macrophage phenotype." J Histochem Cytochem **54**(7): 763-771.

Konig, K., K. Schenke-Layland, et al. (2005). "Multiphoton autofluorescence imaging of intratissue elastic fibers." Biomaterials **26**(5): 495-500.

Kosuge, M., T. Takeuchi, et al. (2008). "Cellular internalization and distribution of arginine-rich peptides as a function of extracellular peptide concentration, serum, and plasma membrane associated proteoglycans." Bioconjug Chem **19**(3): 656-664.

Kratz, F. (2008). "Albumin as a drug carrier: design of prodrugs, drug conjugates and nanoparticles." J Control Release **132**(3): 171-183.

Kratz, F., R. Muller-Driver, et al. (2000). "A novel macromolecular prodrug concept exploiting endogenous serum albumin as a drug carrier for cancer chemotherapy." J Med Chem **43**(7): 1253-1256.

Kratz, F., A. Warnecke, et al. (2002). "Probing the cysteine-34 position of endogenous serum albumin with thiol-binding doxorubicin derivatives. Improved efficacy of an acid-sensitive doxorubicin derivative with specific albumin-binding properties compared to that of the parent compound." J Med Chem **45**(25): 5523-5533.

Kurahara, H., H. Shinchi, et al. (2011). "Significance of M2-polarized tumor-associated macrophage in pancreatic cancer." J Surg Res **167**(2): e211-219.

Laginha, K. M., E. H. Moase, et al. (2008). "Bioavailability and therapeutic efficacy of HER2 scFv-targeted liposomal doxorubicin in a murine model of HER2-overexpressing breast cancer." J Drug Target **16**(7): 605-610.

Larina, I. V., B. M. Evers, et al. (2005). "Enhancement of drug delivery in tumors by using interaction of nanoparticles with ultrasound radiation." Technol Cancer Res Treat **4**(2): 217-226.

Lasic, D. D., B. Ceh, et al. (1995). "Transmembrane gradient driven phase transitions within vesicles: lessons for drug delivery." Biochim Biophys Acta **1239**(2): 145-156.

Lee, H. J. and W. M. Pardridge (2001). "Pharmacokinetics and delivery of tat and tat-protein conjugates to tissues in vivo." Bioconjug Chem **12**(6): 995-999.

Leitner, A., T. Walzthoeni, et al. (2010). "Probing native protein structures by chemical cross-linking, mass spectrometry, and bioinformatics." Mol Cell Proteomics **9**(8): 1634-1649.

Leuschner, F., P. Dutta, et al. (2011). "Therapeutic siRNA silencing in inflammatory monocytes in mice." Nat Biotechnol **29**(11): 1005-1010.

Lewis, C. E. and J. W. Pollard (2006). "Distinct role of macrophages in different tumor microenvironments." Cancer Res **66**(2): 605-612.

Li, L., L. Huang, et al. (2010). "IL-17 produced by neutrophils regulates IFN-gamma-mediated neutrophil migration in mouse kidney ischemia-reperfusion injury." J Clin Invest **120**(1): 331-342.

Li, W., F. Nicol, et al. (2004). "GALA: a designed synthetic pH-responsive amphipathic peptide with applications in drug and gene delivery." Adv Drug Deliv Rev **56**(7): 967-985.

Litzinger, D. C., A. M. Buiting, et al. (1994). "Effect of liposome size on the circulation time and intraorgan distribution of amphipathic poly(ethylene glycol)-containing liposomes." Biochim Biophys Acta **1190**(1): 99-107.

Liu, Y., K. M. Bajjuri, et al. (2012). "Targeting cell surface alpha(v)beta(3) integrin increases therapeutic efficacies of a legumain protease-activated auristatin prodrug." Mol Pharm **9**(1): 168-175.

Lohman, J. R. and S. J. Remington (2008). "Development of a family of redox-sensitive green fluorescent protein indicators for use in relatively oxidizing subcellular environments." Biochemistry **47**(33): 8678-8688.

Low, P. S. and S. A. Kularatne (2009). "Folate-targeted therapeutic and imaging agents for cancer." Curr Opin Chem Biol **13**(3): 256-262.

Luong, A., T. Issarapanichkit, et al. (2010). "pH-Sensitive, N-ethoxybenzylimidazole (NEBI) bifunctional crosslinkers enable triggered release of therapeutics from drug delivery carriers." Org Biomol Chem **8**(22): 5105-5109.

Maeda, H., J. Wu, et al. (2000). "Tumor vascular permeability and the EPR effect in macromolecular therapeutics: a review." J Control Release **65**(1-2): 271-284.

Mai, J. C., Z. Mi, et al. (2001). "A proapoptotic peptide for the treatment of solid tumors." Cancer Res **61**(21): 7709-7712.

Maloney, D. G., A. J. Grillo-Lopez, et al. (1997). "IDEC-C2B8 (Rituximab) anti-CD20 monoclonal antibody therapy in patients with relapsed low-grade non-Hodgkin's lymphoma." Blood **90**(6): 2188-2195.

Marangos, N., R. B. Illing, et al. (2001). "In vivo visualization of the cochlear nerve and nuclei with fluorescent axonal tracers." Hear Res **162**(1-2): 48-52.

Matsumura, Y., T. Hamaguchi, et al. (2004). "Phase I clinical trial and pharmacokinetic evaluation of NK911, a micelle-encapsulated doxorubicin." Br J Cancer **91**(10): 1775-1781.

Matsumura, Y. and H. Maeda (1986). "A new concept for macromolecular therapeutics in cancer chemotherapy: mechanism of tumoritropic accumulation of proteins and the antitumor agent smancs." Cancer Res **46**(12 Pt 1): 6387-6392.

Meister, A. and M. E. Anderson (1983). "Glutathione." Annu Rev Biochem **52**: 711-760.

Melikov, K. and L. V. Chernomordik (2005). "Arginine-rich cell penetrating peptides: from endosomal uptake to nuclear delivery." Cell Mol Life Sci **62**(23): 2739-2749.

Miotti, S., P. Facheris, et al. (1995). "Growth of ovarian-carcinoma cell lines at physiological folate concentration: effect on folate-binding protein expression in vitro and in vivo." Int J Cancer **63**(3): 395-401.

Mirsalis, J. C., J. Schindler-Horvat, et al. (1999). "Toxicity of dolastatin 10 in mice, rats and dogs and its clinical relevance." Cancer Chemother Pharmacol **44**(5): 395-402.

Moghimi, S. M., A. C. Hunter, et al. (2001). "Long-circulating and target-specific nanoparticles: theory to practice." Pharmacol Rev **53**(2): 283-318.

Mohammad, R. M., C. Limvarapuss, et al. (1999). "A new tubulin polymerization inhibitor, auristatin PE, induces tumor regression in a human Waldenstrom's macroglobulinemia xenograft model." Int J Oncol **15**(2): 367-372.

Mohler, W., A. C. Millard, et al. (2003). "Second harmonic generation imaging of endogenous structural proteins." Methods **29**(1): 97-109.

Muggia, F. M. (2001). "Liposomal encapsulated anthracyclines: new therapeutic horizons." Curr Oncol Rep **3**(2): 156-162.

Muggia, F. M., J. D. Hainsworth, et al. (1997). "Phase II study of liposomal doxorubicin in refractory ovarian cancer: antitumor activity and toxicity modification by liposomal encapsulation." J Clin Oncol **15**(3): 987-993.

Murphy, E. A., B. K. Majeti, et al. (2008). "Nanoparticle-mediated drug delivery to tumor vasculature suppresses metastasis." Proc Natl Acad Sci U S A **105**(27): 9343-9348.

Murphy, E. A., B. K. Majeti, et al. (2011). "Targeted nanogels: a versatile platform for drug delivery to tumors." Mol Cancer Ther **10**(6): 972-982.

Murray, P. J. and T. A. Wynn (2011). "Protective and pathogenic functions of macrophage subsets." Nat Rev Immunol **11**(11): 723-737.

Nakase, I., M. Niwa, et al. (2004). "Cellular uptake of arginine-rich peptides: roles for macropinocytosis and actin rearrangement." Mol Ther **10**(6): 1011-1022.

Navath, R. S., Y. E. Kurtoglu, et al. (2008). "Dendrimer-drug conjugates for tailored intracellular drug release based on glutathione levels." Bioconjug Chem **19**(12): 2446-2455.

Ng, K. T., X. Qi, et al. (2011). "Overexpression of matrix metalloproteinase-12 (MMP-12) correlates with poor prognosis of hepatocellular carcinoma." Eur J Cancer **47**(15): 2299-2305.

Nguyen, Q. T., E. S. Olson, et al. (2010). "Surgery with molecular fluorescence imaging using activatable cell-penetrating peptides decreases residual cancer and improves survival." Proc Natl Acad Sci U S A **107**(9): 4317-4322.

Noiva, R. and W. J. Lennarz (1992). "Protein disulfide isomerase. A multifunctional protein resident in the lumen of the endoplasmic reticulum." J Biol Chem **267**(6): 3553-3556.

O'Malley, M. R., J. E. Wittkopf, et al. (2006). "Fluorescent retrograde axonal tracing of the facial nerve." Laryngoscope **116**(10): 1792-1797.

Olson, E. S., T. A. Aguilera, et al. (2009). "In vivo characterization of activatable cell penetrating peptides for targeting protease activity in cancer." Integr Biol (Camb) **1**(5-6): 382-393.

Olson, E. S., T. Jiang, et al. (2010). "Activatable cell penetrating peptides linked to nanoparticles as dual probes for in vivo fluorescence and MR imaging of proteases." Proc Natl Acad Sci U S A **107**(9): 4311-4316.

Orditura, M., F. Quaglia, et al. (2004). "Pegylated liposomal doxorubicin: pharmacologic and clinical evidence of potent antitumor activity with reduced anthracycline-induced cardiotoxicity (review)." Oncol Rep **12**(3): 549-556.

Ouyang, M., H. Huang, et al. (2010). "Simultaneous visualization of protumorigenic Src and MT1-MMP activities with fluorescence resonance energy transfer." Cancer Res **70**(6): 2204-2212.

Overall, C. M. and O. Kleifeld (2006). "Tumour microenvironment - opinion: validating matrix metalloproteinases as drug targets and anti-targets for cancer therapy." Nat Rev Cancer **6**(3): 227-239.

Pan, J. and S. S. Feng (2009). "Targeting and imaging cancer cells by folate-decorated, quantum dots (QDs)- loaded nanoparticles of biodegradable polymers." Biomaterials **30**(6): 1176-1183.

Pan, X. Q. and R. J. Lee (2005). "In vivo antitumor activity of folate receptor-targeted liposomal daunorubicin in a murine leukemia model." Anticancer Res **25**(1A): 343-346.

Park, J. W. (2002). "Liposome-based drug delivery in breast cancer treatment." Breast Cancer Res **4**(3): 95-99.

Pasqualini, R. and E. Ruoslahti (1996). "Organ targeting in vivo using phage display peptide libraries." Nature **380**(6572): 364-366.

Pastorino, F., D. Di Paolo, et al. (2008). "Enhanced antitumor efficacy of clinical-grade vasculature-targeted liposomal doxorubicin." Clin Cancer Res **14**(22): 7320-7329.

Pettit, G. R. (1997). "The dolastatins." Fortschr Chem Org Naturst **70**: 1-79.

Pierschbacher, M. D. and E. Ruoslahti (1984). "Cell attachment activity of fibronectin can be duplicated by small synthetic fragments of the molecule." Nature **309**(5963): 30-33.

Plank, C., B. Oberhauser, et al. (1994). "The influence of endosome-disruptive peptides on gene transfer using synthetic virus-like gene transfer systems." J Biol Chem **269**(17): 12918-12924.

Qian, B. Z. and J. W. Pollard (2010). "Macrophage diversity enhances tumor progression and metastasis." Cell **141**(1): 39-51.

Qian, Z. M., H. Li, et al. (2002). "Targeted drug delivery via the transferrin receptor-mediated endocytosis pathway." Pharmacol Rev **54**(4): 561-587.

Qu, P., H. Du, et al. (2009). "Matrix metalloproteinase 12 overexpression in lung epithelial cells plays a key role in emphysema to lung bronchioalveolar adenocarcinoma transition." Cancer Res **69**(18): 7252-7261.

Rapoport, N. Y., D. A. Christensen, et al. (2004). "Ultrasound-triggered drug targeting of tumors in vitro and in vivo." Ultrasonics **42**(1-9): 943-950.

Richard, J. P., K. Melikov, et al. (2003). "Cell-penetrating peptides. A reevaluation of the mechanism of cellular uptake." J Biol Chem **278**(1): 585-590.

Richmond, F. J., R. Gladdy, et al. (1994). "Efficacy of seven retrograde tracers, compared in multiple-labelling studies of feline motoneurones." J Neurosci Methods **53**(1): 35-46.

Ruoslahti, E. (2002). "Specialization of tumour vasculature." Nat Rev Cancer **2**(2): 83-90.

Ryder, M., R. A. Ghossein, et al. (2008). "Increased density of tumor-associated macrophages is associated with decreased survival in advanced thyroid cancer." Endocr Relat Cancer **15**(4): 1069-1074.

Ryser, H. J., R. Mandel, et al. (1991). "Cell surface sulfhydryls are required for the cytotoxicity of diphtheria toxin but not of ricin in Chinese hamster ovary cells." J Biol Chem **266**(28): 18439-18442.

Safra, T., S. Groshen, et al. (2001). "Treatment of patients with ovarian carcinoma with pegylated liposomal doxorubicin: analysis of toxicities and predictors of outcome." Cancer **91**(1): 90-100.

Saito, G., G. L. Amidon, et al. (2003). "Enhanced cytosolic delivery of plasmid DNA by a sulfhydryl-activatable listeriolysin O/protamine conjugate utilizing cellular reducing potential." Gene Ther **10**(1): 72-83.

Saito, G., J. A. Swanson, et al. (2003). "Drug delivery strategy utilizing conjugation via reversible disulfide linkages: role and site of cellular reducing activities." Adv Drug Deliv Rev **55**(2): 199-215.

Sarrio, D., S. M. Rodriguez-Pinilla, et al. (2008). "Epithelial-mesenchymal transition in breast cancer relates to the basal-like phenotype." Cancer Res **68**(4): 989-997.

Sato, H., T. Takino, et al. (2005). "Roles of membrane-type matrix metalloproteinase-1 in tumor invasion and metastasis." Cancer Sci **96**(4): 212-217.

Schadlich, A., H. Caysa, et al. (2011). "Tumor accumulation of NIR fluorescent PEG-PLA nanoparticles: impact of particle size and human xenograft tumor model." ACS Nano **5**(11): 8710-8720.

Schaer, D. J., F. S. Boretti, et al. (2001). "Molecular cloning and characterization of the mouse CD163 homologue, a highly glucocorticoid-inducible member of the scavenger receptor cysteine-rich family." Immunogenetics **53**(2): 170-177.

Schenke-Layland, K., I. Riemann, et al. (2005). "Imaging of cardiovascular structures using near-infrared femtosecond multiphoton laser scanning microscopy." J Biomed Opt **10**(2): 024017.

Schwarze, S. R., A. Ho, et al. (1999). "In vivo protein transduction: delivery of a biologically active protein into the mouse." Science **285**(5433): 1569-1572.

Schwarze, S. R., K. A. Hruska, et al. (2000). "Protein transduction: unrestricted delivery into all cells?" Trends Cell Biol **10**(7): 290-295.

Senter, P. D. (2009). "Potent antibody drug conjugates for cancer therapy." Curr Opin Chem Biol **13**(3): 235-244.

Seymour, L. W., D. R. Ferry, et al. (2002). "Hepatic drug targeting: phase I evaluation of polymer-bound doxorubicin." J Clin Oncol **20**(6): 1668-1676.

Seymour, L. W., D. R. Ferry, et al. (2009). "Phase II studies of polymer-doxorubicin (PK1, FCE28068) in the treatment of breast, lung and colorectal cancer." Int J Oncol **34**(6): 1629-1636.

Shabo, I. and J. Svanvik (2011). "Expression of macrophage antigens by tumor cells." Adv Exp Med Biol **714**: 141-150.

Shmeeda, H., L. Mak, et al. (2006). "Intracellular uptake and intracavitary targeting of folate-conjugated liposomes in a mouse lymphoma model with up-regulated folate receptors." Mol Cancer Ther **5**(4): 818-824.

Sica, A., T. Schioppa, et al. (2006). "Tumour-associated macrophages are a distinct M2 polarised population promoting tumour progression: potential targets of anti-cancer therapy." Eur J Cancer **42**(6): 717-727.

Silletti, S., T. Kessler, et al. (2001). "Disruption of matrix metalloproteinase 2 binding to integrin alpha vbeta 3 by an organic molecule inhibits angiogenesis and tumor growth in vivo." Proc Natl Acad Sci U S A **98**(1): 119-124.

Snyder, E. L., B. R. Meade, et al. (2003). "Anti-cancer protein transduction strategies: reconstitution of p27 tumor suppressor function." J Control Release **91**(1-2): 45-51.

Society, A. C. (2012). "Cancer Facts & Figures 2012."

Sonawane, N. D., F. C. Szoka, Jr., et al. (2003). "Chloride accumulation and swelling in endosomes enhances DNA transfer by polyamine-DNA polyplexes." J Biol Chem **278**(45): 44826-44831.

Speck, U. (2008). "Contrast agents: X-ray contrast agents and molecular imaging--a contradiction?" Handb Exp Pharmacol(185 Pt 1): 167-175.

Stubbs, M., P. M. McSheehy, et al. (2000). "Causes and consequences of tumour acidity and implications for treatment." Mol Med Today **6**(1): 15-19.

Sulahian, T. H., P. Hogger, et al. (2000). "Human monocytes express CD163, which is upregulated by IL-10 and identical to p155." Cytokine **12**(9): 1312-1321.

Talvensaari-Mattila, A., P. Paakko, et al. (2003). "Matrix metalloproteinase-2 (MMP-2) is associated with survival in breast carcinoma." Br J Cancer **89**(7): 1270-1275.

Turk, M. J., G. J. Breur, et al. (2002). "Folate-targeted imaging of activated macrophages in rats with adjuvant-induced arthritis." Arthritis Rheum **46**(7): 1947-1955.

Tyagi, M., M. Rusnati, et al. (2001). "Internalization of HIV-1 tat requires cell surface heparan sulfate proteoglycans." J Biol Chem **276**(5): 3254-3261.

Vives, E. (2003). "Cellular uptake [correction of utake] of the Tat peptide: an endocytosis mechanism following ionic interactions." J Mol Recognit **16**(5): 265-271.

Vives, E. (2005). "Present and future of cell-penetrating peptide mediated delivery systems: "is the Trojan horse too wild to go only to Troy?"." J Control Release **109**(1-3): 77-85.

Vives, E., J. P. Richard, et al. (2003). "TAT peptide internalization: seeking the mechanism of entry." Curr Protein Pept Sci **4**(2): 125-132.

Wadia, J. S., R. V. Stan, et al. (2004). "Transducible TAT-HA fusogenic peptide enhances escape of TAT-fusion proteins after lipid raft macropinocytosis." Nat Med **10**(3): 310-315.

Weissleder, R. and M. J. Pittet (2008). "Imaging in the era of molecular oncology." Nature **452**(7187): 580-589.

Whitney, M., J. L. Crisp, et al. (2010). "Parallel in vivo and in vitro selection using phage display identifies protease-dependent tumor-targeting peptides." J Biol Chem **285**(29): 22532-22541.

Xiong, X. B., Y. Huang, et al. (2005). "Enhanced intracellular delivery and improved antitumor efficacy of doxorubicin by sterically stabilized liposomes modified with a synthetic RGD mimetic." J Control Release **107**(2): 262-275.

Yang, J., H. Chen, et al. (2006). "Evaluation of disulfide reduction during receptor-mediated endocytosis by using FRET imaging." Proc Natl Acad Sci U S A **103**(37): 13872-13877.

Yang, J. J., S. A. Kularatne, et al. (2012). "Characterization of in vivo disulfide-reduction mediated drug release in mouse kidneys." Mol Pharm **9**(2): 310-317.

Yang, S. and S. May (2008). "Release of cationic polymer-DNA complexes from the endosome: A theoretical investigation of the proton sponge hypothesis." J Chem Phys **129**(18): 185105.

Yoshimori, T., A. Yamamoto, et al. (1991). "Bafilomycin A1, a specific inhibitor of vacuolar-type H(+)-ATPase, inhibits acidification and protein degradation in lysosomes of cultured cells." J Biol Chem **266**(26): 17707-17712.

Zhu, L., J. Xie, et al. (2011). "Dual-functional, receptor-targeted fluorogenic probe for in vivo imaging of extracellular protease expressions." Bioconjug Chem **22**(6): 1001-1005.

Zhu, X. D., J. B. Zhang, et al. (2008). "High expression of macrophage colony-stimulating factor in peritumoral liver tissue is associated with poor survival after curative resection of hepatocellular carcinoma." J Clin Oncol **26**(16): 2707-2716.